THE UNIVERSITY *of* EDINBURGH

$mCCD_{cl1}$ Cells Exhibit a Transitional Phenotype:

Implications for Collecting Duct Plasticity

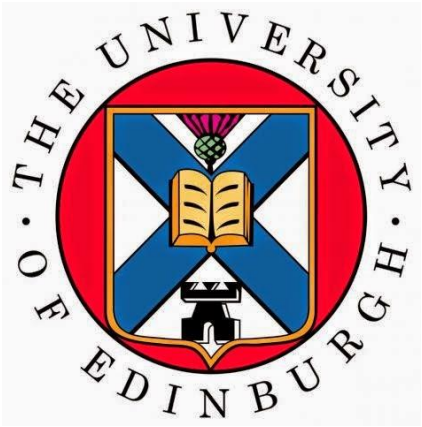

Adrienne Madeleine Assmus

Centre for Cardiovascular Science

University of Edinburgh

A thesis submitted for the degree of

PhD

March 2018

Declaration

I declare that this thesis and the work presented in it are the result of my own independent investigation except where stated in the text. This work has not been and is not currently submitted for any other degree or professional qualification from this or any other university. The collaborative contributions have been indicated clearly and acknowledged.

June 2018

Adrienne Madeleine Assmus

Acknowledgements

First and foremost, I must thank my supervisor John, for all the help, support and opportunities given during this PhD. Your guidance has been invaluable and has allowed me to grow as a student and scientist. I also really appreciated the long discussions about bio-engineering and the ideas exchanged during these times. A massive amount of thanks goes to Linda, for the great help provided during these years, from proof-reading to genetics knowledge. Thank you to the rest of my advisory committee, Matt, Margarete, and Will, who have given me great advice at key moments of my project. I greatly appreciated you input and guidance.

I cannot thank Audrey enough, who have provided sorely needed lab expertise and help during the project. I owe you a great deal and can only hope my TC skills can be compared to yours. Thank you so much for all your work and advice! Thank you to the fantastic staff in the histology lab, that has given me great advice and useful tips for my experiments, and have always answered my questions with patience and skill. I wouldn't have been able to produce any good image without the help of the amazing Charlotte, Rachel, and Seb, who helped me with all the microscopy equipment, and who in general were patient enough to answer so many questions and give so much help, from kidney expertise to PCR protocols and language troubles. I must add Jess to that list; you all have shared so much expertise and knowledge and I can't be thankful enough. I also need to specially thank Morag, who has been absolutely fantastic in teaching me electrophysiology and was kind enough to lend me her equipment. Your input has been invaluable. From my visit to Sheffield, I must thank John for welcoming me to your lab and Colin for sharing your expertise in polymers. In Edinburgh, thanks so much to Richard for your help with the 3D printing, and your kindness. It was a pleasure to collaborate with you.

To all my friends in Scotland, Charlotte, Rachel, Jess, Seb, Sofia, Morag, Nicole, for all the fun times, hiking, bubbles, movies, week-ends and shared birthdays. To complete the office crew, I must mention Amelia and Rob. Thanks to my friends in France, Sam, Adri, and Alex, for the encouragements and the memories. I'm not seeing you guys enough. Finally, I want to mention my family, who has been supporting me unconditionally during my studies. Maman, Papa, Adele, Jaja, Mamie, thanks so much; I hope I can make you proud.

Abstract

The cortical collecting duct of the mammalian kidney plays a critical role in the regulation of body volume, sodium pH and osmolarity and is composed of two distinct cells types, principal cells and intercalated cells. Each cell type is detectable in the kidney by the localization of specific transport proteins such as Aqp2 and ENaC in principal cells and V-ATPase B1 and Cx30 in intercalated cells. $mCCD_{cl1}$ cells have been widely used as a mouse principal cell line on the basis of their physiological characteristics. In this study, the $mCCD_{cl1}$ parental cell line and three sub-lines cloned from isolated single cells (Ed1, Ed2, and Ed3) were grown on filters to assess their transepithelial resistance, transepithelial voltage, equivalent short circuit current and expression of the cell-specific markers Aqp2, ENaC, V-ATPaseB1 and Cx30. The parental $mCCD_{cl1}$ cell line presented amiloride-sensitive electrogenic sodium transport indicative of principal cell function, however immunocytochemistry and RT-PCR showed that some cells expressed the intercalated cell-specific markers V-ATPase B1 and Cx30, including a subset of cells also positive for Aqp2 and ENaC. The three subclonal lines contained cells that were positive for both intercalated and principal cell-specific markers. The vertical transmission of both principal and intercalated cell characteristics via single cell cloning, reveals the plasticity of $mCCD_{cl1}$ cells, and a direct lineage relationship between these two physiologically important cell types, and is consistent with $mCCD_{cl1}$ cells being precursor cells. For observation of live $mCCD_{cl1}$ in an environment closer to *in vivo* conditions, a model of collecting duct was designed and developed using 3D printing of porous polymers. $mCCD_{cl1}$ were cultured successfully and demonstrated improved characteristics compared to classic culture such as improved lifespan, different morphology and increased protein expression, and retained their phenotypic plasticity.

Contents

List of Figures

List of Tables

List of Abbreviations

3D	three-dimensional
11βHSD2	11β-hydroxysteroid dehydrogenase type 2
AE1	anion exchanger 1
Aqp2	aquaporin 2
ATP	adenosine triphosphate
BK	large conductance potassium channel
BMP7	bone morphogenic protein 7
Bp	base-pairs
cAMP	cyclic adenosine monophosphate
CCD	cortical collecting duct
cDNA	complementary DNA
CNT	connecting tubule
Cx30	connexin 30
DAPI	4',6-diamidino-2-phenilindol
DCT	distal convoluted tubule
ddH_2O	deionised water
DMSO	dimethyl sulfoxide
DNA	deoxyribonucleic acid
ECM	extracellular matrix
ENaC	epithelial sodium channel
ES cells	embryonic stem cell
EVOM	epithelial volt-ohm meter
FITC	fluorescein isothiocyanate
GDNF	glial-derived neurotrophic factor
GR	glucocorticoid receptor
HGF	hepatocyte growth factor
Hsd11b2	mouse gene Hsd11b2 (encoding 11βHSD2)
IC	intercalated cell
IC_{50}	half maximal inhibitory concentration
I_{sc}	equivalent short-circuit current
ID	internal diameter
IFCs	injection and flow chambers
Kb	kilo-base-pairs
KCC	potassium/chloride co-transporter
KJU	Koefoed-Johnsen and Ussing
$mCCD_{cl1}$ cells	mouse cortical collecting duct clone 1 cells

MDCK	Madin-Darby canine kidney epithelial cells
MEK	mouse embryonic kidney cells
min	minute
MR	mineralocorticoid receptor
Na^+/K^+ ATPase	ATP-dependant sodium/potassium exchanger
NCC	thiazide-sensitive sodium/chloride co-transporter
NKCC2	sodium/potassium/2 chloride co-transporter
OD	outer diameter
P63	transformation-related protein 63
PC	principal cell
PCT	proximal convoluted tubule
PBS	phosphate-buffered saline
PCR	polymerase chain reaction
PDMS	polydimethylsiloxane
PFA	paraformaldehyde
PKD	polycystic kidney disease
PLGA	poly(lactic) acid
PolyHIPEs	porous polymers from high internal phase emulsions
PTEC	proximal tubule epithelial cells
R_{te}	transepithelial resistance
RAAS	renin-angiotensin-aldosterone system
RNA	ribonucleic acid
ROMK	renal outer medullary potassium channel
RT-PCR	reverse transcriptase polymerase chain reaction
SAME	syndrome of apparent mineralocorticoid excess
SD	standard deviation
SGK-1	serine/threonine protein kinase 1
SPs	serine proteases
TGFβ	transforming growth factor β
TRITC	tetramethylrhodamine
UB	ureteric bud
UBTC	ureteric bud tip cells
UV	ultraviolet
V_{te}	transepithelial voltage
V-ATPase	vacuolar proton pump
WT	wild type

1 Introduction

1.1 Thesis overview

The regulation of blood pressure partly rests in the kidney, where homeostasis is maintained by coordinated physiological actions, including water and sodium reabsorption, acid balance, and potassium level regulation by the collecting duct, the final filtration segment of the kidney. The study of collecting duct function relies on animal models, or on classic culture of immortalized cell lines like the $mCCD_{cl1}$ cells (mouse cortical collecting duct cells), that offer an appropriate response to physiological concentrations of hormones.

Plasticity has recently been demonstrated *in vivo* in collecting ducts. The ratio of two cell types, principal and intercalated cells, that compose the collecting duct can change under pathological conditions, and transition cells are observed. Although $mCCD_{cl1}$ cells have been shown to be a good model for studying the transport properties of the principal cells (PCs) of the collecting duct, a lot of questions remain about the cell line properties and the capacity to extend the model to intercalated cells (ICs) functions or collecting duct development.

3D biological models have been shown to be a viable solution to replace some animal models or to enable some cell functions that are inactive in classic cell culture conditions. A 3D model would allow for an environment closer to *in vivo* conditions, particularly important in the kidney. The development of an adapted 3D model is therefore the next logical step for renal transporting cells, and for $mCCD_{cl1}$ in particular, considering the demonstrated physiological abilities of the cell line. Development of this model of collecting duct may contribute to the development of new physiological studies and resulting new therapies.

1.2 Renal tubular anatomy and functions

1.2.1 Kidney diseases

Kidney malfunctions are often life threatening and require intensive treatment. Kidney disease is tightly linked to cardiovascular disease: heart failure is the leading cause of death in end-stage renal disease, and subjects with chronic renal failure are exposed to increased morbidity and mortality as a result of cardiovascular events [1], [2]. This link is due to the effect of sodium intake on extracellular fluid volume homeostasis, directly impacting blood pressure, the regulation of which is sacrificed in favour of sodium balance [3]. Elevated blood pressure also has a deleterious effect on the highly-vascularized kidney structures, leading to a worsening disease feedback loop and chronic kidney disease [4].

1.2.2 Anatomy and physiology of the nephron

The basic functional and structural unit of the kidney is the nephron (Figure 1.1). The human kidney contains between 800,000 to 1.5 million nephrons [5], located throughout the renal cortex and medulla. The nephron is composed of three main parts: the glomerulus, Bowman's capsule, and the tubule. The tubule itself possesses five functionally different parts, including the collecting duct (described in more details in Section 1.2.3). The glomerulus is situated in the renal cortex, as well as the first (or proximal) segment of the tubule. The tubule then loops down in the renal medulla, forms the loop of Henle, and returns to the renal cortex [6]. This convoluted anatomy allows for anatomical proximity and better feedback between the different segments, which possess different but tightly linked functions [7].

The main kidney function is to produce urine, but more specifically to regulate the pH and concentration of solutes, electrolytes, metabolites, and water in the body. The concentration of solutes is independently regulated, a consequence of tubular anatomy

and highly specialized cell functions throughout the nephron, leading to a selective reabsorption along the nephron. Tubules are lined with a monolayer of transporting polarized epithelial cells. Tubular cells express different proteins on their apical (along the tubular filtrate) and basolateral (along the peritubular blood capillaries) membranes, meaning that the transport paths of specific molecules are unilateral [8]. Together with reabsorption, kidneys also have a filtration function enabled by the glomerular filtration barrier, depending on the size and charge of molecules. Kidney functions are highly regulated by endocrine hormones such as aldosterone or vasopressin (antidiuretic) [9].

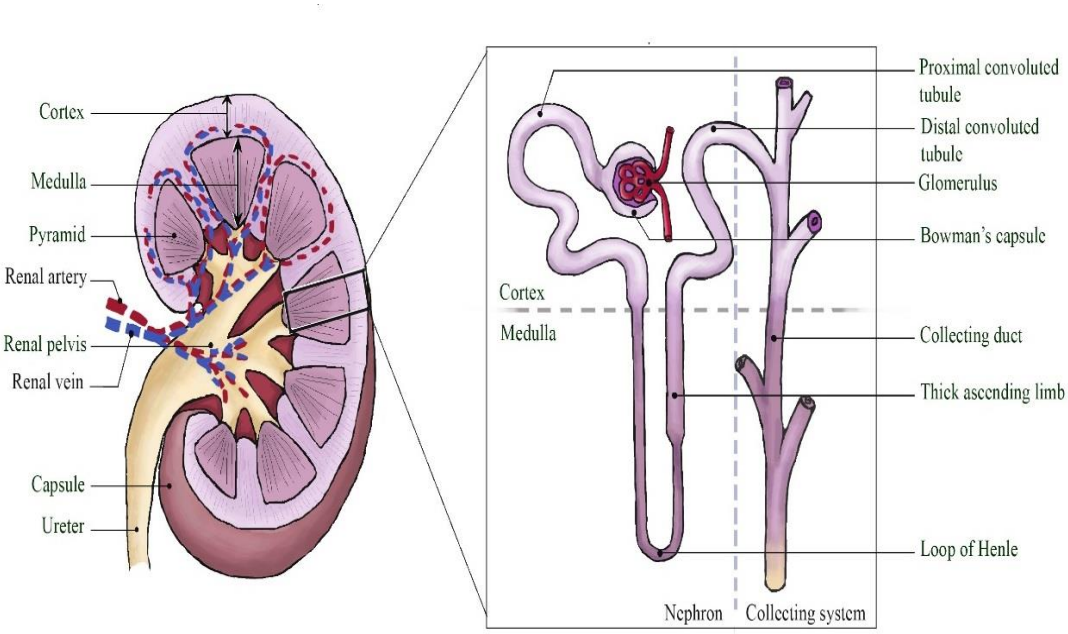

Figure 1.1. Anatomy of the kidney and nephron. Blood is brought to the nephron through the renal afferent arteries (red dotted lines) that lead to the glomeruli in the renal cortex. After filtration in the glomeruli, the blood heads to the peritubular capillary network where it will keep exchanging water and solutes with the nephron. It then exits the kidney through the renal veins (blue dotted lines). The filtrate travels through the nephron going back and forth between the renal cortex and renal medulla. The concentrated filtrate becomes urine, and flows in the renal pelvis and the ureter to be eliminated.

1.2.2.1 Glomerulus and Bowman's capsule

Situated in the renal cortex, the glomerulus consists in a network of capillaries delivering the blood from an afferent arteriole of the renal circulation to the first stage of the filtration process. The extremely effective filtration process in the glomerulus results from the high pressure in the afferent arterioles, pushing the plasma filtrate through the epithelial cells forming the filtration barrier [10]. The blood exits the glomerulus through an efferent arteriole. The Bowman's capsule, the sac surrounding the glomerulus, receives the filtrate. Typically, the glomerulus allows small, positively charges molecules to pass freely (e.g. Na^+, K^+), while retaining large, negatively charged molecules (e.g. hemoglobin, albumin) [11]. In addition to an epithelial lining, the glomerulus and Bowman's capsule possess specialized cells such as intraglomerular mesangial cells, which can reduce the glomerular surface area to control the filtration rate, and renin cells on the afferent arteriole, which play an important role in the renin-angiotensin system [12] and the regulation of blood pressure.

1.2.2.2 Proximal convoluted tubule (PCT)

Situated just after the Bowman's capsule, the main function of the PCT is to regulate the pH of the filtrate. The PCT possesses a distinctive brush border epithelium to increase the surface area of the cells, and numerous acid-base pumps on the apical and basolateral membranes. Approximately two-thirds of the filtered water and sodium are reabsorbed in the proximal tubule, through passive transcellular transport, and Na^+/K^+-ATPase pumps on the basolateral membrane [8]. The sodium transport in the PCT is unaffected by hormones like aldosterone but is regulated by extracellular fluid volume, blood pressure, sympathetic nervous system, and the renin-angiotensin system [13].

Approximately 65% of potassium ions are reabsorbed in this section [14], together with organic solutes such as glucose and amino-acids.

1.2.2.3 Loop of Henle

The loop of Henle section possesses three different parts: the thin descending limb, the thin ascending limb, and the thick ascending limb. The main function of the loop of Henle is to dilute the filtrate by reabsorbing water and sodium (approximately 20% of the total sodium). The descending limb is lined with squamous epithelium and is permeable to water. It has passive transport only and does not actively reabsorb sodium [15]. The thin ascending limb also has passive transport, is highly permeable to sodium and chloride ions, but not to water. The thick ascending limb, impermeable to water, possesses active transport through a sodium/potassium/2 chloride co-transporter (NKCC2) [16]. Regulation of reabsorption in the loop of Henle is mostly driven by the difference of osmolarity between descending and ascending limbs (a countercurrent system, due to the different permeability of each of the limbs), but also by vasopressin, which stimulates active NaCl absorption in the thick ascending limb [17].

1.2.2.4 Distal convoluted tubule (DCT)

The distal convoluted tubule is the last tubule segment before the collecting duct. It plays a key role in extracellular volume regulation and electrolyte homeostasis by reabsorbing sodium (approximately 10% of total tubular fluid sodium) and chloride through electroneutral transport (via the thiazide-sensitive sodium chloride cotransporter NCC) [18]. Water-impermeable DCT cells possess a high density of Na^+/K^+-ATPase, and are also responsible for most of the magnesium reabsorption. Functions of the DCT are regulated by hormones like angiotensin II [19], that increases NCC activity, and

aldosterone, that increases Na^+/K^+ pump activity and the number of NCC co-transporters. Regulation also occurs through the sympathetic system and plasma concentration of potassium. Indeed, DCT cells have three different potassium channels on their basolateral membrane, the function of which is tightly linked to those of the basolateral Na^+/K^+-ATPase, and to sodium reabsorption [20]. Morphologically, DCT cells are recognizable because of their high number of mitochondria and the absence of microvilli.

1.2.3 The kidney collecting ducts

It is important to note the existence of a transitional segment of the tubule situated between the DCT and the collecting duct, named the connecting tubule (CNT), which plays a critical role in the maintenance of Na^+ and K^+ homeostasis [21].

Its origin is not clear and CNT cells possess characteristics of both the DCT and the CCD, with specific CNT cells, and intercalated cells similar to those of the CCD. The transition between DCT and CCD is gradual and the CNT has sodium absorption properties associated with potassium excretion, with higher flux than that of the CCD. The CNT-specific cell characteristics are different between species, especially in rabbits where the transition is clearer between the segments [22].

1.2.3.1 General function

The main function of the collecting system is to receive the filtrate from the nephron and reabsorb water and sodium, regulated in part by the renin-angiotensin-aldosterone system (RAAS) [12]. Collecting ducts are lined by simple cuboidal epithelium, less specialised than that of the proximal or distal tubules. They merge as they go through

the medulla, and lead to the ureter. The CCD plays a central role in the final volume and concentration of urine: two thirds of the hypo-osmotic fluid entering the collecting duct is reabsorbed in the CCD [23].

The collecting ducts are responsible for between 4 and 5% of total sodium reabsorption in the kidney, and up to 10% of total water reabsorption under normal conditions [9]. They also reabsorb urea and bicarbonate, and secrete protons and potassium for the acid-base regulation. While the amount of sodium and water reabsorbed in the collecting duct may appear low, it actually represents the "fine-tuning" of kidney function, and the reabsorption is highly selective, regulated, and adaptable. For example, in case of extreme dehydration, the CCD can reabsorb up to 24% of the filtered water [24].

1.2.3.2 Composition

The collecting ducts are composed of principal cells (PCs) and intercalated cells (ICs) α and β, with PC to IC ratio at approximately 70:30 in the mouse CCD [25]. PCs and ICs possess key functional and morphological differences, and cooperate to regulate acid-base and volume homeostasis. Morphological differences include the presence of a primary central cilium on PCs while the apical membrane of ICs are covered with a dense layer of microvilli [26]. Furthermore, PCs are more polygonal in shape, while ICs are more circular. The basolateral membrane of PCs and ICs also present morphological differences, showing deeper and more numerous invaginations on ICs [27]. A general model for the collecting duct is shown in Figure 1.2.

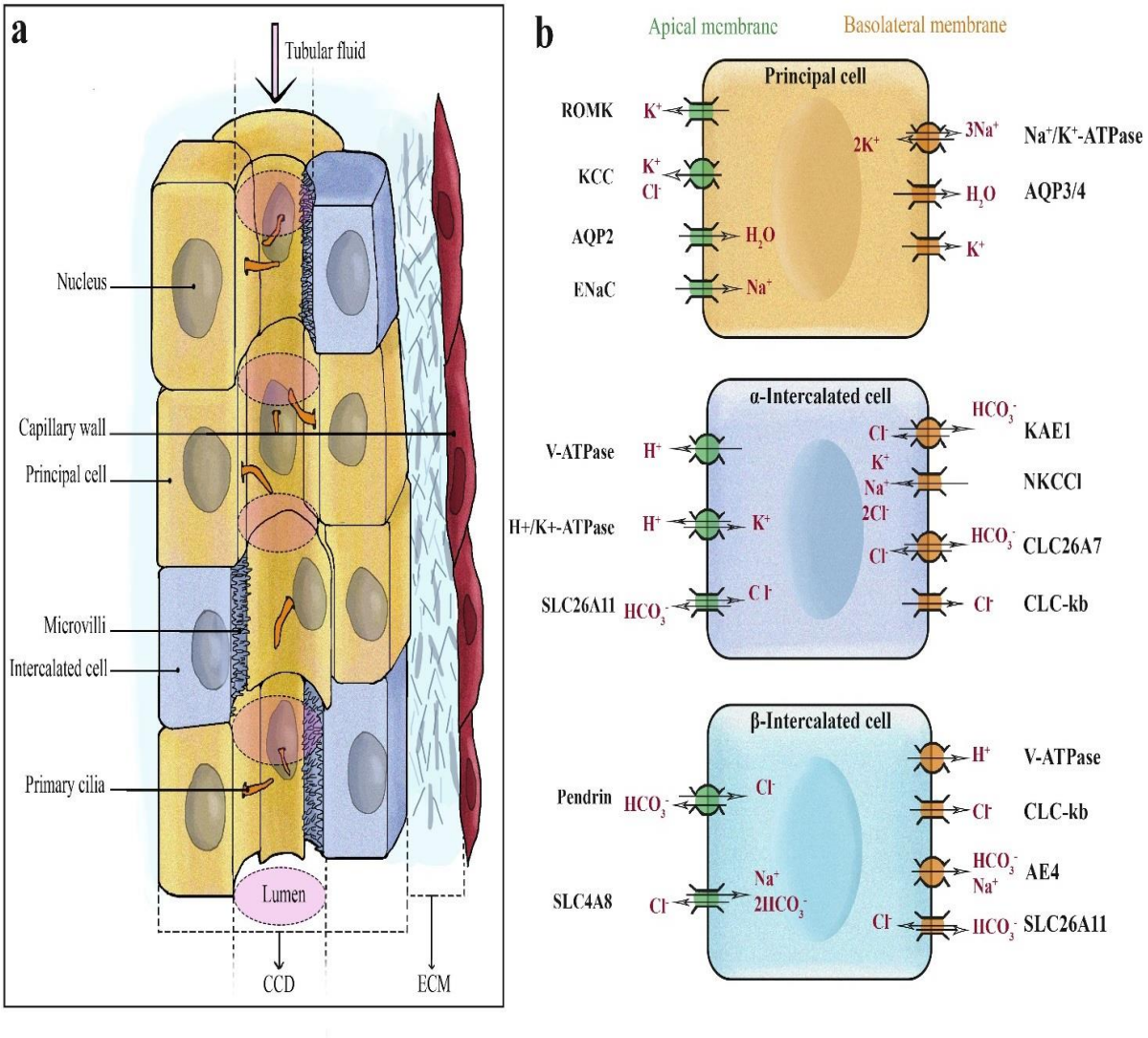

Figure 1.2. Cortical collecting duct morphology and physiology. Made up of principal cells (blue) and intercalated cells (yellow), the collecting duct exchanges water and solutes with the surrounding blood capillaries. (a) Principal cells represent around 70% of total cells in the CCD and possess a distinctive primary cilia (orange) on their apical membrane. Intercalated cells α and β have a tight layer of microvilli on their apical membrane. The CCD cells lie on a specific extracellular matrix (ECM). (b) Apical membrane transport proteins are shown in green, basolateral proteins in orange. Principal cells, α-intercalated, and β-intercalated cells possess different and complementary transporters.

1.2.3.2.1 Principal cells

PCs reabsorb water and sodium through aquaporin2 (Aqp2) and epithelial sodium channels (ENaC)[28] respectively, are responsible for K^+ excretion and express several physiologically important genes including HSD11b2. In general, the basolateral Na^+/K^+-ATPase pump sets the electrochemical gradient for K^+ and Na^+ transport in the principal cells of the collecting duct.

Water reabsorption: The CCD plays a role in final volume and concentration of urine by a process regulated by vasopressin, antidiuretic hormone, for which PCs have two receptors in the basolateral membrane [27]. Vasopressin induces an increase in water permeability with the translocation of Aqp2 from the intracellular vesicles to the apical membrane of PCs [29]. Aqp2 also plays a role during apoptosis by acting as a sensor leading to the activation of ion channels for potassium and chloric efflux [30]. The regulation of Aqp2 expression is complex and still under investigation, and has been linked to β-catenin activity [31], extracellular pH, and even sex hormone levels in female mice [32]. Aqp2 expression also seems to be linked to those of aquaporin 3 (Aqp3), aquaporin 4 (Aqp4), and Na^+/K^+-ATPase in other parts of the tubule [33], leading to a cascade of effects on urine concentration if expression of one of those protein is impaired.

Water is transported through the basolateral membrane using Aqp3 and Aqp4, with Aqp3 also permeable to urea and glycerol [34].

Sodium reabsorption: Situated on the apical membrane of principal cells when active, ENaCs represent the main transport pathway for Na^+ reabsorption in the CCD by working with the basolateral Na^+/K^+-ATPase, following the Koefoed-Johnsen and Ussing "two-membranes" model [35](see Figure 1.3.a). ENaCs are composed of three subunits called α- β- and γ-ENaC which each play different roles in the regulation of

ENaC activity and expression (Figure 1.3.b); however the co-expression of the three subunits in the apical membrane of the cell is necessary for ENaC activity [23]. Na^+ reabsorption via ENaCs is amiloride-sensitive and electrogenic, and generates a lumen-negative trans-epithelial voltage, the value of which varies between species [36].

ENaC regulation factors are numerous and affect the expression, channel properties, and intracellular trafficking (Figure 1.3.c). First, extracellular and intracellular Na^+ concentration, as well as membrane potential can affect ENaC activity [37], [38]. But sodium transport is mostly regulated by the action of aldosterone and vasopressin, other hormones like insulin and endothelin also playing a role. ENaC is a target of aldosterone, that binds to the cytoplasmic mineralocorticoid receptor with high affinity. PCs also express the enzyme 11β-steroid dehydrogenase type 2 (11βHSD2), that protects mineralocorticoids receptors from glucocorticoids by selectively modifying them [39]. Typically, aldosterone is responsible for an increase in sodium reabsorption in the CCD, by increasing the biosynthesis of the α-ENaC subunit, which in turn increases the presence of active ENaC on the cell apical membrane through a mechanism which is not completely understood [40], [41]. Aldosterone also has an effect on ENaC stability in the membrane, preventing the endocytosis of the channel, and inducing a number of ENaC regulatory proteins such as SGK-1 [42].

Similarly, the hormone vasopressin has an amiloride-sensitive stimulating effect on sodium reabsorption [43]–[45], but this requires a higher concentration than that required to effect water reabsorption [46].

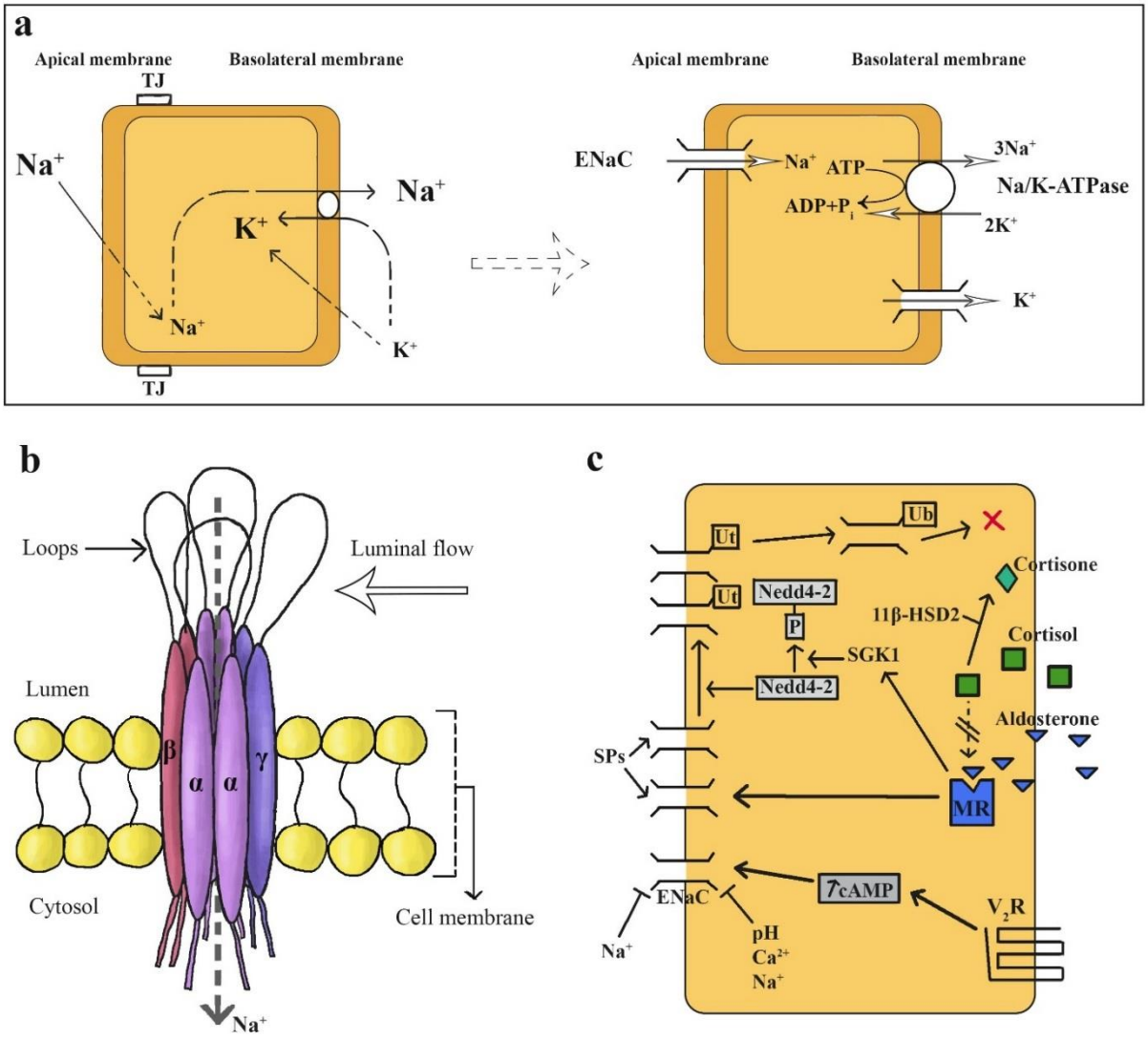

Figure 1.3. Principle of sodium reabsorption in epithelial cells, ENaC structure and regulation. a) Figure adapted from Koefoed-Johnsen and Ussing (KJU) two-membranes model of sodium reabsorption. On the left, the initial model proposed by KJU (1958), where Na^+ passes the apical membrane down an electrochemical gradient. Na^+ is then extruded in exchange for a K^+ on the basolateral membrane. TJ for tight junction (with the neighbooring cells). On the right, the updated model using ENaC for apical Na^+ transport and Na+/K+-ATPase on the basolateral membrane. b) ENaC composition and structure. The main body of ENaC is formed by eight transmembrane domains, four α, two β, two γ, placed to form a channel through the cell apical membrane. The identical subunits are linked by extracellular loops that "float" in the luminal fluid and are involved in mechano-sensitive regulation. Intracellular termini are involved in regulation processes by providing binding sites. c) Main regulation mechanisms of ENaC. Aldosterone regulates the number of ENaC transported on the apical membrane, Nedd4-2 control the stability of the channels and serine proteases (SPs) activate them. Red cross represents degradation; cAMP is cyclic adenosine monophosphate. Figure adapted from Gamba *et al*., "Sodium Chloride Transport in the Loop of Henle, Distal convoluted tubule, and collecting duct" [228].

Potassium transport: Potassium secretion occurs mostly through the renal outer medullary K^+ (ROMK) channels, situated at the apical membrane of PCs and which activity is inhibited by angiotensin II [47], coupled with the basolateral Na^+/K^+-ATPase. Multiple factors are known to regulate potassium excretion through ROMK channels, including mineralocorticoid hormones, plasma K^+ concentration, and pH sensitivity. For example, aldosterone acts through mineralocorticoid receptors to increase the expression of serine/threonine-protein kinase SGK-1 [48], involved in ROMK regulation pathway. ROMK conductance is also increased by insulin, which increases K^+ secretion [49], and is known to regulate SGK-1 activity.

Principal cells also contain Ca^{2+}-activated large conductance "maxi"-potassium channels (BK) on their apical membrane, which contribute to K^+ excretion during an increase in tubular flow rate, and during dietary K^+ overload [50]. Contrary to ROMK, BK activity is insensitive to aldosterone, and is Ca^{2+} activated. BK channels have been shown to have very low open probability in the CCD, but this may reflect experimental conditions eliminating flow, an important contributor to BK activity [51].

The third contributor to potassium secretion in the CCD is the potassium-chloride (KCl) cotransporter KCC. The K^+ secretion is regulated by luminal and basolateral Cl concentration, which dictates the K^+ flux direction through this channel [52], [53]. KCC is insensitive to amiloride [54] but may be stimulated by vasopressin [55].

Primary cilia: The primary cilium is a protrusion situated at the apical membrane of a very large range of cells in the body, including CCD PCs, where they have a length of approximately 7-10μm [56]. They are involved in several mechanical and chemical sensing and signalling pathways. Stimulation of the primary cilium leads to a slow increase in intracellular Ca^{2+} concentration [57], which is transmitted to neighbouring cells. Ca^{2+} signalling leads to a cascade of regulatory effects in the cells, after being amplified by a mechanism involving ATP. Primary cilia are extremely sensitive and detect smaller

changes in flow than that required to get an effect from other mechanosensitive cell components (sheer stress of 0.1-0.2 dyn/cm^2 *versus* 8-10 dyn/cm^2 respectively)[58].

1.2.3.2.2 Intercalated cells

The morphological differences between α-IC and β-IC (seen in Figure 1.2.b) include reduced luminal surface for β-ICs compared to α-ICs [59]. Non-α non-β ICs, described in more details in Section 1.2.3.3, have also been observed, but as yet these cells do not have a defined function.

Acid-base balance: ICs regulate urinary pH through the vacuolar proton-potassium ATPase (V-ATPase), the main function of which is the acid-base balance of tubular fluid, regulated by the secretion of protons (H^+) [60]. Mutations in subunits of V-ATPase cause renal tubular acidosis [61]. Both α and β-ICs contain V-ATPase on their apical and basolateral membranes respectively, making α-ICs the proton-secreting cells. CCD ICs also express either pendrin or anion exchanger 1 (AE1) depending on their subtype, both of which are Cl^-/HCO_3^- anion exchangers.

Regulation of PC sodium reabsorption: ICs produce ATP via Connexin 30 (Cx30) hemichannels, situated on the apical membrane. ATP released from Cx30 is an inhibitory regulator of sodium and water reabsorption in PCs via calcium signalling [62], [63]. ATP release by Cx30 is increased by increased luminal flow rate. ATP binds to the purinergic ATP receptor $P2Y_2$ on PCs, inducing Ca2+ intercellular signalling, which has an inhibitory effect on ENaC and Aqp2 channels.

Sodium reabsorption: There is conflicting evidence regarding the presence of sodium transporters on the apical membrane of ICs [64]. An electroneutral thiazide-sensitive Na^+-driven Cl^-/HCO_3^- exchanger named NDCBE/SLC4A8 was found at the apical membrane of β -IC. In that study, it was suggested that the parallel action of NDCBE

and pendrin was driving thiazide-sensitive sodium reabsorption in intercalated cells. The "NCC-like" activity of this exchanger was demonstrated by blocking ENaC activity in isolated mouse CCD and showing a net electroneutral NaCl absorption, blocked by hydrochlorotiazide (HCTZ). Though the effect of this IC-driven transport was described as "substantial", and able to partly compensate the loss of ENaC in the CCD [64], those results are challenged in other studies. For example, a recent MR knock-out model showed severe Na^+ loss resulting from downregulation of ENaC, with NCC downregulation and no evidence for compensatory activity [65]. Whilst this does not exclude the existence of a sodium reabsorption mechanism in ICs, its level of activity appears very limited. Evidence for sodium transporters on the basolateral membrane, needed for transcellular sodium transport, is also limited, but it may be because the transporters have yet to be discovered or characterized.

Potassium reabsorption: α-ICs possess an H^+/K^+-ATPase exchanger on their apical membrane, suggesting that the cells may be involved in the recovery of some of the potassium secreted via ROMK in PCs. α-ICs also display NKCC1 channels on their basolateral membrane, a secretory isoform of the Na-K-Cl-co-transporter [48], [60]. ICs have been reported to have BK channels on their apical membrane but the activity they represent is not clear yet [48]. β-ICs do not seem to be involved in potassium transport.

1.2.3.3 Origin, differentiation, and cell plasticity

The lineage relationship between PCs and ICs remains unclear. Although PCs and ICs appear distinct, they exhibit a degree of functional overlap and inter-regulation. PCs and ICs have also shown a certain degree of plasticity in multiple studies.

Collecting duct development: Collecting ducts have different developmental origins than the rest of the kidney, which explains the nomenclature difference made between collecting ducts and nephrons. More specifically, the collecting duct forms from the ureteric bud, an outgrowth from the end of the Wolffian duct, itself a mesonephros duct that will become a vestigial organ in females and form part of the reproductive system ducts in males. The ureteric bud then grows into the metanephrogenic mesenchyme (part of the intermediate mesoderm), begins to branch, and induces parts of the mesenchyme to differentiate into nephrons [66]. Factors from the mesenchyme such as glial-derived neurotrophic factor (GDNF), hepatocyte growth factor (HGF), transforming growth factor β (TGFβ), or bone morphogenetic protein 7 (BMP7) are necessary for collecting duct formation [67]–[70].

Cell differentiation between PC and IC appears quite early during embryonic development, with the presence of cells displaying differentiation characteristics just before the first branching stage of collecting duct development [71]. Whilst the differentiation mechanisms are mostly unknown, it has recently been reported that a subset of ureteric bud tip cells (UBTCs) expressing p63 act as progenitors for cortical collecting duct cells, and that an isoform of p63 (ΔNp63) is expressed specifically in progenitor intercalated cells. Cell determination, at least for this population of IC cells, may already be specified at this early stage of development [72].

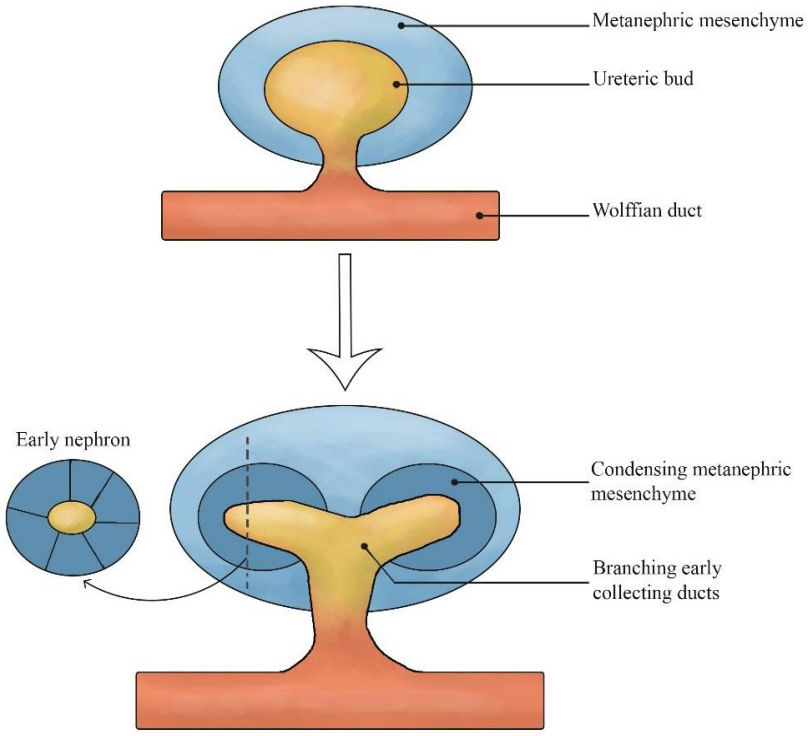

Figure 1.4. Origin and early development of the collecting ducts. The collecting ducts derive from the ureteric bud. Ureteric bud and metanephric mesenchyme then undergo interdependent developmental phases with the parallel branching of the future collecting system and condensation of the metanephric mesenchyme around those branches, that will form the nephrons. Figure adapted from [66].

PC/IC ratio: The ratio of the number of principal cells to intercalated cells (typically 70:30 in healthy mice) has been shown to be influenced by multiple factors, including the transcription factor Adam10 and the E3 ubiquitin ligase Mib1, both of which are required for Notch signalling, and the histone H3 K79 methyltransferase Dot1l. The deletion of floxed alleles of Adam10, Mib1 and Dot1l results in a reduced number of principal cells and an increased number of intercalated cells [25], [73], [74], suggesting that the CCD could switch between cell types to adapt to new conditions.

Plasticity between cell types: The distinction between the different types of ICs is the subject of speculation. Plasticity between α- and β-ICs has been described under acidotic conditions or the deletion of the extracellular matrix protein DMBT1 [75], [76]. Collecting ducts also display a third IC type called non-α non-β ICs characterized by the presence of apical V-ATPase but lacking the bicarbonate exchanger AE1 on the basolateral membrane [59]. These cells do not show polarity in regards to V-ATPase, and appear morphologically larger, with a smooth surface [77]. The presence of these cells raises the question of whether intercalated cells subtypes could represent different functional stages of one cell type, adapting to environmental cues.

The inter-relationship between PC and IC cells, both during development and in the adult, is complex and is yet to be fully elucidated. Earlier studies on primary mouse β-ICs showed they can give rise to both α-ICs and PCs, however cultures of primary PCs did not appear to show the same capacity for interconversion [78]. The changing IC/PC ratio mentioned before suggests a transitional cell type and a degree of cell plasticity, with Adam10, Mib1 and Dot1l as important factors for cell type determination and collecting duct development. In *Dot1l*$^{-/-}$ mice ICs lacked di-methyl K79, indicating that the cells had previously expressed Aqp2-cre and suggesting that *Dot1l*$^{-/-}$ cells originate

from PC cells [74]. In *Foxi1*$^{-/-}$ mice the collecting ducts were comprised of a single cell type that was positive for both principal and intercalated cell markers [79].

1.2.4 The mouse cortical collecting duct clone 1 ($mCCD_{cl1}$) cell line

1.2.4.1 Overview

The $mCCD_{cl1}$ cell line is a spontaneously transformed cell line derived from a single clone, which was obtained by microdissecting the cortical collecting duct of a wild type mouse [80]. In a number of studies, $mCCD_{cl1}$ cells have been shown to possess some of the functions of *in vivo* CCD PCs, and are therefore considered to be a "highly differentiated murine principal cell line" [81]. In culture, they form a monolayer and divide until confluency, at which point they randomly start forming domes (Figure 1.5).

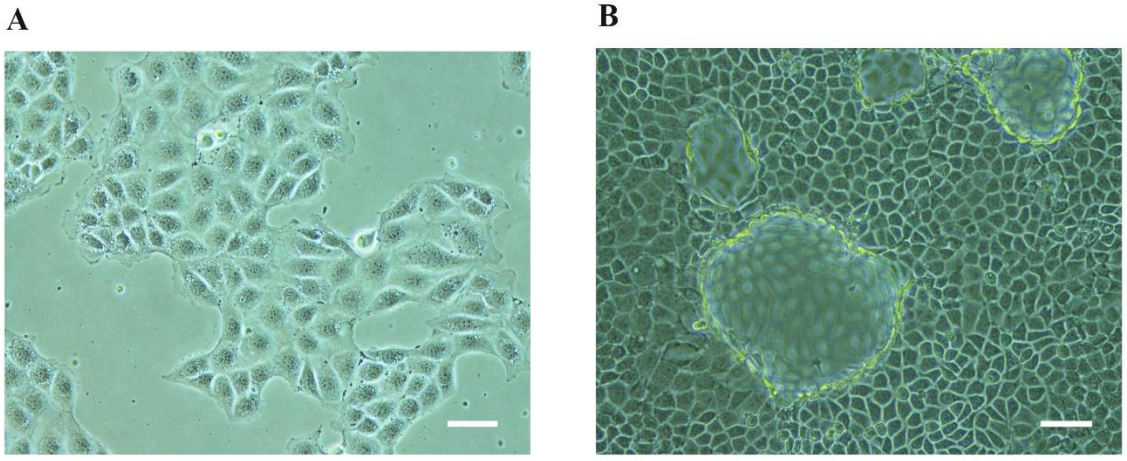

Figure 1.5. Light microscope imaging of $mCCD_{cl1}$ culture. (A) Image of non-confluent $mCCD_{cl1}$ cells cultured for 2 days. Scale bar 20µm. (B) Cells imaged after confluency, forming typical "domes", a monolayer of live cells detached from the flask. Scale bar 50µm.

1.2.4.2 Properties

$mCCD_{cl1}$ cells express ENaC as well as the necessary cellular machinery to enable their stimulation by physiological concentrations of aldosterone, including 11 beta-hydroxysteroid dehydrogenase (HSD11b2), mineralocorticoid and glucocorticoid receptors (MR and GR), and have therefore been used as a model for the study of PC physiology. The $mCCD_{cl1}$ cells have proved to be a useful tool for studying the regulation of principal cell ion transporters such as ENaC or ROMK channels. Mechanisms of electrogenic transport have repeatedly been shown to function and react to physiological concentrations of hormones in $mCCD_{cl1}$ cells. Culturing on porous membranes allows the measurement of transepithelial voltage and resistance. $mCCD_{cl1}$ cells have an appropriate equivalent short-circuit current reflecting an electrogenic secretion of cation, electrogenic absorption of anions, or a combination of both. Physiological concentration of aldosterone (3nM) elicit a transient and early increase in sodium reabsorption peaking at 3 hours after stimulation [80].

In the original work by Gaeggeler *et al.*, the short-circuit current measured using $mCCD_{cl1}$ cells is between -10 and -20 $\mu A/cm^2$ (before and after 3nM aldosterone), that can be compared to measurements in dissected rat CCD between -19.6 and -78.1 $\mu A/cm^2$ [80], [82].

Sodium reabsorption related characteristics: The cell line has been used to explore the mechanisms of hypertension due to sympathetic activity, by demonstrating a stimulation of amiloride-sensitive sodium transport by norepinephrine [81]. Other ENaC-related regulation pathways studied include the role of sorting nexin 3 (SNX3) in the regulatory action of vasopressin [83], and the effect of inflammation on SGK-1 and α-ENaC subunit expression [84]. The original study of the newly created cell line, dealt with the occupancy of MR versus GR and the effect on amiloride-sensitive transport [80]. More

recently, $mCCD_{cl1}$ cells have been shown to express ENaC-activating palmitoyltransferases (DHHCs), that play an important role in apical membrane ENaC regulation by acting on the -β and -γ subunits [85].

Potassium excretion related characteristics: $mCCD_{cl1}$ cells were tested for K^+ secretion following the establishment of the cell line [86]. Significant levels of K^+ secretion were observed, which were not affected by aldosterone but increased under overnight exposure of a high K^+ concentration, indicating the presence of ROMK channels.

In addition to functional ROMK channels, the $mCCD_{cl1}$ cell line expresses functional BK channels that are regulated by a range of factors including the mechanosensitive $TRPV_4$ channel and calcium signalling [87]. Other channels including SK1 and SK3, both high $Ca2^+$-binding affinity small-conductance SK channels, and IK1, the intermediate conductance channel, involved in the regulation of K^+ secretion by BK channels have also been detected [88].

1.2.5 The case for a new *in vitro* model of CCD

1.2.5.1 The CCD environment and characteristics

The kidney is an extremely complex organ with dozens of regulatory mechanisms and loops. As seen in Section 1.2.3.2, protein expression in early sections of the nephron, together with circulating hormones, and the concentration of the different components of the luminal filtrate have a direct effect on CCD function and levels of protein expression.

Cells throughout the kidney are subjected to a continuous flow [89], either from the blood stream, plasma filtrate, or urine. Flow, and the sheer stress it causes on the cells, have important physiological consequences and contribute to functional regulation of the nephron segments, through mechano-sensitive mechanisms. Although sheer stress has a

negative effect on the development of embryonic kidney cells [90], a physiologically relevant flow rate appears to be essential to the functions of adult cells. Single nephron physiological flow in rats has been measured, at around 4 to 30nl/min with variable pressure depending on the nephron segment [91], [92]. As described before, sodium reabsorption is highly dependent on flow rate, in particular in the loop of Henle and in the distal tubule. Flow rate also regulates potassium secretion and nitric oxide and superoxide (NO and O_2^-) along the nephron, indirectly influencing Na and water reabsorption [93].

Rat IMCD primary cells exhibit better viability under conditions of oxidative stress when subjected to flow, and show different cytoskeleton organisation, increased tight junctions, and different adhesion sites [94]. Canine kidney cells have been shown to proliferate faster under flow conditions, and to increase their glucose consumption and NH3 production compared to static cultures [95].

Both luminal fluid flow and apical membrane stretch (pressure) effect the regulation of CCD cells physiology [96]. As described previously, the primary cilium is part of that mechanism and is an important feature of PCs. While pressure has an effect on the whole cell surface, the flow rate is mostly transformed as information through the cilia of the monolayer of cells lining the tubules. Its flow response is maximum at relatively low sheer stress values, too low to be detected by non-ciliated cells. Loss of apical cilium on collecting duct principal cells impairs ATP secretion across the apical cell surface and ATP-dependent and flow-induced calcium signals [97].

The length of primary cilia is linked to kidney disease, in particular to polycystic kidney disease (PKD), with impaired protein transport when the cilia are shortened or absent [98]. PKD-induced cilia impairment is also linked to kidney fibrosis [99].

While ENaC was initially thought to be insensitive to mechanical effects [100],

contradictory studies described the regulatory mechanisms of ENaC in non-epithelial tissues such as nerve endings [101]. The consensus view is that sheer force has a regulatory effect on ENaC, by increasing the single-channel open probability. Though the mechanisms remain unclear, it is likely that ENaC extracellular loops are involved (See Figure 1.3.b)[102]. BK channel expression and function is also regulated through mechano-sensitive mechanisms [51] while intercalated cells are also rendered flow-sensitive, through the expression of Cx30 at their apical surface.

In addition to regulatory effects, flow has been shown to modify cellular structure and organisation [94]; the shear stress provoked by flow over renal tubular cells in this study was sufficient to induce cell polarization and the rearrangement of cytoskeleton and cell junctions. These characteristics argue for the development of a fluidic model of CCD to study regulatory mechanisms.

1.2.5.2 2D cultures *versus* 3D cultures

The functioning of cells in a 3D environment has not been extensively studied, due to the relative novelty of reliable 3D scaffolds and commercialized models.

An important structural support for 3D organisation *in vivo* is the extracellular matrix (ECM). Most of the kidney is made up of tubular structures (nephrons, collecting ducts and vasculature) organized in a specialized ECM, which serves as both support structure and active cell signalling component [103]. While the main ECM components are collagens, elastin and glycoproteins, each area has specific components related to the functions of the cells present. In certain areas of the kidney, the ECM acts like a selective filtration barrier between vascular and urinary cells, and changes in the composition of the matrix are linked to decreased renal function and kidney diseases [104]. Kidney cells

are also sensitive to the mechanical characteristics of the surrounding ECM, in particular to the elasticity or rigidity. During development, stem cell differentiation is partially directed by matrix elasticity [105]. On Madin–Darby canine kidney epithelial cells (MDCK), the matrix rigidity has a direct effect on apoptosis and epithelial-mesenchymal transition mechanisms [106]. The ECM stiffness (elastic modulus) is also closely associated to diseased states like renal fibrosis [107].

Studies involving renal cells in 3D cultures are limited but renal cells have been shown to behave differently on 2D and 3D culture scaffolds. In one case, an immortalized human renal cortical cell line proved to be more sensitive to toxicity in a 3D scaffold and was able to respond to repeated dosing, contrary to the 2D tissue [108]. Other comparisons between classic cell culture and 3D culture showed that, together with altered morphologies, cells in 3D develop increased tissue organisation and specialized functions, and that primary cells retain more differentiated tissue-specific phenotypes [109].

In vitro models using $mCCD_{cl1}$ now consist of classic cell culture or filter culture for electrophysiological assay. The development of a 3D model could be used to study different characteristics of the cell line and to more closely reproduce the *in vivo* collecting duct environment.

1.3 3D bioprinting, a new tool for biology

1.3.1 Overview

3D bioprinting is the process of creating cell patterns using 3D printing technologies, where cell function and viability are preserved within the printed structure [110]. It is a relatively new engineering tool that can be used in the fields of tissue reconstruction, transplantation therapies, and the generation of lab-on-a-chip. The technology is developing rapidly because of multiple varied applications and functions, from drug testing [111] to the potential replacement, or improvement of malfunctioning body parts [112]. Bioprinting represents a promising step in the field of tissue engineering and is starting to emerge as a discipline on its own, due to the necessary and complicated intersection of biological and engineering fields.

The concept of printing cell-integrated structures is not new, but the convergence of engineering and biology for the creation of a strong biology-based design is still in development. Bio-printing has previously been used for the enhancement of classic cell culture techniques, for example by printing specialized culture plate coating. Inkjet-like technology was used to print gelatine infused with different concentrations of growth factor directly on culture plates for special guiding of stem cell growth [113].

3D bio-printing with the goal of mimicking *in vivo* structures started in 1998, with an engineered blood vessel obtained by wrapping a sheet of vascular cells around a tube [114]. Even though that technique may not be considered bio-printing, this engineered vessel opened a lot of possibilities for techniques to evolve at the same time as non-biological 3D printing technologies.

In vivo, tissues are organized in a complex three-dimensional architecture, permitting them to ensure the entirety of their biological functions. *In vitro*, new techniques will soon permit the creation of accurate biological models for understanding the fundamental

mechanisms of physiology, the evolution of disease processes [115] or drug processing. In fact a study using 3D-printed liver structures in a microfluidic device demonstrated that the bio-fabrication of in vitro models can optimally simulate the higher functions of organs, such as drug metabolising ability [116]. On a wider perspective, the use of bio-printing to create 3D models of tissues and organ functions is a new tool for biology, and replicating in vitro models of mammal and human tissues, although challenging, could facilitate drug screening to determine the consequences of mutations, and the understanding of cell biology and physiology without resorting to animal models.

The interest in bio-printing is exponential (Figure 1.6), and the technology is rapidly evolving. Research groups and companies now offer 3D printed skin and liver samples for drug screening (Organovo®), cartilage, and cell injected scaffolds for heart valves replacement [117]. As an efficient way to obtain personalized, reproducible, adaptable models, 3D bio-printed biological structures are in theory more accessible financially; they also offer the possibility for easier access and monitoring of live cells (injection of drugs and solutes, imaging, transgenic cells) than existing models.

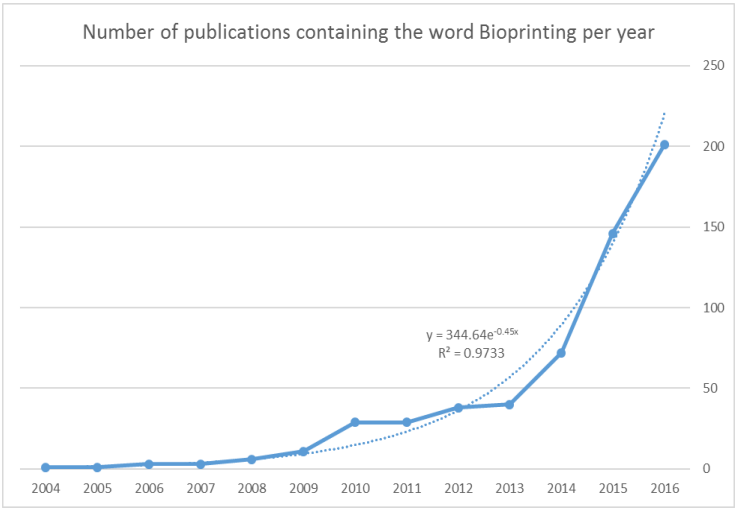

Figure 1.6. The number of publications containing the word "bioprinting" has increased during the past 13 years, with a rate following almost exactly an exponential curve. Source: Web of Science (Thomson Reuters), using the keyword "bioprinting".

1.3.2 3D printing techniques

3D printing has been a rapidly evolving field in the past two decades [118]. Several techniques exist, varying in cost, resolution, speed, and applications. Two main techniques are used: fused deposition modelling, more commonly called extrusion printing, and stereolithography. Other techniques involve the melting of metal salts by lasers or electron beam, and are used for the manufacturing of medical or aerospace instruments.

1.3.2.1 Extrusion

Extrusion 3D printing was developed in 1980 [119]. It consists of melting a material (thermoplastic) and extruding it through a nozzle in the desired shape in the x and y axis. Objects are printed layer-by-layer on a platform that moves in the z axis (see Figure 1.7). The material hardens once out of the nozzle and fuses to the preceding layer. Some extrusion printers apply an easily-removable support material at the same time as the printed layer to avoid collapse of the structure.

1.3.2.2 Stereolithography

Stereolitography was patented in 1986 by Charles Hull (3D Systems, Inc). Also called photo-solidification printing, stereolithography is a technology that creates object in a layer by layer fashion using photopolymerization [120]. The solidified material is then moved in the z-axis using an elevator platform and the next layer light sheet is projected (Figure 1.7). Projection micro-stereolithography uses a digital micro display technology that provides dynamic masks, working as a virtual photomask [121]. This technique allows for rapid photopolymerization of an entire layer with a flash of UV illumination at micro-scale resolution. In some set ups, the mask can control individual pixel light intensity, allowing control of material properties of the fabricated structure with desired spatial distribution.

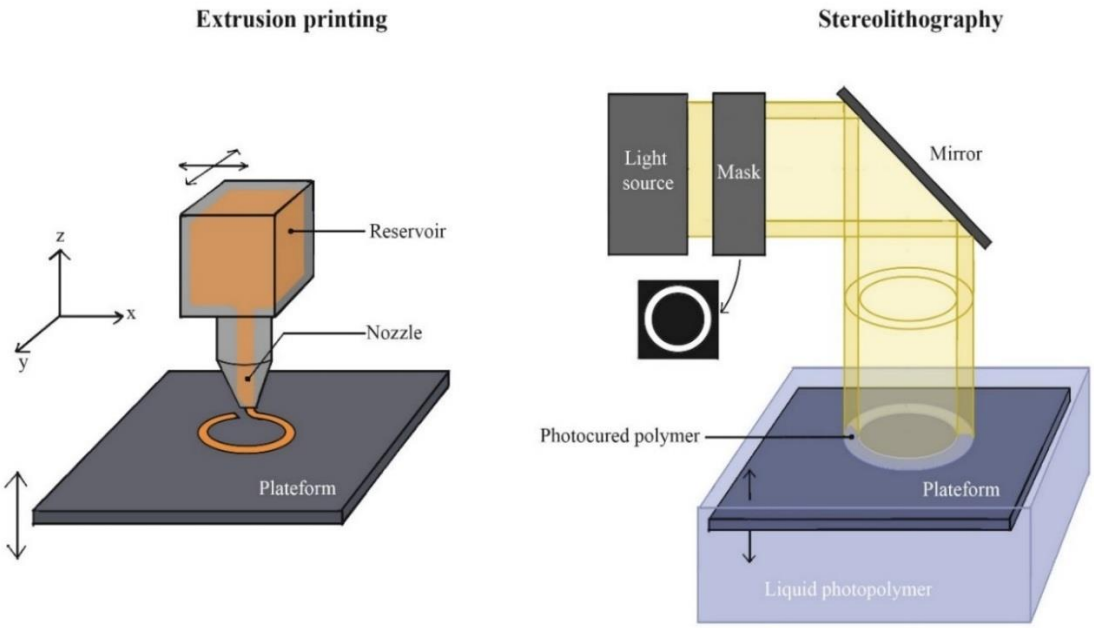

Figure 1.7. Basic principle of the two main 3D printing techniques. Extrusion printing consists of ejecting the material through a nozzle in a spacially controlled manner: the printer moves in the x and y plains. Once a layer is done, the support platform goes down and the next layer is printed. Stereolithography consist of projecting a sheet of UV light on a photocurable liquid polymer, with the desired shape. Once the layer is polymerized, the platform moves down and the next layer is illuminated and photocured.

1.3.3 3D bioprinting of kidney structures

1.3.3.1 Challenges

The kidney structures present an important challenge for bio-printing technologies. Renal cell biology is still not completely understood, and kidney functions are intimately linked to its complex three-dimensional organisation [9].

Meanwhile, the need for kidney research and organ replacement has never been so great: approximately 83% of people on a waiting list for life-saving organ transplant are waiting for a kidney [122]. Kidney disease leads to increased risks of cardiovascular diseases and decreased life expectancy [123]. Partially replacing animal models is another desirable application for *in vitro* models of kidney structures. Widely-used animal models can be costly, and unreliable for a number of renal pathologies. For example, weaknesses in models for renal fibrosis include the absence of data for renal functions, no glomerular involvement, differences between species susceptibility, technical difficulties and high mortality rates [124]. Models for chronic kidney diseases also present approximations and imperfections, even after the development of gene transfer techniques and humanized rodent transgenic animals [125].

Printed renal structures are also useful for basic cell biology research. The demand is increasing for new adaptable and reproducible *in vitro* models of kidney structures offering the possibility for easy visualization of live cells in a 3D physiologically relevant environment. Nephrotoxicity assays are another important use for *in vitro* renal tissues, since drug-induced kidney injuries represent 1 in 5 cases of phase 3 clinical trial failures [126].

To be relevant, bio-printed kidney structures need to be able to reproduce *in vivo* functions like solute and ion transport. Transport functions limit the 3D printing techniques available and make the design of an adapted scaffold more complex, since cells

cannot be seeded or printed on an obstructive scaffold as in classic 2D cell culture. Kidney epithelial cells are indeed known to form domes (monolayers of cells transporting water and solutes, detached from the support) when cultured classically, because they cannot access a "basal side" [127]. Other parameters for the composition of renal micro-environment need to be taken into consideration, like the local pH, as kidneys maintain the blood plasma acid base balance by reabsorbing bicarbonate and excreting H^+. Options include 3D porous scaffolds, or gel-embedded cell culture that have previously been used to sustain cells for more than 6 weeks without over-proliferation even with immortalized lines [108], [128].

1.3.3.2 Techniques

There are two main techniques available for the creation of tubular structures allowing kidney cells to attach, grow, and form tight functional layers. The first technique uses hydrogels as a support structure in an effort to mimic ECM. The second technique uses "hard 3D scaffolds", chemically neutral porous 3D support structures, which can subsequently be coated with hydrogels if needed. Around those structures, several techniques can be adapted to deliver flow.

Flow and vascularization: An effective engineered kidney structure needs a flow system, and a vast number of microfluidic devices have been available for decades. Kidney-on-a-chip technologies in particular already use cells on porous membranes integrated in a microfluidic device for the injection of drugs and nutrients [129].

Microfluidic devices for bio-engineering are most often fabricated using PDMS (polydimethylsiloxane), a silicon based organic polymer routinely used for precision manufacturing of microfluidics. PDMS in a liquid form is mixed with a crosslinking agent

and poured in a mould before being left to harden (or baked for faster results). PDMS has more recently been used as a convenient tool for integrating engineered renal tissues in a fluidic system [94]. However, these structures remain a 2D cell culture environment. The flow rate of the nutritive fluid can be controlled by a large variety of devices, including syringe pumps, peristaltic pumps, specialized microfluidic pumps, gravity-based flow system or simple manual injection.

Hydrogels: Hydrogels are polymeric materials with a hydrophilic structure allowing them to retain a large amount of water. They have a good biocompatibility and are now used as cell-laden materials for bioprinting. Several studies used the hydrogel approach for the development of 3D bioprinted tubular structures.

Among the engineered kidney structures involving hydrogels, the work from Weber *et al* (2016) used proximal tubule epithelial cells injected in a microfluidic microchip previously developed for 3D vascular constructs [130], [131]. The chip is obtained by casting a hydrogel around mandrels, which are removed once the gel sets, forming hollow channels. The hydrogel bloc is then sandwiched between two PDMS layers, forming the microfluidic device. It is possible to cast the gel around several mandrels to obtain several parallel channels. This design was used to inject vascular cells in one channel and growth factor in another, effectively creating a chemical gradient in the hydrogel surrounding the cells. For use with kidney cells, human primary proximal tubule cells were seeded and cultured in a one-channel chip of collagen type 1 hydrogel for up to four weeks [131]. The cells presented specific markers for epithelial (CD13 and E-cadherin) and proximal tubule cells (aquaporin 1 and lotus lectin), as well as normal proximal tubule cell morphology. The cells also polarized and developed primary cilia in response to fluid shear stress. Functional studies showed that proximal tubule epithelial cells (PTECs) in this microchip

could reabsorb glucose and metabolise vitamin D, as well as transport different anionic solutes.

Using a similar system, Homan *et al.* [132] applied an immortalized PTEC cell line to create an equivalent 3D-engineered perfused proximal tubule structure. Instead of using retractable mandrels to create the channels in the hydrogel, a fugitive ink (material that liquefies at low temperatures) was printed in the distinct convoluted shape of a proximal tubule and encased in a gelatin-fibrinogen ECM hydrogel. Once the gel set, the fugitive ink was removed, creating the channel. As in the previous study, the cultured cells in the channel presented their expected morphology, with a height comparable to cells *in vivo*, and the tubules remained viable for several weeks after confluency. Polarization was demonstrated by the presence of primary cilia and microvilli as well as the localisation of several markers: Na^{+}/K^{+-}ATPase and organic cation transporter (OCT2) on the basal membrane, lotus lectin on the apical membrane. Functionality assays concentrated on albumin uptake by the cells, which appeared significantly higher in the 3D tubule than in 2D controls. The same group also used the gelatin-fibrin hydrogel for 3D-printed vascularized tissues (Kolesky *et al.* [133]), showing that this ECM is potentially adapted to several cell types. It also possesses the same elastic modulus as a healthy adult kidney cortex.

Similar results were obtained using a network of 3D-printed agarose [134]. To obtain the channels, a network of agarose microtubules was 3D-printed, then covered with a hydrogel. The agarose tubular network was then manually removed, creating hollow channels in the hydrogel that could then be injected with cells. In this study, the technique worked with a vast range of hydrogel composition, that can be adapted to different cell types. The principle to create hydrogel channels used in all those models is shown in Figure 1.8.

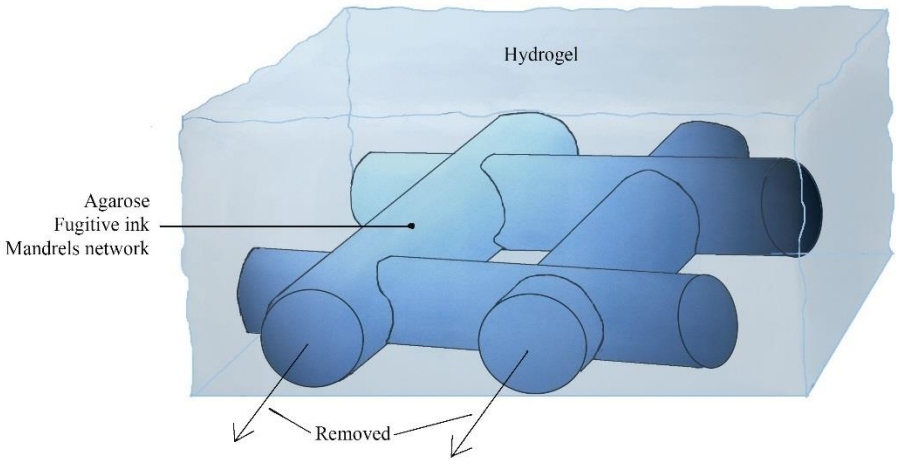

Figure 1.8. Principle of fabrication of hydrogel tubular networks. A network of tubular structures is printed or made using different materials like agarose, fugitive ink or mandrels. Hydrogel is cast on top, and the materials are then removes to create a hollow hydrogel network in which cells are injected.

Extrusion printing of hydrogels was used to create a network involving multiple layers of perfusable channels [135]. In this case, extrusion printing refers to the spatially controllable ejection of material through a specially designed nozzle, that printed hydrogel directly into a hollow tubular shape. The hydrogel components were cross-linked as soon as they exited the nozzle so the channel would not collapse. Only tested with human umbilical vein endothelial (HUVEC) cells so far, this technique offers an alternative and convenient way to obtain a complex network of hydrogel channels.

Extrusion printing is also used for the 3D bioprinting of "blocks" of cells (Figure 1.9). The cells are embedded in hydrogel, then the resulting bio-ink is inserted in the printer to be extruded. This technique was used in the early days of channels bioprinting to

create channels lined with embedded vascular cells, but the resulting product was unstable and its 3D shape difficult to maintain.

Hydrogel scaffolds have some drawbacks: in the work of Weber *et al* [131], the porous and pliable collagen ECM may have been responsible for variability in some transport assay results. The design of the structure also made it difficult to measure ion transport. Functional assays involving ion transport was also not addressed by Homan *et al* [132]. Hydrogels present challenges for imaging of live cells in particular. The tubules are encased in a layer of hydrogel, which makes the close-up imaging of small groups of cells difficult, especially with confocal microscopy. Furthermore, the quality of 3D-printed structures is heavily linked not only to printing parameters (pressure, printing rate, distance between nozzle and structure) but more importantly to the composition of the gel [136]. Those results limit the possibilities for precise extrusion-based bioprinting of embedded kidney cells, which need specialized ECM to function. In some cases hydrogels are also too soft to sustain physiological conditions [137] such as pressure and flow rates, or the total weight of the printed structure. Those observations led some groups to experiment with different support structure for kidney constructs.

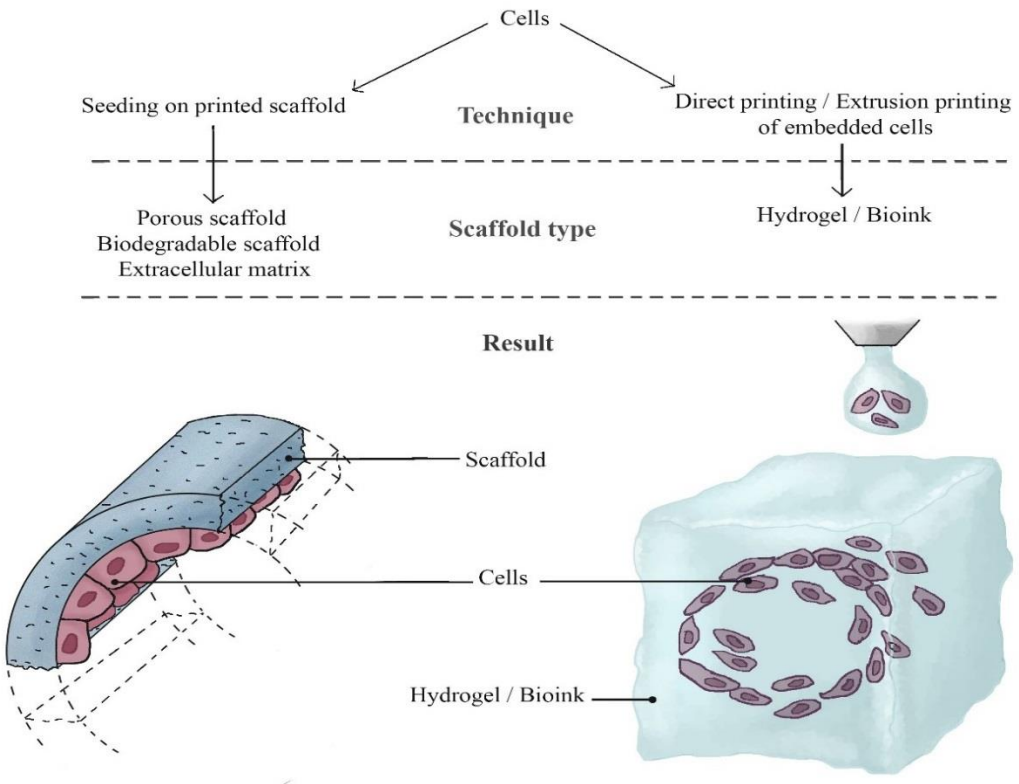

Figure 1.9. Summary of bioprinting techniques. The cells are either injected in / seeded on a printed scaffold or embedded in a hydrogel / bioink and printed directly.

Other scaffolds: Hard scaffolds for 3D cell culture are now commonly produced and commercialized (Alvetex®, Cellusponge®), but functional kidney cells require adaptable specificities as described above. Different "hard scaffolds" have been tested with different kidney cell types, in most cases coated with a hydrogel for cell attachment. Hard scaffolds are produced by moulding or 3D printing.

Among those, Subramanian *et al* [128] used a porous silk sheet coated with different ECM before cell seeding. Silk possesses the required qualities for long-term kidney cell culture: strong mechanical properties, low bio-degradation rate, stable structure and porosity. The mouse embryonic kidney (MEK) epithelial cells used on the scaffold showed a better development on a mixed collagen-matrigel ECM coating, and an increase in branching and tubular structure when co-cultured with fibroblasts. However, even with silk fibers the constructs started to collapse after 3 weeks in culture. Another study used "hollow fibers" as a support structure for human primary PTEC [138]. Hollow fibers are porous membranes used in commercialized hemodialysis filtration systems, and were first adapted to create bioartifical renal tubule assist devices [139]. The design and fabrication of new hollow fibers was adapted to the reabsorption function of renal proximal tubule cells by changing the fiber diameter and moulding methods for better cell attachment, proliferation, and reabsorption functions. Considering that the internal porosities of the channels were too large for the cells to form a tight monolayer, the fibers were coated with a fibrin ECM before seeding the cells. The final structure therefore combines a porous hard scaffold as a support structure and a hydrogel for cell attachment, with the hope that the cells would replace the fibrin with their own ECM in time. The cells formed a confluent monolayer in the channel, expressing PT markers and numerous microvilli at their apical membrane, but no primary cilia. Several transport profiles for general reabsorption of urea, creatinine and glucose suggested that the cells were functional, but with a large variation in reabsorption rates due to the poor biological replication between

the different hollow-fibers. The design also makes imaging technically challenging, since the tubules need to be fixed and cut before any type of microscopy. 3D-printing techniques are now used to produce porous tubular support structures for cells, offering the possibility for the reproducible production of adapted scaffolds.

PolyHIPEs are emulsion based polymer materials offering a highly interconnected microporosity network, and have been routinely used as 3D static cell culture membranes. PolyHIPEs are produced using a templating process: the precursor to the porous material consists of two phases, one of which will be removed to form the pores. HIPEs stand for High Internal Phase Emulsions, which are used to create porosities by removing the internal phase [140]. PolyHIPEs are the result of the polymerisation process on the HIPEs. Polymerisation can be induced thermally or chemically [141]–[143], or using light to cure the HIPEs rapidly [144], [145]. In 2013, Johnson *et al.* described the use of microstereolithography for 3D-printing PolyHIPEs in highly controllable, reproducible, and adaptable scaffolds [140](Figure 1.10). Microstereolithography printing parameters offer the possibility to control the shape of the scaffold, the porosity size, and their interconnectivity ratio. The PolyHIPEs composition can also be adapted to obtain different elasticity modulus and mechanical properties. Human hES-MP cells seeded on PolyHIPEs attached and grew without hydrogel coating [146]. Developed for bone tissue engineering, PolyHIPEs materials are easily adapted to other applications including kidney cells, by choosing the relevant printing parameters for ideal mechanical properties and porosity size.

For the development of *in vitro* renal tissues, another manufacturing technique called electrospinning has recently been used [147]. In this study, the biodegradable polymer poly(lactic acid) (PLGA) was spun to create thin fibres and projected on a mandrel, creating an airy network of randomly interleaved fibres. Rat kidney primary cells were

then seeded on the scaffold, that showed the ability to sustain a multi-population of cells over a week.

A summary of the existing studies on renal cells using bioprinting or equivalent can be found in Table 1.1.

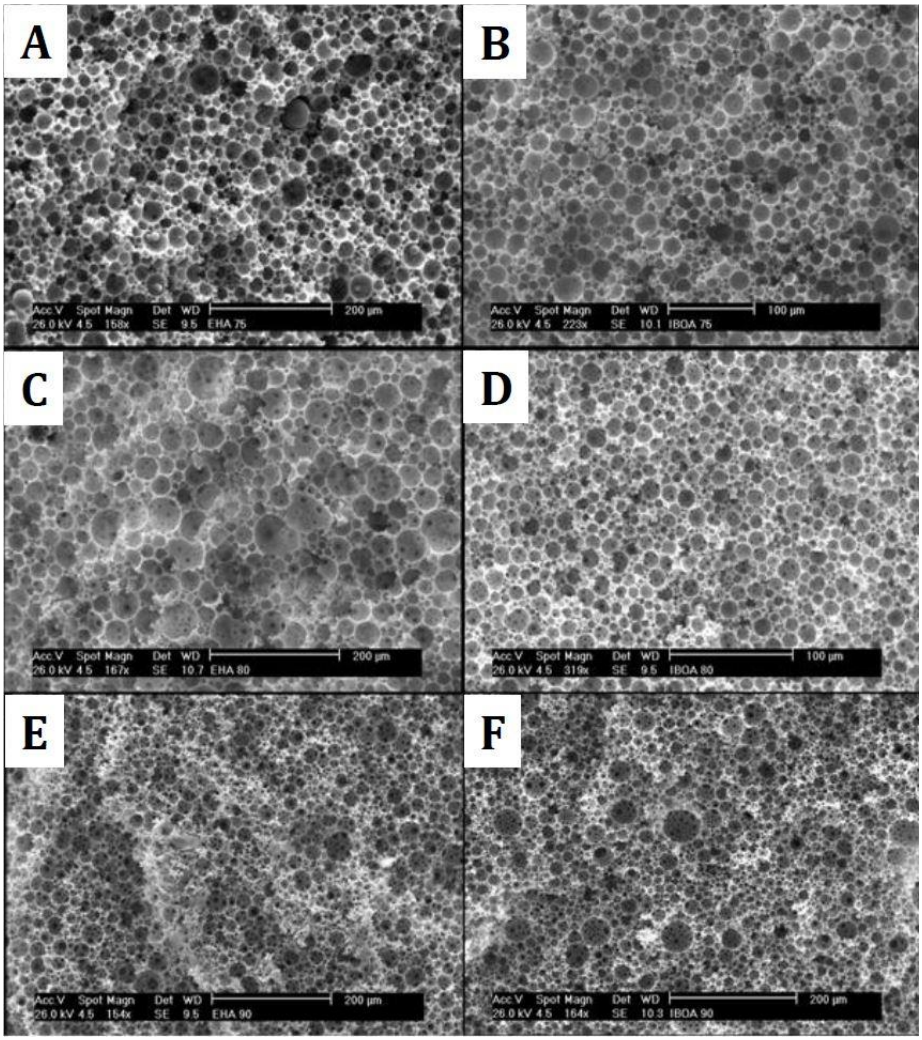

Figure 1.10. 3D printed PolyHIPEs samples. Each sample (A-F) has a different polymer composition that has an effect on the finished product porosity sizes. Image adapted from "Macrostructuring of emulsion-templated porous polymers by 3D laser patterning", Johnson et al. [140]

Scaffold type	Scaffold composition	Cell types	References
Hydrogel	Collagen type I	Human PTEC (proximal tubule epithelial cells)	[131]
		MDCK (Madin-Darby canine kidney cells)	[128]
	Matrigel	Mouse IMCD (inner medullary collecting duct)	[148]
		Embryonic UB cells	[148]
	Mix Collagen I and Matrigel	Human cortical epithelial cells	[149]
	Hyaluronic acid	Pig PTEC	[139]
	PEG (polyethylene glycol) based	MDCK	[106]
	Gelatin-fibrin mix	PTEC-TERT1	[132]
Other	Silk coated with collagen I	MEK (mouse embryonic kidney epithelial cells)	[128]
	PolyHipes (polymers)	*$mCCD_{cl1}$ (mouse cortical collecting duct cells)*	*Current*
	Fibrin based hollow fiber construct	PTEC (primary proximal tubule epithelial cells)	[138]
	Polyester membrane	PTEC-TERT1	[150]
		Primary rat IMCD	[94]
	Poly(lactic acid)	Primary rat whole kidney	[147]

Table 1.1. Summary of existing 3D bioprinting of kidney cells studies. A wide range of cell types and scaffolds have been used, with mixed results. In italics, the subject of this current thesis.

1.4 Aims and hypothesis

Although the main collecting duct functions are well known, many fundamental questions remain unanswered, particularly with regards to the relationship between principal and intercalated cells, and the physiological response to pathological conditions, changes in solutes concentration, or genetic mutations. Until recently, $mCCD_{cl1}$, a self-immortalized murine collecting duct cell line, has been used for the study of a limited number functions of principal cells. I hypothesise that $mCCD_{cl1}$ cells offer a complete model for the study of CCD physiological mechanisms and aim to characterize the cell line and to study the transport mechanisms of the cortical collecting duct principal cells under different conditions.

For this project, I also aim to develop a 3D printed model of an $mCCD_{cl1}$-composed collecting duct, using the $mCCD_{cl1}$ cell line and the appropriate 3D printing technologies among those available, to show that the cells function properly after the process.

2 Materials and methods

2.1 Standard solutions

Ultrapure water "ddH_2O" was obtained from a Milli-Q Ultrapure Water Purification System. When required, pH was adjusted using HCl or NaOH and a pH-meter (Corning pH meter 240). Recipes for standard solutions can be found in Table 2.1.

Solution	Recipe	Reference
1X PBS	10 tablets, 1L ddH_2O	OXOID (BR0014G)
Goat/Donkey blocking buffer	2% Goat serum, PBS 10% Donkey serum, PBS	BioSera GO-605500 BioSera AS-2281500
4% PFA	4% paraformaldehyde, PBS 1M NaOH until pH 7.2	Sigma (D2650)
5M NH_4Cl	NH_4Cl 0.267g ddH_2O 100mL	
DEPC water	Diethylpyrocarbonate 0.01% ddH_2O Autoclave	
EDTA 0.5M	EDTA, ddH_2O NaOH until pH 8.0	VWR Chemicals
50X TAE	Tris Base 242g Glacial acetic acid 57.1 mL 0.5M EDTA 100mL ddH_2O Autoclave	VWR Chemicals Promega

Table 2.1. Standard solutions used.

2.2 Cell culture techniques

2.2.1 General conditions

Cells were cultured at 37°C in 5% CO_2 and 95% air in a HERA cell 150i CO_2 incubator (ThermoScientific), in Sarstedt culture flasks with vent cap (25cm^2 or 75 cm^2). The culture media and all the solutions used on the cultured cells were warmed at 37°C in a

waterbath unless otherwise stated. Cells were manipulated in a sterilized laminar-flow tissue culture hood.

2.2.2 Culture of $mCCD_{cl1}$ cells

The primary culture medium used during this project, called growth medium, was based on the medium described previously for culture of $mCCD_{cl1}$ cells [80]. The recipe used for the growth medium is detailed in Table 2.2.

Cells were consistently cultured in growth medium until total confluency before using TE for passaging or other uses. Total confluency was determined by observing the formation of "domes", areas of cells spontaneously polarizing and detaching from the flask.

Medium	Recipe	Supplier
Growth	Phenol red free DMEM/F12 (500ml)	Life Technologies (21041033)
	Insulin (5µg/ml) *	|
	Sodium selenite (60nmol/l) *	| Sigma (l1884-1vl)
	Apotransferrin (5µg/ml) *	|
	Dexamethasone (50nmol/l)	Sigma (D8893-1mg)
	Triiodothyronine (1nmol/l)	T6397-100mg
	L-glutamine (2nmol/l)	Sigma (G7513)
	EGF (10ng/ml)	Life Technologies (PHG-0311)
	FBS (2%)	Bio&Sell(DE)
	Penicillin-streptomycin (100µg/ml)	Sigma (P4333-100ml)
Experimental	Phenol red free DMEM/F12 (500ml)	Life Technologies (21041033)
	Penicillin-streptomycin (100µg/ml)	Sigma (P4333-100ml)
Charcoal-stripped	Phenol red free DMEM/F12 (500ml)	Life Technologies
	Charcoal-stripped FBS (2%)	Sigma (F6765)
	Penicillin-streptomycin (100µg/ml)	Sigma (P4333-100ml)
Freezing	DMSO (10%)	
	FBS (90%)	Bio&Sell(DE)

Table 2.2. Recipes for the media used with mCCDcl1 cells. * Components supplied combined in one solution by the company.

2.2.3 Passaging cells

When confluency was observed for $mCCD_{cl1}$ cells, medium was aspirated and the cells washed 3 times with PBS. Depending on the culture flask (25 or 75 cm^2), 333µl or 1ml of Trypsin-EDTA (Lonza; 0.25% Trypsin) was added, and the flask left for a maximum of 15 minutes at 37°C to allow for the cells to detach. Pre-warmed growth medium was then added to the flask to inactivate the TE, and the cells were pelleted at 1000 rpm for 5 minutes (about 200x g) using a Biofuge primo centrifuge. Cells were then carefully resuspended in the medium and transferred to a new flask at a 1/10 dilution.

2.2.4 Cryopreservation and thawing of cells

Cells were passaged as described previously in Section 2.2.3, but instead of growth medium they were resuspended in freshly prepared and filtered freezing medium (Table 2.2). The cell suspension was then immediately aliquoted in 2mL cryotubes (Sigma) and transferred to the -80°C freezer where it was stored for no longer than a week before transfer to the liquid nitrogen storage (-230°C). Cells coming out of liquid nitrogen storage were transferred first to dry ice (-78.5°C), then to room temperature for a few minutes, before slowly thawing the cell suspension by pipetting warmed growth medium in the aliquot. The thawed suspension was then added to 5mL of growth medium, pelleted down at 1000 rpm for 5 minutes (about 200x g) using a Biofuge primo centrifuge, and the cells resuspended and transferred to a flask for culture.

2.2.5 Fixation and mounting of cells

Cells cultured on glass coverslips were washed three times with PBS, fixed with 4% PFA for 20 minutes, washed three times in PBS, incubated for 10 minutes in 50mM

NH_4Cl, and washed three times in PBS. The coverslips were mounted by using the DAPI Prolong Gold Antifade mounting medium (Thermofisher Scientific), after airdrying for a few seconds. They were applied on a glass slide and left to set at 4°C overnight before applying transparent nail varnish on the borders of the coverslip to fix it in place and avoid drying. The slides are then stored at 4°C.

The same protocol was applied to cells cultured on filter membranes, described in Section 2.2.7.

2.2.6 Cloning

Clonal cell lines derived from $mCCD_{cl1}$ cells were established using the dilution method [151]. Confluent $mCCD_{cl1}$ cells were trypsinized and re-suspended in culture medium to obtain a cell suspension at $2x10^4$ cells/mL. 200 µL of cell suspension was added to the upper left well of a 96-well plate and serially diluted 2-fold from top to bottom in the first column. Using a multichannel pipettor, the first column was then serially diluted 2-fold from left to right in the remaining columns. The presence of single cells is most likely to occur in the bottom right corner of the plate, were the cell suspension is most diluted. Single cells were independently identified by two individuals and confirmed by observing the growth of the resulting single colonies in the wells over 3 days of culture. The colonies were then trypsinized and transferred to a T75 flask for culture. The cloning process produced 8 clonal sub-lines, among which 3 lines (named Ed1, Ed2 and Ed3) were selected for further studies based on morphological differences.

2.2.7 Cell culture on Transwells

Cells were polarized by growing cells on Corning Costar™ Snapwell™ Permeable Support inserts (12mm, 0.4 µm pore size). Those porous membranes, suspended in a 6-well plate, allow for the cells to have access to medium on both sides and develop polarity.

Cells were seeded on day 0 at a 1:1 split ratio and grown for 10 days. Cells were fed with growth medium on days 1, 3, 5, 6, and 7, by adding 500µL of medium on the apical side of the insert and 2.5mL on the basal side. On day 8, the cells were fed with charcoal-stripped medium and on day 9 with experimental medium (Table 2.2). The process was repeated with cells from passage 26 to 30.

2.2.8 Aldosterone and amiloride assay

Solutions were prepared by diluting aldosterone (Sigma Life Science) in experimental medium to a 1µM concentration, and amiloride (Sigma Life Science) in 100% EtOH to a 1mM concentration. Aldosterone treatment was conducted by adding 1.5 and 7.5µl of the previously prepared solution to the apical and basal sides of cells cultured on Snapwell™ insert respectively, bringing the final concentration to 3nM. Amiloride treatment was conducted by adding 5µL of the previously prepared solution to the apical side of the cells only, bringing the final concentration to 10µM.

2.2.9 EVOM measurements

Measurements for transepithelial voltage (V_{te}) and transepithelial resistance (R_{te}) were made with a transepithelial volt-ohm-meter and a set of chopstick "STX" electrodes (EVAOM^2, World Precision Instruments) on cells cultured on Snapwell™ membranes, described in Section 2.2.7. Electrodes are placed on each side of the membrane, near the

apical and basolateral membranes of the cells (Figure 2.1). The equivalent short circuit current (I_{sc}) is then calculated using Ohm's law (Equation 2.1).

$$I(\mu A.cm^{-2}) = \frac{U(mV).1000}{R(\Omega.cm^2)}$$

Equation 2.1: Ohm's law applied to EVOM2 measurements

By convention, a negative Isc reflects either electrogenic secretion of cations, electrogenic absorption of anions, or a combination of both.

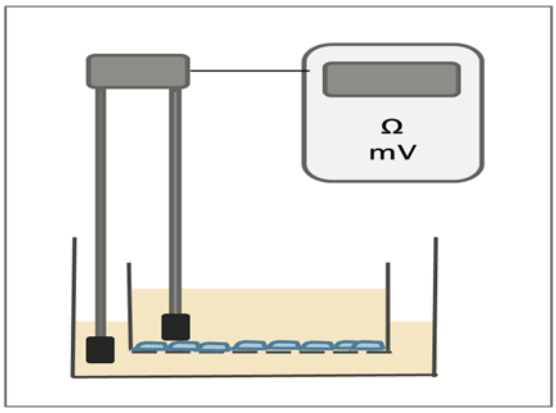

Figure 2.1. EVOM measurements principle. Principle of measurement process using EVOM2 on cells cultured on Snapwell™ porous membrane. Cells are culture on a porous membrane, with access to culture medium on both apical and basolateral sides. For EVOM measurements, chopstick electrodes are placed in basal and apical baths.

2.3 Histological analysis

Unless otherwise stated, all staining protocol were performed at room temperature and the washes performed three times with 1X PBS.

2.3.1 Fluorescent labelling

Fluorescent labelling of Na^+ in solution was performed using CoroNa™ Green Sodium Indicator (Molecular Probes, Invitrogen). The fluorescent dye was reconstituted from its desiccated stock using DMSO, then added to cell culture medium to obtain a final concentration of 5μM. After 30 minutes of incubation at 37°C, the culture was washed twice with warmed growth medium before observing the distribution of the fluorescence with an appropriate microscope.

2.3.2 Immunocytochemistry

Cells fixed as described in Section 2.2.5 were blocked using goat or donkey blocking buffer (Table 2.1) for one hour at room temperature. Cells were then incubated overnight at 4°C in fresh goat or donkey serum containing primary antibodies as described in Table 2.3. Cells were then washed and incubated for 1 hour with fresh goat or donkey serum containing the appropriate secondary antibodies conjugated with fluorescent probes as listed in Table 2.4. After a final wash, the cells were mounted on microscope slides using the protocol described in Section 2.2.5.

Antigen	Host	Conjugated	Blocking buffer	Dilution for ICC / IHF	Source	Reference number
Cx30	Rabbit	No	Goat Donkey	1:500 /NA	Invitrogen	712200
Aqp2	Goat	No	Goat Donkey	1:200/ 1:1000	abcam	ab105171
V-ATPase A1	Goat	No	Donkey	1:50 / NA	Santa Cruz	sc-28801
α-ENaC	Rabbit	No	Donkey	1:1000 /	Loffing*	NA
Acetylated α-tubulin	Mouse	Alexa Fluor 488	Donkey	1:50 / NA	Santa Cruz	Sc-23950 AF488
Nanog	Rabbit	No	Donkey	1:500 / NA	Millipore	AB5731
Pendrin	Rabbit	No	Donkey	1:200 /1:1000	abcam	ab98091
p63	Goat	No	Donkey	1:200 /1:1000	abcam	ab114059
ΔNp63	Rabbit	No	Donkey	1:500 / NA	Biolegend	619001
V-ATPase B1	Rabbit	No	Donkey	1:25 / 1:200	Life Tech	PA535052

Table 2.3. Detail of antibodies and conditions used for immunocytochemistry staining. All antibodies were polyclonal except for the mouse anti-acetylated α-tubulin which was monoclonal, as well as already conjugated to a fluorescent probe. *The anti-ENaC antibody was a generous gift from professor J. Loffing (Zurich).

Secondary antibody	Conjugate	Dilution	Company	Reference number
Donkey anti-rabbit	Alexa Fluor 594	1:500	Life Technologies	A-21207
Donkey anti-goat	Alexa Fluor 488	1:500	Life Technologies	A-11055
Goat anti-rabbit	Alexa Fluor 594	1:500	Life Technologies	R-37117
Donkey anti-goat	Alexa Fluor 647	1:500	Life Technologies	A-21447
Donkey anti-sheep	Alexa Fluor 488	1:500	Life Technologies	A-11015

Table 2.4. Secondary antibodies (IgG H+L) used for immunofluorescence staining

2.4 Microscopy

For each experiment, images were taken during a single-day imaging session, using the same settings between control and experimental samples.

2.4.1 Epifluorescence microscopy

Images were taken with a Q-Imaging camera (Canada) on a Nikon Eclipe Ti fluorescent microscope, with DAPI, FITC, TRITC, and CY5 filters applied, for DAPI/Hoerscht, Alexa fluor 568, 488, and 647 expressions respectively. Excitation was performed at 405nm, 488nm, and 569nm. Both 60X 1.4 NA Plan Apo and 40X 1.3 NA Plan Flur oil objectives were used. Images were taken with the same appropriate exposure time for each channel. As a light source, a mercury arc lamp (X-cit 120 series, Lumen Dynamics) was used.

2.4.2 Confocal light scanning microscopy

Imaging acquisition was performed on a DMI 6000 inverted microscope, using a Leica SP5 confocal scan head and the Leica LCS imaging software. Either the 20X, 40X 1.25 NA or 63X 1.4 NA Plan Ap oil objectives were used. Laser lines were used for excitation at 569 and 488nm as well as a 405nm diode laser; the signal was collected between 494-537nm (green) or 606-719nm (red). Gain, offset and laser power were kept constant between similar experiments.

2.4.3 Confocal spinning disc microscopy

Imaging was performed using an Andor Revolution spinning disc microscope (Oxford Instruments), with the iQ3 imaging software and the iXon EMCCD camera. The 20x 0.75 NA, 40x 1.3 NA, 60x 1.62 NA, or 100x 1.4 NA (oil immersion except for 20x) objectives were used. Excitation was performed at 405nm, 488nm, and 569nm, for detection of DAPI, Alexa Fluor 448, and Alexa Fluor 594 fluorophores.

2.4.4 Multiphoton microscopy

Two-photon imaging was performed using a TriM Scope II 2-photon inverted microscope (LaVision BioTec, Germany). DAPI was excited using a Ti:Sapphire pulsed laser emitting 2 photons at 800nm. Another Ti:Sapphire pulsed laser was used to excite GFP/autofluorescence at 860nm. GFP / Autofluorescence and DAPI emission signal were separated by a 495 long-pass dichroic filter (Chroma Technologies) and collected through 525/70nm and 470nm short pass filters respectively. Depth stacks were acquired using a Nikon Apo wi 25X objective (NA = 1.25) with a step size of 1µM.

2.5 Image and data analysis

2.5.1 General image processing

Unless otherwise stated, all biological image processing was performed using the Fiji/ImageJ software. Images were processed by separating or combining colour channels, and applying visualisation aides like zoom or contrast adjustment. ImageJ was also used to reduce background fluorescence on epifluorescence images, and to perform 3D image reconstruction of z-stacks when relevant. All modifications were applied equally to the entire image as well as between images of a same experiment, including controls.

2.5.2 Cell quantification based on fluorescent labelling

For cell culture quantification, data was obtained by measuring the mean grey value of the cell surfaces (Figure 2.2). The mean grey value corresponds to the mean brightness level of the selected surface, and it was measured in 50 immuno-positive cells for each cell passage (n=4) in the ENaC and V-ATPase color channels, for a total of 200 immuno-positive cells per cell line. The grey values attributed to background auto-fluorescence on

the different channels were measured on a control area (no cells) and subtracted from the grey values of the cells.

For quantification on kidney sections, areas corresponding to the collecting duct were determined by observation of staining for Aqp2, which is specific to that kidney segment. In these areas, red-labelled or green-labelled cells (for V-ATPase B1 and Aqp2 respectively) were then counted using the cell counter plug-in in ImageJ.

For quantification of general levels of ENaC expression, the mean grey value was measured over an entire image, taken at x40 magnification on the epifluorescence microscope (described in Section 2.4.1). The surface of an image corresponds to approximately 200 cells.

A

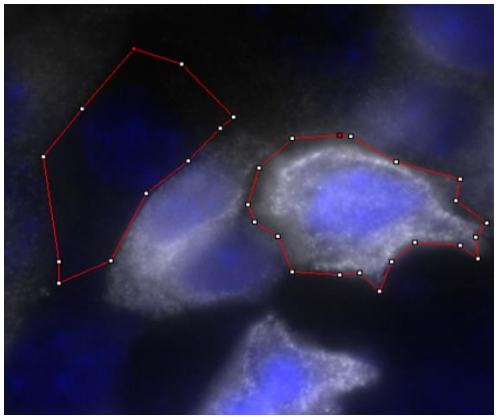

B

	Area	Mean	Min	Max	IntDen	RawIntDen
1	444.889	16.924	6	121	7529.207	289498
2	976.151	12.303	4	130	12009.909	461781
3	321.977	23.667	10	129	7620.338	293002
4	447.932	15.631	6	107	7001.586	269211
5	188.791	2.783	0	12	525.488	20205
6	265.696	9.397	3	83	2496.801	96002.000
7	468.010	16.687	4	121	7809.675	300282

Figure 2.2. Technique used for measurement of fluorescence values. (A) The cell outline is selected using the ImageJ selection tool and transferred in each colour channel. (B) The grey values, area selected (µm2), and total intensity are automatically measured using one of the software's feature. The mean grey value of the selected area was used (red rectangle in the table).

2.5.3 Sodium fluorescent labelling

Sodium in solution was labelled using CoroNa™ Green Sodium Indicator (Molecular Probes™, Invitrogen), a dye emitting a green fluorescent light upon binding to Na^+. The desiccated product was reconstituted in DMSO and added to the culture medium at a concentration of 5μM. The cells were left to incubate for 30 min and then washed twice with fresh medium before observing the fluorescence. CoroNa™ Green has an absorption maximum at 492nm, and an emission maximum at 516nm, detectable with standard green filters on fluorescence microscopes.

2.5.4 Data analysis

Data were analyzed using GraphPad Prism 7.0 (GraphPad Software) and statistical significance was assessed using a Student paired t-test or one-way ANOVA where appropriate. Data are expressed as mean ± SD, and n values refers to the number of repeats in an experiment. For each repeat, experimental conditions were matched as closely as possible.

2.6 Preparation of RNA from cultured cells

2.6.1 RNA extraction

Cells were grown to confluence in a 6-well plate and lysed directly in the well using 1ml of TRIzol® reagent. If needed, the lysate was stored at -80°C at that stage. For each sample, RNA was extracted by adding 200 μL chloroform, spinning and isolating the supernatant, then precipitated by adding 500μL isopropanol. After spinning, the pellet was washed with ethanol and resuspended in 100μL RNA-free water.

Samples were treated with rDNAseI (Ambion, Life Technologies) to remove contaminating DNA. RNA concentration and integrity were then determined using the nanodrop spectrophotometer.

2.6.2 RNA sequencing

2.6.2.1 Preparation of the RNA

For RNA sequencing, cells were cultured in T75 flasks for one week then each line was passaged in three T25 flasks and cultured for one week before using Trizol to extract the RNA. RNA was purified from genomic DNA using DNase Kit RNeasy Plus (Qiagen, USA). The process gave 12 samples comprising of three replicates of each cell line. The concentration, purity and integrity of the RNA obtained were verified using the 260-to-280-nm optical density ratio on NanoDrop, and by running the RNA on a 1% agarose gel to visualize ribosomal RNA 28S and 18S bands, for which the results were sent to the company (Figure 2.3). The RNA samples were sent frozen on dry ice at an exact concentration of mg/mL in DNA-free water.

2.6.2.2 Sequencing

RNA purity and concentration were determined as described above. Stranded total RNA libraries were prepared (Source Bioscience Plc (Nottingham, UK)) according to the Illumina TruSeq Stranded mRNA sample preparation protocol and validated on the Agilant BioAnalyser 2100. Illumina Paired-End multiplexed sequencing was undertaken using the Illumina NextSeq sequencing platform. Read quality was checked using FastQC [152] and reads were trimmed with Trimmomatic [153] yielding 20-58 million read pairs per sample. Reads were aligned with HISAT2 [154] to the Ensembl mouse GRCm38 genome (mm10). Strandedness and read distribution was assessed using RSeQC [155] and

quasi-alignment using Salmon [156] for transcript quantification. Estimated counts were adjusted for library size and transcript length using tximport [157]. Matices were filtered and normalised using the trimmed Mean of M values method [158] and differential expression was carried out using edgeR version 3.12.0 [159].

2.6.2.3 Data analysis

Data were returned in Microsoft Office Excel spreadsheets comparing samples (e.g. sample 1 *vs* sample 2 difference significance). For more in-depth analysis, the results were sent to Edinburgh Genomics, who produced a webpage allowing to search for specific genes data, compare samples, and visualize statistical analysis.

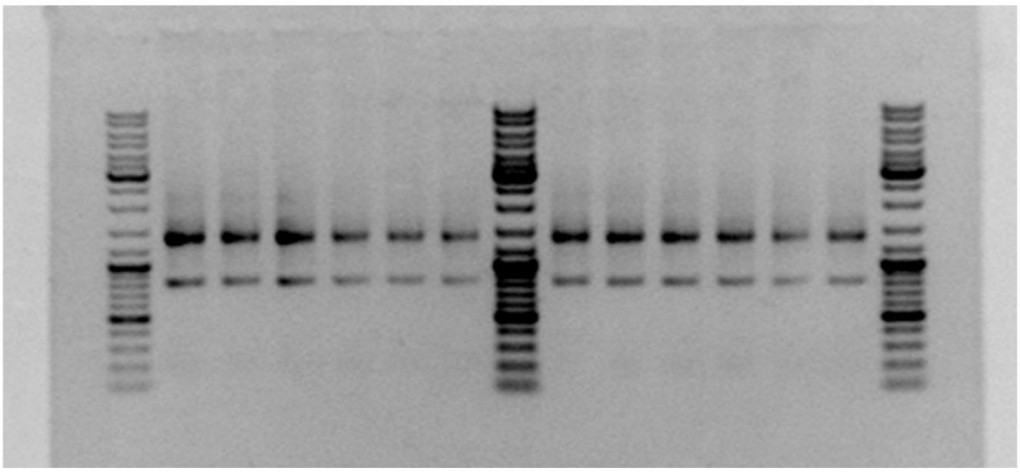

Figure 2.3. RNA integrity verification on 1% agarose gel. The 12 RNA samples run on the gel display clear 28S and 18S bands.

2.7 Polymerase chain reaction

2.7.1 Reverse transcription of RNA

For each sample, reverse transcription was performed on 500ng of RNA extracted from cultured cells as described in Section 2.6.1, using a High Capacity cDNA Reverse Transcription kit (Applied Biosystems). A 10μL mastermix was prepared containing dNTPs (0.8μL, 100mM stock), random primers (2 μL, 10X stock), reaction buffer (2 μL, 10X stock), and the multiscribe reverse transcriptase (1 μL). The mastermix was added to 10 μL DNA-free H_2O containing 500ng of RNA. Synthesis of cDNA was enabled by heating the samples 10 minutes at 25°C, then 120 minutes at 37°C, then 5 minutes at 85°C.

2.7.2 RT-PCR

PCR was performed using Taq2 DNA polymerase Mastermix (VWR Chemicals). A 25 μL reaction for each sample was constituted of 12.5 μL Mastermix, 9.5 μL H2O, 0.5 μL of forward and reverse primer, 2 μL of 25ng/μL cDNA. The reaction was enable with the following temperatures in a thermocycler (Veriti 96-well Thermal Cycler, Applied Biosystem): 4 minutes at 94°C; 35 cycles of 10 seconds at 94°C, 30 seconds at 60°C and 1 minute at 72°C; finally 7 minutes at 72°C, and eventual preservation at 4°C.

2.7.3 Agarose gel electrophoresis

A 1.5% gel was prepared by mixing SeaKem® LE agarose (Lonza, 50050) to TAE 1X solution and ethidium bromide (1μg/mL, Sigma 46066) for visualization. The gel was poured in a specialized holder and left to set. When ready, the gel is transferred to an electrophoresis tank filled with 1X TAE, and the DNA or RNA samples loaded alongside

a Gene Ruler DNA ladder for size comparison. Gels were run at 75V and 300mA for an hour. RNA or DNA was then visualized using an UV Transilluminator (UVP Inc.) and an Olympus C-4000 digital camera.

2.8 3D printing and bioprinting

3D printing work for this project was done in collaboration with Professor John Haycock's group of the Kroto Institute (University of Sheffield), and in particular with Dr. Colin Sherborne. Professor Haycock's group developed a printer using the principle of stereolithography to print different kind of polymers into very small shapes [140], [146], as described in Section 1.3.2.2.

2.8.1 PolyHIPEs

The specific PolyHIPES used in this study were first developed for bone tissue engineering [146]. They were polymerised using micro-stereolithography (see Section 2.8.2).

2.8.1.1 Composition

PolyHIPES were made up using 2 polymers, a crosslinker, a surfactant, and an initiator. The first compound was 2-Ethylhexyl acrylate or EHA (formula $C_{11}H_{20}O_2$, Sigma-Aldrich 290815), an acrylate that polymerizes into a relatively elastic product. The second compound was Isobornyl Acrylate or IBOA (formula $C_{13}H_{20}O_2$, Sigma-Aldrich 524759), another acrylate that polymerizes into a more rigid product. The two polymers can be mixed at varied percentages depending on the use for the final product, and the need for elasticity. For this study, the mix was set at 1:1 EHA/IBOA, before adding the

crosslinker, surfactant and initiator. The crosslinker (for linking the 2 polymers) used was trimethylolpropane triacrylate or TMPTA (Sigma-Aldrich, 246808), the surfactant/emulsifier (to reduce surface tension) was Hypermer™ B246 (Croda), and the initiator (that reacts with the crosslinker) was biphenyl(2,4,6-trimethylbenzoyl) (Sigma-Aldrich, 415952).

2.8.1.2 Fabrication process

The fabrication process was as follows:

- EHA and IBOA were mixed at a 50/50 ratio (corresponding masses and volumes in Table 2.5.A)
- Crosslinker, surfactant, and initiator were measured and mixed to the polymer mix (masses in Table 2.5.A), and the surfactant and initiator allowed to dissolve by gently stirring the solution.
- The resulting mix was protected from the light by wrapping the flask in foil.
- The desired volume of internal phase (75% to 90% ddH_2O) (Table 2.5.B) was added drop by drop over a period of approximately 5 minutes while vigorously mixing using an overhead chemical stirrer (IKA RW 11 basic) at 350 rpm.
- The emulsion was stirred for 2 more minutes.
- The appropriate volume of HIPEs (40ml) was transferred to a narrow glass beaker for photo-polymerisation using micro-stereolithography.

A

Component	Nominal mass (g)	Nominal volume (mL)	Density
EHA	10.4448	11.8154	0.8840
IBOA	10.4448	10.5610	0.9890
Crosslinker	5.6320	5.1200	1.1000
Surfactant	0.7956	-	-
Initiator	1.3261	-	-
Total Organic	26.5216	27.4964	0.9647

B

Internal phase percentage (%)	Continuous phase (ml)	Internal phase (ml)
75	10	30
85	6	34
90	4	36

Table 2.5. (A) Volumes and masses for PolyHIPEs fabrication. These numbers were used as a base and adapted depending on the final volume needed. (B) Volumes of ddH_2O used depending on the desired internal phase percentage.

2.8.2 3D printing of PolyHIPEs

Tubes and half-tubes were produced using projection micro-stereolithography (Section 1.3.2.2 and Figure 1.7).

2.8.2.1 Printing set-up

A 150mW, 405nm laser was used as a light source (Vortran Laser Technology Inc, Sacramento, CA, USA), producing a 5mm diameter beam that was then reflected using a Digital Micromirror Device (DMD) (Texas Instruments Incorporated, TX, USA). The DMD acted as a programmable mask, for the projection of the desired shape on the photocurable polymers. The image projected from the DMD was re-directed onto the polyHIPEs using a silver-coated mirror.

The polyHIPEs were poured in a narrow beaker and placed under a motorized, remote-controlled z-axis translation stage (Thorlabs Ltd, Cambridgeshire, UK). A L-shaped copper lip attached to the stage was lowered until just slightly covered by a thin layer at the surface of the polyHIPEs. For a perfect focus of the projected image on the surface of the copper lip, a lens was placed and adjusted in the way of the projected image, after re-direction by the mirror. The laser was then switched on and the copper stage translated in the z-axis at constant speed to produce a 3D object by continuous polymerisation of the liquid's surface (Figure 2.4).

Tubes and half tubes were printed by projecting circles and half circles of laser-emitted light on the surface of the liquid polymers, with dimensions of 1.5mm for external diameter, 1mm internal diameter.

2.8.2.2 Flat samples

Some flat samples were fabricated by releasing drops of PolyHIPEs on a coverslip and curing under a UV lamp, creating disks of approximately 1cm in diameter and 1mm thick.

2.8.1 Design of an imaging-flow chamber

To allow the perfusion of tubes and half-tubes, and imaging of the cells cultured within, Imaging and Flow Chambers (IFCs) were designed with the appropriate dimensions for the integration of the polyHIPEs objects. IFC models were designed using Autodesk™ (San Rafael, CA, USA) AutoCAD™ software, and saved in a .STL format (known as Standard Triangle Language or Standard Tessellation Language). STL files are standard for 3D printing, and describe a raw triangulated surface using a three-dimensional Cartesian coordinate surface.

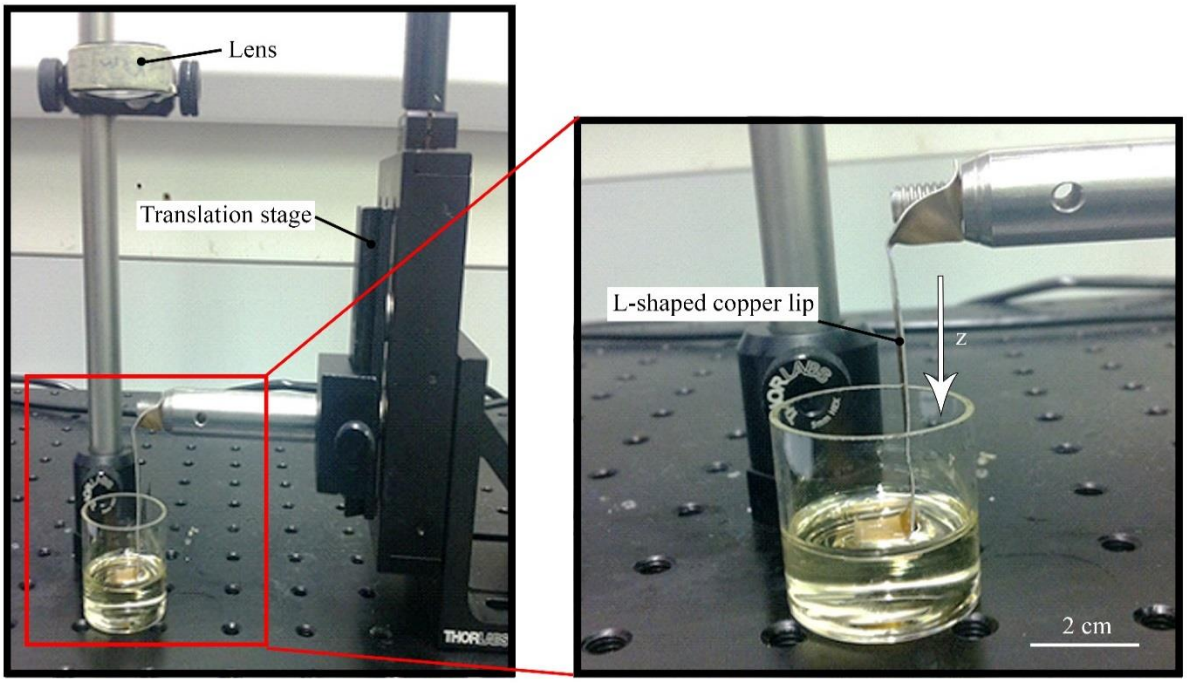

Figure 2.4. Set-up for the production of 3D objects using micro-stereolithography on polyHIPEs. The projected image is focused on the liquid's surface and the copper stage using the lens. The stage then translates down in the z axis, inducing the continuous polymerisation of the liquid polymers.

2.8.2 3D printing

2.8.2.1 Makerbot Replica 2

Objects were 3D-printed using MakerBot Replica 2 (Makerbot™, Stratasys company, New York, USA) (Figure 2.5.A), an extrusion-based 3D printer with a theoretical resolution of 100nm. The Replica 2 melts a 1.77 mm diameter filament through a nozzle heated at 230°C, extruding a 100µm diameter filament. The printer works on each layer at 30mm/s (moving speed in x and y planes).

STL files (2.8.1) were transferred on the MakerBot Desktop software (Makerbot™, New York, USA) to determine placement on the 3D printer platform, and resolution settings. The printing was set with high resolution characteristics, with a raft layer facilitating the recovery of the object after printing, and support structures printed with 20% density. The process produces a specialized file (.x3g) that is transferred to the 3D printer.

2.8.2.2 Connex3 Objet260

A Connex3 Objet260 3D printer (Stratysys, MN, USA) (Figure 2.5.B) was also used with the help of Richard Collins through a collaboration with the Edinburgh College of Art. The Connex3 Objet260 is a printer using jetting-based additive manufacturing and stereolithography to build objects with a theoretical resolution of 16µm (the thickness of one layer deposition). The printer is able to deposit up to 16 different photosensitive resins during the printing, as well as a support material (removable gel). The .STL files were modified as necessary on the Rhinoceros 5 software (Robert McNeel & Associates, USA), then transferred to the Objet Studio software (Startysys) for set-up of printing settings.

IFCs were printed using Veroclear™ (Stratysys), a transparent photopolymer close to acrylic used to print see-through objects. SUP705 (Stratysys), a removable gel-like photopolymer, was used as support material during the printing.

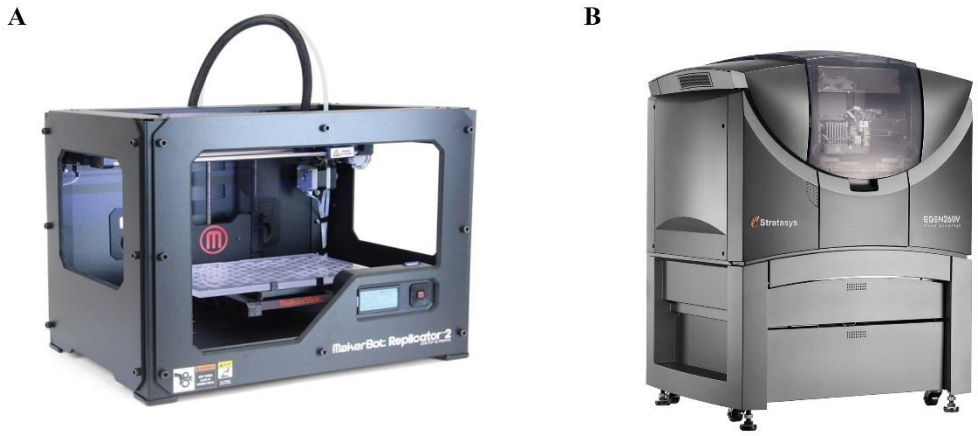

Figure 2.5. 3D printers. (A) MakerBot Replica 2 (Makerbot, Stratasys company, New York). (B) Connex3 Objet260 (Stratysis, MN). Images adapted from the Stratasys website.

2.8.3 Assembly

Assembly of the different parts of the 3D model (IFCs, polyHIPEs tubes, glass coverslip) was realized using aquarium silicone sealant (Bond-It HA6 Transparent marine adhesive premium silicone sealant). Other tools included small plastic spatulas and tweezers. A scalpel blade was used to shorten the polyHIPEs tubes if necessary and remove excessive silicone (Figure 2.6).

The following protocol was followed:

- IFCs were thoroughly cleaned of remaining printing support material using a 70% ethanol bath and a toothbrush.
- Silicone was coated inside the IFC's central opening sleeves with the tip of a small spatula.
- Half-tubes were taken out of ethanol and air dried, then placed with tweezers between the sleeves, each end glued by the pre-coated silicone.
- Tubes and IFCs were left to dry for 12 hours.

- Fresh silicone was applied to the underside of the IFCs and half tubes using a spatula.
- A glass coverslip (BDH Coverglass, 22 x 50mm) was applied and pressed until sealing was considered ideal (complete coverage of the necessary parts with silicone without clogging the tubing).
- Complete devices were left to dry for 24 hours then tested for leakage by injecting PBS.

2.8.4 Flow system

Transparent flexible tubing for microfluidics was purchased from Cole Palmer Instrument (UK) (C-Flex clear tubing, WZ-06422-00). Tubing dimensions are 500µm inner diameter and 2.07 outer diameter. Tubing can be sterilized and was developed for biomedical use. Reservoirs for culture medium were made using 50ml Falcon tubes (Corning), pierced at the bottom to accommodate the tubing. Leakage between Falcon and tubing was prevented using PDMS (Sylgard 184 Silicone Elastomer, Dow Corning).

2.8.5 Immunocytochemistry on 3D scaffold

Antibodies and concentrations are listed in Table 2.3 and Table 2.4, and were prepared following the instructions described in Section 2.3.2. For flat polyHIPEs samples or tubes not integrated in IFCs, the same immunocytochemistry protocol was followed. For intergrated tubes, 4% PFA, and antibody solutions were injected in the devices (100µl) through the channels openings on top of the chamber. PBS washes were realized by continuous injection of 3 x 1ml PBS.

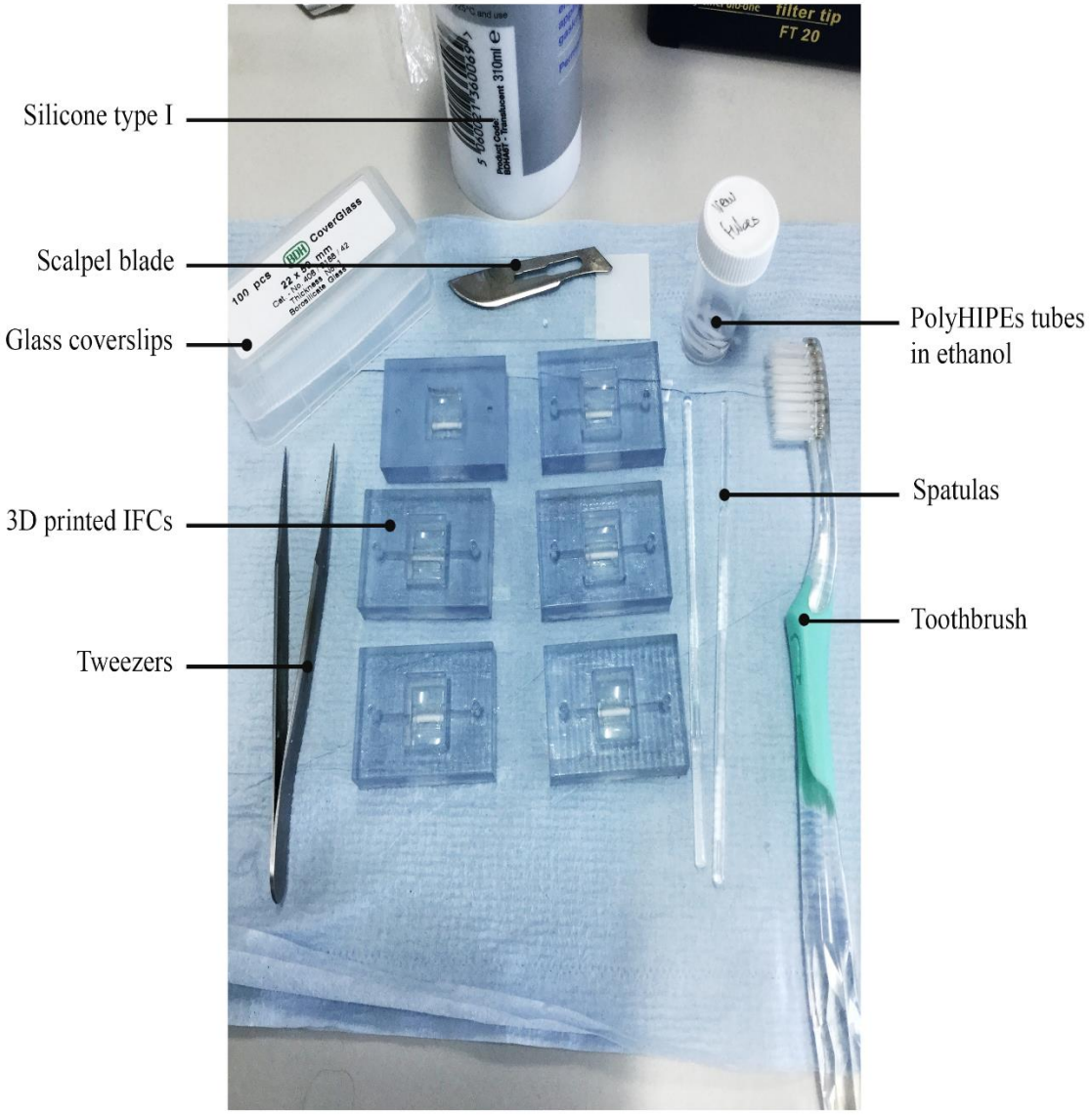

Figure 2.6. Typical setup for IFC's assembly. The scalpel blade is used to shorten the PolyHIPEs tubes to the right length if needed. The toothbrush is a useful tool to clean the printed chambers from the support wax, in an ethanol bath. Silicon is applied on the relevant parts using the plastic spatulas and the tweezers for precision. The chambers are sealed on glass coverslip for imaging purposes.

3 Establishment of a cell culture protocol specific to the mCCD$_{cl1}$ cell line: effect of media and passages on electrophysiological properties

3.1 Introduction

$mCCD_{cl1}$ cells are extremely sensitive to environmental cues (temperature, CO_2 levels), as well as to "rough" handling, for example during cell passaging (unpublished observations). Development and optimization of a protocol for $mCCD_{cl1}$ cells culture is necessary for the recording of consistent and meaningful data involving these cells. Functional characteristics such as ion fluxes are an excellent indicator of cell activity and health, and can be recorded directly on the live cells with a low signal-to-noise ratio [160], [161].

In this study, functional characteristics were assessed using electrophysiological measurements [162], which here means the recording of electrogenic transport in $mCCD_{cl1}$ cells. An electrogenic transport leads to the translocation of a net charge (+ or -) across both membranes (transepithelial). ENaC and ROMK are the main electrogenic channels in the collecting duct, and Na^+ transport represents the bulk of electrogenic movements in most parts of the tubule and collecting duct [163], [164].

For electrophysiological measurements, cells are cultured on porous membranes that allow access to culture medium on both apical and basolateral sides. Transepithelial electrical measurements (V_{te} and R_{te}, see Section 2.2.9) are typically performed either by using electrodes directly on the membranes (type EVOM®)[165] or by transferring the cells to an Ussing chamber [166], which provides live data recording for short-term experiments. Drugs and hormones are added to the surrounding medium to test hypotheses on their functional effects and on the cells' physiological reaction.

Transepithelial measurements provide valuable information on the nature, direction and scale of electrogenic transport in polarized cells.

3.1.1 Aims

. The following experimental aims were addressed:

- Observe the effects of environmental changes, specifically using different media additive sources.
- Use functional data to determine the stability of the $mCCD_{cl1}$ cell line.
- Establish a specific protocol for consistent culture and functional measurements of $mCCD_{cl1}$ cells.

3.2 Results

$mCCD_{cl1}$ cells were seeded on day 0 of the experiments using a 1:1 dilution ratio (confluent density) to allow for the rapid formation of a monolayer, and cultured in 6 different growth media, named M1-6. All media were based on the recipe used in the original study of $mCCD_{cl1}$ cells by Gaeggeler *et al.* [80], but contain additives with different sources. The media composition and source are detailed in Table 3.1. M1 and M2 use different sources of the following additives: Insulin, Sodium Selenite and Apotransferrin, EGF and FBS. M1 also uses L-glutamine as an additive, not present in M2. Media M3-6 are variations of M1 and M2, substituting one additive at a time.

$mCCD_{cl1}$ cells removed from cryopreservation were thawed using two different methods, called T1 and T2 (for Thawing method 1 and Thawing method 2). T1 consists in covering the frozen cells directly in warm media (37°C) for a rapid thawing. T2 consists in leaving the cell vial in dry ice for a few minutes, then at room temperature for a few minutes, followed by the incremental application of warmed water (37°C) on the outside of the vial for a slow thawing process.

Experiments for the development of a cell culture protocol were conducted on the $mCCD_{cl1}$ cells from passage 24, and the electrophysiological measurements were conducted following the specific EVOM® measurements protocol described in Section 2.2.9.

Medium name	Recipe	Supplier
M1	Phenol red free DMEM/F12 (500ml)	Life Technologies (21041033)
	Insulin (5µg/ml) *	|
	Sodium selenite (60nmol/l) *	| Sigma (l1884-1vl)
	Apotransferrin (5µg/ml) *	|
	Dexamethasone (50nmol/l)	Sigma (D8893-1mg)
	Triiodothyronine (1nmol/l)	T6397-100mg
	L-glutamine (2nmol/l)	Sigma (G7513)
	EGF (10ng/ml)	Life Technologies (PHG-0311)
	FBS (2%)	Bio&Sell(DE)
	Penicillin-streptomycin (100µg/ml)	Sigma (P4333-100ml)
M2	Phenol red free DMEM/F12 (500ml)	Life Technologies (21041033)
	Insulin (10µg/ml) *	|
	Sodium selenite (600nmol/l) *	| Gibco (41400045)
	Apotransferrin (5.5µg/ml) *	|
	Dexamethasone (50nmol/l)	Sigma (D8893-1mg)
	Triiodothyronine (1nmol/l)	T6397-100mg
	EGF (10ng/ml)	Gibco (PMG8044)
	FBS (2%)	Gibco (10500064)
	Penicillin-streptomycin (100µg/ml)	Sigma (P4333-100ml)
M3	M2	-
	+ L-glutamine (2nmol/l)	Sigma (G7513)
M4	M2	-
	FBS replaced by M1 FBS (2%)	Bio&Sell(DE)
M5	M2	-
	Insuline/Sodium selenite/Apotransferrin replaced by M1 ITS	Sigma (l1884-1vl)
M6	M2	-
	EGF replaced by M1 EGF	Life Technologies (PHG-0311)

Table 3.1. Recipes for the alternative media used with $mCCD_{cl1}$ cells. * Components supplied combined in one solution by the company.

3.2.1 Culture media additives: testing of two media

The first series of experiments was performed in parallel with Dr. Morag Mansley to assess any measurement differences due to the user's cell culture technique and handling. No significant difference was observed between the two sets of results, so data from different users was considered as technical repeats.

Culture media M1 and M2 were tested during 2 cell passages (numbers 24 and 25). Passage 24 (p24) was the earliest passage available, kindly provided in 2006 by Prof. Bernard Rossier's group (University of Lausanne, Lausanne, Switzerland). General principle of the experiment can be found on Figure 3.1.

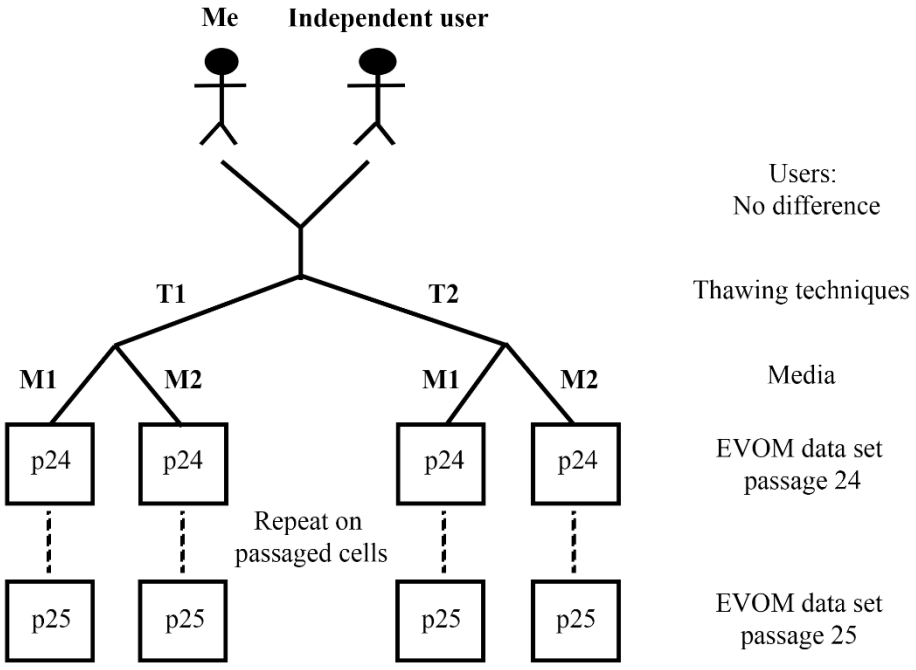

Figure 3.1. Principle of experimental process for testing of 2 culture media on $mCCD_{cl1}$ cells. Both users measured electrophysiological data using EVOM® electrodes on $mCCD_{cl1}$ cells cultured in media M1 and M2 after being thawed using 2 different techniques. The process was repeated for one cell passage.

3.2.1.1 Passage 24 (p24)

Transepithelial electrophysiological measurements of parental $mCCD_{cl1}$ cells (passage 24) were taken on cells thawed using two different techniques (T1 and T2) and cultured in two different media (M1 and M2), over 10 days. The measurements did not reveal any significant differences between the two thawing techniques T1 and T2 (Figure 3.2). Culture in M1 and M2 revealed baseline I_{sc} values of -8.6 ± 1.5 $\mu A/cm^2$ and -0.8 ± 1.1 $\mu A/cm^2$ respectively (data averaged for T1 and T2). Cells in M2 failed to develop a significant V_{te} (Figure 3.2.B), which made I_{sc} calculation irrelevant for this group (dashed lines on Figure 3.2). R_{te} developed to 1.00 ± 0.12 $k\Omega \cdot cm^2$ for cells in M1, and only to 0.39 ± 0.11 $k\Omega \cdot cm^2$ for cells in M2 (Figure 3.2.A).

For cells in M1, the application of amiloride (10µM, 10 min) to the apical bath inhibited I_{sc} by 96.5 ± 1.2 % (Figure 3.2.D), indicating that the basal current can mostly be attributed to the transport of Na^+ via ENaC. The addition of aldosterone (3nM, 3 h) increased I_{sc} by a factor of 2.2 ± 0.1 fold, to reach values of -20.2 ± 4.6 $\mu A/cm^2$.

From day 8, the medium is progressively stripped of additives (only charcoal-stripped FBS and antibiotics on day 9, and only antibiotics added for day 10), which explains the drop in V_{te} and incidentally in I_{sc} to attain the "baseline" value at day 10.

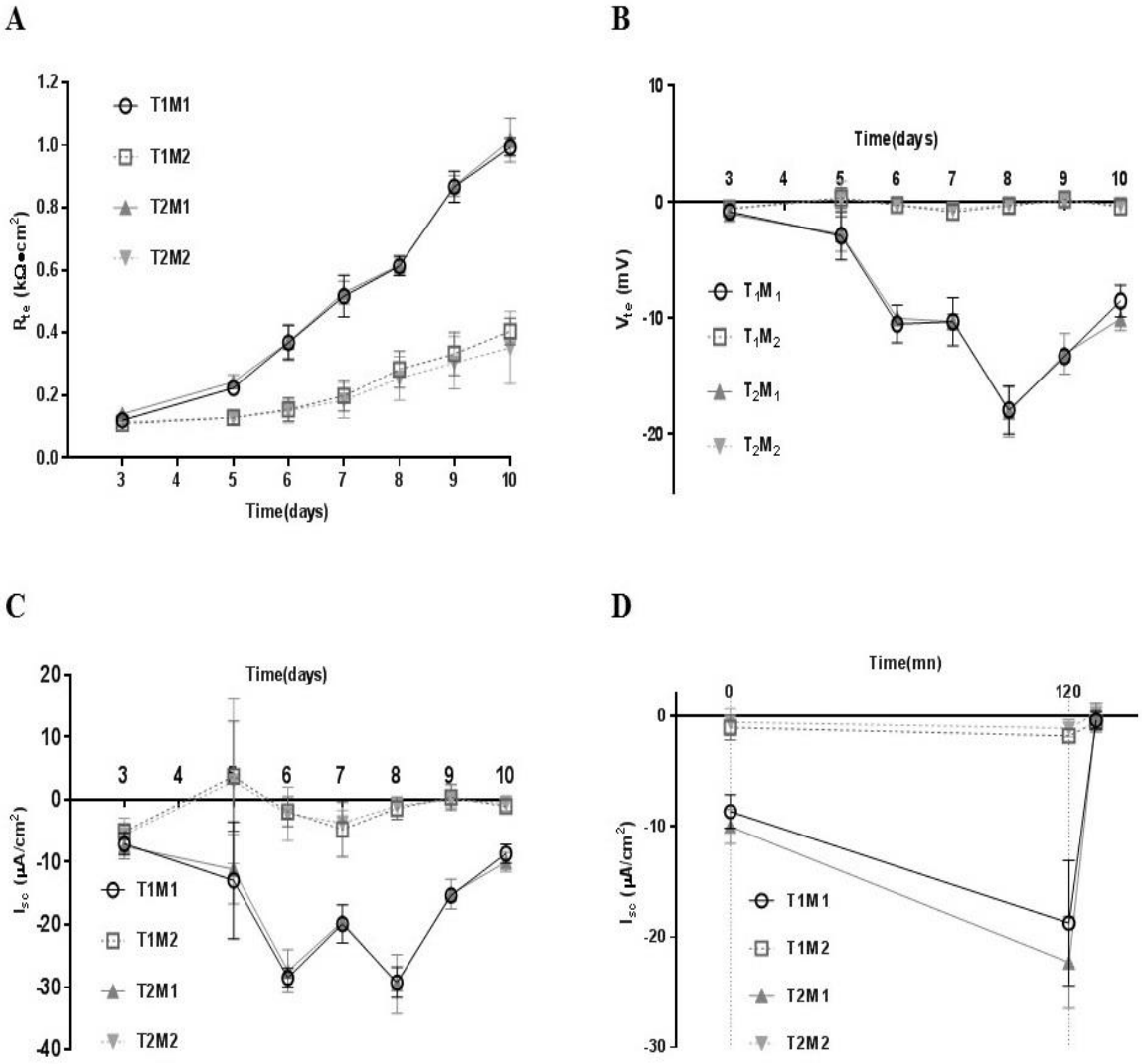

Figure 3.2. **Media composition has an important effect on mCCD$_{cl1}$ sodium transport.** T1 and T2 correspond to thawing techniques 1 and 2. M1 and M2 correspond to culture media 1 and 2. (A) Transepithelial voltage (V_{te}) measured across monolayers of mCCD$_{cl1}$ grown on Snapwells filters, between day 3 and 10 after seeding. (B) Transepithelial resistance (R_{te}) measured across monolayers of mCCD$_{cl1}$ cells. (C) I_{sc} was calculated using Ohm's law. Values are shown as mean ± SEM (n=4). (D) Effects on baseline I_{sc} of aldosterone (3nM) and amiloride (10µM, apical bath) added at t=0 and t=120min respectively. Values are shown as mean ± SEM (n=4).

3.2.1.2 Passage 25 (p25)

The experiment was then conducted with the same cells, cultured and passaged in M1 or M2 in parallel to the p24 experiment. The transepithelial voltage (V_{te}) for p25 exhibited a similar pattern compared to p24 cells, with a negligible value for cells in M2. For M1 cells however, p25 V_{te} values attained -28 ± 2.3 mV at day 8 of the experiment, against -18.0 ± 2.1 mV for p24 (Figure 3.3.B), inducing an overall higher I_{sc} from day 3 to day 8 (Figure 3.3.C) for p25 cells compared to p24 cells.

As the V_{te} of cells cultured in M2 remained insignificant, the current value did not vary from p24 to p25. On the other hand, the transepithelial resistance (R_{te}) of p25 cells cultured in M2 increased compared to p24, from 0.39 ± 0.11 kΩ·cm^2 at p24 0.98 ± 0.13 kΩ·cm^2 at p25 (Figure 3.3.A), a significant increase from one passage to the other. Baseline current in M1 was identical for p24 and 25 (about -9 μA/cm^2), but the effect of aldosterone was more important at p25, with a 2.8 ± 0.5 fold increase of I_{sc}, *versus* 2.1 ± 0.6 fold increase for p24.

In summary, for cells in M1, V_{te} and I_{sc} improved slightly from p24 to p25 from day 3 to day 8, but were identical when cultured in basal medium (baseline values). For cells in M2, V_{te} didn't change from p24 to p25, but R_{te} improved dramatically (See Table 3.2).

	M1		M2	
	R_{te}	V_{te}	R_{te}	V_{te}
p24	High	High	Low	Insignificant
p25	Slight increased	Slight increase	Large increase	Insignificant

Table 3.2. Summary of differences between $mCCD_{cl1}$ cells in culture media M2 and M2, from passage 24 to passage 25 (p24-5). R_{te} for transepithelial resistance. V_{te} for transepithelial voltage.

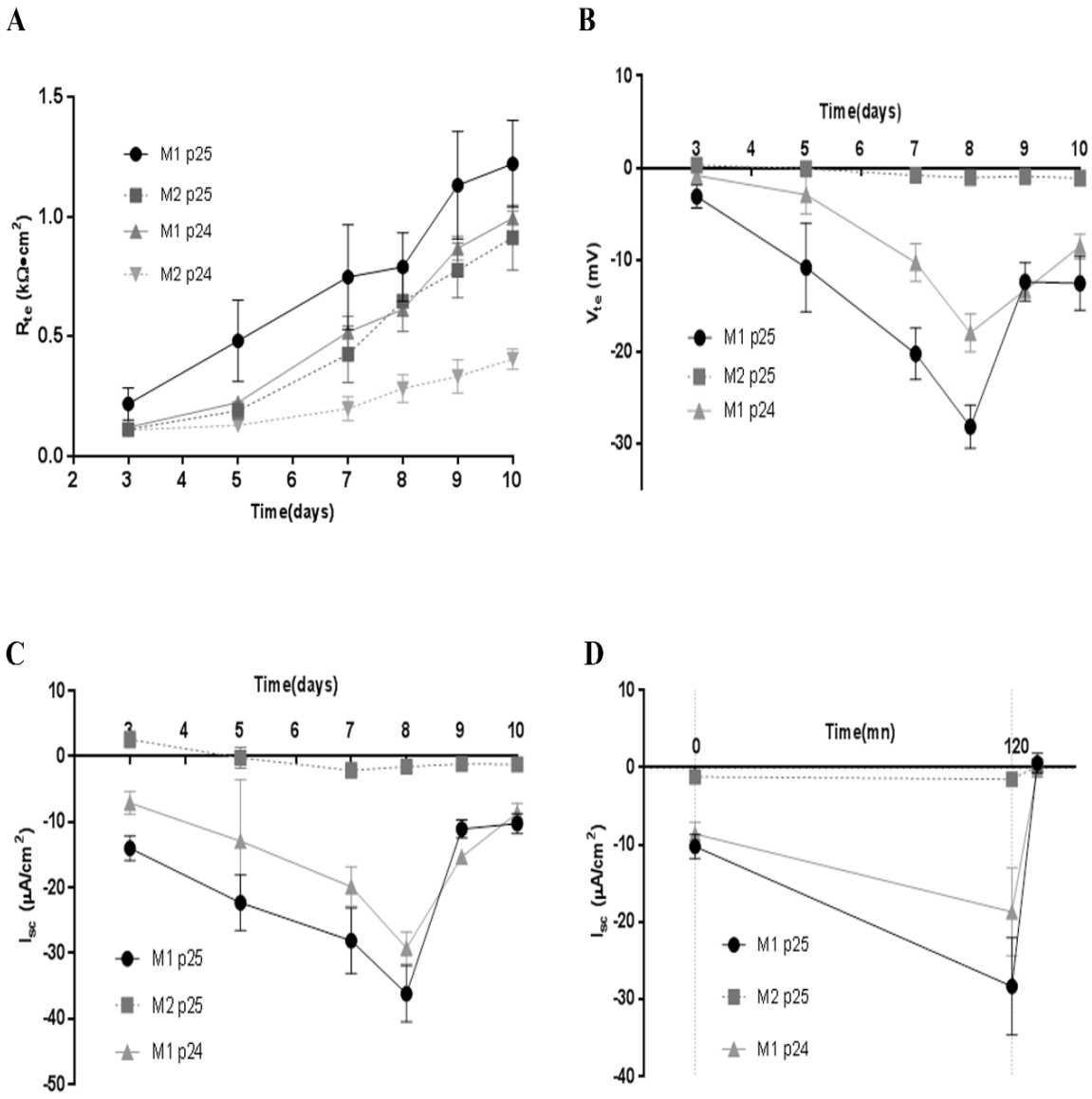

Figure 3.3. Electrophysiological differences drift with time. M1 and M2 correspond to culture media 1 (full lines) and 2 (dashed lines). p24 and p25 for passages numbers. (A) Transepithelial voltage (V_{te}) measured across monolayers of $mCCD_{cl1}$ grown on Snapwells filters, between day 3 and 10 after seeding for p24 and p25. (B) Transepithelial resistance (R_{te}) measured across monolayers of $mCCD_{cl1}$ cells for p24 and p25. (C) I_{sc} was calculated using Ohm's law. Values are shown as mean ± SEM (n=3 or 4 for p24). (D) Effects on baseline I_{sc} of aldosterone (3nM) and amiloride (10µM, apical bath) added at t=0 and t=120min respectively. Values are shown as mean ± SEM (n=3 for p25 or n=4 for p24).

3.2.2 Testing the medium's components

To identify the factors responsible for the functional differences observed between cells cultured in M1 and M2, electrogenic transport was measured for the parental line, passaged and cultured in 6 media: 2 controls (M1 and M2 as previously described), and 4 media in which one additive of M2 was substituted at a time by the corresponding additive from M1. These media were named M3, M4, M5, and M6 (Table 3.1).

Compared to the experiments detailed in Section 3.2.1, the difference was pronounced for M2, with the cells developing a significant V_{te} over the course of the 10 days of culture (Figure 3.4). R_{te} in M2 also developed to values close to cells in M1, at 1.5 ± 0.1 kΩ·cm^2 and 1.3 ± 0.1 kΩ·cm^2 respectively (day 10). However, cells cultured in M1 behaved comparably to those in previous experiments, with stable V_{te} maximum value of – 30.8 ± 2.1 mV (- 28.2 ± 2.2 mV previously).

Values of V_{te} for M2 stayed lower than M1 values from day 3 to day 9, and lower than any of the other media, which translated to a lower I_{sc}. V_{te} for all media types became very close or identical at day 10 (baseline value, without added hormones), at approximately -10 mV.

Comparison of M1 and M2 to M3-6 did not clearly show any additive as responsible for the functional loss, since many of the differences between groups were not significant and quite variable from one plate to the other. However, when cultured in basal media only (at day 10), all the groups exhibited a close and consistent I_{sc}, with low variability (see day 10 I_{sc} on Figure 3.4.C), which suggests a definitive effect of the additives on sodium transport abilities.

Medium name	Recipe differences
M1	Suppliers for: ITS, EGF, FBS.
M2	Suppliers for: ITS, EGF, FBS. No L-Glutamine
M3	M2 + L-glutamine
M4	M2 with M1 FBS
M5	M2 with M1 ITS
M6	M2 with M1 EGF

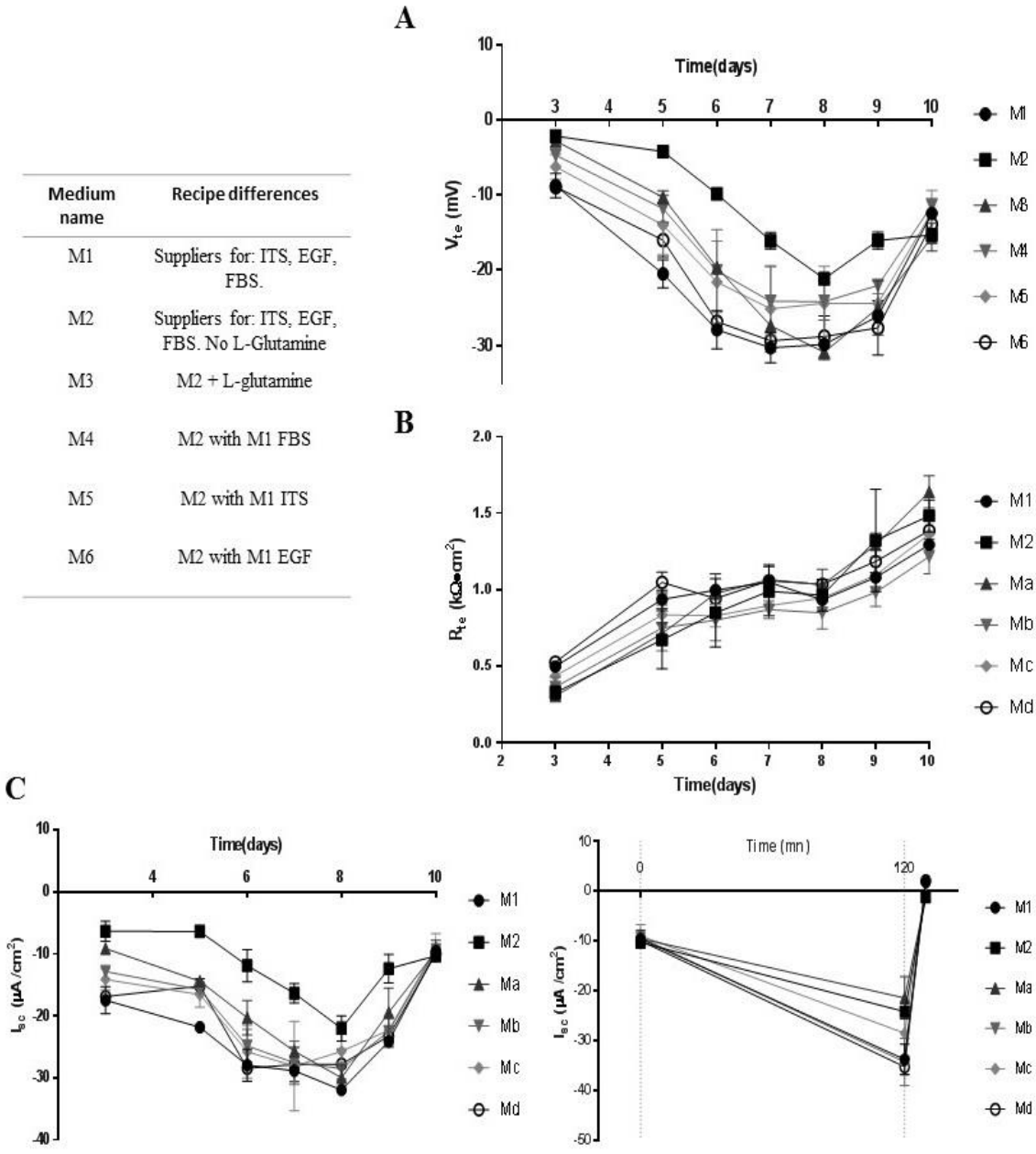

Figure 3.4. Electrophysiological measurements of $mCCD_{cl1}$ using alternate media additives. Top left, a summary table of the differences between media (For detailed composition, see Table 3.1, p.69). (A) Transepithelial voltage (V_{te}) measured across monolayers of $mCCD_{cl1}$ grown on Snapwells filters, between day 3 and 10 after seeding. (B) Transepithelial resistance (R_{te}) measured across monolayers of $mCCD_{cl1}$ cells. (C) I_{sc} was calculated using Ohm's law. Left panel, I_{sc} through the 10 days of culture. Right panel, effects on baseline I_{sc} of aldosterone (3nM) and amiloride (10µM, apical bath) added at t=0 and t=120min respectively. Values are shown as mean ± SEM (n=3).

A significant effect of the media composition on the aldosterone response was observed. The aldosterone response values and their significance can be seen in Table 3.3. Three groups emerged: M1, M4 and M6 had the same effect with an I_{sc} increase of about 3.5-fold (group 1); M3 and M2 with a lower I_{sc} increase of about 2.3-fold (group 2); and M5 situated in the middle (but with no significant difference with one group or the other).

Group 1 corresponds to M2 media with M1 FBS (fetal bovine serum) and EGF, group 2 to the addition of L-glutamine to M2. In terms of aldosterone response, the source of FBS and EGF seems to have a similar impact, single-handedly driving cells in M2 to behave like cells grown in M1. The addition of L-glutamine to M2 didn't have any impact. ITS, the additive replaced in M5, seemed to improve the aldosterone response, however with a lesser impact that FBS or EGF.

Media	M1	M2	M3	M4	M5	M6
Isc Fold change, aldosterone treatment ± SD	3.5 ± 0.2	2.3 ± 0.2	2.2 ± 0.1	3.7 ± 0.5	3.2 ± 0.1	3.5 ± 0.3
Multiple comparison test (significance)	*					
		*				
			*			
				*		
					*	
						*

Table 3.3. Isc fold changes after aldosterone application on cells cultured in different media. Fold changes are in mean ± SD (n=3). Lines indicate which groups have a significant different detected between them using one-way ANOVA test and Tukey's multiple comparison test. The beginning and end of each line indicates with group is pointed out, for example M1 and M2 for the first line.

3.3 Conclusions

3.3.1 Chapter summary

Using the $mCCD_{cl1}$ cell line, a protocol was developed for the recording of consistent and reliable electrophysiological data. Cells were grown using different thawing techniques, and different sources of media additives (and concentrations in some cases).

In M1, cells immediately developed high R_{te} and V_{te}, and a slight increase was observed over one cell passage, before stabilization was observed. In M2, cells failed to develop a significant V_{te} and exhibited low R_{te}. However, R_{te} increased dramatically after one passage. After another passage, $mCCD_{cl1}$ cells developed significant V_{te} in M2, but still lower than cells in M1. Testing of different media additives sources in alternative media M3-6 did not single out one additive responsible for the differences observed between cells cultured in M1 and M2, but significant difference in aldosterone response was observed with different sources of FBS and EGF (additive effects summarized in Table 3.4).

Additives	Differences	Effect	
ITS	Supplier Concentration	No effect	Stability after thawing
EGF	Supplier	Aldosterone response	
FBS	Supplier	Aldosterone response	
L-Glutamine	Presence/Absence	No effect	

Table 3.4. Summary of additives differences and effects on $mCCD_{cl1}$ cells. ITS stands for Insuline/Apotransferrin/Sodium Selenite.

3.3.2 Discussion

$mCCD_{cl1}$ cells are obviously able to exhibit variable functional characteristics. The differences were quite dramatic, with cells from the same thawed sample recovering

quickly from the process or completely losing their sodium transport functions after being cultured in slightly different media. The effect of different media composition was however not directly visible, as cell growth did not seem impaired in cells cultured in flasks in M2. $mCCD_{cl1}$ cultured in all media exhibited doming after confluency. For functional characteristics, a very consistent protocol, medium, and conditions seem necessary in all studies involving $mCCD_{cl1}$ cells, as well as repeated recordings over several passages to ensure stabilization of the cell line. All media tested in this chapter were based on the recommended medium used with $mCCD_{cl1}$ cells in the original work [80]. However, additives sources proved to be critical and cells cultured in M1 exhibited electrophysiological characteristics closest to the expected values (personal communication from Dr. Mansley, and comparison to previous work with $mCCD_{cl1}$ cells [80], [81], [84]). M1 was chosen as the growth medium for $mCCD_{cl1}$ cells, due to the rapid stabilization of cells R_{te} and V_{te}, the higher values recorded after thawing, and the larger response to aldosterone. In theory, media M4 and M6 could also be used (FBS and EGF identical as M1).

3.3.3 Final protocol

Considering the changing values from one passage to the other after thawing, even in M1, electrophysiological measurements from this point onwards were taken after strictly adhering to the following protocol:

- $mCCD_{cl1}$ cells were cultured using the medium M1 exclusively. M1 was consequently constantly prepared using the same batch of FBS (Bio&Sell), EGF (Life Technologies), ITS (Sigma) and L-Glutamine (Sigma) for all experiments.
- $mCCD_{cl1}$ cells were grown for one week after thawing, fresh medium M1 added every 2 days.

- Fresh medium was added the day before passaging.
- Cells were passaged using delicate handling, avoiding excessive pipetting.
- Cells were left once again to grow until reaching confluency and exhibiting doming, fed every 2 days.
- Seeded on the Transwell® membranes (day 0) for electrophysiology (which technically constitutes another passage). The cells were seeded at confluent density for the rapid formation of a resistive monolayer.

4 Immunocytochemistry characterization of $mCCD_{cl1}$ shows plasticity consistent with the ability to transition between principal and intercalated cells.

4.1 Introduction

The collecting duct plays a critical role in the regulation of urine volume, pH and osmolarity, with two thirds of the hypo-osmotic fluid entering the collecting duct being reabsorbed in the CCD [23].

The CCD is composed of two distinct cells types, principal cells (PCs) and intercalated cells (ICs), the latter being sub-divided into α and β subtypes [167]. The different cell types are detectable in the kidney by immunostaining. Typically, PCs show apical membrane staining for Aqp2 or ENaC channels. V-ATPase localises to the apical membrane of α-ICs, and to the basolateral membrane in β-ICs. Morphological differences include the presence of a primary central cilium on PCs while the apical membrane of ICs are covered with a dense layer of microvilli [26]. The collecting duct is currently the subject of growing interest due to a potential capacity for plasticity between PCs and ICs, as demonstrated in several studies using KO animals or induced diseases [25], [61], [73], [74].

The $mCCD_{cl1}$ cell line was established by microdissecting the cortical collecting duct of a wild type mouse [80]. It is derived from a single clone (cl1), that "spontaneously transformed". They have been used in multiple studies for studying PC physiology and are considered to be a "highly differentiated murine principal cell line" [81].

Chapter 3 showed variability of electrophysiological data measured on $mCCD_{cl1}$ cells grown in different culture media. This observation led to a growing number of questions about the nature of the cell line. Therefore, the aim of this chapter is to characterize the $mCCD_{cl1}$ cells using immunocytochemistry, to determine the composition and understand the functional variability of the cell line.

4.1.1 Aims

To address the questions about the nature of $mCCD_{cl1}$, the following experimental aims were addressed:

- Observe the cells in a culture environment allowing for polarization (filters).
- Confirm the preliminary immunostaining results using PC and IC specific markers.
- Establish clonal cell lines to:
    - Analyse the composition of $mCCD_{cl1}$ cells in more detail.
    - Determine the capacity of $mCCD_{cl1}$ cells to transmit "intermediate" characteristics vertically through single cell cloning.

4.2 Results

4.2.1 Preliminary immunostaining

To verify the nature of the cell line, preliminary immunocytochemistry studies were performed on $mCCD_{cl1}$ cells cultured on glass coverslips for imaging purposes (Section 2.3.2).

Since the $mCCD_{cl1}$ cell line has been previously described as a principal cell line, Aqp2 was chosen as a positive marker for PC cells and Cx30 (a marker of intercalated cells) was selected as a negative marker. Aqp2 and Cx30 were first looked at on separate cultures (Figure 4.1). As predicted, Aqp2 was expressed widely within the cultured cells (Figure 4.1.A). However, surprisingly, Cx30 was also observed in a subset of cells (Figure 4.1.B), raising the suspicion that the cell line might have been contaminated prior to being frozen.

However, double immunostaining of the cells for Aqp2 and Cx30 revealed that the population did not fall into a bi-modal distribution between distinct cells types ("PC-like" and "IC-like"), with cells clearly expressing one or the other characteristic marker. Instead, cells presented a range of expression of both markers (Figure 4.2.A). At higher magnification (Figure 4.2.B), the localization of Cx30 and Aqp2 staining in $mCCD_{cl1}$ cells showed that many cells expressed both markers, suggesting an "intermediate" cell type.

This preliminary immunocytochemistry study of $mCCD_{cl1}$ cells showed the expression of a marker typically associated with ICs. Whilst this could be a sign of contamination by intercalated cells during the establishment of the cell line, the localization of both PC and IC markers in the same cells suggests an intermediate cell type.

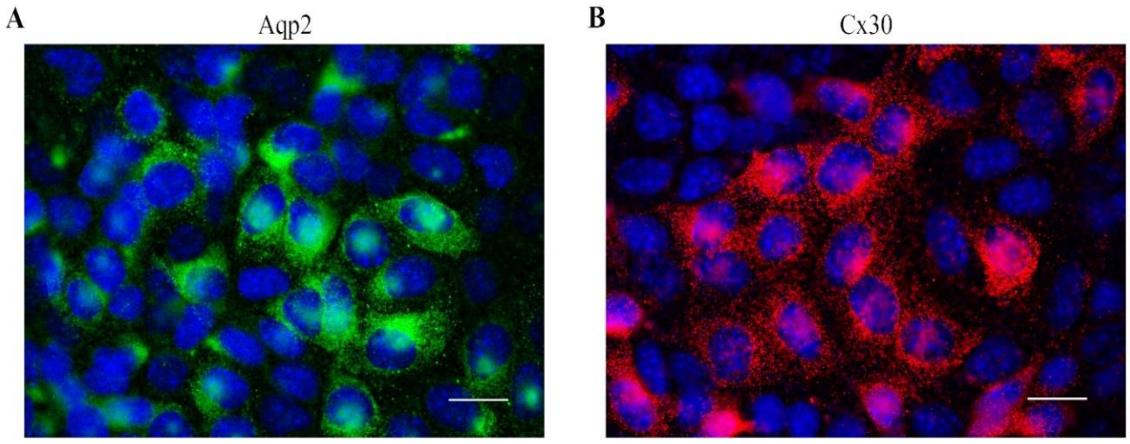

Figure 4.1. Immunostaining of $mCCD_{cl1}$ cultured on glass slides using anti-Aqp2 and anti-Cx30 antibodies. (A) Immunostaining for Aqp2 across the cell line (green). Scale bar 15µm. (B) Immunostaining for Cx30 across the cell line (red). DAPI staining of cell nuclei in both images. Scale bar 15µm.

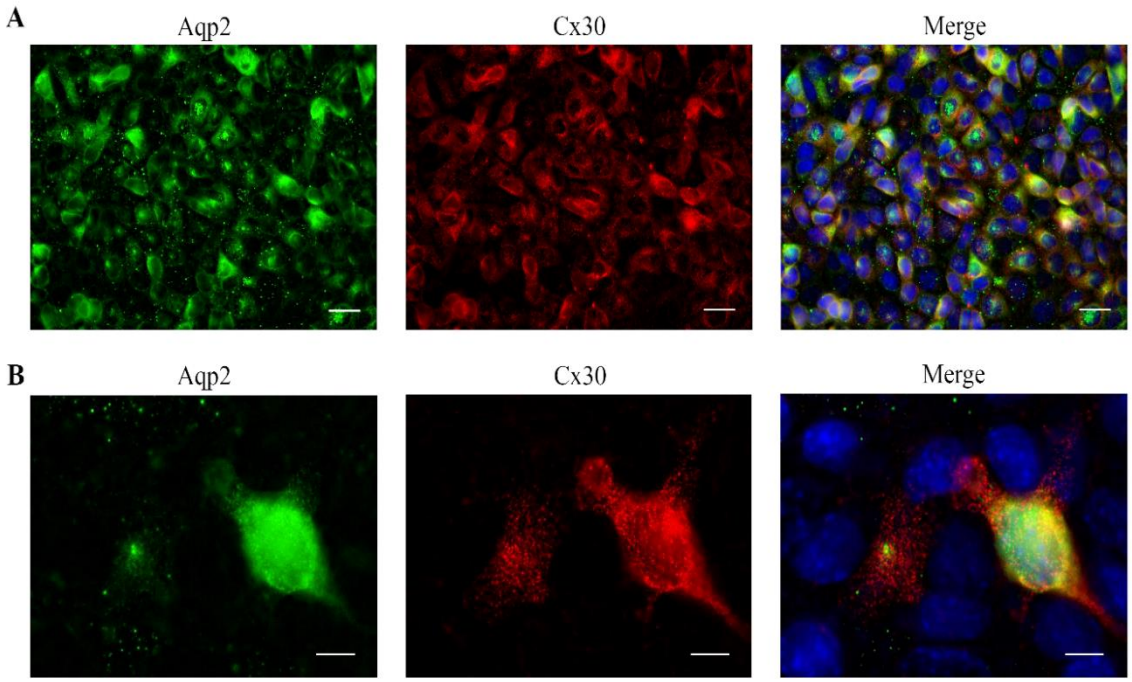

Figure 4.2. Double immunostaining of mCCD$_{cl1}$ cultured on glass slides using anti-Aqp2 and anti-Cx30 antibodies. (A) Double immunostaining for Aqp2 (green) and Cx30 (red). Scale bar 20µm. (B) Higher magnification of Aqp2 (green) and Cx30 (red) staining in mCCD$_{cl1}$ cells. Scale bar 5µm - DAPI staining of cell nuclei in merged pictures.

4.2.2 General observations

mCCD$_{cl1}$ cells form a tight layer of confluent cells after three to five days of culture at 37°C, with cells seeded at 1:10 and fed using the specific media described in Section 2.2.2. Cultured in flasks or on Corning® Transwell® membrane filters (see Section 2.2.7), they have the shape of a flattened cobblestone or "fried egg" (Figure 4.3), with the apical membrane flattening around the nucleus. mCCD$_{cl1}$ cells' dimensions are up to approximately 20µm in diameter, and 10µm in height, and they acquire a polygonal shape after confluency, typical of epithelial monolayers.

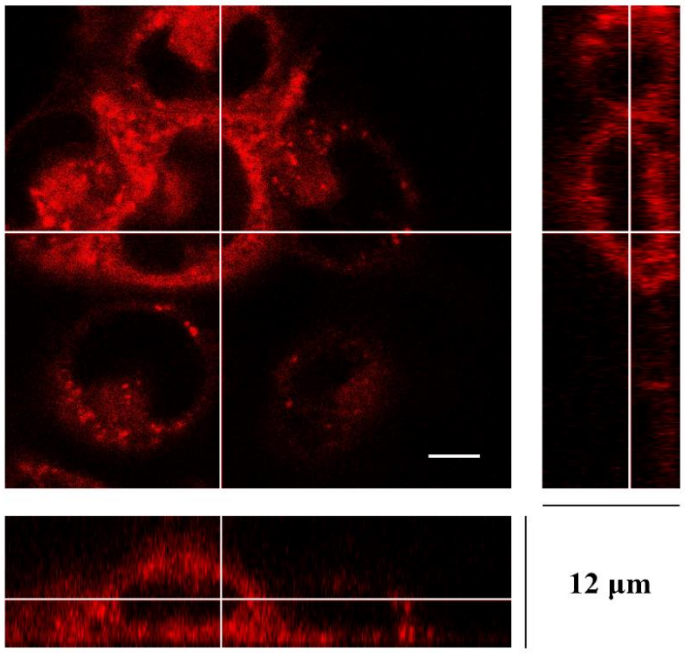

Figure 4.3. mCCDcl1 have flattened cobblestone shape. Confocal imaging of live $mCCD_{cl1}$ cultured on glass and z-projections on right and bottom. The cells have been stained with Fuse-It™ membrane dye (red). The projections correspond to the white lines on the centre image. White scale bar is 5µm.

4.2.3 Heterogeneity of the $mCCD_{cl1}$ cell line

Unless otherwise specified, $mCCD_{cl1}$ cells were cultured on Corning® Transwell® permeable membranes to allow for cell polarization, as described in Chapter 2 Section 2.2.7, and following the specific protocol described in Section 3.3.3. The same cells were used simultaneously to conduct the studies described in Chapter 5 ("Electrophysiological analysis of the $mCCD_{cl1}$ cell line"), and for the immunocytochemistry described in this Chapter, to eventually link phenotypical and functional data.

4.2.3.1 Immunocytochemistry of Aqp2 and Cx30 on polarized cells

The cells cultured on Transwell® permeable membranes expressed the expected PC marker Aqp2. As with the preliminary immunostaining, numerous cells also expressed the typical IC marker Cx30 (Figure 4.4.B). At higher magnification, the co-localisation of Cx30 and Aqp2 staining in $mCCD_{cl1}$ cells showed that while some cells only stained for the PC or IC marker, many cells expressed both markers, suggesting an "intermediate" or transition cell type (Figure 4.4.D).

4.2.3.2 Immunocytochemistry of Aqp2 and V-ATPase B1 on polarized cells

A similar phenotype was observed with cells stained for V-ATPase B1, a V-ATPase subunit specific to intercalated cells, and Aqp2 (Figure 4.4.B), specific to PCs. Whilst 47% of total cells did not show any significant staining, 42% of cells stained for both markers and ~9% and ~2% cells stained exclusively for Aqp2 and V-ATPase respectively.

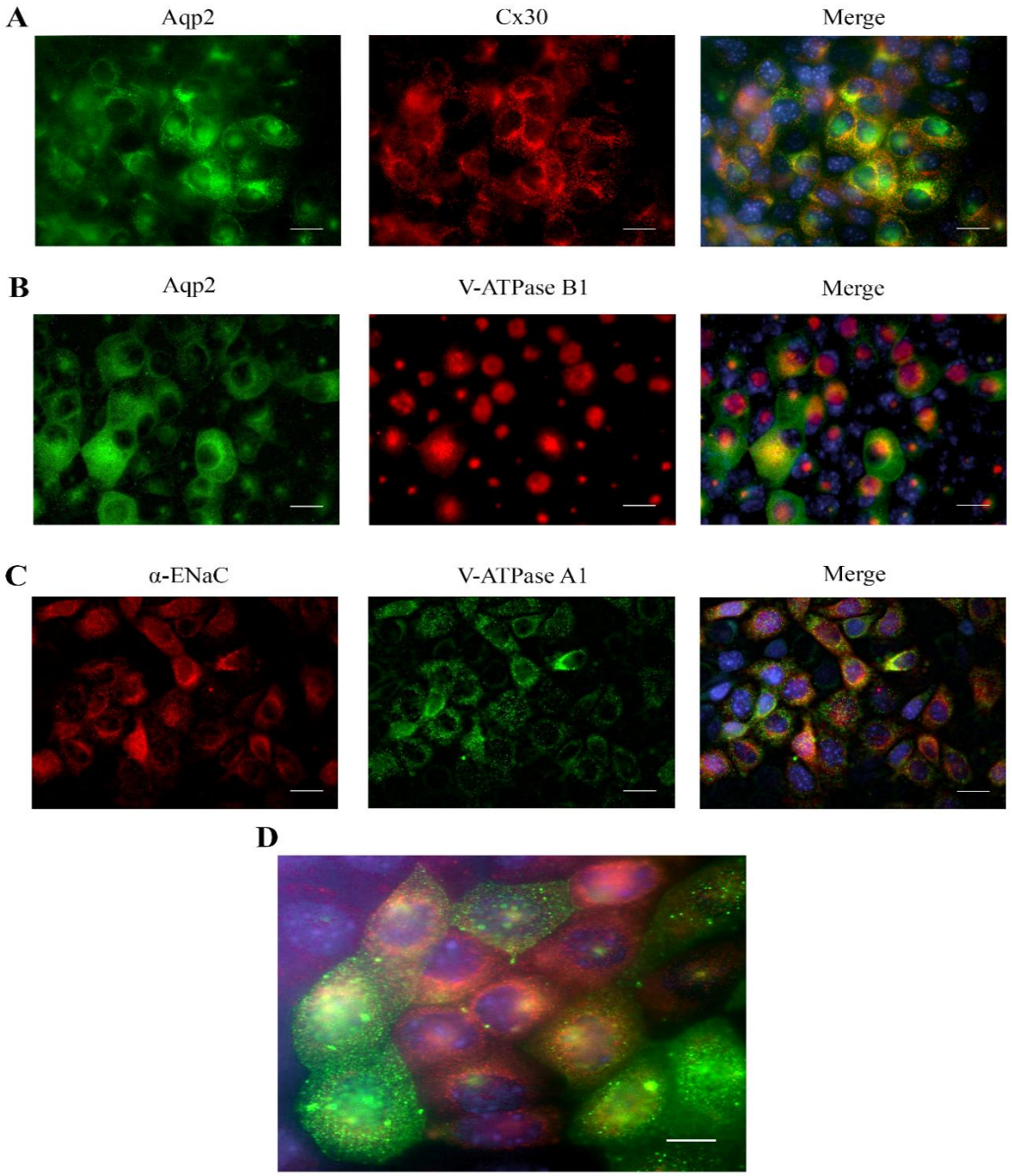

Figure 4.4. mCCD$_{cl1}$ cells express both PC and IC markers. (A) Immunostaining of mCCD$_{cl1}$ cells cultured on filters using anti-Aqp2 (green) and anti-Cx30 (red) antibodies as PC and IC markers respectively. Scale bar 20µm. (B) Immunostaining of mCCD$_{cl1}$ cells using anti-Aqp2 (green) and anti-V-ATPase B1 (red) antibodies PC and IC markers respectively. Scale bar 20 µm. (C) Immunostaining of mCCD$_{cl1}$ cells using anti-α-ENaC (red) and anti-V-ATPase A1 (green) antibodies. Scale bar 20µm. (D) Higher magnification of Aqp2 (green) and Cx30 (red) immunostaining of mCCD$_{cl1}$ cells. Scale bar 10µm. In all the merged images, DAPI staining of cell nuclei is shown in blue.

4.2.3.3 Immunocytochemistry of Acetylated alpha tubulin and V-ATPase A1 on polarized cells

Immunocytochemistry using an anti-acetylated α-tubulin antibody showed that only a few cells staining positively for α-ENaC also displayed primary cilia, and in those that did the cilia appeared short (~2 to 3 µm), compared to those in IMCD cells (~10 µm), known for their robust formation of primary cilia in culture [56]. The anti-acetylated α-tubulin antibody also stains the intracellular acetylated micro-tubular cytoskeleton, considered more stable than its non-acetylated counterpart. Cells displaying strong V-ATPase A1 staining showed a lack of staining for acetylated α-tubulin (Figure 4.5.A). This observation was confirmed by quantification of the mean grey value for both markers in 60 immuno-positive cells displaying a range of different V-ATPase A1 staining intensities, with mean grey values $< 5\%$ considered low, and $>5\%$ considered high (Figure 4.5.C). A paired t-test applied to both populations (high or low V-ATPase A1) showed a significant difference between the mean fluorescence intensities of V-ATPase A1 and acetylated α-tubulin, and an inverse correlation between these two markers (Figure 4.5.C). These data suggest that an acetylated alpha-tubulin-positive cytoskeleton could be used as an additional marker for PCs as well as cells possessing both PC and IC characteristics.

Morphologically different cell populations were revealed by imaging the auto-fluorescence of the cells (Figure 4.6). Different populations correspond to areas with more or less acetylated α-tubulin or V-ATPase A1. Cells with high acetylated α-tubulin staining had the appearance of a tighter, more condensed population (light grey cells on Figure 4.6.A). Acetylated α-tubulin is visible in green on the figure (Figure 4.6.B), and corresponds specifically to the lighter area of cells on the auto-fluorescence channel. Similarly, cells with high V-ATPase A1 staining appeared more scattered and sparse, with staining in light blue specific to darker area of cell auto-fluorescence. α-ENaC was

found on most cells without an obvious pattern. The immunocytochemistry data led to the description of four groups of cells, PC^+/IC^-, PC^-/IC^+, PC^+/IC^+, and PC^-/IC^- the characteristics of which are summarized in Table 4.1.

	PC^+/IC^-	**PC^-/IC^+**	**PC^+/IC^+**	**PC^-/IC^-**
Aqp2 staining	yes	no	yes	no
V-ATPase-B1 staining	no	yes	yes	no
Acetylated α-tubulin staining	high	low or absent	low or absent	low or absent

Table 4.1. Summary of the cell characteristics based on the immunocytochemistry data.

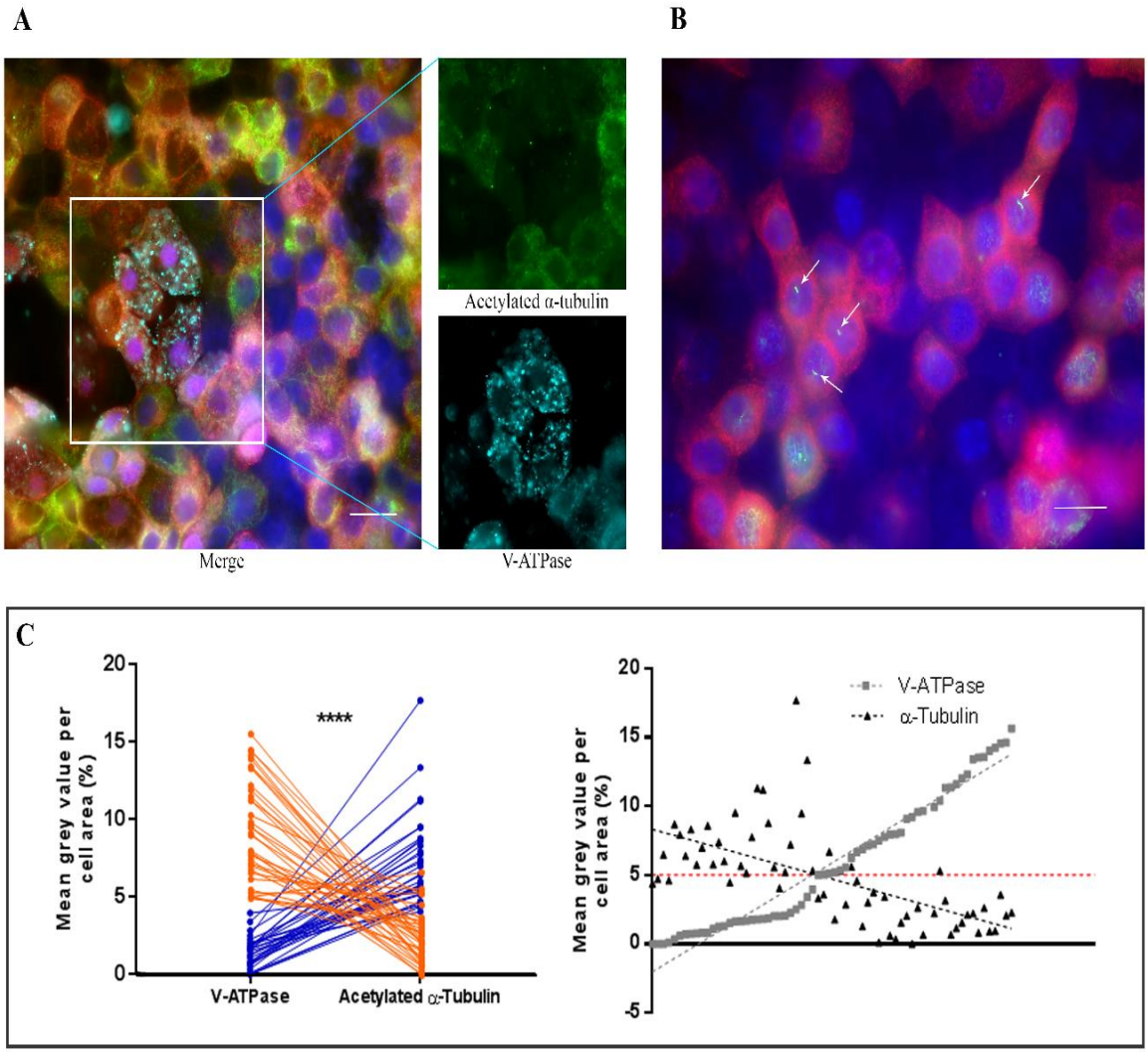

Figure 4.5. Acetylated α-tubulin staining detects primary cilia, but also tubular cytoskeleton of PC-like cells. (A) Immunostaining of $mCCD_{cl1}$ using anti acetylated α-tubulin (green), anti-V-ATPase A1 (light blue) and anti-α-ENaC (red) antibodies. DAPI staining of cell nuclei in the merged image is shown in blue. The magnified area highlights a region of interest where the inverse correlation between V-ATPase A1 and acetylated α-tubulin, quantified in (C), is particularly notable. Scale bar 20µm. (B) Immunostaining of acetylated α-tubulin and α-ENaC. The focal plane highlights the apical membrane of $mCCD_{cl1}$ cells to detect primary cilia, which are shown by white arrows. Scale bar 20µm. (C) Mean grey value of cells showing different expression levels of V-ATPase A1 and acetylated α-tubulin. Left panel: paired t-test, orange for high levels of V-ATPase A1, blue for low levels. Right panel: data ordered by increasing V-ATPase A1 mean grey value. Red dotted line at 5% indicates the limit chosen to define high and low levels of V-ATPase A1.

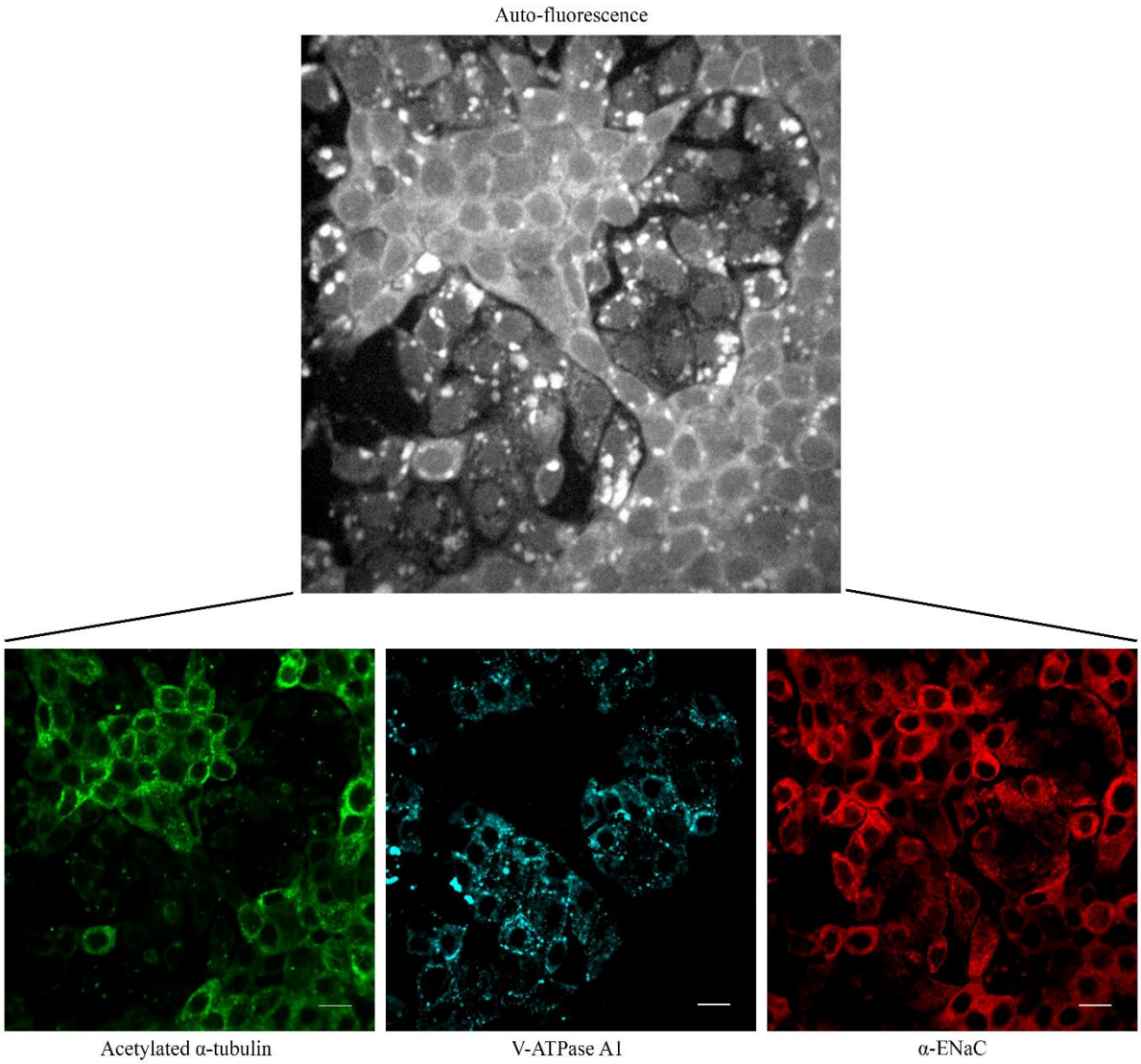

Figure 4.6. mCCD$_{cl1}$ cells show heterogeneous morphologies. Spinning disc confocal images of mCCDcl1 cultured on filters for 10 days and stained with acetylated α-tubulin (green), V-ATPase A1 (light blue) and α-ENaC (red). The grey image corresponds to cells auto-fluorescence of the same area. Scale bar 20 µm.

4.2.4 Parental heterogeneity is transmitted through single cell cloning

4.2.4.1 Establishment of clonal lines

The cloning process (See Section 2.2.6) produced 8 clonal lines from single cells obtained after serial dilutions. Briefly, $mCCD_{cl1}$ cells were suspended in media and separated using a high number of serial dilutions until a single cell was left in a culture plate well. That single cell was then left to divide to produce a clonal cell line. Three clonal lines were selected for further studies based on morphological differences (Figure 4.7.A), and named Ed1, Ed2 and Ed3. Ed1 cells were on average approximately half the size of the Ed2 cells, with an average cell area of 237.5 ± 5.06 μm^2 against 432.7 ± 36.62 μm^2 respectively (Figure 4.7.B). Ed3 cells had the appearance of the parental line, with an intermediate size (338.1 ± 8.34 μm^2). All lines formed domes after confluency, however they formed infrequently for Ed2. The cells maintained their respective morphologies with passaging.

4.2.4.2 PC and IC characteristics are observed in clonal lines

4.2.4.2.1 Cx30, Aqp2, and V-ATPase B1

RT-PCR of Aqp2 and Cx30 (Figure 4.9.B) showed expression of both PC and IC markers in all three sublines. Immunocytochemistry of V-ATPase B1 and Aqp2 (Figure 4.8) in the three sublines showed the presence of PC^+/IC^+ characteristics as described in Table 4.1 for the parental line, meaning the presence of cells positive for both Aqp2 and V-ATPase B1 staining. These PC^+/IC^+ cells were detectable in different proportions when comparing each clone and the parental line (Figure 4.9.A). PC^+/IC^+ cells comprised 24.1 ± 7.1 % of Ed1, 32.8 ± 7.2 % of Ed2 and 45.5 ± 5.7 % of Ed3 respectively. PC^-/IC^+ cells were most represented in Ed2 with 5.7 ± 1.9 %. Ed3 is the closest to the parental

line ($mCCD_{cl1}$), with PC^+/IC^+ cells representing $45.5 \pm 5.7\%$ of the total. In the parental and clonal sublines, the PC^+/IC^+ group makes up more than 50% of the cells showing significant staining, showing that the capacity for the cells to possess both IC and PC characteristics can be transmitted through a single cell of the $mCCD_{cl1}$ parental line.

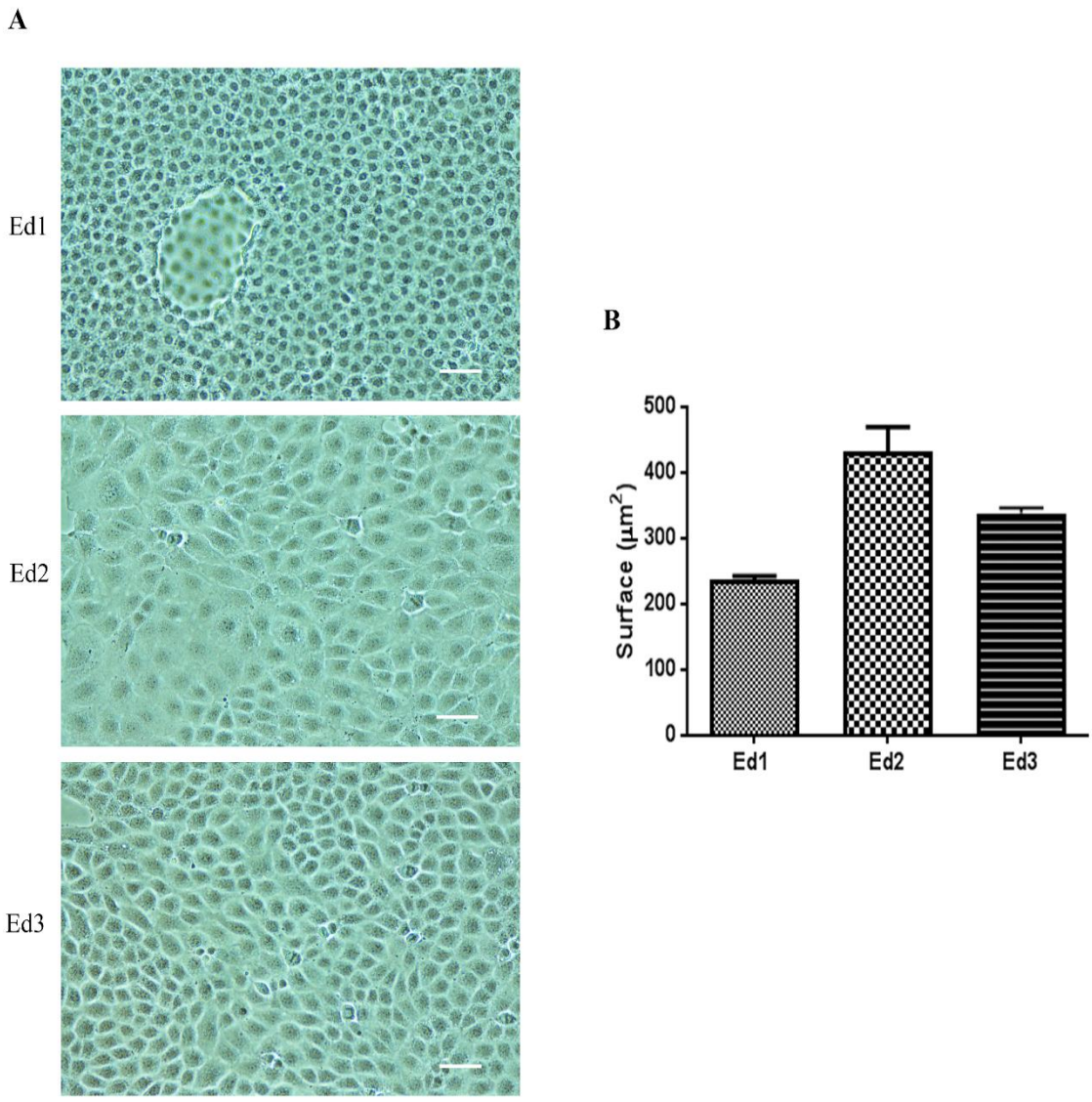

Figure 4.7. Clonal cell lines present morphological differences. (A) Brightfield images of Ed1 (showing dome), Ed2, and Ed3 cultured for 3 days after seeding. Scale bars 50µm. (B) Average size of Ed1, Ed2, and Ed3.

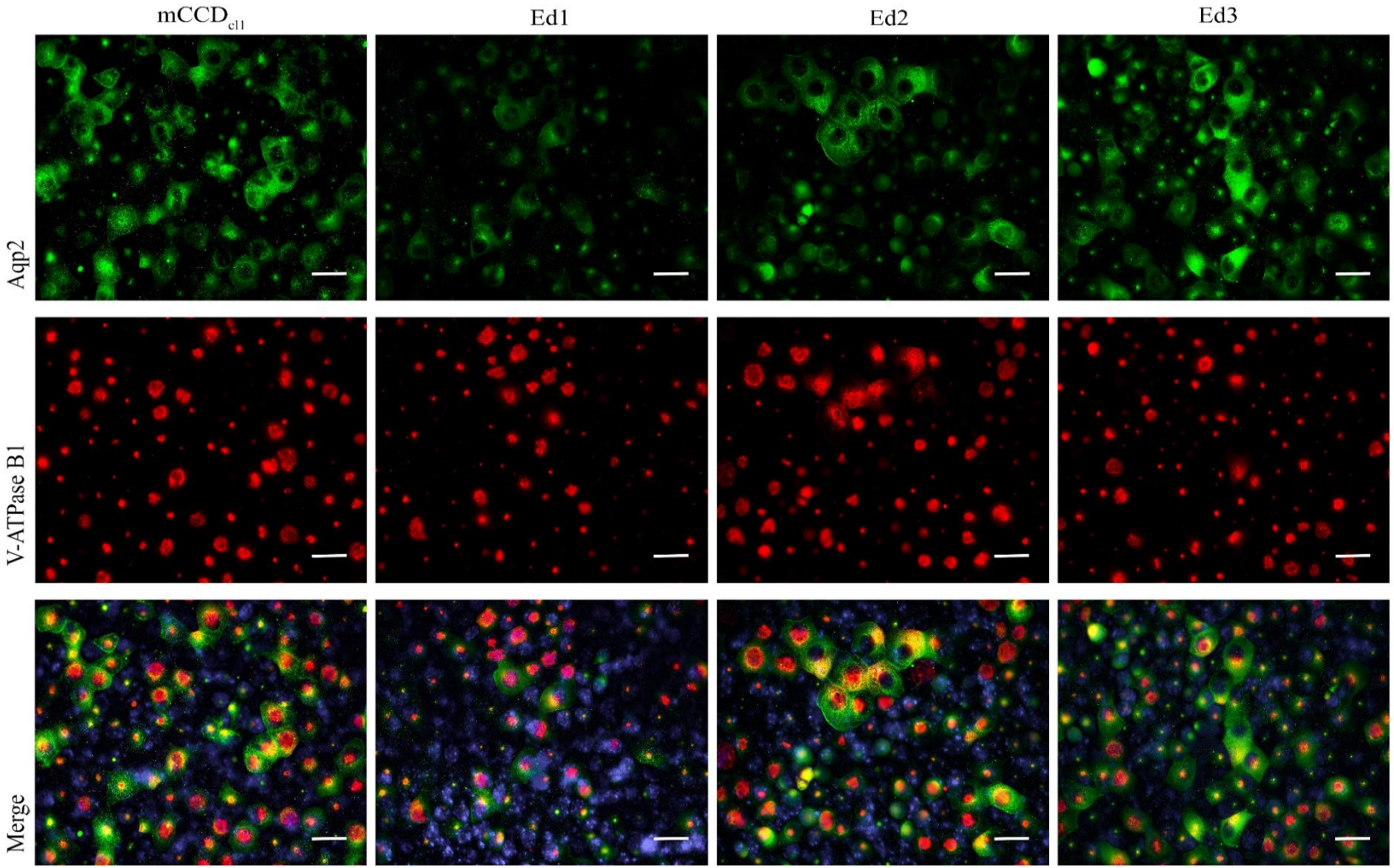

Figure 4.8. Both PC and IC phenotypes are transmitted to the clonal cell lines. Representative images of mCCD$_{cl1}$, Ed1, Ed2, and Ed3 stained with anti-Aqp2 (green) and anti-V-ATPase B1 (red) antibodies. DAPI staining of cell nuclei is shown in blue in the merged images. Magnification x40. Scale bar 20µm.

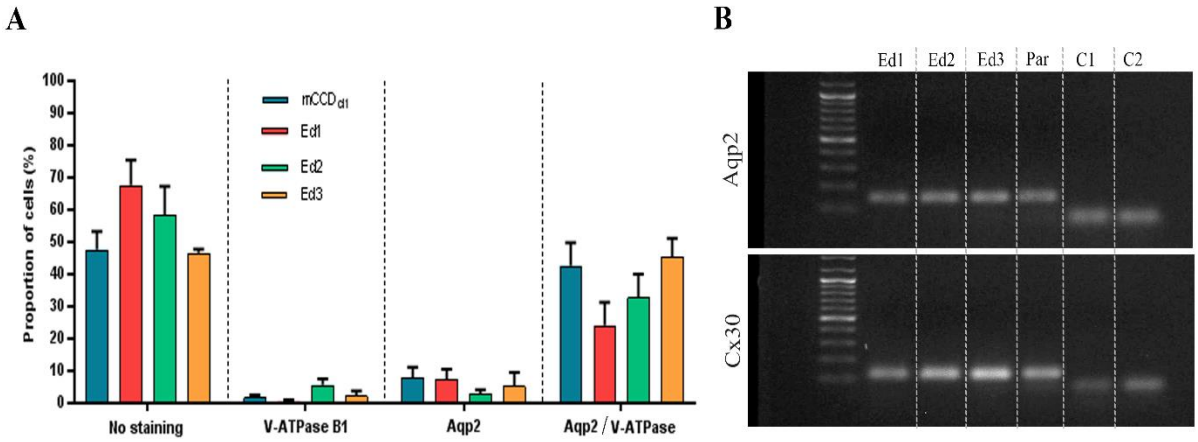

Figure 4.9. Both PC and IC phenotypes are transmitted to the clonal cell lines, in different proportions. (A) Quantification of the proportion of cells (%) not presenting any staining, staining for V-ATPase B1 only, Aqp2 only, or both, in $mCCD_{cl1}$, Ed1, Ed2, and Ed3. (B) RT-PCR results of Aqp2 and Cx30 in the $mCCD_{cl1}$ parental (Par), and clonal lines Ed1, Ed2, and Ed3. C1, C2 are negative controls.

4.2.4.2.2 ENaC and V-ATPase A1

Immunocytochemistry of V-ATPase A1 and α-ENaC (Figure 4.10) in the three sublines showed a heterogenous expression between cells lines. $ENaC^{+}$/V-ATPase $A1^{+}$ cells comprised 88.8 ± 1.6% of Ed1, 55.3 ± 1.9% of Ed2 and 56.4 ± 1.6% of Ed3 respectively. $ENaC^{-}$/V-ATPase $A1^{+}$ cells represent 40.3 ± 0.6% of Ed2, while the $ENaC^{+}$/V-ATPase $A1^{-}$ group was noticeably absent in this subline, and 3.8 ± 1.7% of cells did not stain for either marker. Ed3 is the closest to the parental line, with $ENaC^{+}$/V-ATPase $A1^{-}$ cells representing 36 ± 3.3% of the total (Figure 4.11).

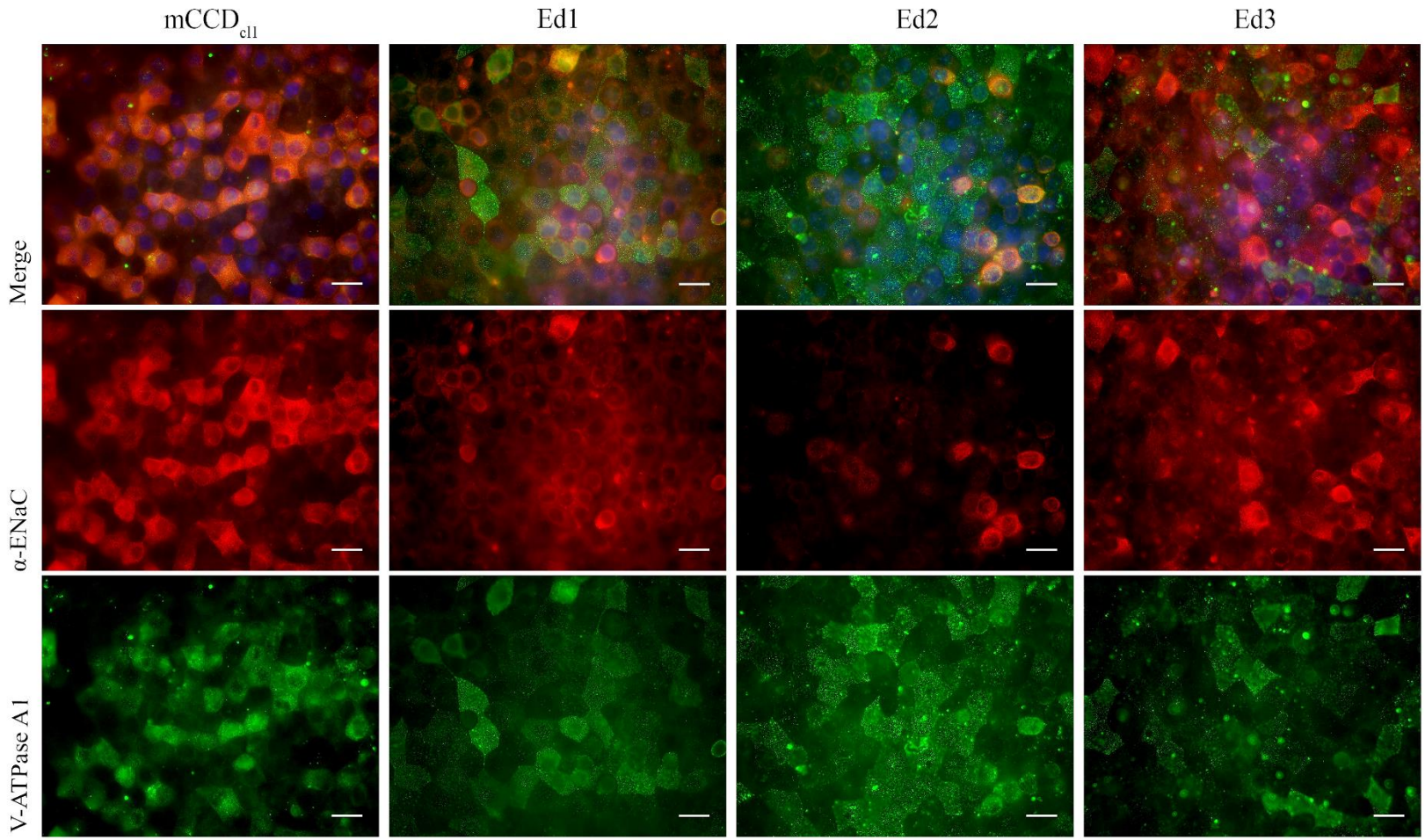

Figure 4.10. mCCDcl1 and clonal lines show heterogenous composition. Representative images of mCCDcl1, Ed1, Ed2, and Ed3 stained with anti-α-ENaC (red) and anti-V-ATPase A1 (green) antibodies. DAPI staining of cell nuclei in the merged pictures. Magnification x40. Scale bar 20µm.

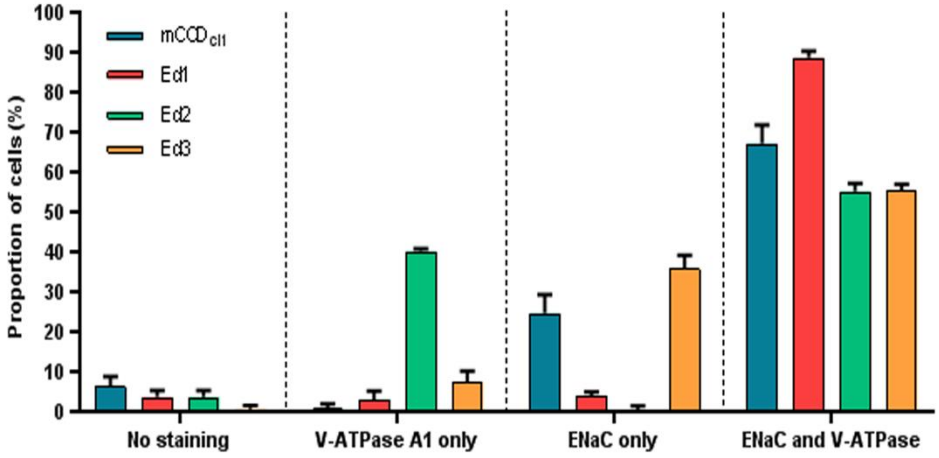

Figure 4.11. Heterogenous expression of ENaC and V-ATPase A1 in $mCCD_{cl1}$ and clonal lines. Quantification of the proportion of cells (%) staining for V-ATPase A1 only, ENaC only, both, or neither in $mCCD_{cl1}$, Ed1, Ed2, and Ed3.

4.2.4.2.3 RNA Sequencing of $mCCD_{cl1}$ parental and clonal cell lines

RNASeq was performed on RNA obtained from parental $mCCD_{cl1}$ cells and the Ed1, Ed2, and Ed3 (n=3).

Visualization of the data by principal component analysis shows the differences between the clonal lines and the parental line (Figure 4.12.A). The first three principal components (PC1-3) represent 90% of the total variability observed in the dataset. PC1 corresponds to 59.8% of total variability, PC2 18.3% and PC3 11.9%. Whilst the repeats are grouped together, indicating the stability of expression between different samples of the same cell line, the projection of the data on the three main principal components axis shows heterogeneity of expression between the parental $mCCD_{cl1}$ cells and the three sublines. These differences are easily visualized using a clustering dendrogram (Figure 4.12.B), showing the variance between the four cells lines by using the top 1000 genes with the most important variability between samples. The extent of the difference between $mCCD_{cl1}$ and the three sublines can be interpreted by looking at the height of

the bars linking each sample. The data show that whilst the transcriptome was reproducible between repeats, it differed significantly between the four lines and that Ed3 and Ed1 showed the greatest similarity and difference, respectively, with $mCCD_{cl1}$. The top twenty transcripts showing the widest differential expression between parental and clonal cell lines, highlighting the heterogenous nature of the $mCCD_{cl1}$ cell line are shown in Table 4.2.

As predicted from the immunocytochemistry data, the expression of genes associated with differentiated ICs and PCs varied between the individual clones. Expression of the α-IC-specific sodium potassium chloride co-transporter NKCC1 (SLC12A2), β-IC specific genes such as the sodium bicarbonate exchanger NDCBE-3 (SLC4A8), the ATPase H^+ transporter (Atp6v1b1), the potassium chloride co-transporter KCC (SLC12A5) and the chloride channel ClCK2 (CLCNKB), and the α/β-IC-specific sulphate transporter SLC26A11 were observed in the parental cell line and all three sub-clones. PC-specific genes such as the renal outer medullary potassium channel ROMK (Kcnj1), Kir4.1 (Kcnj10), 11βHSD2 (HSD11B2), aquaporin 4 (AQP4), and sodium-potassium ATPase (ATP1A1) were also detected in all four cell lines. The expression of several genes of interest for the identification of PCs and ICs was highly up- or down-regulated in the different cell lines, such as ROMK, severely down-regulated in Ed2 and Ed3 compared to the parental line, but also Kir4.1 in Ed2, and V-ATPase B1 in Ed3 (see Table 4.2).

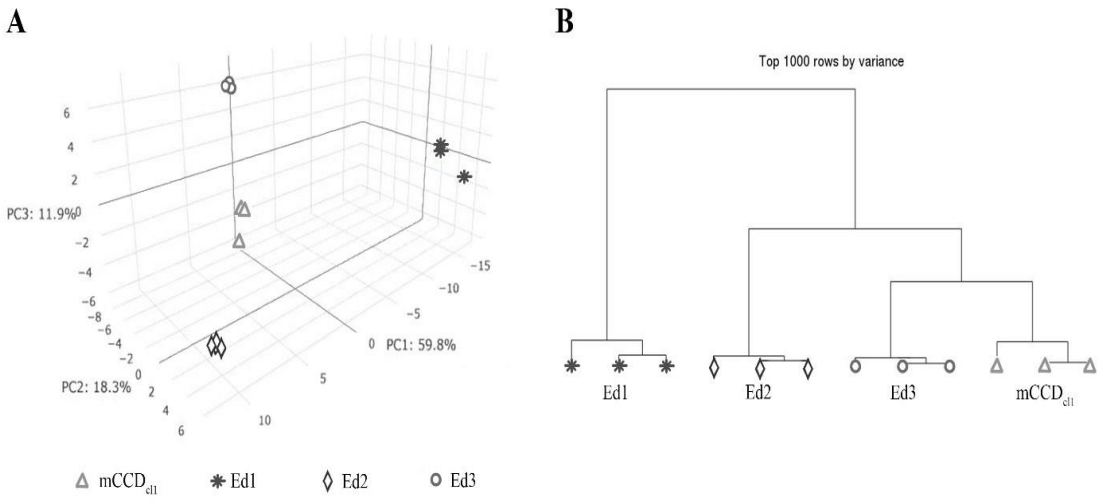

Figure 4.12. Transcriptomes of mCCD$_{cl1}$, Ed1, Ed2, and Ed3 are distinct. (A) Principal component analysis results displayed in a 3D matrix. The axes are the first three principal components (PC1, PC2, and PC3), with the corresponding percentage of total variability they represent in the dataset. Each geometric figure represents one sample, with the repeats (n=3) given the same shape. (B) Clustering dendrogram analysis, based on the top 1000 genes with the most important variance between the samples. The height of the bars is a measure of dissimilarity between samples. The repeats of the same cell line are marked as follows: triangles for parental mCCD$_{cl1}$, asterisks for Ed1, diamonds for Ed2, and circles for Ed3.

Parental vs Ed1				Parental vs Ed2			
Gene name	Ed1 (cpm)	Parental (cpm)	Fold change	Gene name	Ed2 (cpm)	Parental (cpm)	Fold change
Gm20388	0.12	94.13	784.42	Pdlim1	0.16	6.52	40.73
Ldoc1l	0.12	6.79	56.58	Crip1	0.29	9.4	32.4
Ap1m2	0.37	15.47	41.82	Kcnj10*	0.27	8.01	29.68
Ndn	0.19	5.5	29.48	Rhcg	1.99	56.87	28.53
Gm13212	0.61	14.7	24.23	Sirpa	0.14	3.67	26.21
Egln3	4.81	109.13	22.69	Bsnd	2	49.82	24.95
Eya4	0.14	2.31	16.5	Nid2	0.2	4.24	21.56
Gm13157	1.63	25.53	15.69	Gm20388	4.62	94.13	20.39
Tmem22a	0.21	3.22	15.56	Arrdc4	0.19	3.24	16.78
Lhx1	0.23	3.38	14.5	Kcnj1*	1.63	26.93	16.55
Igfbp5	53.05	4.61	-11.5	Tmem25c	1.84	0.26	-7.09
Ccl17	8.09	0.7	-11.5	Egr2	11.26	1.26	-8.91
Chst11	3.43	0.29	-11.83	Pga5	3.78	0.41	-9.3
Gm26822	669.62	54.73	-12.24	Nr4a3	3.43	0.36	-9.45
Gm15039	7.28	0.44	-16.41	Prss56	1.42	0.15	-9.49
Peg3	684.3	38.41	-17.82	Areg	12.01	1.15	-10.44
Nt5e	16.32	0.8	-20.31	Angpt2	66.68	5.03	-13.25
Mgp	6.51	0.27	-23.82	Gm9755	4.47	0.28	-15.96
Vgf	12.77	0.53	-24.1	Vgf	17.4	0.53	-32.84
Arvcf	10.31	0.12	-85.94	Arvcf	9.96	0.12	-82.97

Parental vs Ed3			
Gene name	Ed3 (cpm)	Parental (cpm)	Fold change
Gm10443	0.12	5.22	43.47
Gm20388	2.34	94.13	40.17
Gm45140	0.5	15.36	30.93
Atp6v1b1*	0.56	10.89	19.57
Kcnj1*	1.46	26.93	18.44
Pcdh17	2	34.27	17.17
Naip6	0.81	12.43	15.41
Clcnkb	0.22	3.1	13.87
Eva1b	0.18	2.28	12.45
Fam84a	0.12	1.43	11.92
Loxl1	2.83	0.49	-5.78
Gm26778	2.94	0.45	-6.59
Mmp24	7.31	1.1	-6.67
Dmrtc1a	1.51	0.2	-7.44
Tmem254c	1.94	0.26	-7.46
Kctd12	84.5	11.16	-7.57
Gm11749	1.7	0.18	-9.29
Sytl2	60.2	6.37	-9.45
Trps1	6.51	0.69	-9.48
Arvcf	8.15	0.12	-67.89

Table 4.2. Top twenty differentially expressed transcripts between parental cell line and each clonal cell line, ordered by decreasing fold change. *Genes of interest for the identification of PCs and ICs.

4.2.5 Expression of progenitor markers

RNA-Seq data revealed expression of a number of progenitor cell markers, including p63, Pax2, CD24, CD133, Sca-1, and NfatC1, the latter previously ascribed to apoptosis-resistant renal progenitor cells [168].

4.2.5.1 Nanog

Cells from the parental line showed expression of transcription factor Nanog, critically involved with self-renewal of undifferentiated embryonic stem cells (ES cells). Nanog was most often observed localized around/in the nuclei of cells also expressing Aqp2 (Figure 4.13). No cells solely expressing Nanog (without Aqp2) were observed, but some cells expressed Aqp2 without Nanog.

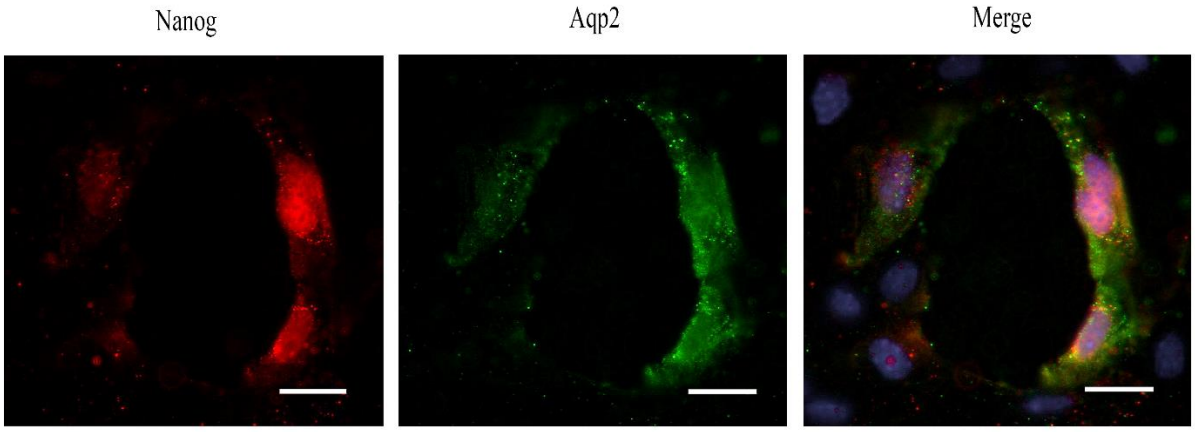

Figure 4.13. mCCDcl1 express ES cells transcription factor Nanog. Representative image of $mCCD_{cl1}$, stained with anti-Nanog (red) and anti-Aqp2 (green) antibodies. DAPI staining in blue in the merged picture. Magnification x60. Scale bar 15µm.

4.2.5.2 P63 and ΔNp63

The expression of specific collecting duct precursor cell markers in the RNA-Seq was confirmed by staining the parental $mCCD_{cl1}$ cells and the clonal lines for p63, which has been observed in the ureteric bud, and ΔNp63, a subunit of p63 specific to intercalated cells lineage [72]. All the cell lines show significant staining for both markers (Figure 4.15), but with variable sub-cellular localization: p63 was either localized around the nucleus or, infrequently, more widely throughout the cell. ΔNp63 showed a wider localisation throughout the cells. The p63 marker was found to co-localise in cells expressing V-ATPase B1 (Figure 4.14), notably in cells with a higher expression of the IC marker.

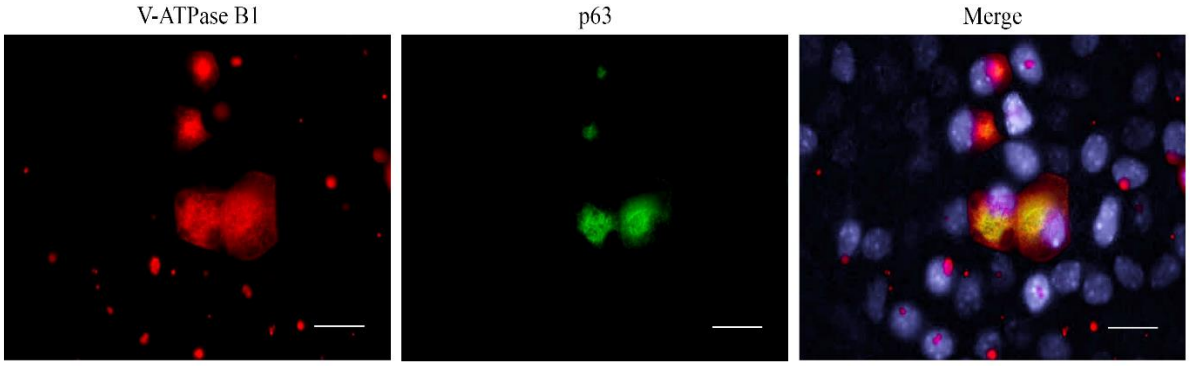

Figure 4.14. p63 co-localises in cells with V-ATPase B1. Representative images of mCCDcl1 stained with anti-V-ATPase B1 (red) and anti-p63 (green) antibodies. DAPI staining in blue in the merged picture. Magnification x60. Scale bar 15µm.

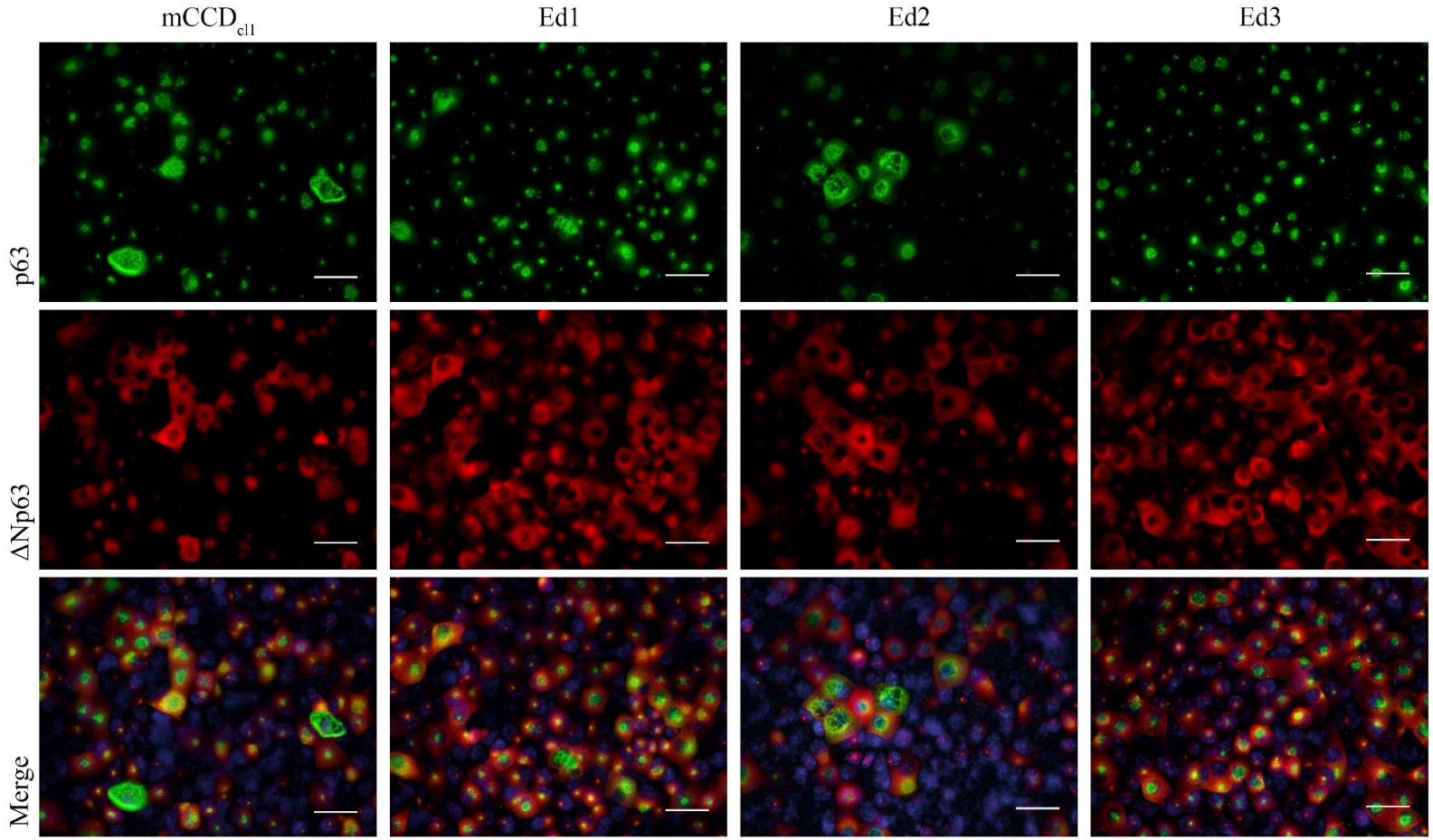

Figure 4.15. mCCD$_{cl1}$, Ed1, Ed2, and Ed3 express collecting duct progenitor markers p63 and ΔNp63. Representative images of mCCD$_{cl1}$, Ed1, Ed2 and Ed3 stained with anti-p63 (green) and anti-ΔNp3 (red) antibodies. DAPI staining in blue in the merged picture. Magnification x40. Scale bar 20µm

4.2.6 Spontaneous and induced polarization of $mCCD_{cl1}$

4.2.6.1 Spontaneous polarization of $mCCD_{cl1}$ in culture flasks: doming

When grown in culture flasks using their defined medium (Section 2.2.2) and after reaching confluency, $mCCD_{cl1}$ cells spontaneously formed domes consisting of monolayer of cells covering a "bubble" of fluid through the detachment of a subset of cells from the flask.

Sodium Green™ is a green fluorescent dye that binds to sodium in a concentration-dependent manner with fluorescence being directly proportional to the concentration of sodium. The inclusion of Sodium Green™ in the medium demonstrated that the cells actively transported sodium inside the domes (Figure 4.16). Whilst fluorescence was weak in the culture medium, the fluid under the domes exhibited a strong signal which differed between the domes and reflected a range of sodium concentrations within the fluid-filled domes (Figure 4.16.a). These experiments showed that $mCCD_{cl1}$ cells were able to actively transport water and sodium and were presumed to spontaneously polarize, at least partially, in these culture conditions.

However, not all cells within a dome expressed water and sodium channels. Immunocytochemistry of α-ENaC and Aqp2 on fixed domes showed staining for ENaC on the outside (apical) membrane of some cells constituting the dome (Figure 4.17.b), with $ENaC^+$ cells distributed randomly across the dome. In the same manner, $Aqp2^+$ cells only made up a small subset (2 or 3 cells) of cells constituting the dome (Figure 4.17.a), but were localized on the top as seen on Figure 4.17. These $Aqp2^+$ cells were most likely to be responsible for the formation of the dome.

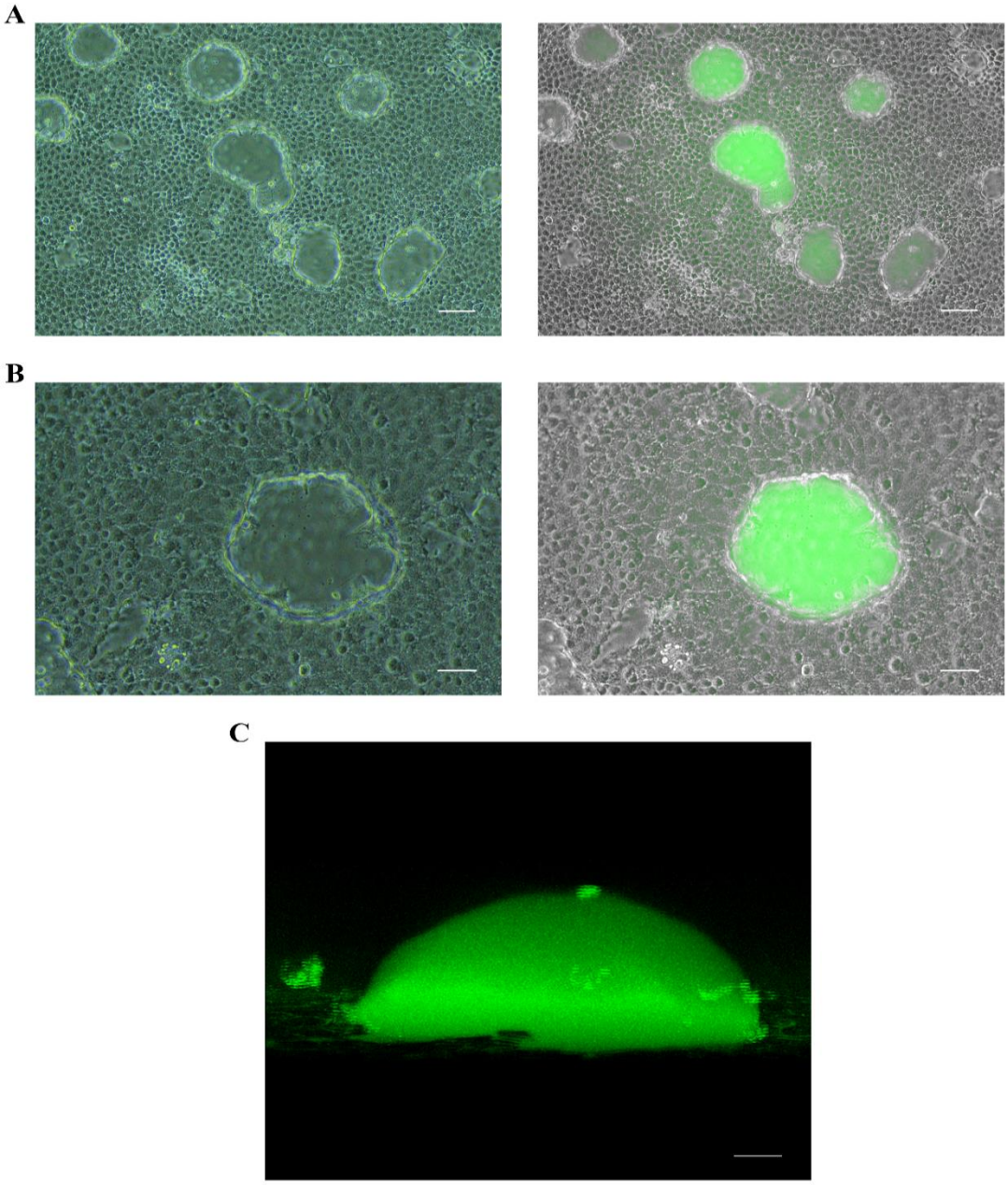

Figure 4.16. $mCCD_{cl1}$ polarization in classic culture conditions. (A) On the left, brightfield image, typical view of mCCDcl1 cells forming domes after confluency. On the right, merged image of the same area with the green fluorescent Sodium Green dye. Different fluorescence intensities in different domes. Scale bar 100µm. (B) Higher magnification view of a dome and of sodium concentrated under the detached cell monolayer, visible using Sodium Green™. Scale bar 50µm. (C) 3D reconstruction view of a confocal microscope z-stack imaging of a dome containing sodium in solution. Scale bar 20µm.

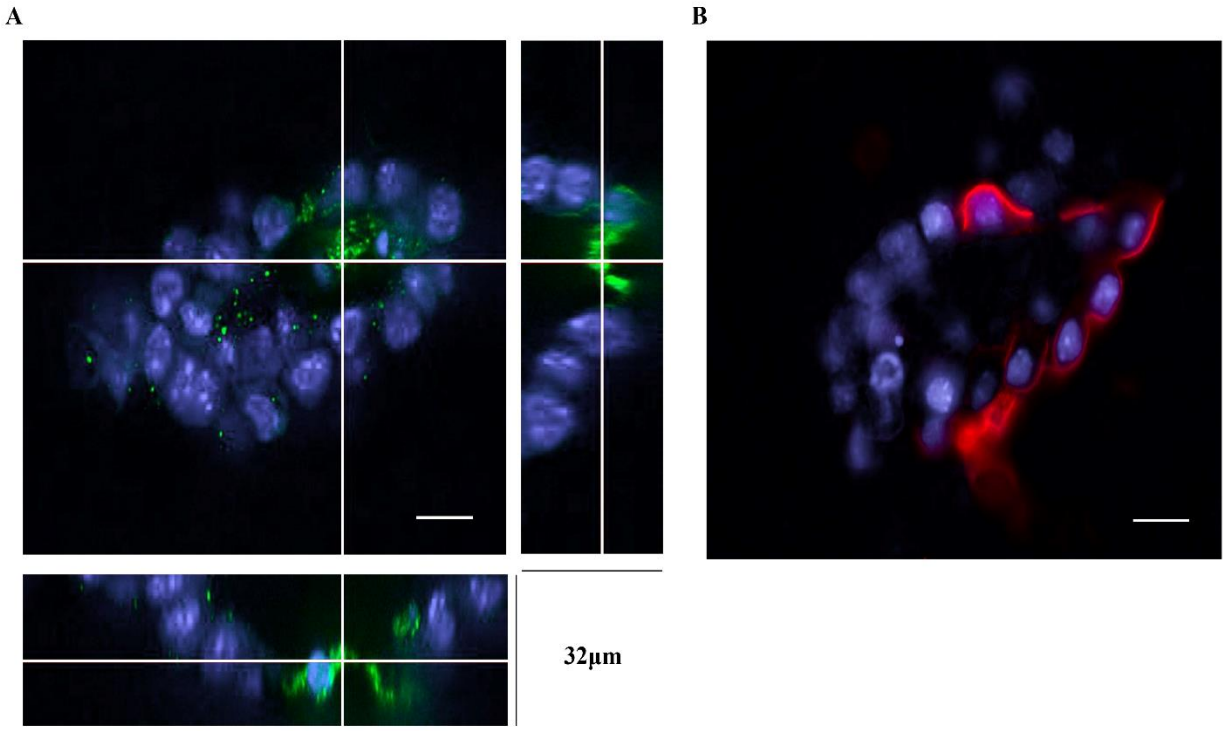

Figure 4.17. Only a subset of cells express water and sodium channels in domes. (A) Confocal imaging of a $mCCD_{cl1}$ dome stained with Aqp2 (green). Z-projections on right and bottom correspond to the plans shown by the white lines. Scale bar 20µm. (B) Epifluorescence microscopy of α-ENaC (red) expressed within a dome. Scale bar 20µm. On both images, DAPI staining in blue.

4.2.6.2 Polarization of mCCD$_{cl1}$ cultured on Transwell® permeable membranes

Polarization of mCCD$_{cl1}$ was observed using spinning disc confocal microscopy on cells grown on Corning Transwell® (Section 2.2.7) permeable culture membranes and stained for α-ENaC, and for Aqp2 and V-ATPase B1. Orthogonal projections of z-stack images obtained with confocal microscopy show the apical localization for α-ENaC (Figure 4.18.A, ENaC in red) and for both Aqp2 and V-ATPase B1 (Figure 4.18.B, green and red respectively).

In immuno-positive cells, α-ENaC was often localized over the entire cell apical membrane, which has the shape of a slightly flattened cobblestone. The staining pattern of Aqp2 was similar, most often distributed over the entire cell surface. V-ATPase B1 positive cells, however, consistently showed localized staining on the apical membrane of the cells, predominantly over the nuclei (in red on Figure 4.18.B).

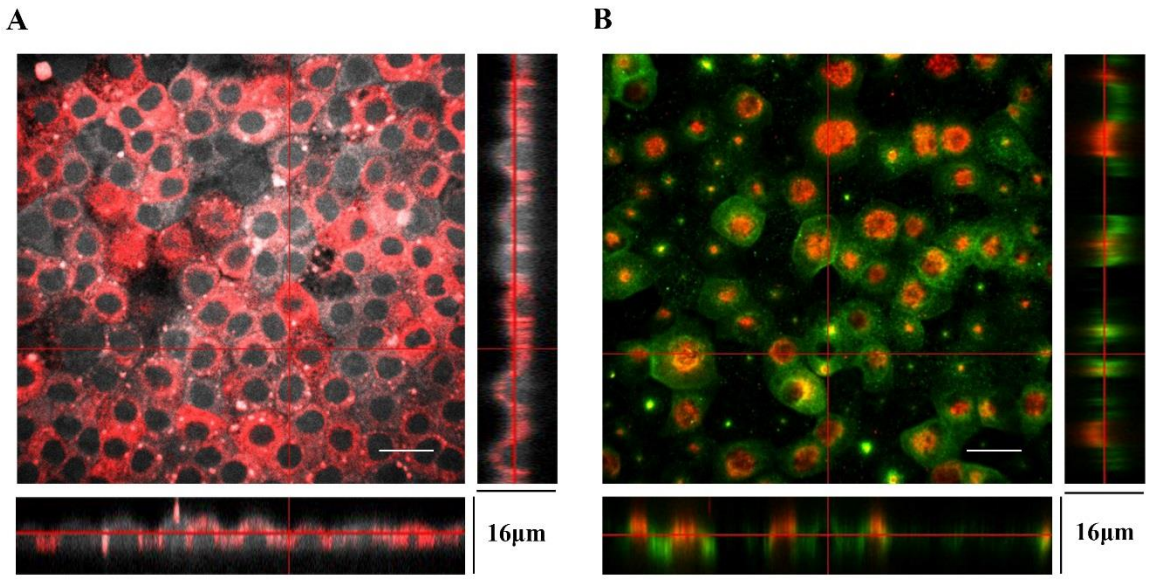

Figure 4.18. Polarisation of mCCDcl1 cells cultured on Transwell® membranes. (A) Confocal image and orthogonal projections (right and bottom) of mCCD$_{cl1}$ cells cultured on Transwell® membranes with α-ENaC immunostaining in red over the greyscale auto-fluorescence of the cells. (B) Confocal image and orthogonal projections (right and bottom) of mCCD$_{cl1}$ cells cultured on Transwell® membranes with Aqp2 (green) and V-ATPase B1 (red) immunostaining. In both panels, the orthogonal planes correspond to cells along the crosshairs (red lines). White scale bar is 20µm.

4.3 Discussion

4.3.1 Chapter summary

In order to detect possible contamination in the $mCCD_{cl1}$ cell line, considered in the literature to be a highly differentiated principal cell line, separate immunocytochemistry of Aqp2 and Cx30 was performed on $mCCD_{cl1}$ cells (PCs and ICs markers respectively). Since the cells exhibited staining for Cx30, a double immunostaining was performed. Instead of a bi-modal distribution of PC and IC markers, the cells presented a range of expression for both markers and a large subset exhibited an "intermediate" state, with labelling for both Aqp2 and Cx30. The cells were then cultured in conditions allowing for polarization (Corning® Transwell®). Double labelling of Cx30 and Aqp2 was repeated in these culture conditions, and new analyses were performed using anti-Aqp2 and anti-V-ATPase B1 antibodies. Immunocytochemistry using these PC and IC specific markers confirmed the intermediate state observed previously. Clonal cell lines were established to study the vertical transmission of these characteristics through single cells. All clonal lines exhibited the intermediate phenotype, however in different proportions, confirming the bi-potential nature of $mCCD_{cl1}$ cells. Antibodies against α-ENaC and V-ATPase A1 were also used, as well as anti-acetylated alpha tubulin to visualize primary cilia and acetylated cytoskeleton. The $mCCD_{cl1}$ cell line showed heterogenous morphological characteristics, and an inverse relationship between the presence of V-ATPase A1 and acetylated alpha-tubulin. The heterogenous composition was observed on cells cultured in "classic" flasks (Section 2.2.2) where a subset of cells spontaneously polarized and formed domes, transporting water and sodium. However, only a small number of the doming cells exhibited significant staining for Aqp2 or ENaC.

RNA sequencing of $mCCD_{cl1}$ and clonal lines showed the expression of a large variety of PCs and ICs specific genes, as well as several precursor cells markers.

Immunocytochemistry against collecting duct precursor markers p63 and ΔNp63 was performed, in conjugation to the V-ATPase B1 antibody. Parental $mCCD_{cl1}$ cells and clonal cell lines all exhibited positive staining for p63 and ΔNp63, with a co-localization of p63 with V-ATPase B1. The embryonic stem cell marker Nanog was also observed in a subset of cells.

The ability of $mCCD_{cl1}$ to exhibit both PCs and ICs as well as progenitor cells characteristics led to the description of these intermediate, bi-potential cells as "transition" cells.

4.3.2 Discussion

In-depth characterization of the $mCCD_{cl1}$ cell line has not been performed previously, apart from the evidence for PC functional characteristics, specifically sodium and potassium transport. Personal communication from another research group working with $mCCD_{cl1}$ cells reported the presence of V-ATPase B1, but the observation was not followed up. Considering the wide use of the $mCCD_{cl1}$ cell line by the renal community, part of the results presented in this chapter have been published in the American Journal of Physiology – Renal Section, under the title of "$mCCD_{cl1}$ cells show Plasticity Consistent with the Ability to Transition between Principal and Intercalated Cells" (Appendix 2, page 205), and have been the subject of the Journal's editorial focus (Appendix 1, page 202).

The characterization of $mCCD_{cl1}$ cells exclusively using immunocytochemistry presents limitations, as protein expression is not necessarily linked to functional levels and characteristics. These limitations have been addressed by using $mCCD_{cl1}$ parental and clonal lines in electrophysiological studies (Chapter 5, page 114).

The use of Transwell® culture membranes, necessary for cell polarization, limited the number of samples screened, but the high repeatability of the data between the samples allowed us to draw clear conclusions about $mCCD_{cl1}$ parental and clonal cell lines. The culture conditions have also proven to be critical for the level of expression of the different markers observed in this study. Aqp2, Cx30, and V-ATPase B1 were expressed more widely in cells cultured on porous membranes compared to flasks, where the expression tended to be observed on "doming" areas only, and in a reduced number of cells in general.

4.3.2.1 Data summary

The gathering of immunofluorescence data from the different experiments gave a more complete picture of the composition of the $mCCD_{cl1}$ and clonal cell lines (Figure 4.19), showing a range of expression in the $mCCD_{cl1}$ cell line. It must be noted that the data for Cx30 was collected with a low n number. Most cells in the parental cell line $mCCD_{cl1}$, Ed1, and Ed3, expressed ENaC (around 90%). Ed2 had low expression of ENaC (around 55% of cells) in comparison, as well as lower expression of Cx30. Aqp2 was expressed in around 50% of cells in parental line and Ed3, with lower expression in Ed1 and Ed2 (around 35% of cells). V-ATPase B1 was expressed in similar proportions of cells in parental line, Ed2 and Ed3, with lower levels in Ed1. In summary, expression levels of all markers were very similar in parental $mCCD_{cl1}$ and Ed3, while Ed1 showed high ENaC expression but low Aqp2 and V-ATPase B1. Ed2 distinguished itself by a lower ENaC expression. The comparison of data from one experiment to the other (Aqp2 as a PC marker and Cx30 or V-ATPase B1 as IC markers) showed a relatively consistent proportion of intermediate cells, with parental $mCCD_{cl1}$ and Ed3 exhibiting the highest proportion (more than 40% or cells) (See Figure 4.19.B).

A

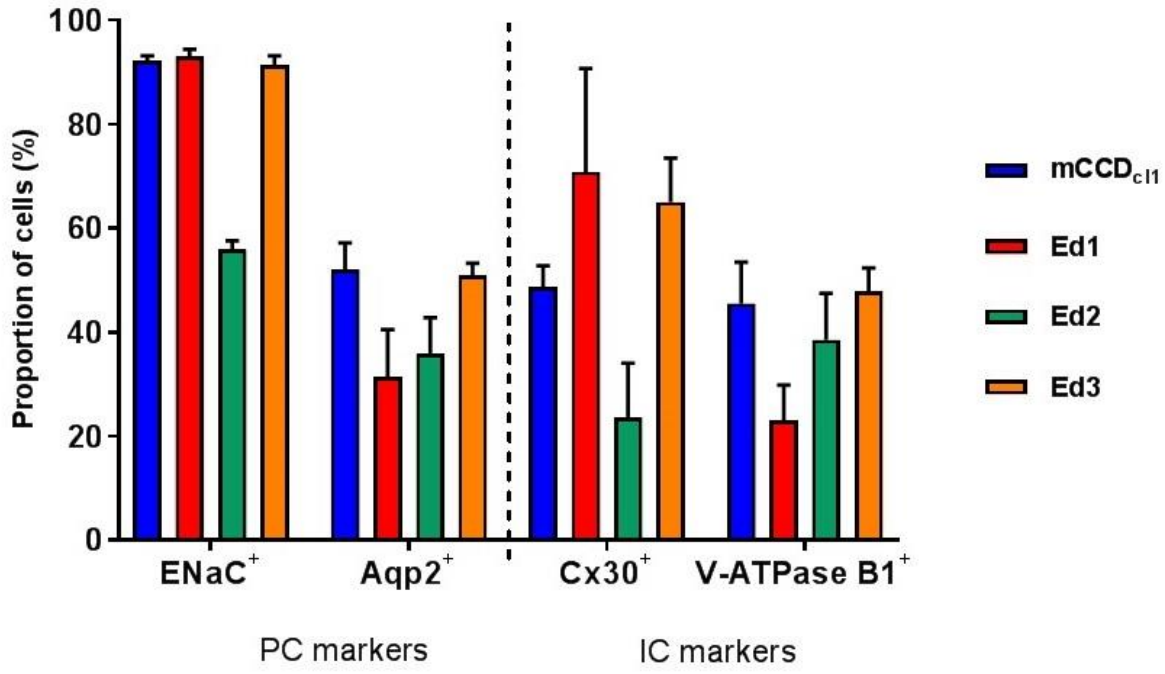

B

	Proportion of intermediate cells			
Experiment	$mCCD_{cl1}$	Ed1	Ed2	Ed3
Aqp2/Cx30	~ 42%	~37%	~24%	~43%
Aqp2/V-ATPase B1	~ 43%	~24%	~32%	~45%

Figure 4.19. Data summary of the expression of PC and IC markers in $mCCD_{cl1}$ and clonal cell lines. (A) Quantification of the proportion of cells (%) showing positive staining for PC markers ENaC and Aqp2, and for IC markers Cx30 and V-ATPase B1 in mCCDcl1, Ed1, Ed2, and Ed3. (B) Summary table of approximate proportion of intermediate cells (expressing PC and IC markers) in $mCCD_{cl1}$, Ed1, Ed2, and Ed3. The proportions are shown for two experiments: expression of Aqp2 and Cx30, and Aqp2 and V-ATPase B1.

4.3.2.2 Implication for *in-vivo* collecting ducts

The literature, and this project, paint an increasingly complicated portrait of collecting ducts and the relationship between PCs and ICs (Section 1.2.3.3). However, data is missing on the effect of well-established kidney disease models on collecting ducts cell types. An in-depth study of CCD role in pathological conditions would give insight into the mechanisms involved in collecting duct cells differentiation.

Preliminary data, not presented in this thesis, used samples from 11βHSD2 KO mice, an excellent genetic and phenotypic model for the syndrome of apparent mineralocorticoid excess (SAME) [169]. SAME results in hypertension and hypokalemia and pronounced changes to the collecting duct of the kidney [170]–[172]. These data show a significant decrease of the number of PCs between controls and KO mice, and an increase in number of intermediate cells, and are indicative of a trend towards cells de-differentiation in pathological conditions.

4.3.3 Conclusion

Characterization of the $mCCD_{cl1}$ cell line using immunocytochemistry has shown an heterogenous composition and cells expressing not only both PCs and ICs phenotypes, but also progenitor markers. The transmission of these characteristics to clonal cell lines show a plasticity consistent with the ability to transition between cell types. This study provides solid evidence for the establishment of $mCCD_{cl1}$ as a good model for the study of the relationship between the CCD different cell types.

5 Electrophysiological analysis of the $mCCD_{cl1}$ cell line confirms the heterogenous composition of the cell line.

5.1 Introduction

Immunohistochemical analysis of $mCCD_{cl1}$ cells and sub-clones gave a good insight into the expression of key proteins; however, protein levels are not necessarily indicative of functionality, which is dependent on many factors such as protein localization, active or inactive state, or the effect of hormones such as aldosterone [28], [173]. As demonstrated in the previous chapter, protein levels and expression vary widely in $mCCD_{cl1}$ cells and sub-clones, and knowing the functional capacities of each sub-clone is an essential step for characterization.

Considered a principal cell line, $mCCD_{cl1}$ has been used before for numerous electrophysiological measurements principally for studies on sodium and potassium transport, the main functions of PCs [80], [84], [86]–[88]. Knowing the heterogenous nature and expression of $mCCD_{cl1}$, functional data on the clonal lines would allow for a better understanding of their composition and abilities, and provide insight on the measures taken using the parental line.

Electrophysiology is a convenient and non-destructive way to observe $mCCD_{cl1}$ functions in real time, and was used in this study to further characterize the parental and clonal cell lines.

5.1.1 Aims

The following experimental aims were addressed:

- Make functional characterization of parental and clonal cell lines.
- Confirm the heterogeneity of the $mCCD_{cl1}$ cell line.
- Compare and eventually link protein expression levels to functionality.

5.2 Parental and clonal cell lines exhibit different functional characteristics.

Using the protocol established in Section 3.3 for cell culture and handling, electrophysiological measurements were made on parental $mCCD_{cl1}$ cells, Ed1, Ed2, and Ed3. Parental and clonal lines were cultured on separate plates of Transwell® membranes for several passages. During each experimental process, the protocol for cell culture on the membranes and for EVOM® measurements was carefully kept consistent between each measurement and each passage (time in culture, time out of the incubator, measurement process and timing, drugs preparation).

5.2.1.1 Electrophysiological properties

Transepithelial electrophysiological measurements of parental $mCCD_{cl1}$ cells revealed baseline I_{sc} measurements of -9.0 ± 1.0μA/cm^2 (n=4), consistent with previous reports [80], [81]. The application of 10μM amiloride (10 min) to the apical bath inhibited I_{sc} by 82.1 ± 8.2%, indicating that the basal current can mostly, but not totally, be attributed to the transport of Na^+ via ENaC. The concentration of amiloride yielding 50% ENaC inhibition (IC_{50}) was reported in $mCCD_{cl1}$ cells at about 650nM, with increasing concentrations of amiloride from 0.01 to 10 progressively and fully inhibiting both the baseline-and the aldosterone-stimulated sodium transport [80]. The addition of aldosterone (3nM, 3 h) increased I_{sc} by a factor of 3.8 ± 0.2 fold, to reach values of -34.0 ± 1.2 μA/cm^2. I_{sc}, R_{te} and V_{te} values are shown in Figure 5.1 and Table 5.1.

Basal currents in Ed1 and Ed3 were 81.8 ± 7.0 and 88.4 ± 3.1% amiloride sensitive, respectively, indicating that, similar to the parental line, their basal currents can principally be attributed to the transport of Na^+ via ENaC. Baseline I_{sc} in Ed2 was

negligible compared to the parental line (-1.4 ± 0.4 μA/cm^2 v -9.0 ± 1.0 μA/cm^2, respectively).

Ed1, consisting of ~90% of dual-staining cells, did not develop a cell layer as resistive as the parental line, with a maximum R_{te} at day 10 of 0.8 ± 0.1 kΩ·cm^2. V_{te} of Ed1 cells also remained lower than for the parental line throughout the experiments, reaching a maximum of -18.1 ± 0.5 mV on day 8, compared to V_{te} of parental cells at day 8 of -32.7 ± 1.0 mV.

Baseline I_{sc} for $mCCD_{cl1}$, Ed1 and Ed3 were similar, but the aldosterone responses of the sub-lines were significantly lower than the parental line, with I_{sc} fold changes for baseline-to-aldosterone treatment at 3.8 ± 0.3 for the parental line, and 2.1 ± 0.2 for Ed1 and Ed3 (Table 5.1). The responses to aldosterone and amiloride for Ed2 were considered not relevant due to the negligible baseline I_{sc}. Electrophysiological measurements made from clonal sublines and the parental line remained consistent throughout experiments (n=4), suggesting that at a cell population level, the cells exhibit a stable phenotype.

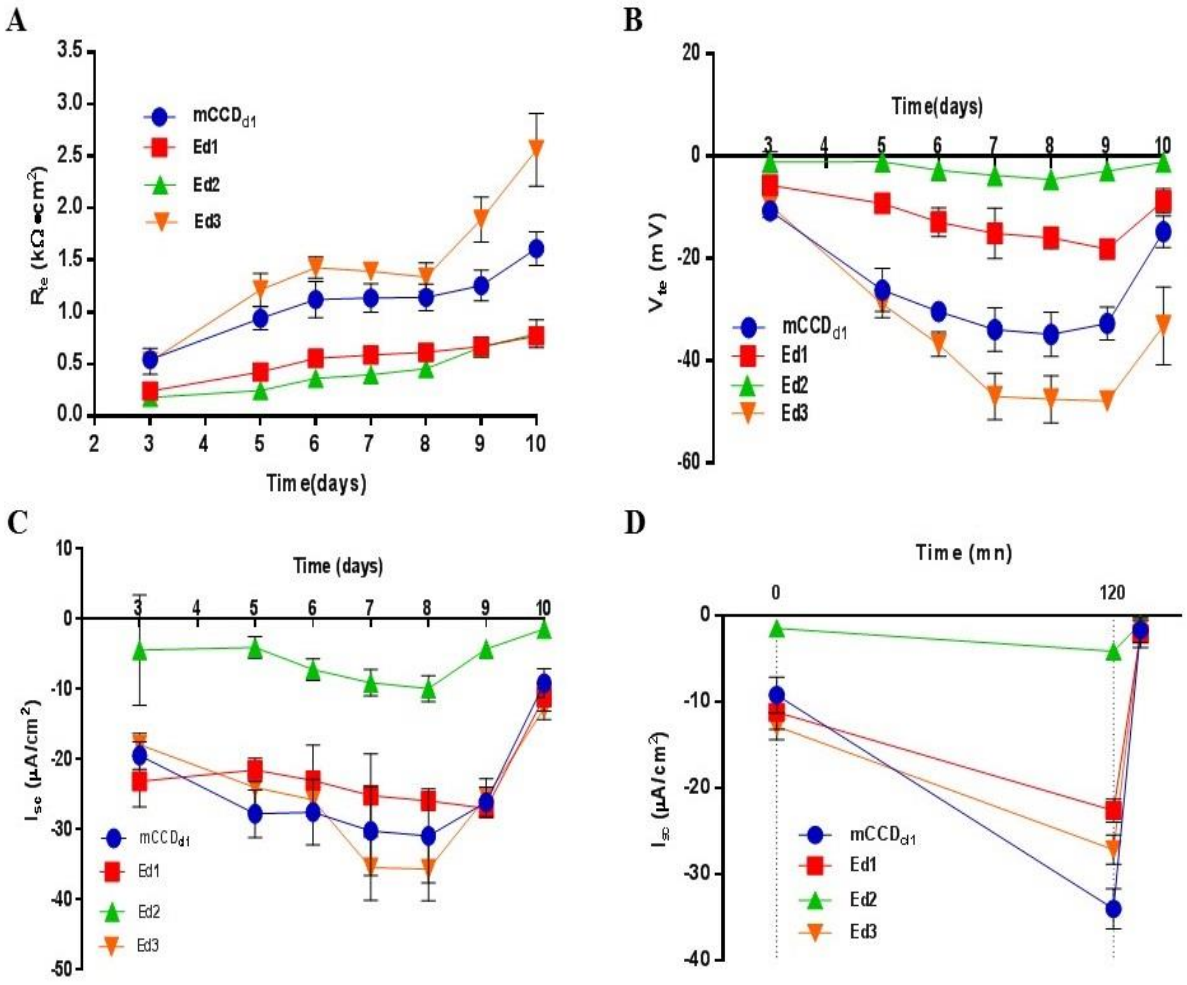

Figure 5.1. Parental mCCD$_{cl1}$ and subline cells have different electrophysiological properties. (A) Transepithelial resistance (R_{te}) measured across monolayers of mCCD$_{cl1}$, Ed1, Ed2, and Ed3 cells. (B) Transepithelial voltage (V_{te}) measured across monolayers of mCCD$_{cl1}$, Ed1, Ed2, and Ed3 cells grown on Snapwells filters, between day 3 and 10 after seeding (C) I_{sc} was calculated using Ohm's law. Values are shown as mean ± SEM (n=4). (D) Effects on baseline I_{sc} of aldosterone (3nM) and amiloride (10µM, apical bath) added at t=0 and t=120min respectively. Values are shown as mean ± SEM (n=4).

		Baseline ± SD	Aldosterone 3h ± SD	Amiloride 10min ± SD	Isc Fold change, aldosterone treatment ± SD	% of Isc blocked by amiloride ±SD
$mCCD_{cl1}$	I_{sc} ($\mu A/cm^2$)	-9.0 ± 1.0	-34.0 ± 1.2	-1.6 ± 0.7	3.8 ± 0.3	82.1 ± 8.2
	R_{te} ($k\Omega \cdot cm^2$)	1.6 ± 0.1	1.0 ± 0.1	2.1 ± 0.1		
	V_{te} (mV)	-14.7 ± 1.5	-37.6 ± 0.8	-3.5 ± 1.6		
Ed1	I_{sc} ($\mu A/cm^2$)	-11.4 ± 0.9	-22.6 ± 0.7	-2.1 ± 0.8	2.1 ± 0.2	81.8 ± 7.0
	R_{te} ($k\Omega \cdot cm^2$)	0.8 ± 0.1	0.7 ± 0.0	1.0 ± 0.1		
	V_{te} (mV)	-8.7 ± 1.2	-16.0 ± 0.8	-2.1 ± 0.8		
Ed2	I_{sc} ($\mu A/cm^2$)	-1.4 ± 0.4	-4.1 ± 0.2	-0.9 ± 0.3	3.9 ± 1.2	36.4 ± 7.0
	R_{te} ($k\Omega \cdot cm^2$)	0.8 ± 0.1	0.8 ± 0.1	1.0 ± 0.1		
	V_{te} (mV)	-1.2 ± 0.4	-3.4 ± 0.4	-0.9 ± 0.3		
Ed3	I_{sc} ($\mu A/cm^2$)	-12.8 ± 0.8	-27.1 ± 0.8	-1.4 ± 0.4	2.1 ± 0.2	88.4 ± 3.1
	R_{te} ($k\Omega \cdot cm^2$)	2.6 ± 0.2	-2.0 ± 0.1	4.1 ± 0.3		
	V_{te} (mV)	-33.1 ± 3.8	-54.0 ± 1.9	-6.3 ± 2.1		

Table 5.1. Electrophysiological measurements for the parental mCCDcl1 cell line and the clonal sublines Ed1, Ed2 and Ed3, and calculated I_{sc} fold change after aldosterone treatment and I_{sc} blocked from amiloride treatment.

5.2.1.2 Consistent measurements recorded with freshly thawed cells

The experiment was repeated with fresh cells (newly thawed $mCCD_{cl1}$, Ed1, Ed2 and Ed3) in the exact same conditions, over 3 cell passages instead of 4 passages previously. The measurements were similar to the values presented in Section 5.2.1.1. Figure 5.2 shows I_{sc} value during the experiment (Figure 5.2.A), and the effect of aldosterone and amiloride (Figure 5.2.B) added on day 10 as described previously in Section 5.2.1.1. Baseline I_{sc} was close to the first experiment for all cell lines, at about 11 $\mu A/cm^2$ for parental $mCCD_{cl1}$, Ed1, and Ed3; Ed2 Isc was still considered negligible considering the low recorded V_{te}. Aldosterone similarly affected sodium transport with comparable I_{sc} fold changes. As observed previously, values weren't affected by cell passages.

The experiment confirmed the stability of the cell lines and the repeatability of measurements using $mCCD_{cl1}$, Ed1, Ed2, and Ed3, if following the appropriate cell culture protocol.

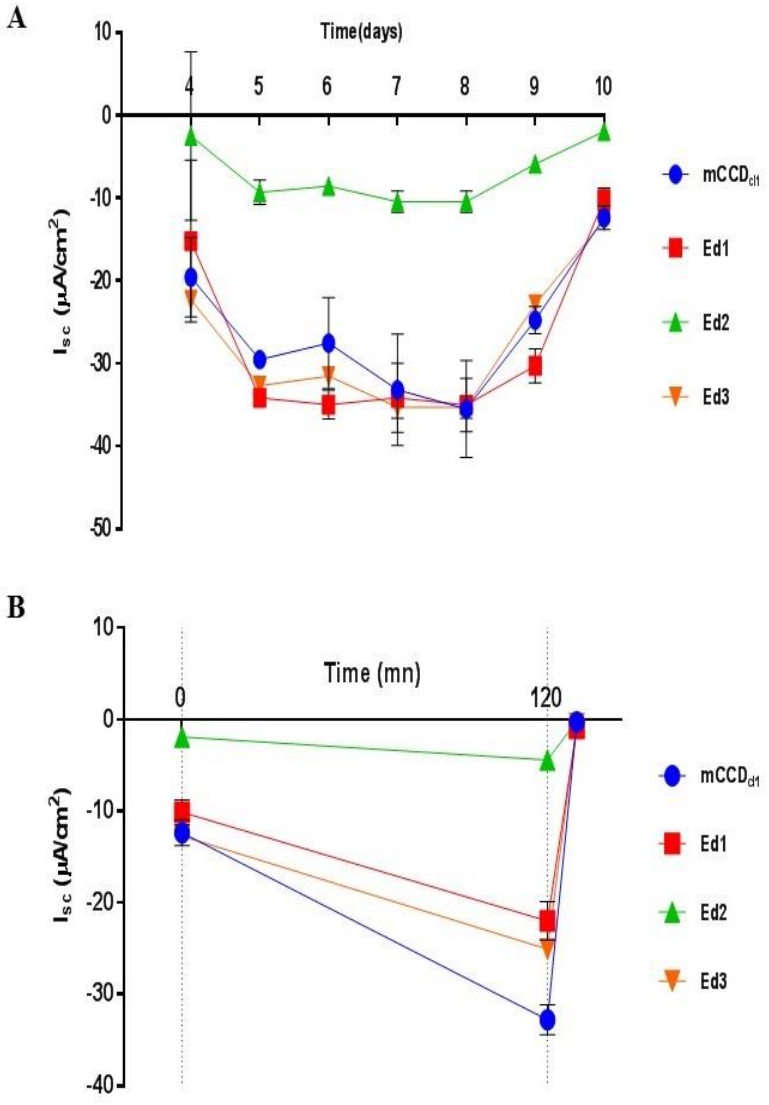

Figure 5.2. Repeated experiment on newly thawed cells shows comparable electrophysiological properties. (A) I_{sc} was calculated using Ohm's law, using measured Rte and Vte measured across monolayers of mCCD$_{cl1}$, Ed1, Ed2, and Ed3 cells grown on Snapwells filters, between day 3 and 10 after seeding. Values are shown as mean ± SEM (n=3). (B) Effects on baseline I_{sc} of aldosterone (3nM) and amiloride (10µM, apical bath) added at t=0 and t=120min respectively. Values are shown as mean ± SEM (n=3).

5.2.1.3 Link between electrophysiology and ENaC expression levels

Cells were fixed and stained with anti-α-ENaC antibody directly following the electrophysiological measurements described in section 5.2.1.1 (Figure 5.3.A), using the protocol for immunocytochemistry described in Chapter 2 (Section 2.3.2). In parental and clonal lines, most of the cells showed some degree of ENaC staining, but the level of expression differed greatly between cell lines. The mean grey value for ENaC in each cell line was taken over randomly selected areas of Transwell® membranes, over the different cell passages, and reflected the expression level (Figure 5.3.B). Electrophysiological measurements for Ed1 correlated to the ENaC mean grey value, which at 3.5 ± 0.4 % sits between Ed2 and $mCCD_{cl1}$. Ed2 presented the lowest expression with a mean grey value of 1.9 ± 0.5 %, and also had the weakest V_{te} and I_{sc}. Ed3 was identical to the parental line in terms of ENaC immunostaining levels (mean grey value at 7.1 ± 0.6 % and 7.2 ± 0.7 % respectively), and developed strong R_{te} and V_{te}, even greater than the parental line, which translated to an equivalent I_{sc}.

ENaC expression levels (Figure 5.3.A-B) were indicative of electrophysiological performances by the different cell lines, represented by V_{te} measured at day 8 after seeding (Figure 5.3.C, and see Figure 5.1), with high V_{te} for $mCCD_{cl1}$ and Ed3, low V_{te} for Ed2 and intermediate for Ed1.

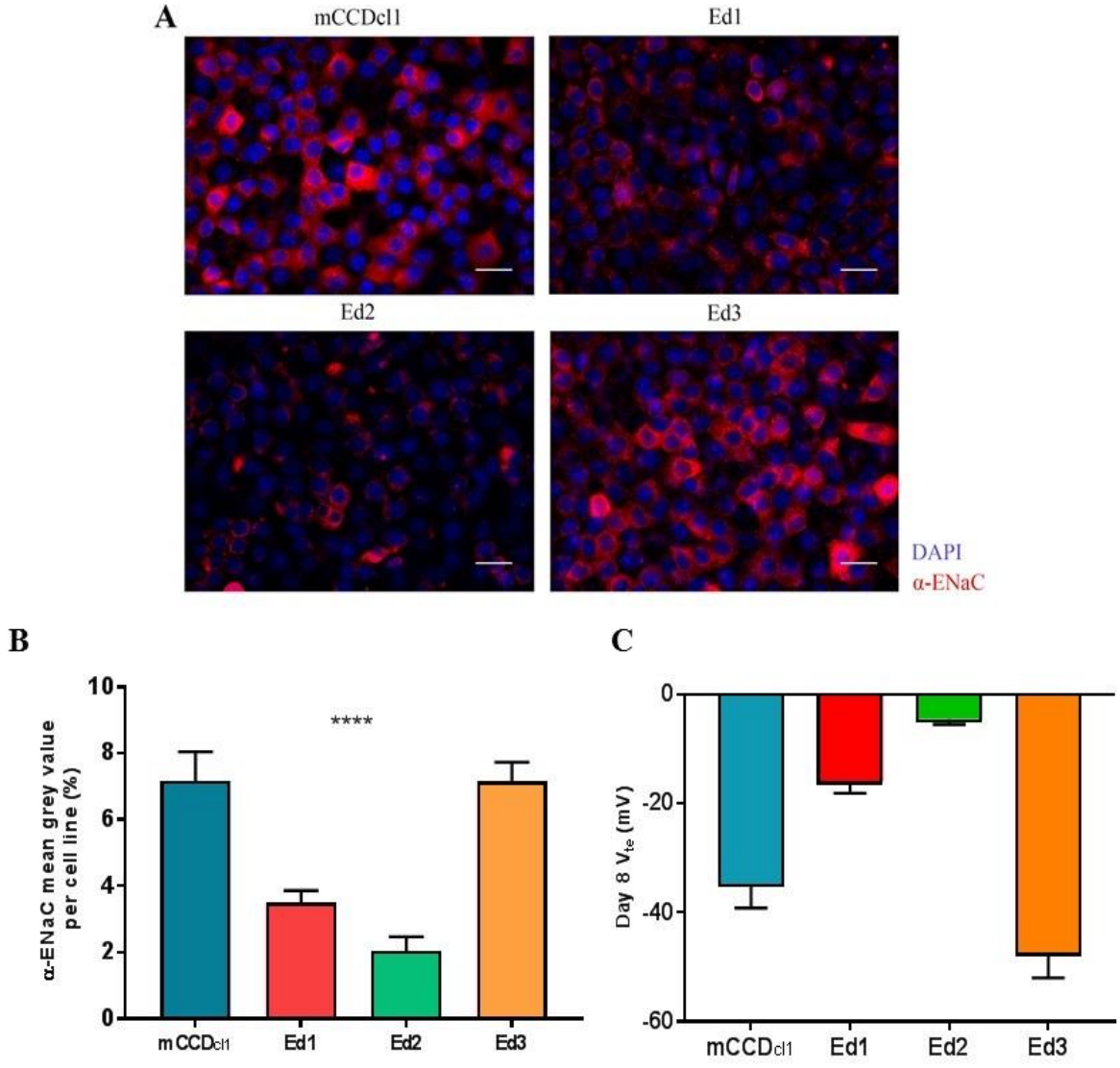

Figure 5.3. ENaC expression differences between cell lines. (A) Representative images of $mCCD_{cl1}$, Ed1, Ed2, and Ed3 cells stained with anti-α-ENaC (red), and DAPI staining of cell nuclei. Magnification x40. Scale bar 20µm. (B) Mean grey value per cell line showing different expression levels of α-ENaC in $mCCD_{cl1}$, Ed1, Ed2, and Ed3 cells. (C) Transepithelial voltage (V_{te}) measured across monolayers of $mCCD_{cl1}$, Ed1, Ed2, and Ed3 cells grown on Snapwells filters, on day 8 after seeding.

5.3 Discussion

5.3.1 Chapter summary

Using the protocol developed in Chapter 3 for meaningful electrophysiological measurements, $mCCD_{cl1}$ parental line, Ed1, Ed2, and Ed3 were grown on Transwell® membranes and their R_{te} and V_{te} recorded over 10 days, for 4 cell passages. Aldosterone and amiloride assays were also conducted. Parental and clonal cell lines showed significantly different levels of sodium transport and of aldosterone response, with extremely consistent results over 4 passages. The experiment was repeated with newly thawed cells over 3 passages with similar results. Observation of ENaC over the 4 cell lines showed a correlation between expression levels and electrophysiological performances.

These functional data confirmed the heterogenous composition of $mCCD_{cl1}$, and suggested that the composition of each cell line parallels their function. The electrophysiological properties, stable over several passages, also support the argument for a stable intermediate, precursor-like state of the $mCCD_{cl1}$ cell line suggested by the immunocytochemistry data.

5.3.2 Discussion

In complement to the immunocytochemistry data from Chapter 4, the extremely different sodium transport capacities between clonal sublines demonstrates the transitional nature of $mCCD_{cl1}$ cell line, composed of an heterogenous cell population.

Using Ussing chambers [166], other electrophysiological data could be obtained from parental and clonal sub-lines for further characterization, for example their response to stimulants such as norepinephrine, that has been shown to increase ENaC-mediated

sodium transport [81], or the potassium transport capacities of the $mCCD_{cl1}$, that have demonstrated ROMK expression [86]. Testing IC-related functions is more difficult considering the scale of electrogenic transport in ICs compared to PCs, but the study of V-ATPase B1 functions is in theory possible using bafilomycin, a specific blocker [58].

5.3.2.1 With a consistent protocol, the sodium transport stayed constant with passages

The electrophysiological data measured over 4 cell passages, then over 3 cell passages, have been used as biological repeats. No drifting of V_{te} or R_{te} values have been observed over these passages, due to the recovery protocol established in Section 3.3.3.

The functions of clonal lines stayed constant and stable over 4 passages, with a maximum V_{te} standard deviation (SD) at baseline of $\pm$ 3.8 mV for Ed3 (over a mean of -33.1 mV, see Table 5.1). The standard deviations for all other measures (R_{te}, V_{te}) stayed very low at baseline, aldosterone, and amiloride timepoints, making the repeated values for each cell line extremely significant in their similarities. It was noted that the deviation between passages was smaller when the cells were cultures in basal media only, and larger when in complete media, showing the cells sensitivity to additives such as FBS.

5.3.2.2 Is the culture medium introducing a bias?

During the experimental process, and while discovering the transitional nature of $mCCD_{cl1}$ cells, the use of a defined medium raised the question of the introduction of a bias in the results. The additives chosen to culture $mCCD_{cl1}$ cells clearly have an effect on their performances, but considering the nature of these cells, should we define low electrophysiological performances as “bad” (implying stressed, unhealthy cells)? Or are we

seeing the effect of additives on different physiological mechanisms, inducing a differentiation or transition state?

The medium used during this project (M1) gave the best V_{te} and R_{te} overall; it is based on the medium developed for the culture of $mCCD_{cl1}$ cells when the cell line was first established, and considered a PC line [80]. First considered as a sign of healthy cells, strong R_{te} and V_{te} could be due to this specific culture medium, that induces the most differentiation in PCs direction. More work is necessary to determine factors that can push $mCCD_{cl1}$ towards PCs or ICs, and is discussed in more details in Chapter 8 (Section 8.5). For this project, M1 was used as it still permitted the observation of bi-potential characteristics in $mCCD_{cl1}$, and offered the most stable conditions, but different media could have produced different data, and offer a convenient tool to investigate cell determination mechanisms.

5.3.3 Conclusion

In conclusion, a successful cell culture protocol was established to obtain significant data using $mCCD_{cl1}$. From there, electrophysiological data obtained on parental $mCCD_{cl1}$ and clonal lines confirmed the heterogenous nature of the cells, with subpopulations of cells presenting a wide range of functional capacities, and suggesting a parallel between protein expression and functionalities. It also showed the sensitivity of the cells to the culture conditions. These results suggest that using a well-established protocol, electrophysiological assays can be a powerful tool to identify cell types within the $mCCD_{cl1}$ population as well as eventual plasticity. Finally, the repeatability of measures over passages in clonal lines supports the idea that $mCCD_{cl1}$ possess precursor cell characteristics.

6 Development of a 3D model of tubular structure for cell culture and imaging

6.1 Introduction

Bioprinting of tubular structures is one of the path taken for the development of functional 3D-engineered live tissue. The focus has mainly been directed at the development of vascularization for *in vitro* bio-printed models, in order to ensure long-term survival of the model and closer mimicking of *in vivo* structures [174]–[176]. Due to the nature of kidney nephrons and collecting units, design of tubular scaffolds is one of the techniques chosen for the development of *in vitro* models of renal structures. In addition to shape, engineered kidney structures need the ability to let cells transport water and solutes, hence be porous.

In order to mimic in vivo CCD conditions, $mCCD_{cl1}$ cells need to form a tightly confluent monolayer of cells with access to an apical and a basal side for polarization [8]. For this project, the choice of polyHIPEs was directed by the need for a neutral support structure for $mCCD_{cl1}$ cells, allowing cell attachment, polarization, and function, and adds the benefits of 3D scaffolds compared to conventional cell culture supports such as flasks or flat porous membranes (see Section 1.3). Since hydrogels can interfere with proper cell-cell interaction [177], polyHIPEs were chosen as a 3D scaffold. The integration of cell 3D support structures in a set-up for imaging and fluidic studies is traditionally realized using PDMS (silicone-based polymer) devices [178], [179]. However, PDMS microfluidics present biocompatibility challenges and have been shown to affect the composition of the circulating fluid in long-term experiments [180], [181]. In this project, conventional 3D printing was therefore the chosen technique for fabrication of a flow and imaging set-up integrating polyHIPEs structures.

This chapter details the design and fabrication of a 3D scaffold for $mCCD_{cl1}$ cell culture, of the surrounding set up for the integration of the scaffold, and of the assembly of the complete set-up.

6.1.1 Aims

In this chapter, the following aims were addressed:

- Design and development of a tubular structure using a porous, 3D scaffold.
- Design of a device allowing for easy injection of culture medium, drugs, and flow system.
- Development of a device allowing the imaging of cells on a 3D scaffold.

6.2 Results

6.2.1 Principle

The 3D model was designed and developed following the principle shown on Figure 6.1. Cells are cultured in a half tube of 3D porous scaffold (polyHIPEs, Section 2.8.1), and directly observable using an inverted high-resolution microscope. The set-up is sealed using a conventional microscope cover slip (170 µm thick) for optimal imaging capacities. The set-up also enables flow and fluid injection inside the polyHIPEs tube.

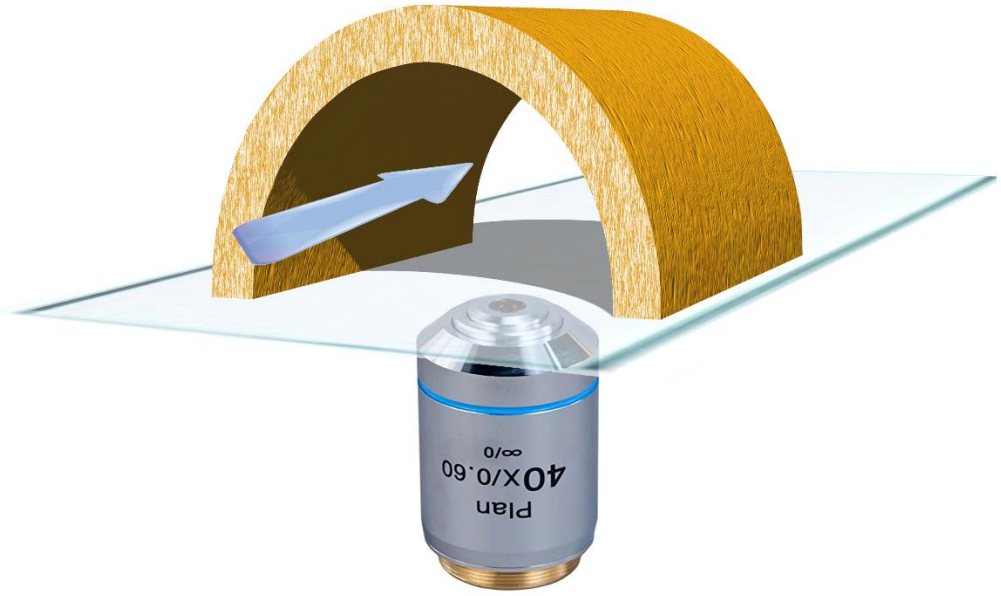

Figure 6.1. General principle of the 3D model of tubular structure. The yellow half tube corresponds to the 3D porous scaffold for cell culture. The blue arrow represents the fluid injection or flow enabled by the set-up. The scaffold is placed on a conventional glass coverslip for sealing and imaging purposes using an inverted microscope, represented by the 40x objective. Scale not accurate.

6.2.2 Printing of a 3D scaffold for cell culture

6.2.2.1 Printing process

PolyHIPEs tubes and half tubes were printed using the set-up described in Section 2.8.2.1, with a 50:50 ratio of EHA and IBOA polymers (summary of the set up on Figure 6.2). Samples were printed up to 4 at a time by projecting laser light through an appropriately patterned mask on the surface of the HIPEs. The stage was translated in the z axis at a speed of 0.6 mm.s^{-1} (printing speed), for a total printing time of 20 seconds for 12mm long samples. The stage was raised back to the starting position, lifting the printed tubes out of the liquid HIPEs (Figure 6.3.A). The samples were detached from the stage using tweezers and cleaned from uncured HIPEs in a 100% ethanol wash, and

stored in ethanol. The 50:50 EHA/IBOA polymer blend produced samples resistant enough to be easily manipulated with tweezers or directly by hand (Figure 6.3.B). HIPEs appear white due to the emulsion process during their fabrication, comparable to egg whites being whisked.

The printing process and tube characteristics were optimized for reproducibility of printing and for ease of set-up for imaging. The final dimensions were measured over 12 half-tubes by imaging on a wide field microscope, then measuring sections with ImageJ software. The half tubes were printed with a wall thickness of around 375 µm, and an OD of around 1.34 mm. Over 12 half-tubes, the measurements showed a high repeatability (Figure 6.4).

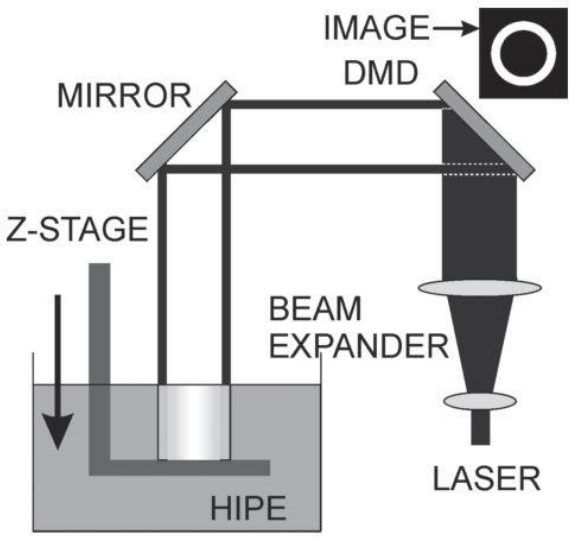

Figure 6.2. Schematic view of the set-up for 3D printing of polyHIPEs. The laser beam (405 nm) is expanded and reflected on a digital mask (DMD) that projects the image to be printed on polyHIPEs using a mirror and a focusing lens (not visible here). Image adapted from [140]

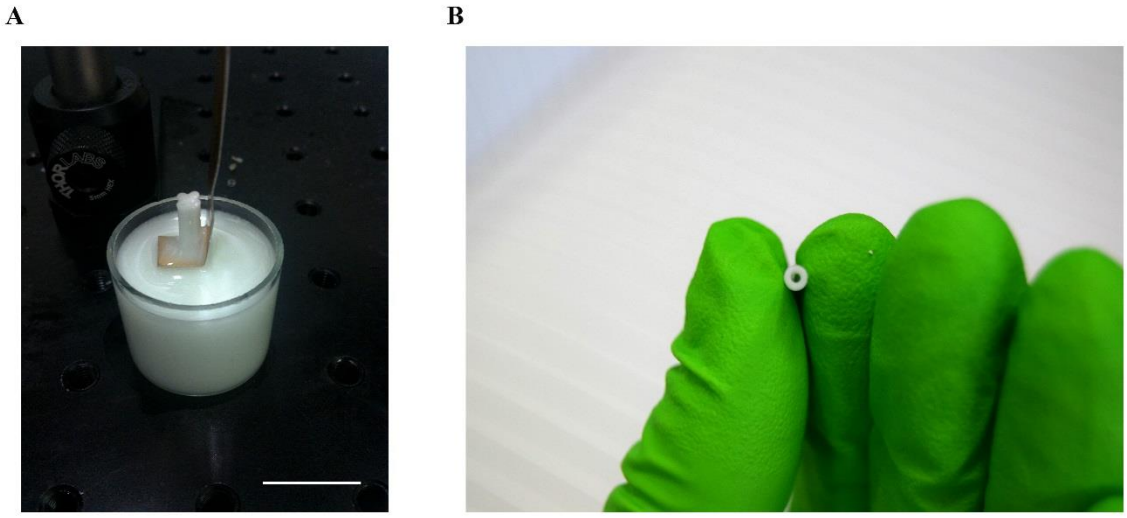

Figure 6.3. Printed polyHIPEs tubes. (A) Four tubes lifted out of the remaining liquid HIPEs at the end of the printing process. Scale bar is 2 cm. (B) PolyHIPEs tubes are easily manoeuvrable.

	Theoretical dimensions (µm)	Practical dimension (µm ± SD)
OD (outer diameter)	1500	1339 ± 57
ID (inner diameter)	1000	589 ± 46
Wall thickness	250	374 ± 28

Table 6.1. PolyHIPEs half-tubes dimensions.

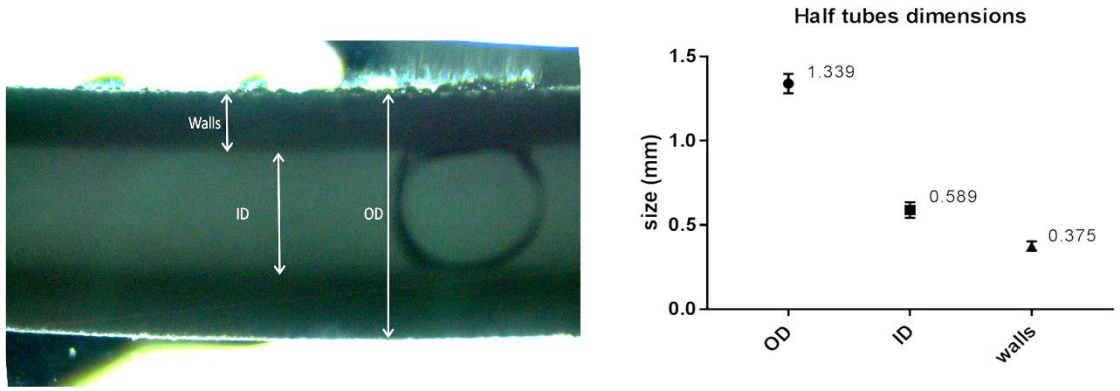

Figure 6.4. Measurement of the half-tubes dimensions. On the left, the measurement process, with a wide field image of a polyHIPEs half-tube captured from below, and the different sections measured (ID, OD, walls). On the right, measurements for each section over 12 tubes show high repeatability.

6.2.2.2 Properties of the printed polyHIPEs

The half tubes were produced using HIPEs with an 85% internal phase that, together with the printing speed, gave the appropriate porosity size - in theory under 20 µm diameter [140] - and the highest level of interconnection between the pores [146]. The internal phase corresponds to the ddH_2O added drop by drop to the polymer blend to obtain the emulsion (see Section 2.8.1.2), which creates the porosity network in the polyHIPEs. The process was optimized by testing different z-translation speeds, laser intensity, and internal phase percentages until a combination appropriate for this project was obtained. Porosity characteristics were observed using a multiphoton microscope at 850nm and the auto-fluorescence properties of HIPEs (Figure 6.5). Measurement of pore sizes show that above 90% of pores had a diameter of less than 20µm, and more than half had a diameter between 4 and 10µm (Figure 6.6). Pores with a diameter under 2µm could have been present but were difficult to observe. The maximum size detected was a diameter of 28.8µm.

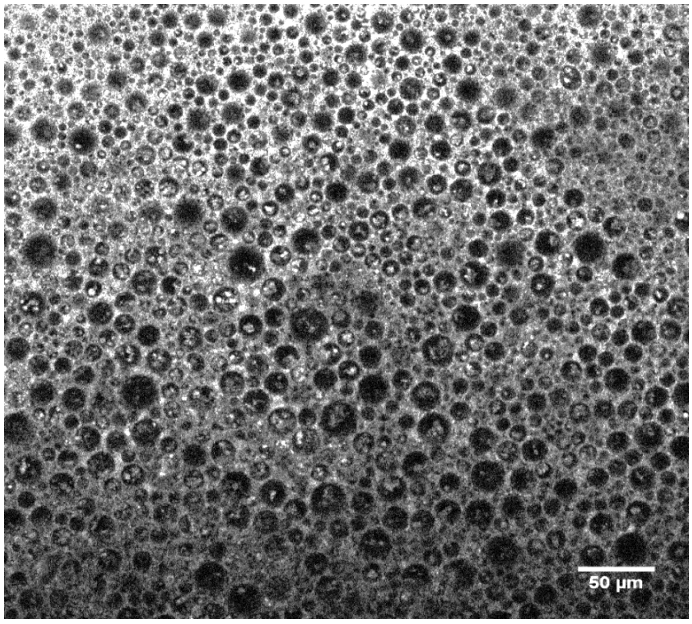

Figure 6.5. PolyHIPEs surface. 3D reconstruction of multi-photon imaging of polyHIPEs surface. The surface presents a variety of pore sizes. Scale bar 50 µm.

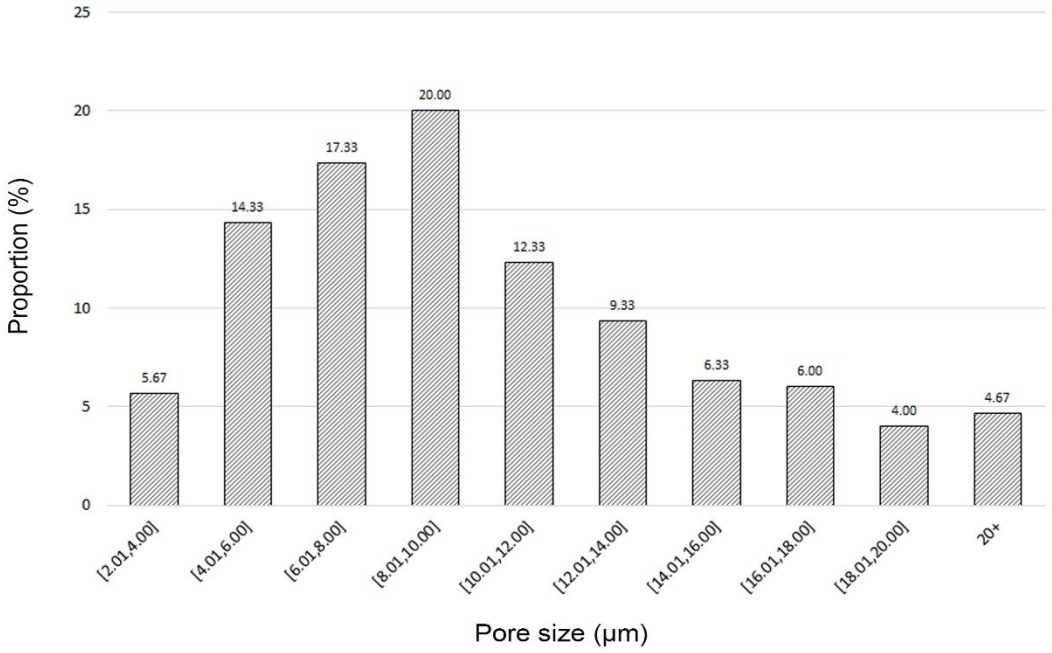

Figure 6.6. PolyHIPEs pore sizes distribution. Pore diameter sizes are distributed between 2 and 30µm, with under 5% of pores over 20µm. Pores under 2µm were not detectable on the image.

6.2.3 Printing of an imaging and flow chamber

6.2.3.1 Design

Imaging and flow chambers were designed using AutoCAD™. For the integration of 1.5mm external diameter polyHIPEs half tubes, chambers needed to be watertight, easy to handle, transportable, and enable the injection of cell culture medium or other fluids inside the tubes. For that purpose, a 40 x 30 x 10 mm (x y z) plastic block was designed, with a central opening of 12 x 15 x 10 mm for the integration of polyHIPEs half tubes. Channels were integrated on both sides of the central opening (1.2 mm diameter), with 2 mm long sleeves at each end for fitting the half tubes (Figure 6.7). Two versions of the chamber were created, one with 3 sets of channels and sleeves (Figure 6.7), one with a single set of the same dimensions.

The dimensions of the chamber enabled the imaging of the set-up on most inverted microscopes, using the standard stage platform for sample holding.

6.2.3.2 Printing

Prototypes were 3D-printed using the Makerbot Replicator 2 printer (see Section 2.8.2.1) (Figure 6.8). The design with one set of tubing was chosen for further developments (Figure 6.8.B), for handling and practicality reasons, but more complex designs were shown to be possible by printing the design with three sets of tubing. Prototypes were used for design alteration and development but were not suitable for the final IFCs, as the MakerBot Replica 2 layer-by-layer extrusion printing process, as well as the filament material, do not guarantee water tightness.

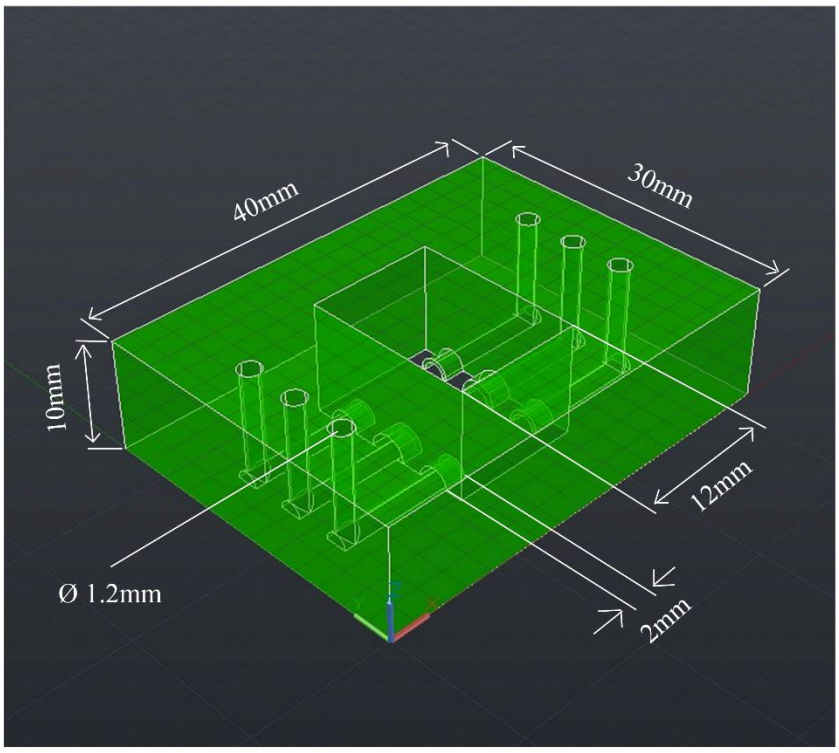

Figure 6.7. Imaging and flow chamber designed on AutoCAD™, and dimensions. Chambers were created with a maximum of 3 outlets for polyHIPEs half tubes. They contain tunnels with a diameter of 1.2mm for the future integration of tubing, and 2mm sleeves in the central opening for the half tubes ends.

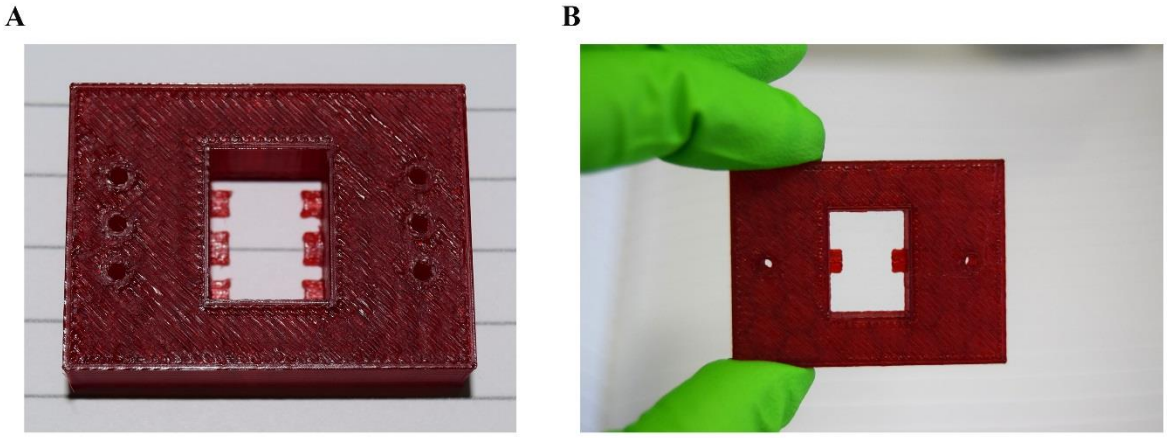

Figure 6.8. 3D printing of IFC prototypes. (A) Prototype with three sets of tubing for the integration of three half tubes. (B) Prototype with one set of tubing, chosen for further developments.

Following initial trials the IFCs channel diameter was modified from 1.2 to 2 mm for the easier future integration of standard tubing. 3D printing was transferred to the Connex3 Objet260 printer (Edinburgh College of Art) (See Section 2.8.2.2), which enables faster printing, the use of a transparent and water tight material, and better printing resolution. A new prototype was printed (Figure 6.9). The IFCs appeared rough on top due to the printing process: the top was printed first, and was in contact with a base layer of support material that leaves small indentations.

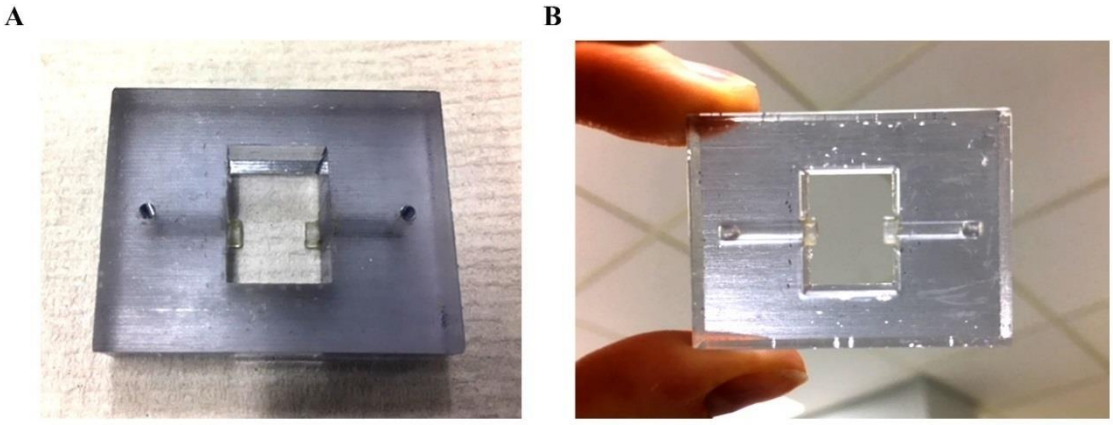

Figure 6.9. IFC prototype 3D printed on the Connex3 Object260 printer. (A) Top view. The top layer appears rough due to the support material of the 3D printer. A single set of channels was printed. (B) Bottom view. The channels extend in the central opening for the future integration of polyHIPEs half tubes.

6.2.4 Assembly

Assembly of IFCs, half tubes, and glass coverslip was finished by hand using aquarium sealant silicone. Silicone was applied using a small spatula or the tip of tweezers for precision, to avoid clogging the channels and polyHIPEs half-tubes (full assembly protocol in Section 2.8.3). Assembled devices were left to dry for at least 24 hours before testing for leaks.

Complete devices (Figure 6.10.A) were tested for leaks using PBS and coloured PBS inside the channels (Figure 6.10.B). General observations could be made:

- Leaks were observed on some devices, mostly along the length of the half tubes, at the contact surface with the glass coverslip.
- Silicone application between the tube and the glass coverslip lead to the clogging of some part of the polyHIPEs if not spread accurately.
- The silicone appeared both resistant and neutral but required manual and precise application.
- Fluid was easily injected in the channels with conventional pipette tips.
- The devices were found to be easy to wash, sterilize and image, and were reasonably resistant to rough handling.

Following these observations, some design modifications were made.

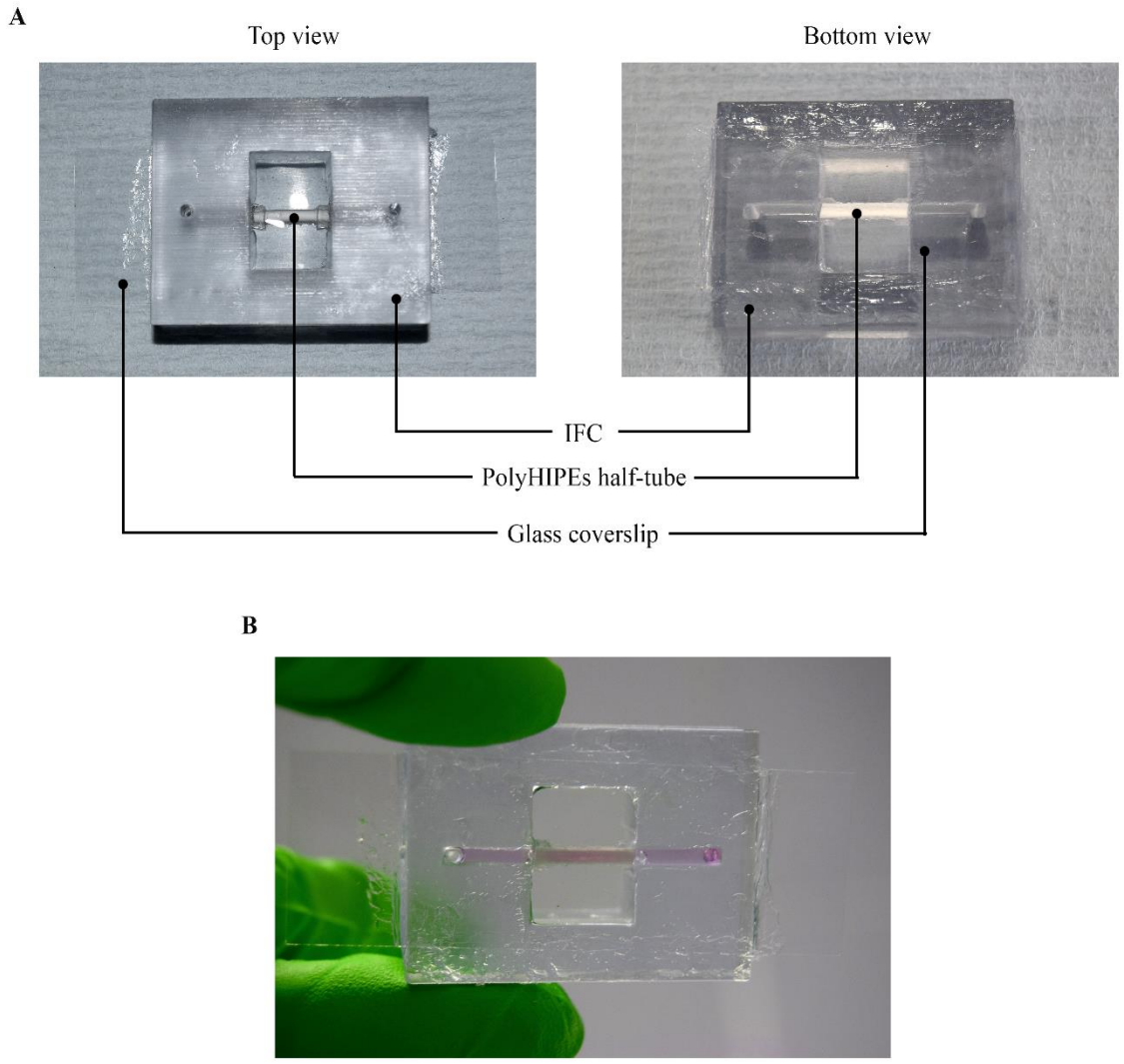

Figure 6.10. Complete IFC and polyHIPEs device. (A) Top and bottom view of the assembled device. PBS has been added in the central opening for leakage testing. (B) Coloured PBS (pink) is used to test for leakage around the half tube. Here the device was found to be watertight.

6.2.1 Troubleshooting

6.2.1.1 IFCs

Leaking problems along the tube's length and concerns of covering the polyHIPEs with silicone were addressed by adding two low borders (width: 1.5 mm) on each side of the tube's path in the central opening (Figure 6.11). Borders were created 100 µm thick to leave most of the surface of the half-tube uncovered, and enable easier and more precise silicone application with less leaking and clogging risks.

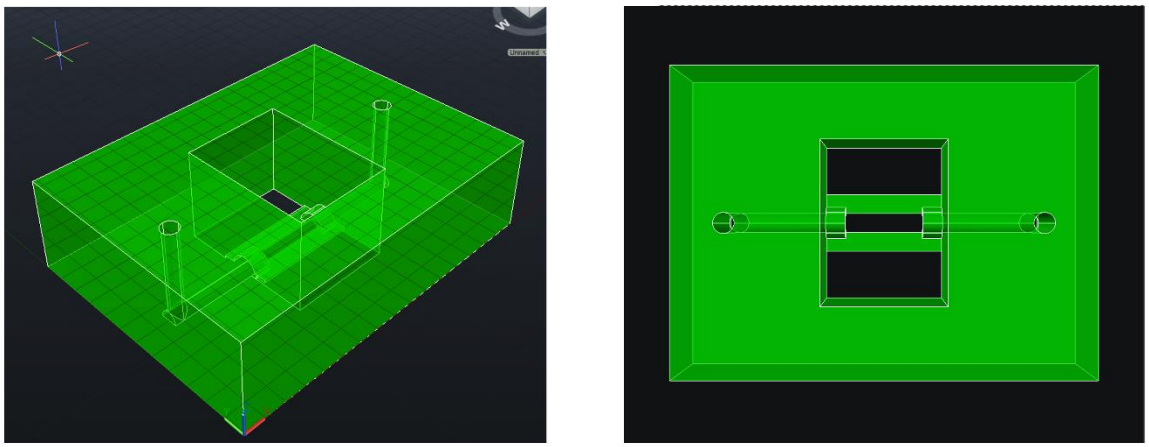

Figure 6.11. Views of design changes on IFCs. On the left, side view of the IFC in AutoCAD software. On the right, top view shows added borders on each side of the half-tube opening.

6.2.1.2 Tubes

Design of the polyHIPEs half-tubes was slightly modified to add "wings" on each side of the tubular section (See Figure 6.12). The 1 mm wide wings were sandwiched between the new IFC's borders and the glass coverslip during assemblage. Printing of these new tubes was handled by Dr. Colin Sherborne, through the collaboration with the Kroto

Research Institute (Sheffield University) where the stereolithography printer for polyHIPEs is situated.

6.2.1.3 Final assembly

The final version of the IFC-polyHIPEs devices used the winged half-tubes and the IFCs with borders (Figure 6.13). Leaking and assembly time were reduced to a minimum.

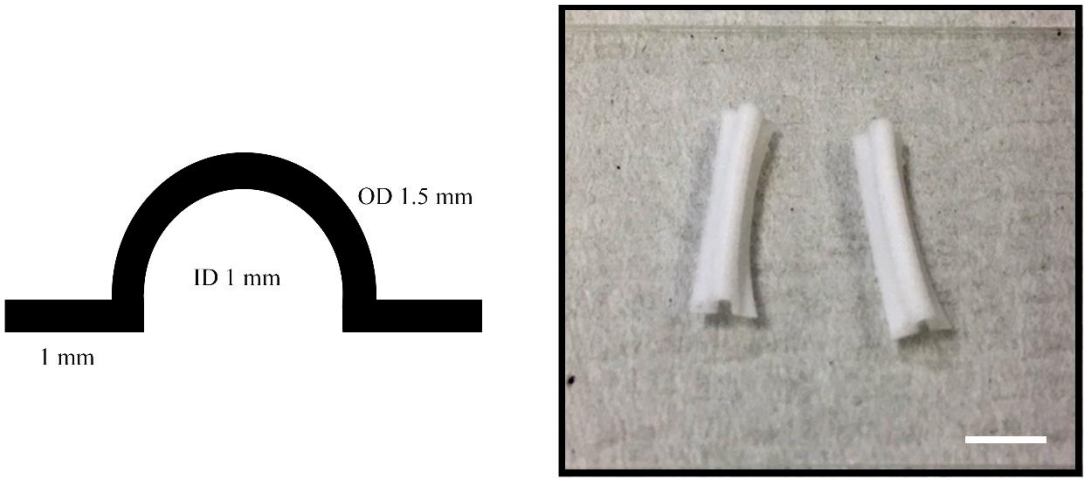

Figure 6.12. Design modifications on the polyHIPEs half-tubes. On the left, the modified mask projected on the liquid HIPEs for printing. ID for inner diameter, OD for outer diameter. On the right, two printed half tubes. Scale bar 5 mm.

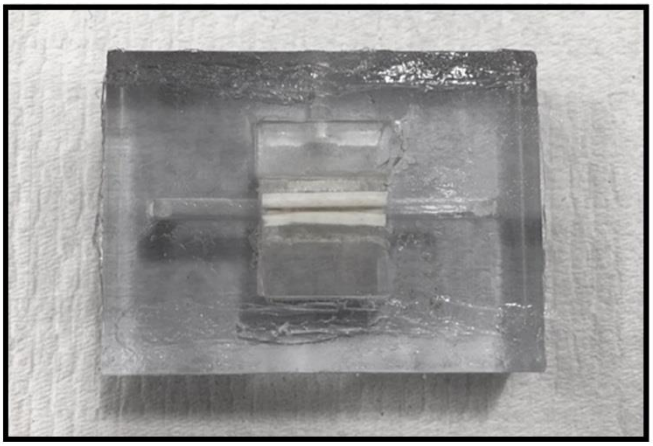

Figure 6.13. New complete device after design modifications. Bottom view of the assembled IFC and polyHIPEs half-tubes.

6.2.2 Medium injection and flow system

A simple system for automatic medium injection and flow was developed, using medical grade microfluidic flexible tubing and Falcon tubes as reservoir and collection tube (Figure 6.14). Tubing OD, at 2.1 mm, was chosen to be just above the OD of the IFC channels (2 mm). Tubing was forced into the channels, ensuring water-tightness. Flow rate was controlled by changing the height of the fluid reservoir, using a burette stand and clamp. The whole set-up could be fit inside a conventional cell culture incubator.

Flow rate of the set-up was measured by weighing the collected liquid at the exit of the device after 30 seconds at different reservoir heights. As expected, a linear correlation was found between height and flow rate (Figure 6.15). A height of 0 cm means that the bottom of the reservoir tube is level with the bottom of the IFC. Using a maximum elevation of 50 cm, flow rate varied between 0 and approximately 10 µl/s.

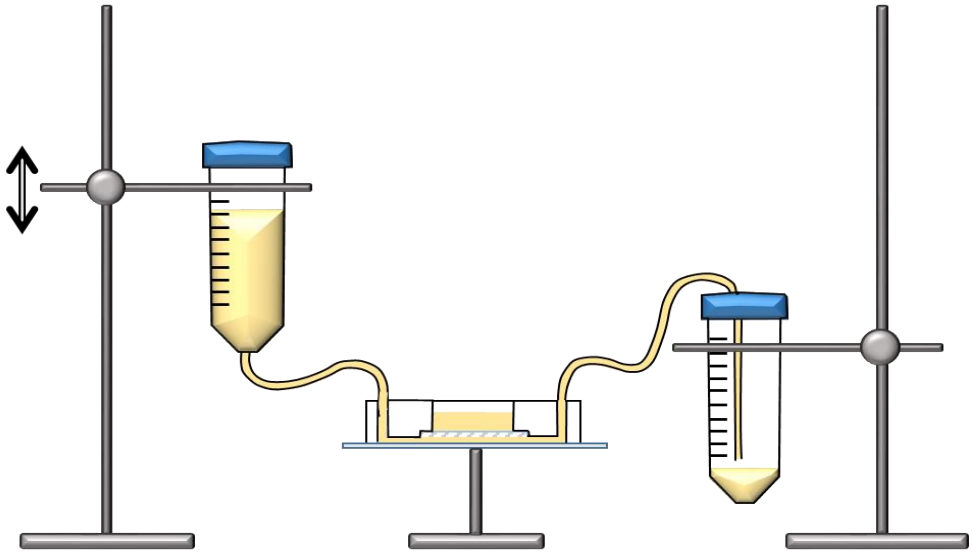

Figure 6.14. Schematic view of the medium injection and flow system. The flow system works using simple fluidic principles. The reservoir on the left is placed higher than the IFC (middle). The culture medium or solution (yellow) flows through the half-tube and is collected in the reservoir on the right, placed lower than the IFC. Flow rate is controlled by changing the height of the left reservoir.

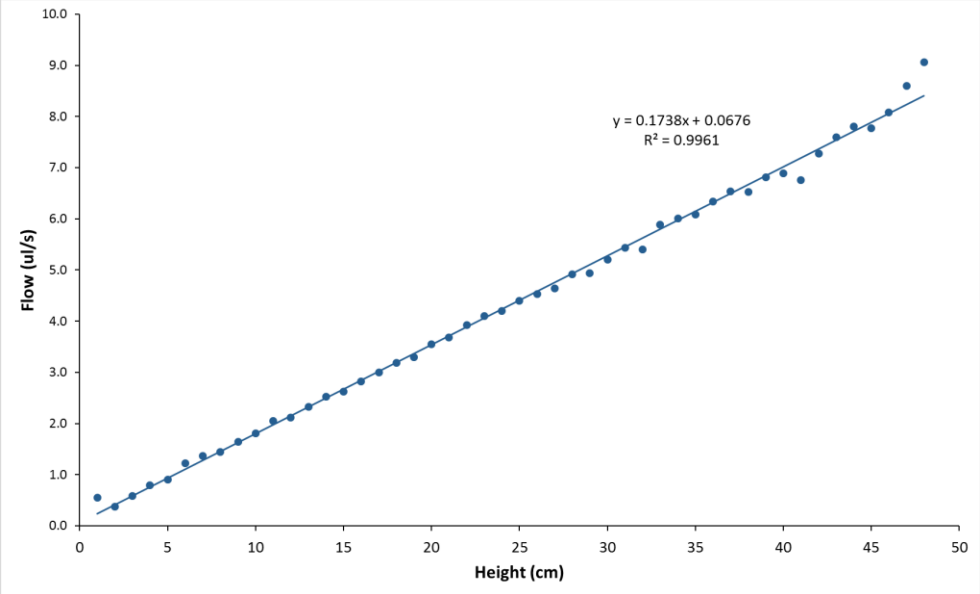

Figure 6.15. Set-up flow rate. A linear correlation was found between flow rate and reservoir height.

6.3 Discussion

6.3.1 Chapter summary

A tubular 3D support scaffold for cell culture was fabricated with the help of Dr. Colin Sherborne (Kroto Research Institute, Sheffield). Scaffolds were created using micro-stereolithography on a polymer blend emulsion (HIPEs), producing polyHIPEs tubes and half tubes. The 3D printing process was optimized to produce tubes of the chosen dimensions with a high repeatability. In parallel, an imaging and flow chamber (IFC) was designed and developed for the integration of polyHIPEs half-tubes. IFC prototypes were 3D printed using an extrusion printer, optimized and bulk-printed using a new-generation 3D printer with transparent and watertight material. Assemblage of the different parts using silicone revealed design flaws causing fluid leaks along the half-tubes. Several optimization steps were taken to reduce leaking, including the addition of borders on the IFCs and wings on the half tubes. The final product was integrated in an injection and flow system able to deliver flow rates up to 10 µl/s.

6.3.2 Discussion

6.3.2.1 Fabrication process

Assemblage of the different parts of the device was made by hand and required precision. While the time to finish every device decreased with experience, the process remained non-automated and would require extensive design changes for more automatic manufacturing to be possible. Attempts were made to use PDMS "stamps" for assemblage and attachment of the glass coverslip, but the process resulted in unavoidable covering of the whole polyHIPEs half tubes in PDMS, clogging the whole tubing and pores. Partial pre-curing of PDMS to avoid its spread showed better results, but was more time-consuming than using silicone by hand, which defeated the object of the whole process.

PolyHIPEs half tubes dimensions varied from the theory (image on mask) to the actual printed object. This can be explained by several factors, such as the focusing lens that may have projected a slightly smaller image on the liquid HIPEs surface. Another factor, to explain the increased wall thickness is the material itself, scattering the laser light at the point of contact and leading to a larger surface being polymerised compared to the projected image. Whilst the process can be optimized to obtain tube dimensions identical to the mask, the repeatability of the printing was prioritized.

6.3.2.2 PolyHIPEs

$mCCD_{cl1}$ cells have an average diameter size of approximately 20µm. The PolyHIPEs structures used in this study therefore allow for the cells to sit on the surface and form a monolayer while offering 3D culture conditions. PolyHIPEs can easily be modified to offer larger porosity sizes to allow cells to grow inside the scaffold, for example for growing bone tissue [146] or multi-layered constructs. The polymers used is this project (EHA and IBOA) can also be replaced by bio-degradable polymers for the development of bio-mimicking structures. However these structures need to take into consideration the timescale for cell culture and the time after which bio-degradation starts.

6.3.2.3 Flow rate

Flow rate here is conditional to the inner diameter of the external tubing chosen for the system (C-Flex tubing, Cole-Palmer), here 500µm. Flow rate observed here, up to 10µl/s, are elevated compared to *in vivo* flow rate. Urine flow rates in the rat have been described at in between 1.5 ml/h (low) and 25 ml/h (high), which corresponds to between 0.4 µl/s and 7 µl/s, but for the whole kidney [182]. Micro-perfusion studies conventionally use single nephron flow rates of between 6 and 16 nl/min [183], controlled by specialized pumps. The flow system developed here is a temporary solution that can be used mainly

as a fluid injection system to test the stability of the device. However, the design of the IFC and the cell culture scaffold are fully compatible with the integration of the device in a fluidic circuit allowing for the lower flow rates found *in vivo*.

6.3.3 Conclusion

In conclusion, two 3D printing techniques were used to develop a 3D tubular cell culture environment. Half-tubes or porous polymers were created using micro-stereolithography 3D printing. A specially designed imaging and flow chamber (IFC) was manufactured using jet-based additive 3D printing, permitting the imaging of half-tubes inner walls on conventional inverted microscopes and the injection of fluid. Half-tubes were integrated in the IFC and flaws leading to leaking were identified and addressed with design modifications. The complete device is a new tool for the culture of $mCCD_{cl1}$ cells and the study of the cell line in a 3D environment.

7 $mCCD_{cl1}$ on polyHIPEs: development of a 3D model of collecting duct

7.1 Introduction

As demonstrated previously in this thesis, $mCCD_{cl1}$ offer the possibility to study the physiology of collecting duct homeostasis, collecting duct cell type determination, and eventually collecting duct development. The idea of designing a cell culture setting mimicking *in vivo* environment has been developing in parallel with the available cell lines for *in vitro* models, but the interest has become exponential in recent years [184]. In general, cells cultured in a 3D environment are more sensitive to lower drug concentrations, have an increased rate of survival as well as gene and protein expression, and tend to be more differentiated than the same cell lines cultured in classic 2D settings [185]. The most commonly used scaffold to create a 3D structure is collagen type I, followed by fibronectin, and gelatine. However these substances and collagen in particular are commonly associated with a diseased kidney and renal fibrosis [186]. The use of extracellular matrix components for 3D culture depends on the cell line used in the model, as each cell type requires different optimal conditions to be determined. Cell-cell and cell-support adhesion are crucial for tissue integrity and physiological mechanisms and functionality [187].

As suggested by the preceding chapter, the use of polyHIPEs for the culture of $mCCD_{cl1}$ cells offer a neutral support for the cells to attach and form a confluent layer in a 3D environment. While mouse CCDs typically have an inner diameter of around 30µm (observations made on WT mouse kidneys, data not shown), the choice was made to develop a larger and more manipulable model allowing for a greater number of $mCCD_{cl1}$ cells to be cultured. The specific PolyHIPEs composition used in this project had been tested before as support for culture of human embryonic stem cell-derived mesenchymal progenitors (hES-MPs) cells, after a simple rehydration protocol [146]. Cells attached on the scaffold without preliminary coating, and displayed a satisfactory proliferation rate.

Since different cell types require different environments, evaluating scaffold suitability, eventual toxicity, and cell attachment is a first and important step in the development of a 3D model of collecting duct using $mCCD_{cl1}$ cells.

7.1.1 Aims

The following aims were addressed:

- Develop a protocol for $mCCD_{cl1}$ cell culture on polyHIPEs.
- Assess polyHIPEs as a support structure for $mCCD_{cl1}$ cells and cell attachment.
- Determine the most adapted imaging methods for cells on polyHIPEs, on isolated samples or in half-tubes.
- Observation of potential differences between cell culture in flasks or on filters, and on polyHIPEs.

7.2 Development of a cell culture protocol on polyHIPEs

7.2.1 Preparation of polyHIPEs

To remove remaining surfactant and curative agents, which are toxic to cells, the polyHIPEs samples (disks and 3D printed half-tubes) were left for at least a week in 100% ethanol, with regular ethanol change and washes. A rehydration protocol was then followed in sterile conditions:

- Baths of decreasing concentration of ethanol: 80%, 60%, 40%, 20% over a day (approximately 2 hours for each concentration).
- PBS bath: polyHIPEs were washed then transferred into fresh PBS for at least 1 day, or until ready for cell culture.
- Before seeding the cells, polyHIPEs were transferred to warmed medium and left to soak in the incubator for a minimum of one hour, or until ready to proceed with cell culture.

7.2.2 Cell seeding technique

7.2.2.1 Isolated PolyHIPEs samples

PolyHIPEs disks or hemitubes were taken out of their culture medium bath and transferred to a dry plate (well of a 6 or 12-wells plate). Depending on the size of the scaffold sample, between 100 and 200 µl of cell suspension (1:1 cell density) was added on top, with the cell suspension obtained following the passaging protocol described in Section 2.2.3. For cell attachment, samples were placed at 37°C for 2 hours, then fresh medium was added (between 1 and 3 mL depending on well size). Cells were fed with fresh medium every day or two days.

7.2.2.2 PolyHIPEs half-tubes integrated in IFCs

PolyHIPEs half-tubes integrated in the IFCs were prepared following the protocol described in Section 7.2.1, by dipping the whole device (IFC and half-tube) into baths of decreasing ethanol solution then PBS. Warm culture medium was injected in the channels and added in the central opening of the IFC and kept at 37 °C for at least one hour before proceeding with the cells (and removed just before seeding the cells). The cell suspension (100 µl) was then injected in the half tube, and the channel openings sealed with a glass coverslip. The chamber was flipped upside down to let the cells settle on the polyHIPEs instead of the glass coverslip, and allowed to attach for 2 hours at 37°C (Figure 7.1). Fresh medium was then injected inside the tube and added on top of it in the central opening of the IFC. Cells were fed with fresh medium every day or two days.

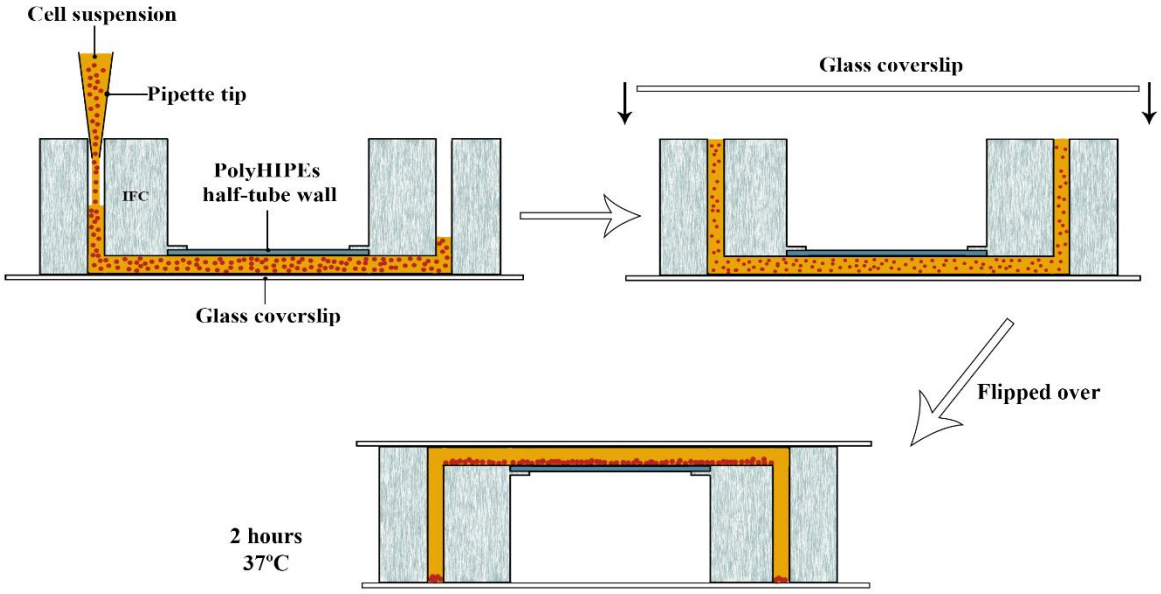

Figure 7.1. Protocol for cell seeding in 3D device. Cross-section view of the IFC channels and polyHIPEs half tubes**.** 100µl of cell suspension is injected in the polyHIPEs half-tubes through the IFC channels. A glass coverslip seals the channels for the device to be flipped over. The cells are left to attach 2 hours at 37°C before injecting fresh culture medium.

7.3 Scaffold suitability and cell attachment

7.3.1 PolyHIPEs disks

On polyHIPEs disks, $mCCD_{cl1}$ cells were seeded without preliminary coating. After 5 days in culture, cells could be observed growing on the borders of the polyHIPEs disks with a brightfield microscope (Figure 7.2), indicating a good coverage of the scaffold by cells proliferating from the original seeding area in the middle of the sample. Cells were then left in culture with regular feeding, and observed using a multiphoton microscope at 4 weeks and 6 weeks. Cells at 4 weeks were left in their culture medium and were observed using only auto-fluorescence, detectable at 860nm. Some cell structures, most likely lysosomes, were clearly visible; a confluent layer of $mCCD_{cl1}$ cells was observed on the surface of the polyHIPEs disks (Figure 7.3), confirming cell attachment, proliferation and survival up to 4 weeks. With this imaging technique, scaffold pores could be seen through the cell layer. After 6 weeks, samples were fixed with 4% PFA and cell nuclei stained with DAPI. Multiphoton microscope imaging showed a comparable cell monolayer to that at 4 weeks (Figure 7.4), confirming survival of the cell layer up to 6 weeks. On different samples, cells were observed on the borders of the polyHIPEs slices (brightfield microscopy, comparable to Figure 7.2) up to 8 weeks, with regular feeding.

The timescale of $mCCD_{cl1}$ cell survival on polyHIPEs disks could be compared to typical $mCCD_{cl1}$ cell culture in flasks. Indeed, in flasks $mCCD_{cl1}$ cells typically started detaching completely from the flask around 10 days after passaging, starting with the doming areas, most likely due to cell polarization. Frequent passaging after confluency were required for survival of the cell line. On polyHIPEs however, no doming was observed, and cells didn't detach from the support up to 6 weeks after seeding. No over-proliferation, for example cells piling up on each other, was observed.

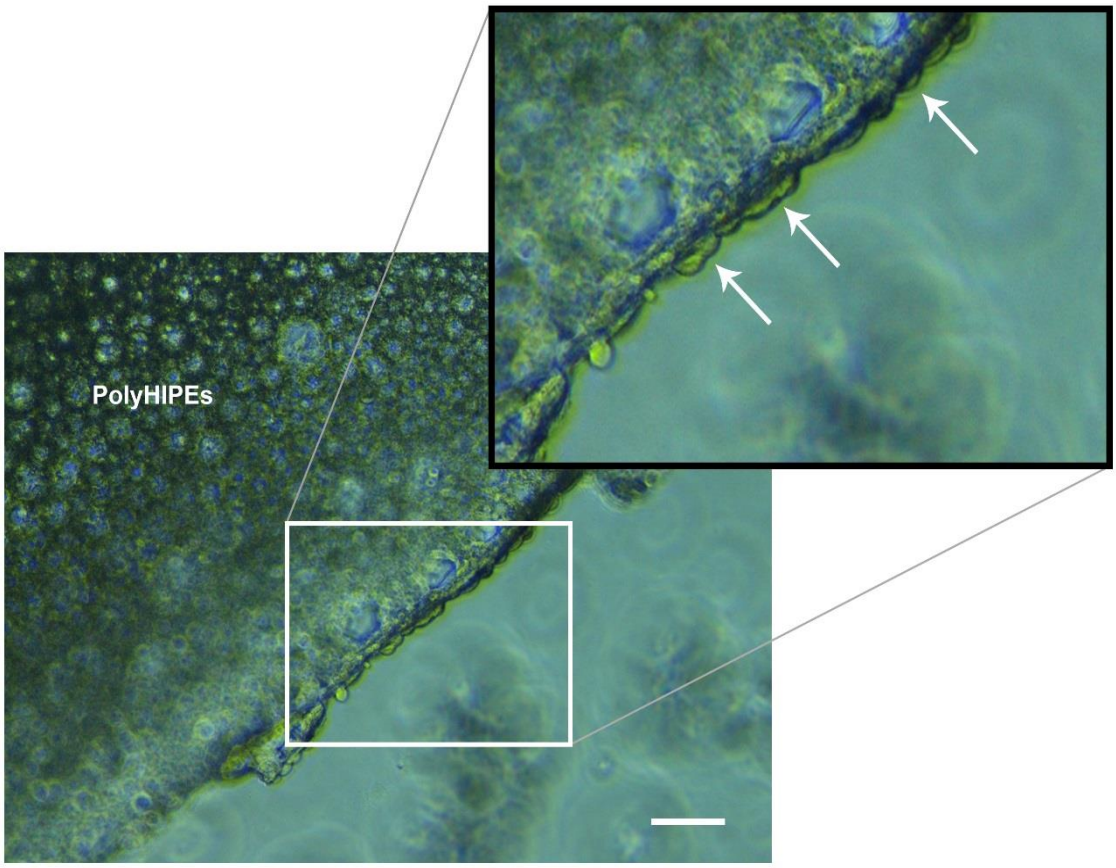

Figure 7.2. Brightfield image of mCCDcl1 cells grown on flat polyHIPEs sample. Cells on the polyHIPEs can be seen in brightfield on the border of the polyHIPEs sample (examples shown by white arrows on the magnified image). Scale bar 50µm.

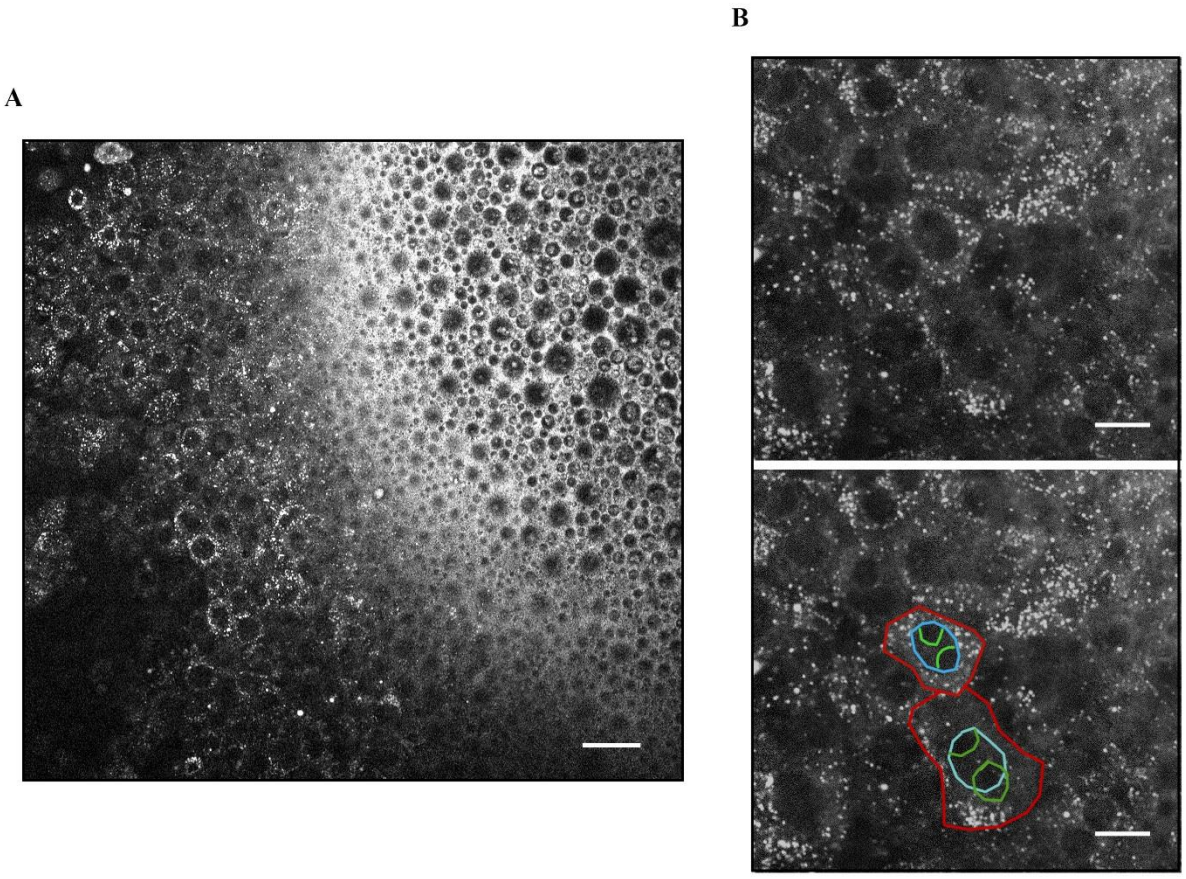

Figure 7.3. Multiphoton imaging of live mCCD$_{cl1}$ cells on polyHIPEs scaffold after 4 weeks. (A) Image of live cells on polyHIPEs, magnification x25. Due to the slight tilt of the sample, both cells and scaffold were visible on the field of view. Cells are visible on the left and scaffold only on the right. Scale bar 30µm. (B) Magnification of mCCD$_{cl1}$ cells on polyHIPEs. Top image shows auto-fluorescent cell structures allowing for the shape of the cells to be seen. On the bottom, the same image with red: example of cell contours, blue: nuclei, and green: example of polyHIPEs pores visible through the cells. Scale bars 10µm.

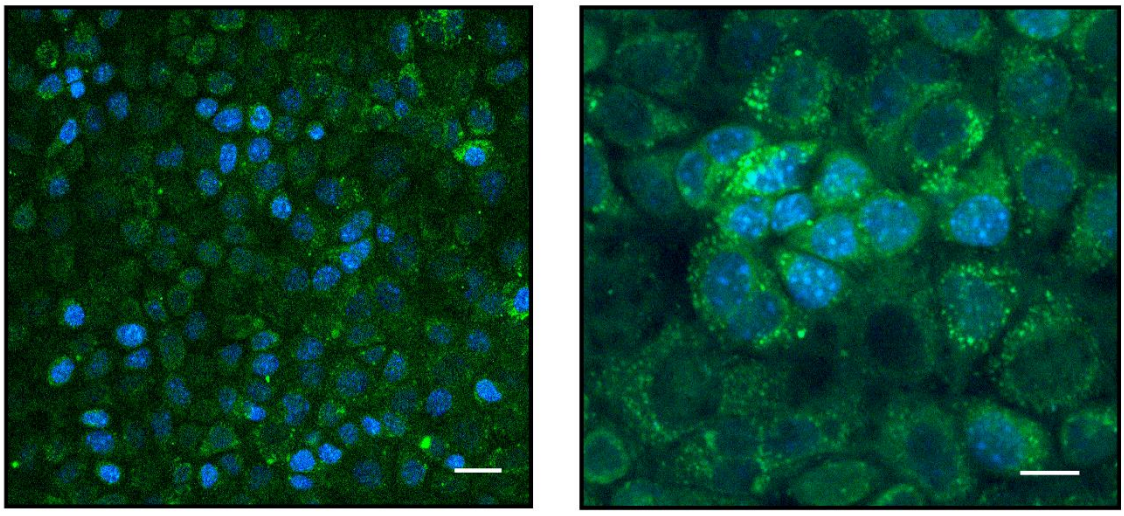

Figure 7.4. Multiphoton imaging of fixed $mCCD_{cl1}$ cells on polyHIPEs scaffold after 6 weeks. On the left, x25 magnification, scale bar 30 µm. On the right, x100 magnification, scale bar 10µm. DAPI staining of cell nuclei in both images (blue). Cells auto-fluorescence in green.

7.3.2 PolyHIPEs half-tubes integrated to IFCs

$mCCD_{cl1}$ cells were injected in polyHIPEs half-tubes following the protocol recently established (Section 7.2.2.2), and cultured for 3 weeks with regular feeding. Live cell nuclei were then stained using Hoechst and the half tubes internal walls imaged using a fluorescent inverted microscope, through the sealing coverslip (Figure 7.5). Intense staining of cells nuclei was detected in the entire tube, showing a confluent layer of $mCCD_{cl1}$ cells on the polyHIPEs surface. Cell attachment and proliferation appeared optimal and the cells were covering the entire inner wall of the half-tube, confirming cell survival up to 3 weeks in the half-tubes. Background fluorescence was observed, due to the strong auto-fluorescence of the polyHIPEs, mostly visible when imaging in the DAPI and FITC channels.

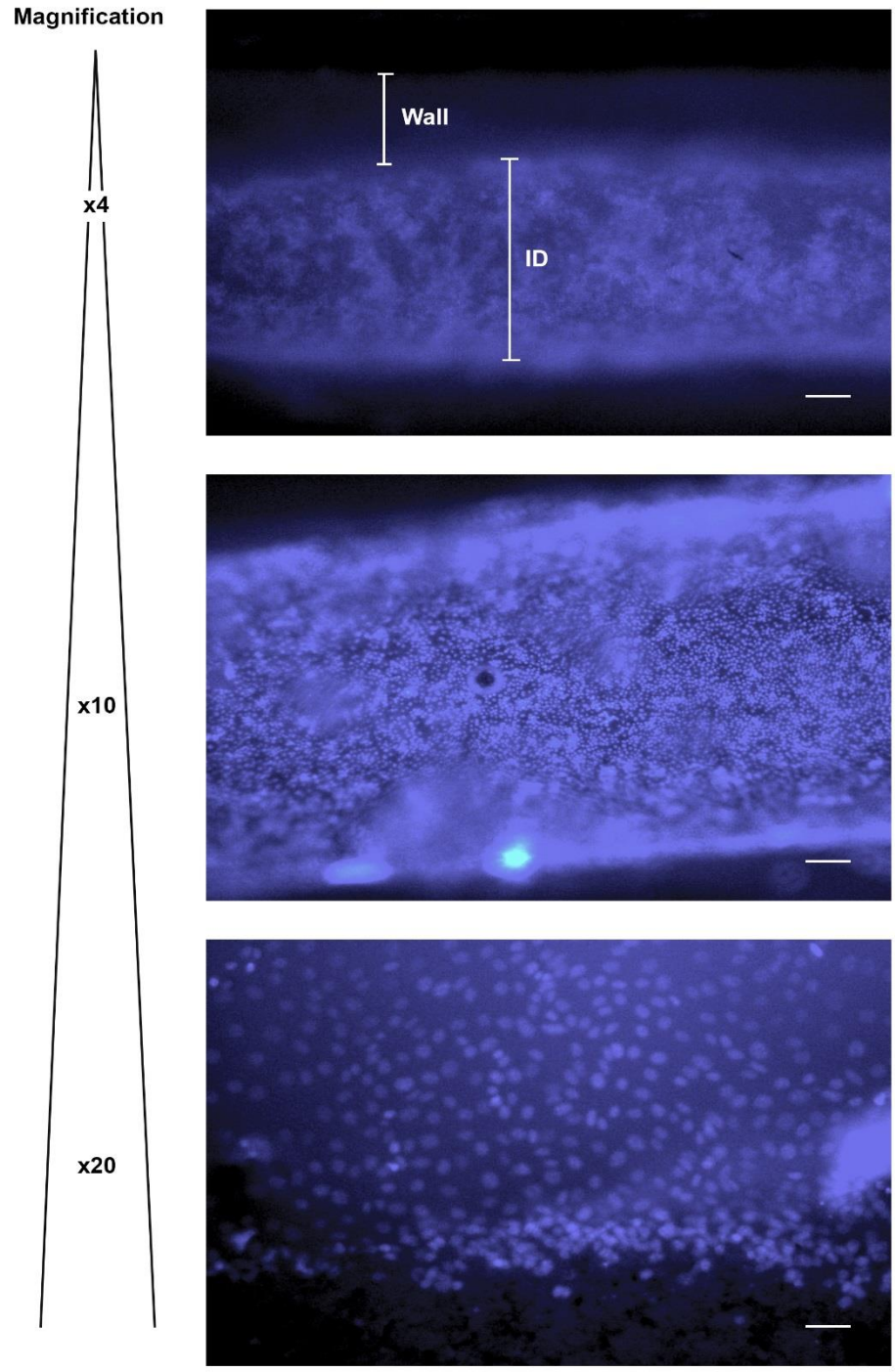

Figure 7.5. Live mCCD$_{cl1}$ cells grown in polyHIPEs half-tubes. Hoechst staining of live mCCD$_{cl1}$ cells nuclei cultured in polyHIPEs half-tubes integrated in an IFC. In the top image, wall indicates the half-tube wall thickness seen from below, ID for inner diameter. From top to bottom, scale bars are 200µm, 100µm, and 50µm respectively.

7.4 $mCCD_{cl1}$ on polyHIPEs scaffolds: results

7.4.1 α-ENaC localization and expression levels

Immunocytochemistry of $mCCD_{cl1}$ cells using anti-α-ENaC antibody was performed according to the protocol described in Section 2.3.2 and adapted for polyHIPEs half-tubes by injecting the solutions in the channels. $mCCD_{cl1}$ cells cultured in polyHIPEs half-tubes for 3 weeks before fixing showed widespread, consistent expression of ENaC throughout the cell layer (Figure 7.6). Light-scanning confocal images of the entire depth of the half-tube's inner diameter (approximately 450µm) were taken. The Z-projection, a combination of all the different focal distances, showed ENaC expression on most cells. 3D reconstruction and orthogonal projection offered a convenient view of the half-tube volume but did not allow for precise localization of ENaC in the cells. On this specific microscope (light-scanning confocal microscope), objectives above 20X did not offer a satisfactory view of ENaC expression.

Localization of ENaC on $mCCD_{cl1}$ cells cultured on polyHIPEs was made possible by the use of a spinning-disc confocal microscope (See Section 2.4.3). $mCCD_{cl1}$ cells were cultured for 2 weeks on polyHIPEs disks, fixed and stained using anti-α-ENaC and anti-acetylated-α-tubulin antibodies. Samples were imaged with a X40 magnification. Image reconstruction showed a tight layer of $mCCD_{cl1}$ cells following the topography of the scaffold, with a clear apical localization of ENaC staining, above the acetylated alpha-tubulin of the cytoskeleton and the DAPI staining in the nuclei (Figure 7.7).

ENaC expression levels were estimated by imaging both cells cultured on porous membranes (Corning® Transwells®)(Figure 7.8.A) and cells cultured on polyHIPEs disks (Figure 7.8.B), and comparing the overall grey value of ENaC staining. ENaC expression levels were significantly up on 3D scaffold compared to porous membranes, from a grey

value of 23.74 ± 2.19 % to 31.64 ± 2.69 % (Figure 7.8.C). The distribution of ENaC staining was different in both settings, with staining forming "rings" around the nuclei, and fainter above the nuclei on cells grown on porous membranes (2D setting), while the staining was more evenly distributed in cells grown on polyHIPEs (Figure 7.8.D). The proportion of cells expressing ENaC was identical in both setting, at about 90%.

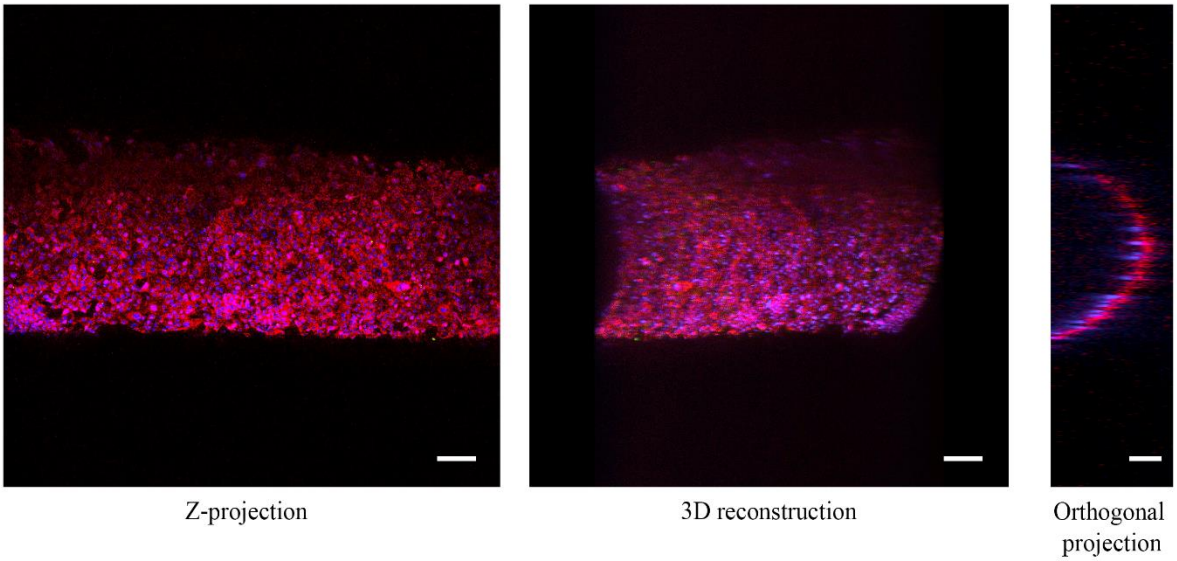

Figure 7.6. Immunostaining of α-ENaC on mCCD$_{cl1}$ cultured in polyHIPEs half tube. Confocal imaging of ENaC expression (red) on mCCD$_{cl1}$ cells. Z-projection: combination of all the images taken at different focal distances (z-stack); scale bar 100µm. 3D reconstruction: slightly rotated image after combination of all the z-stack images, showing 3D volume; scale bar 100µm. Orthogonal projection: Size view of the z-stack shows volume shape; scale bar 200µm. In all images, 20X magnification; DAPI staining of cell nuclei (blue).

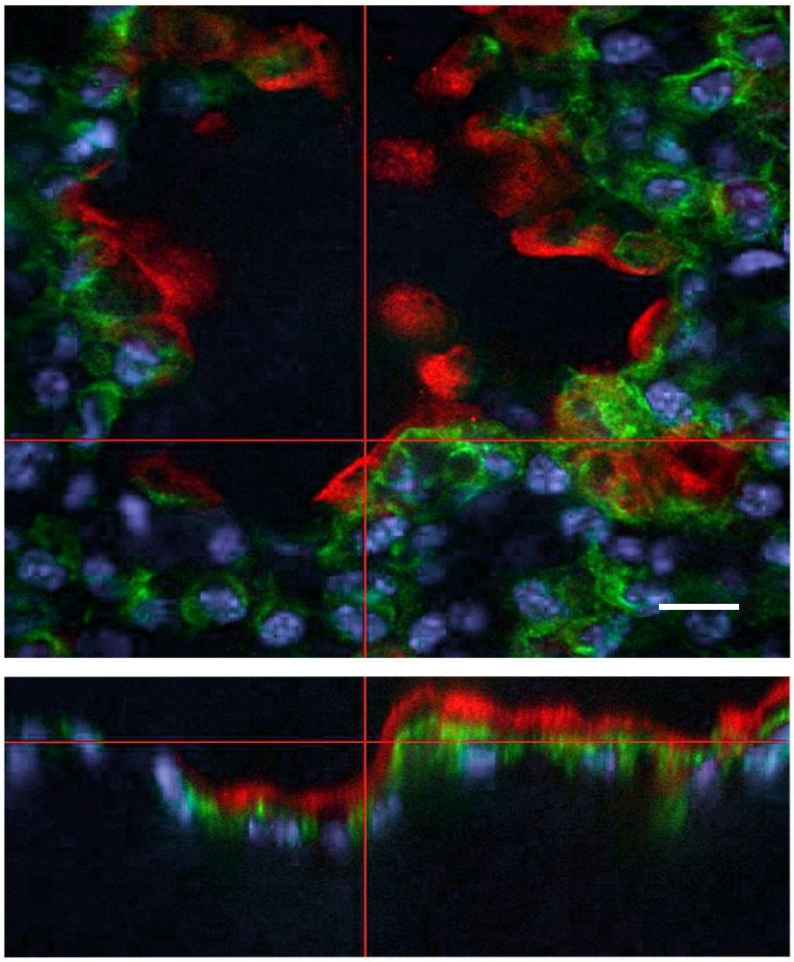

Figure 7.7. Immunocytochemistry of ENaC shows apical localization on mCCD$_{cl1}$. Confocal imaging of mCCD$_{cl1}$ cells cultured on polyHIPEs scaffold and stained with α-ENaC (red) and acetylated α-tubulin (green). Orthogonal projection on the bottom corresponds to the planes shown by the horizontal red line. Scale bar 20 µm. DAPI staining of cell nuclei in blue.

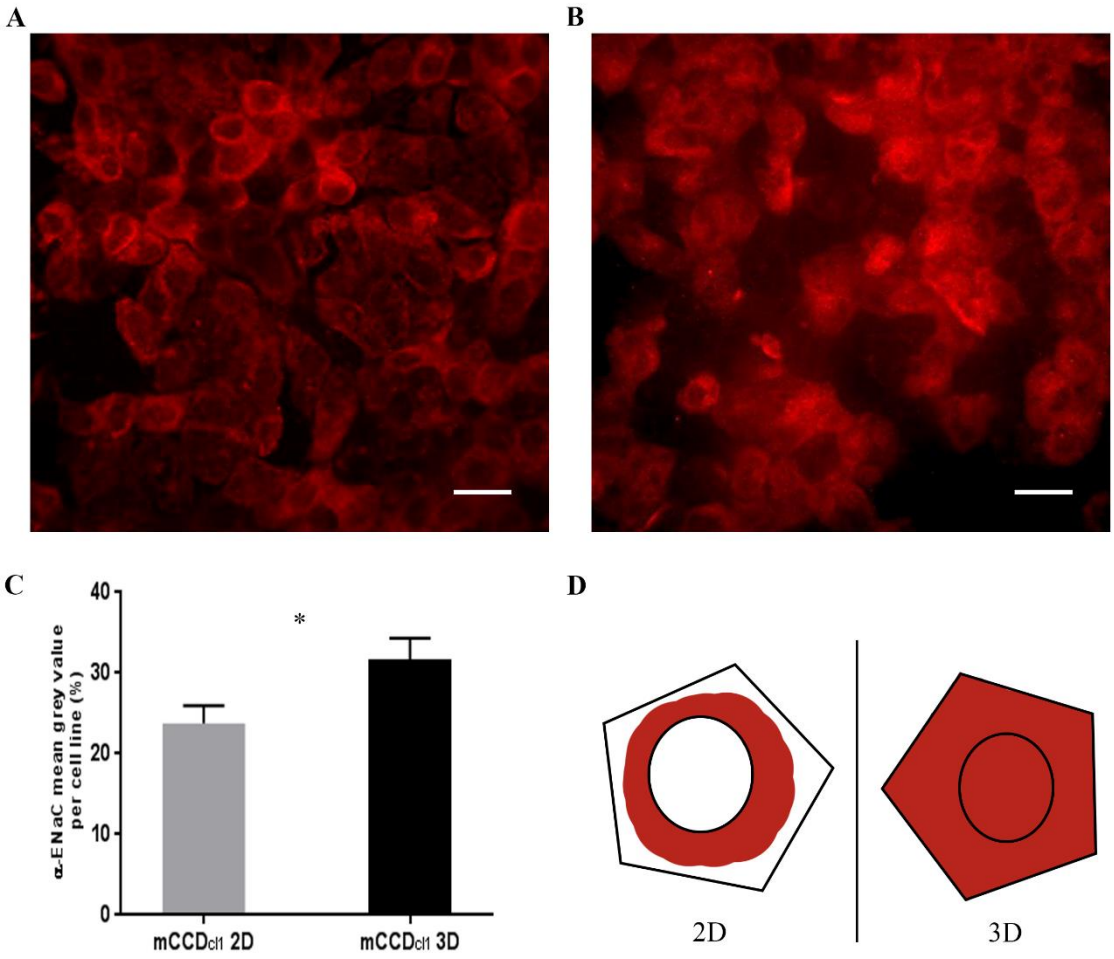

Figure 7.8. Comparison of ENaC expression and distribution in mCCD$_{cl1}$ cells cultured on flat membranes and on polyHIPEs. (A) Representative image of immunocytochemistry staining (red) of α-ENaC on mCCD$_{cl1}$ cells cultured on porous membrane. Scale bar 20µm. (B) Representative image of immunocytochemistry staining (red) of α-ENaC on mCCD$_{cl1}$ cells cultured on polyHIPEs scaffold. Scale bar 20µm. (C) Mean grey value per cell line showing different expression levels of α-ENaC in mCCD$_{cl1}$ in a 2D (porous membrane) *vs* 3D (polyHIPEs) environment (n=4). (D) Simplified schematic representation of ENaC distribution (red) in mCCD$_{cl1}$ cells cultures in 2D *vs* 3D environments, as seen on (A) and (B). Polygonal shape represents cell boundaries. Circular shape represents the cell nucleus.

7.4.2 $mCCD_{cl1}$ cell shape

The shape of $mCCD_{cl1}$ cells can be viewed using the spinning disc confocal microscopy orthogonal projection imaging of cells on polyHIPEs (Figure 7.7) and the orthogonal projection imaging of cells on porous membranes (Figure 4.3, Section 4.2.2). While $mCCD_{cl1}$ on membranes possessed a flattened cobblestone shape, cells on polyHIPEs appear to have a level apical membrane, that doesn't flatten around the nuclei (Figure 7.9.A). Measurement of $mCCD_{cl1}$ cells depth in both conditions showed a significant difference is depth, 7.5 ± 1.1 µm for cells cultured in 2D (porous flat membranes) against 20.2 ± 2.5 µm for cells cultured in 3D (polyHIPEs disks) (Figure 7.9.B).

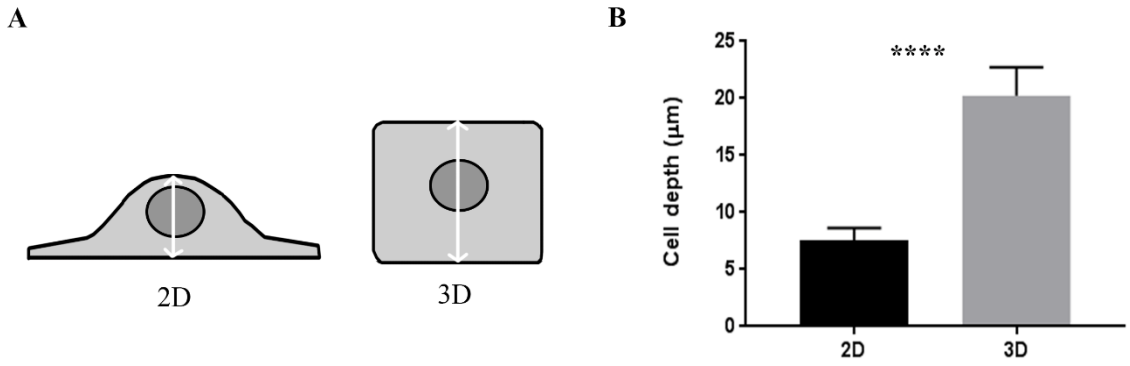

Figure 7.9. mCCDcl1 cultured on polyHIPEs scaffold have different shape and size. (A) Schematic views of mCCDcl1 shapes on porous membranes (2D) and polyHIPEs scaffold (3D). White arrows correspond to cell depth. (B) Cell depth measured on confocal images of mCCDcl1 culture in 2D or 3D (n=20).

7.5 Discussion

7.5.1 Chapter summary

A protocol was developed for the culture of $mCCD_{cl1}$ cells on polyHIPEs, first on isolated samples, then on printed half-tubes integrated in IFCs. This protocol involved extensive washing and rehydration steps to eliminate toxic elements and allow for better cell attachment. $mCCD_{cl1}$ cells seeded on 3D scaffolds exhibited satisfactory attachment and proliferation, and a greatly improved lifespan of six weeks or more without passaging compared to cells cultured in "classic" conditions. $mCCD_{cl1}$ showed a clear polarized phenotype, with ENaC expression on their apical membrane, and a greater level of expression compared to cells cultured on porous flat membranes. ENaC expression also appeared to be distributed more evenly across the cells apical membrane. Finally, the cells exhibited a different shape and a greater depth when cultured in a 3D environment compared to 2D cultures.

7.5.2 Discussion

7.5.2.1 Troubleshooting: rehydration, toxicity

The protocol for $mCCD_{cl1}$ cell culture on polyHIPEs was established after several failures. Crosslinker and surfactant were found to be extremely toxic to cells, as well as the support material used for the 3D printing of the IFCs, leading to extensive washing using ethanol baths. Cells would not attach on scaffolds that were not properly rehydrated. Without a proper preparation protocol, PolyHIPEs appeared extremely water-repellent. After rehydration however, $mCCD_{cl1}$ cells showed a great affinity for the scaffold, without preliminary extra-cellular matrix (ECM) coating, potentially

establishing polyHIPEs as a good "neutral" 3D scaffold allowing cells to create their own ECM.

7.5.2.2 $mCCD_{cl1}$ lifespan and shape

The increased lifespan of $mCCD_{cl1}$ cells without passaging was the first and most remarkable characteristic of cell culture on polyHIPEs. $mCCD_{cl1}$ in flasks typically need passaging every 5 to 7 days to avoid over-proliferation and apoptosis. The cells typically detach from the flask in clumps, starting with the doming areas. On polyHIPEs scaffold however, the cells survived up to 6 weeks, maybe up to 8 weeks (only observed using brightfield microscopy on scaffold borders). The viability may be even higher, as the experiments were stopped for time management purposes and not because of cell apoptosis. Over-proliferation such as vertical growing was never observed on polyHIPEs scaffold, contrary to culture on porous membrane, where confocal microscopy images (not presented) regularly showed pile-ups of cells after 10 days in culture. Lifespan improvement in this study follows reports of improvements with a vast range of cell types cultured on scaffolds compared to classic cell culture conditions [188]. Cell shape greatly differed between $mCCD_{cl1}$ cells cultured in classic conditions or on polyHIPEs, with a cell depth more than doubled, from ~7.5µm to ~20µm respectively. The ENaC staining appeared flat on the apical membrane, suggesting a cuboidal cell shape typical of kidney epithelia, and a greater cell-cell surface compared to classic culture. Cell shape could be further characterized using immunocytochemistry of tight junctions.

7.5.2.3 Imaging options

Considering that $mCCD_{cl1}$ cells form a monolayer cultured on the surface of the polyHIPEs scaffold, the imaging options were limited by the distance between objective and cells, which is a parameter to consider when the cells are growing in a half-tube with

an supra-physiological diameter. The use of polyHIPEs also meant the need for fluorescent reporters and consequent imaging set-up, as the cells could not be directly observed through or on the opaque material. For this project, two different confocal microscopes, a multiphoton, and an epifluorescence microscope were used. The multiphoton microscope gave excellent results for observing the surface of the polyHIPEs using both the material and cell auto-fluorescence properties. This microscope offered a convenient way to observe cell attachment without any preliminary treatment with fluorescent reporters, as well as scaffold surface properties. The best results for observing the cells with a high magnification were obtained with the spinning disc confocal microscope, that allowed rapid imaging of $mCCD_{cl1}$ cell volume. The time scale for a complete z-stack, around 20 seconds, would permit good real-time imaging of eventual changes in phenotypes in live cells.

7.5.3 Conclusion

$mCCD_{cl1}$ cells attached and grew on polyHIPEs scaffold, and exhibited improved lifespan, morphology, and ENaC expression levels and distribution compared to cells cultured in classic conditions. These findings establish polyHIPEs as a viable option for the study of a 3D model of collecting duct using $mCCD_{cl1}$ cells. These results also open the possibility for collecting duct development and cell determination studies in 3D conditions, as well as the study of environmental effects on cell expression and determination.

8 Discussion

8.1 Summary

In this thesis I aimed to characterize $mCCD_{cl1}$ cells in different environments, for the development of an in vitro 3D model of the collecting duct. Using immunocytochemistry, RNA-Sequencing, and electrophysiological methods, I have demonstrated that the $mCCD_{cl1}$ cells are not solely a principal cells line as previously described, but present the characteristics of cells in transition between PCs and ICs. Using single-cell cloning, I have shown that $mCCD_{cl1}$ cells have the ability to vertically transmit a bi-potential phenotype to clonal lines, and present precursor-like characteristics. These discoveries have important consequences for any researchers currently using $mCCD_{cl1}$ cells as a principal cell line, and also open the possibility for the study of collecting duct cell determination and differentiation mechanisms.

Using 3D-printing of porous polymers, I have developed a 3D culture environment for $mCCD_{cl1}$ cells. I have shown that the cells were able to attach and grow on that scaffold, lived longer that in "classic" culture conditions, and presented different morphology, closer to the *in vivo* collecting duct monolayer.

This thesis has established the $mCCD_{cl1}$ cell line as an excellent model for the study of collecting duct cells determination and physiology, and shown the advantages of a 3D culture environment for these cells.

8.2 General observations about $mCCD_{cl1}$ cell line

This study reveals morphological differences between cells cultured *in vitro* and cells *in vivo*. EM images of collecting ducts show that cells have a distinct epithelial cobblestone shape with clear intercellular surface and membranes protein (e.g. tight junctions, connexins) [77]. In culture (flask or filters), the cells had a flattened shape, reducing the intercellular surface area. The culture conditions and cell morphology are important factors that should be taken into consideration when using $mCCD_{cl1}$ cells. Whilst cell-cell interactions and communication through cell junctions are not directly the subject of this study, they have been repeatedly shown to be essential for physiological relevance, and functionality of an epithelium. Tight junctions control paracellular permeability, and serve as barrier to intramembrane diffusion of components between apical and basolateral membranes [189], [190]. Gap junction components such as connexins have been shown to have a role in cell polarization [191], but evidence for intercellular connexins is lacking in the collecting duct, where like for Cx30, only apical hemichannels were detected [192].

Another important observation was the presence of "latent" cells, observed in all the cell lines described here either in flasks or on filters. An important subset of cells did not stain for the markers studied. For example, within the domes, only 2 or 3 cells per dome expressed Aqp2, and approximately only a third of the cells expressed ENaC. On filters, more cells expressed at least one of the markers, which showed the importance of culture environment. The expression level also depended on the clonal cell line, which indicates a complex mix of environmental and inherent factors for cell differentiation and determination.

Interestingly, the cells staining for PC- or IC-markers also expressed progenitor markers. It is possible that these cells were caught in transition at the moment of the staining, and that the "activation" of one progenitor pathway has a domino effect on the activation of other pathways, leading to the expression of a range of different markers.

8.3 $mCCD_{cl1}$ cells: in transition

8.3.1 $mCCD_{cl1}$ cells display bi-potential characteristics

The immunocytochemistry results showed that markers for both cell types were co-expressed in a significant portion (~42%) of the cell population and that the cell line is not simply a mixed population of differentiated PCs and ICs. The preponderance of cells expressing both PC and IC markers was also evident for the clonal sub-lines, thereby reinforcing the conclusion that this is an intrinsic property of $mCCD_{cl1}$ cells.

At the population level, my electrophysiological data show that $mCCD_{cl1}$ cells exhibited the expected transport characteristics of PCs, however the immunocytochemistry and RNA-Seq data suggest that results from the functional data cannot be extrapolated to the behaviour of individual cells.

Electrophysiological measurements from the parental $mCCD_{cl1}$ cell line gave results comparable to previous studies, including a 3.8 ± 0.2 fold change in I_{sc} following treatment with physiological concentration of aldosterone [62]. This response was due to an increase in Na^+ reabsorption via ENaC, but the amiloride-insensitive I_{sc} demonstrates that a portion of the current is due to other electrogenic transport. Indeed, application of $BaCl_2$ inhibited part of the remaining current (personal communication, data not shown), indicating K^+ secretion, likely via ROMK. Our data show that $mCCD_{cl1}$ cells, widely used

as representative of PCs for electrophysiology studies, expressed significant levels of IC markers. It is therefore possible that H^+ secretion via the apical V-ATPase in β-ICs may contribute to the remainder of the amiloride-insensitive I_{sc}.

The presence of IC-specific transporter transcripts (for example the Na^+/H^+ exchanger (NHE3), NKCC1 [64], or H^+/K^+ ATPase [26]) suggests the possibility of IC-specific electroneutral ion transport. Such ion transport mechanisms would not be detectable in our electrophysiology measurements.

The ability of $mCCD_{cl1}$ cells to display differentiated characteristics of both PC and IC cells is reminiscent of the bi-potential of cell lines such as HepaRG [193]. In addition to expressing genes characteristic of ICs and PCs our RNA-seq data showed the expression of progenitor markers. The $mCCD_{cl1}$ cell line originated from a confluent primary culture of micro-dissected CCDs as a clone that spontaneously continued to divide in culture. Its capacity for generating both IC- and PC-like cells suggests that the immortalisation event(s) occurred in a bi-potential precursor cell resident in the CCD.

The fact that the cell line was isolated from the adult tissue raises important questions regarding the potential for continuous physiological plasticity of the CCD in vivo. Further, the data provide evidence for the inter-relationship between these two anatomically co-localised cell types, however the details of this relationship cannot be determined from our present studies. Interestingly, the expression of p63 in particular hints at the pluripotent nature of the $mCCD_{cl1}$ cell line, and the potential for the line to be used as a model for differentiation and determination studies.

8.3.2 Transmission of both PC and IC characteristics to clonal sublines shows cell plasticity

Subclones of subclones: After the first results on the clonal sublines (Ed1, Ed2 and Ed3), new clonal lines (Ed1.1 and Ed2.1) were established using the sub-clones as parental lines, in order to further eliminate the possibility of contamination by other cells during the cloning process. These "subclones of subclones" were grown on glass coverslips for imaging purposes and stained using anti-Aqp2 (green) and anti-Cx30 (red) antibodies (Figure 8.1), as described in Section 4.2.1 for the parental $mCCD_{cl1}$ cell line. The results, identical to the first generation of clonal lines with staining for both markers, confirmed the vertical transmission of bi-potential characteristics over 2 generations of clones and eliminated the doubt of contamination in the clonal lines that were selected for further studies.

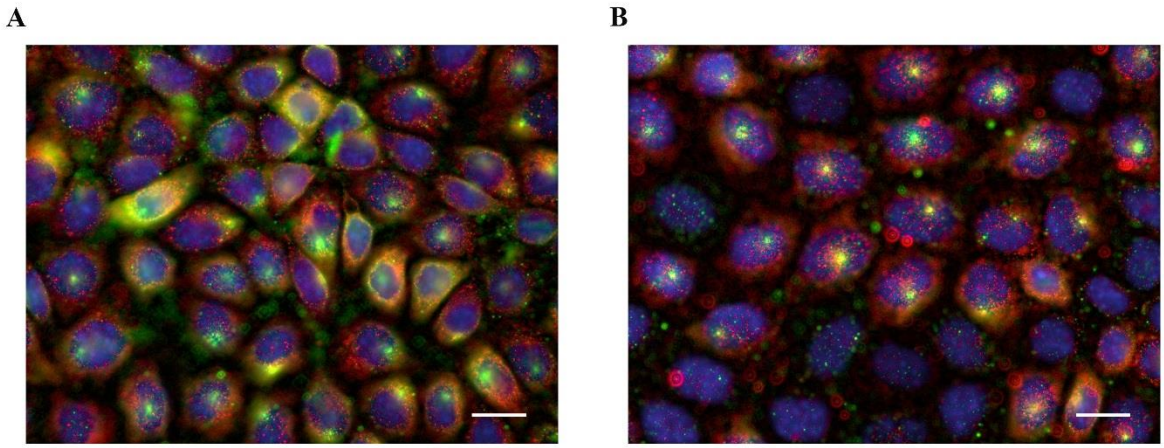

Figure 8.1. Immunostaining of Ed1.1 and Ed2.1 cultured on glass slides using anti-Aqp2 and anti-Cx30 antibodies. (A) Immunostaining for Aqp2 (green) and Cx30 (red) across Ed1.1. (B) Immunostaining for Aqp2 (green) and Cx30 (red) across Ed2.1. DAPI staining of cell nuclei in both images. Scale bar 15µm.

Plasticity: Plasticity of the $mCCD_{cl1}$ cells was confirmed by the data obtained from the $mCCD_{cl1}$ sub-lines following single cell cloning. The nature of the PC^{+}/IC^{+} cells could be described as bi-potential or displaying an 'immature' phenotype characteristic of precursor cells. There is evidence for cells transitioning from α to β-IC and from IC to PC in vitro [78], [194] but data on our clonal $mCCD_{cl1}$ sublines suggests a substantial degree of plasticity rather than unidirectional differentiation. The in vivo studies on Adam10 by Guo et al [25] confirms the existence of factors influencing the fate and ratio of collecting duct IC and PC cells through the Notch signalling pathway. They also showed that expression of Foxi1, which is important in the differentiation of IC cells, was altered, supporting the case for the maintenance of collecting duct cell plasticity in vivo. Ambiguous cell types ("hybrids") were observed by Wu et al. [79], where Dot1l deletion resulted in a ~15% rise in the number of ICs, seemingly derived from $Aqp2^{+}$ cells. In the same manner, ambiguous non-α non-β ICs have been observed and are speculated to be caught in a process of transition between α and β [26].

The RNA sequencing of $mCCD_{cl1}$ populations and the sublines confirmed the heterogenous characteristics of the clones by showing clear differences in expression between the lines. Whilst RNA expression is a good indicator of general transcriptional conditions in a cell population, it does not necessarily translate to protein concentration or function, but provides important evidence for the heterogeneity of the $mCCD_{cl1}$ cell population. These data suggest that studies using $mCCD_{cl1}$ cells should take account of the mixed nature of their phenotype and the influence that cell line composition may have, particularly when measuring the response of a population of cells as a whole, e.g. electrophysiological experiments. The precise culture conditions may affect cell phenotype to a greater or lesser extent and may, in part, explain variability between experiments.

8.3.3 The clonal cell lines maintain their characteristics through passaging.

The argument that the $mCCD_{cl1}$ cell line represents a precursor-like state is supported by the fact that the individual sub-lines maintain a stable sub-line-specific distribution of cell types and electrophysiological properties for a minimum of four passages. Whether, after prolonged passaging, the sub-lines would revert to a common distribution of cell types and electrophysiology closer to that of the parental $mCCD_{cl1}$ cells, is unknown. The general observation with $mCCD_{cl1}$ cells is that too many passages cause the cells to lose their specialized functions altogether, a common phenomenon with immortalized cell lines [195], [196]. An eventual reversal of clonal lines to parental phenotype would then be difficult to observe if it happens over a long time period.

The mechanism through which the sub-lines maintain their differences over passages is unclear but may reflect epigenetic differences, for example methylation status. It is clear that measurements of certain phenotypes, such as the electrophysiological characteristics reported here, are based on the population of cells as a whole and yet the characteristics of individual cells making up the populations vary widely both within, and between, independent sub-lines derived originally from single cells. This raises interesting questions regarding the gene expression profile across a population of cells versus individual cells, and whether neighbouring cells, and the local environment, influence that expression.

8.3.4 The clonal cell lines show different compositions

It is impossible retrospectively to determine the nature of the single cells that gave rise to each sub-line, and they may have originated from any of the PC^+/IC^-, PC^-/IC^+,

PC^+/IC^+, or PC^-/IC^- $mCCD_{cl1}$ cells from the parental population. However, following cloning they each gave rise to progeny that included all four phenotypic groups. We can speculate that all three sub-lines may have arisen from PC^+/IC^+ cells and that only these cells have the capacity to produce progeny of all four classes. From the present study, there is no evidence to prove that this is the case and it does not alter the conclusions that $mCCD_{cl1}$ cells have bi-potential, display a spectrum of phenotypes from IC-like cells to PC-like cells, and that this potential can be transmitted vertically via a single cell. Prospective isolation of single cells of each class may enable further insights into the potential for differentiation of $mCCD_{cl1}$ cells, as would further investigation of the Notch pathway.

In vivo, ICs and PCs cells are clearly distinct. However, collecting ducts in vivo are in a highly regulated environment [27], [197], constantly under the influence of physiological factors that may be the key to keeping cells in a fully differentiated, more stable state. In this work, the correlation between the expression of V-ATPase A1 and the absence of acetylated α-tubulin could be used to identify cell types, but also suggests that the cells are structurally distinct, and that acetylation could be an important factor for the determination of CCD cell type.

8.3.5 The immunocytochemistry results are consistent with the electrophysiological measurements

The presence of PC^+/IC^+ cells was transmitted through single cells of the parental $mCCD_{cl1}$ line to Ed1, Ed2, and Ed3, although in different proportions. The comparison of electrophysiological and immunocytochemistry data suggests that the composition of each cell line parallels their function. One might expect that a higher proportion of ENaC-

expressing cells would result in higher Na^+ transport, however the presence of dual-staining cells complicates the picture. The parental cell line and Ed1 have a comparable proportion of cells expressing ENaC, but V-ATPase B1 is expressed in a greater number of Ed1 cells correlating with lower R_{te} and V_{te} values than in the parental line. A similar relationship between phenotype and function was observed for Ed2 and Ed3. The particularly small R_{te} measured for Ed2 may be the result of a transitioning or undifferentiated state during which cells lose, or have not established, features such as tight junctions.

8.4 PCs and ICs in disease state

Studies using gene knockout mice reported changes in the proportion of ICs and PCs or the existence of "hybrid" cells [79]. Genetic models of kidney disease such as the syndrome of apparent mineralocorticoid excess (SAME) [169] may be informative for understanding the factors influencing collecting duct cell plasticity, through the observation of the CCD cellular response to induced transport modifications, for example the impaired Na^+ transport by ENaC in SAME. Whilst the consequences of common kidney diseases on sodium transport in the collecting duct are well documented, no specific data has been reported regarding the relative number of PCs and ICs, even though the ratio can affect renal fluid homeostasis.

Preliminary data showed a clear difference between WT and KO, and a trend towards de-differentiation or worsening of the disease with age, with a significant increase in dual-staining/mixed cells between 30 and 120 days in KO mice. The experiment would benefit from a repeat with a larger n number, and looking at different species.

The observation of kidney tubules in real time under changing conditions such as drug treatment, acidosis, or sodium intake, could be a useful tool for recording functionally relevant shift between PCs and ICs in vivo.

8.5 Future directions: further characterization and studies of $mCCD_{cl1}$ cells

8.5.1 Available techniques

The first technique that comes to mind for the general characterization of the $mCCD_{cl1}$ cell population is flow cytometry, that would in theory present a quantified distribution of cell types over a large population of $mCCD_{cl1}$ cells, and the possibility for cell sorting [198]. In practice, the cells would need specific antibodies for PC and IC markers, targeting extracellular epitopes. For PCs, Aqp2 or ENaC would be the obvious markers but ENaC is mostly an intracellular protein, and no result was found from an antibody search for Aqp2. Antibodies for ICs also prove difficult to obtain.

The answer to a lack of appropriate antibody is to create transgenic $mCCD_{cl1}$ cells, expressing fluorescent reporters linked to PC and IC specific markers. However, karyotyping of $mCCD_{cl1}$, Ed1, Ed2, and Ed3 (Figure 8.2) showed that the cells were either triploid (60 chromosomes) or quadriploid (80 chromosomes). Both configurations were found in parental $mCCD_{cl1}$ and clonal sublines. No cells were found with the expected number of chromosomes (40 chromosomes).

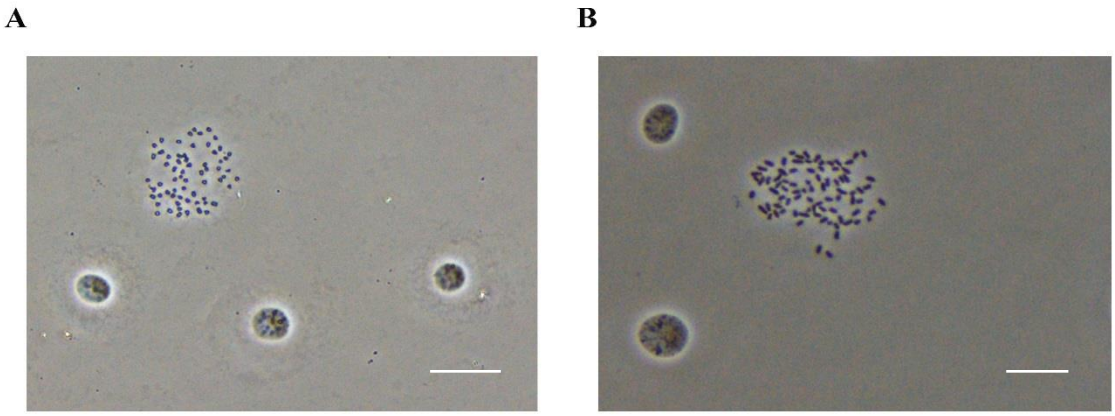

Figure 8.2. Karyotype of $mCCD_{cl1}$ and subclones shows polyploidy. (A) $mCCD_{cl1}$ opened nucleus presents 60 chromosomes. Three intact nuclei are also visible. Scale bar 20µm. (B) Ed1 opened nucleus presents 80 chromosomes. Two intact nuclei are also visible. Scale bar 10µm.

The polyploidy of $mCCD_{cl1}$ cells raises additional questions. Polyploidy, and self-renewal, are associated to cancer cells, and immortalized cell lines in general [199]. This characteristic has not been reported for $mCCD_{cl1}$ before, and has important implications such as the possibility of nonlinear transcriptome changes, which increases cellular heterogeneity through the under or over-replication of specific genome regions [200]. While polyploidy is generally the consequence of environmental stresses, it induces a higher stress tolerance for the cell line. Genetic manipulation is in general challenging in polyploid cells due to gene redundancy, but the solution could be to use CRISPR-Cas9 gene-editing, which has been shown to be highly efficient in a range of polyploid organisms [201], [202].

Single-cell RNA-Seq is another technique to consider for $mCCD_{cl1}$ cells. Typically in single cell RNA-Seq experiments, cells isolated from a population (after sorting using cytometry for example) count as technical repeats [203]. However, $mCCD_{cl1}$ cells are likely to each give different results because of their transitioning nature, which can be clustered according to similarities in transcript profiles. Single cell RNA Seq stays a useful tool in

the characterisation of collecting duct cell types, and has been conducted on α-ICs, β-ICs, and PCs isolated from mouse kidneys [204]. The work of Chen *et al* (2017) on isolated mouse collecting ducts created a database of single-cell RNA-Seq data for each CCD cell type [167]. The analysis identified a small fraction of cells expressing both PC and IC specific markers. A specific analysis and in-depth characterisation of *in vivo* intermediate cells could provide information on transition factors and cell determination in the CCD. However, nothing is known yet about the stability of intermediate cells or the time it takes to switch from one cell type to the other, which makes isolation difficult. The choice of markers is also a challenge, as the cells could be "in transition" in different ways.

8.5.2 Notch signaling pathway and cell interdependence

The Notch signaling pathway has been a common theme in recent publications investigating collecting duct differentiation and determination mechanisms. Notch is involved in the regulation of expression of the Foxi1 transcription factor, that activates expression of IC-related genes [205], [206], and its inactivation leads to the detection of cells in transition between PC and IC [61]. Expression of other Notch regulation factors such as Adam10 and Mib1 lead to cell differentiation into PCs in developing collecting ducts [25], [73]. In the early kidney, other Notch signaling pathway components such as Elf5, RBPJ or Presinilin 1 and 2 are involved in collecting duct cell patterning and differentiation, and are generally markers of PC lineage [207]. The triggered over-expression of Notch in $mCCD_{cl1}$ cells could lead to the shift to a pure principal cell line and offer information on CCD cell differentiation and determination without animal use.

The eventual creation of a pure population of principal cells also raises the question of interdependence between PCs and ICs. Can a pure PC population be maintained? Can a

pure IC population exist? Inter-regulation between the two cells types has been mentioned before. For other cell types, interdependence has been demonstrated, and has led to the development of an interdependence theory of tissue failure [208]. Development of models of cell patterning [209] suggests that punctate patterning of cells such as the "salt and pepper" pattern observed in the CCD, is linked to cell type interdependence. Finally, CCD cells were shown to express specific receptors and their ligands in different cells types, suggesting important signaling cross-talk [167].

8.6 $mCCD_{cl1}$ cells on 3D scaffolds

8.6.1 Microfluidics and the development of an "all-in-one" device

Development of the IFC was necessary for the sealing of the polyHIPEs half-tube and the convenient manipulation and imaging of the cells. However, the development of a more automated process seems necessary. Integration of half-tubes and assemblage were made by hand and required days to produce functional devices. Microfluidics production uses a variety of techniques from PDMS modelling by photolithography [95] to laser ablation [210], and offer a large range of possible designs. Requirements for kidney cells culture, integration of 3D scaffolds, and imaging complicate the picture, and manufactured devices that allow for flow, 3D culture, and easy imaging have yet to be created. However, the field is rapidly evolving an tend towards biomimicking devices [211], [212]. This study offers a step towards understanding requirements for that type of "organ-on-a-chip".

Differences between 2D and 3D cell cultures have been mentioned before. They mostly concern lifespan, proliferation [213], protein and gene expression changes, and sensitivity to drugs [184], all suggesting an improved mimicking of *in vivo* conditions compared to

cells in classic culture conditions. Access to nutrients is a concern for thick engineered tissues, as cells in general need to be situated less than 200µm away from vascularization to survive [214], but in the case of simple monolayers of cells, the problem doesn't arise. One of the main uses of "organs-on-a-chip" is to reduce the number of in vivo studies (and animal use) and offer tailored solutions to scientific hypothesis. The device developed in this study allows for an in-depth characterization of the $mCCD_{cl1}$ cell line in biomimicking conditions, and for the eventual study of CCD development and cell type determination processes by combining long term 3D culture, flow system, and easy imaging.

8.6.2 Imaging challenges in 3D structures

Imaging of 3D constructs and scaffolds present challenges, mostly avoided in this project due to the monolayer nature of $mCCD_{cl1}$ cells, sitting on the surface of the scaffold. However more complex structures, full tubes, or different cell types that could be cultured inside the polyHIPEs structure (with greater pore sizes allowing for cellular penetration) will eventually require deep imaging. It is worth noting that in previous studies, regardless of pore size, osteoblast cellular penetration in polyHIPEs rarely exceeded 1mm, suggesting a limit for tissue thickness using this scaffold [215]. In the work of Owen *et al.* [146], 2-photon microscopy was used to image hES-MP cells that penetrated as deep as 20 µm in a similar polyHIPEs scaffold, with the scaffold auto-fluorescence detectable about 50µm deep, far from the 300µm+ thickness of the polyHIPEs tube walls used in this project. Multiphoton microscopy is the usual technique for deep tissue imaging, due to the use of longer wavelengths, that are less scattered by tissues than short wavelengths and can therefore penetrate deeper [216]. However, most 2-photon microscopes have a maximal imaging depth of around 500µm depending on the tissue's light scattering and absorption

characteristics. Multiphoton imaging of the scaffold with a Ti:Sapphire 860 µm excitation laser in this project allowed for imaging of polyHIPEs scaffold up to about 30µm deep, still a long way from the required depth. Recent developments in multi-photon imaging, involving excitation laser amplification or adaptive optics (shaping of the wavefront of excitation light), achieved imaging depths of 1mm and 700µm respectively in high-scattering tissues [217], [218]. Longer wavelength sources also showed promising results, with imaging depth up to 1.6mm [219], [220]. However, since imaging results are dependent on tissue properties, an in-depth characterization of polyHIPEs scaffolds for imaging is needed, as well as adapted fluorophores.

8.6.3 Development of a 3D in vitro model of kidney structures: lessons from previous studies and future directions

3D tissue engineering constantly has to find a balance between biological requirements and practical matters such as mechanical strength, elasticity, bio-compatibility and scaffold resistance to degradation. As mentioned before, hydrogels often offer good biocompatibility because of their adaptable composition, but poor mechanical strength and resistance [184]. Hard scaffold such as polyHIPEs or electrospun fibers are difficult to image but offer a variety of possibilities for elasticity and strength, and appear biocompatible. Another approach for engineered kidney tissue is to use decellularized tissue [221]. The technique consists of washing away the cells of a kidney to keep the extra cellular matrix and has produced scaffolds able to sustain embryonic stem cells [222]. However, the scaffold has been shown to be mechanically weak and difficult to maintain in 3D [223]. In general, considering the complexity of the renal system, a tailored solution has to be thought out for every project: what part of the kidney is being studied,

what are the environmental conditions in this segment, what is the hypothesis? Whole kidney engineering and CCD engineering will use different techniques and approaches.

For example, transport functions of the CCD are enabled through the kidney vascularization system, with blood capillaries running alongside the collecting system. A step toward a more complex *in vitro* collecting duct system would be the co-culture of $mCCD_{cl1}$ cells with vascular endothelial cells and the development of a complete transport and filtration system comparable to the *in-vivo* CCD. In previous studies, co-culturing endothelial cells with proximal tubule epithelial cells has shown to enhance *in vivo*-like epithelial function [149], [150], [224]. The development of thicker, more complex biological structures could be obtained by using biodegradable polymers such as polylactic acid (PDLA) as cell culture scaffolds. In theory, these scaffolds dissolve after the growth and strengthening of the biological tissue cultured on or inside, leaving only a 3D living tissue of the desired shape. In practice, degradable polymers break into potentially toxic bi-products, and cell-culturing schedule *versus* degradation schedule make these types of culture difficult [225].

Finally, an enhanced control and characterization of the $mCCD_{cl1}$ cells microenvironment such as the fine-tuning of polyHIPEs elasticity seems to be an unavoidable step for an effective *in vitro* system, especially considering the progenitor characteristics of the cell line. Microenvironment has been shown to be important in stem cell lineage specification: naive mesenchymal stem cells (MSCs) specified lineage and committed to phenotypes with extreme sensitivity to tissue elasticity [105]. Other studies have shown the importance of extracellular matrix in cell type determination and cell signalling [226], [227].

To conclude, in this work we have made a case for the use of $mCCD_{cl1}$ cells as a model for the study of cortical collecting duct physiology, differentiation, and cell determination.

3D-printed porous polymers were successfully used as a cell culture scaffold, with $mCCD_{cl1}$ cells showing promising results when cultured in this new environment. The combination of engineering and biological expertise may aid with the development of new and more accurate *in vitro* models for understanding collecting duct physiology.

References

[1] E. L. Schiffrin, M. L. Lipman, and J. F. E. Mann, "Chronic Kidney Disease: Effects on the Cardiovascular System," *Circulation*, vol. 116, no. 1, pp. 85–97, 2007.

[2] P. L. Kimmel and M. E. Rosenberg, "Chapter 1 - Introduction: Chronic Renal Disease BT - Chronic Renal Disease," San Diego: Academic Press, 2015, pp. 3–4.

[3] L. J. Mullins, M. a Bailey, and J. J. Mullins, "Hypertension, kidney, and transgenics: a fresh perspective.," *Physiol. Rev.*, vol. 86, no. 2, pp. 709–46, Apr. 2006.

[4] M. Tonelli, "Chronic Kidney Disease and Mortality Risk: A Systematic Review," *J. Am. Soc. Nephrol.*, vol. 17, no. 7, pp. 2034–2047, 2006.

[5] N. Tsuboi, G. Kanzaki, K. Koike, T. Kawamura, M. Ogura, and T. Yokoo, "Clinicopathological assessment of the nephron number," *Clin. Kidney J.*, vol. 7, no. 2, pp. 107–114, Apr. 2014.

[6] C. J. Lote, "Essential Anatomy of the Kidney BT - Principles of Renal Physiology," C. J. Lote, Ed. New York, NY: Springer New York, 2012, pp. 21–32.

[7] F. Morel and A. Doucet, "Hormonal control of kidney functions at the cell level," *Physiol. Rev.*, vol. 66, no. 2, pp. 377–468, 1986.

[8] D. Brown and J. L. Stow, "Protein trafficking and polarity in kidney epithelium: from cell biology to physiology.," *Physiol. Rev.*, vol. 76, no. 1, pp. 245–97, 1996.

[9] A. J. Vander, D. C. Eaton, and J. P. Pooler, *Renal physiology*, vol. 228. McGraw-Hill New York, 1995.

[10] C. R. Robertson, "A review of transcapillary fluid and solute exchange in the renal glomerulus," *Microvasc. Res.*, vol. 19, no. 2, pp. 131–141, 1980.

[11] B. Haraldsson, J. Nyström, and W. M. Deen, "Properties of the Glomerular Barrier and Mechanisms of Proteinuria," *Physiol. Rev.*, vol. 88, no. 2, pp. 451–487, Apr. 2008.

[12] M. J. Peach, "Renin-angiotensin system: biochemistry and mechanisms of action.," *Physiol. Rev.*, vol. 57, no. 2, pp. 313–370, Apr. 1977.

[13] A. A. Mcdonough, "Mechanisms of proximal tubule sodium transport regulation that link extracellular fluid volume and blood pressure," *Am. J. Physiol.*, vol. 298, pp. 851–861, 2010.

[14] K. Kawahara, M. Hunter, and G. Giebisch, "Potassium channels in Necturus proximal tubule," *Am. J. Physiol. Physiol.*, vol. 253, no. 3, pp. F488–F494, Sep. 1987.

[15] J. P. Pennell, F. B. Lacy, and R. L. Jamison, "An in vivo study of the concentrating process in the descending limb of Henle's loop," *Kidney Int.*, vol. 5, no. 5, pp. 337–347,

1974.

[16] R. Greger, "Ion transport mechanisms in thick ascending limb of Henle's loop of mammalian nephron.," *Physiol. Rev.*, vol. 65, no. 3, pp. 760–797, Jul. 1985.

[17] M. A. Knepper, G. H. Kim, P. Fernández-Llama, and C. A. Ecelbarger, "Regulation of thick ascending limb transport by vasopressin," *J. Am. Soc. Nephrol.*, vol. 10, no. 3, pp. 628–634, 1999.

[18] A. R. Subramanya and D. H. Ellison, "Distal Convoluted Tubule," *Clin. J. Am. Soc. Nephrol.* , May 2014.

[19] P. San-Cristobal, D. Pacheco-Alvarez, C. Richardson, A. M. Ring, N. Vazquez, F. H. Rafiqi, D. Chari, K. T. Kahle, Q. Leng, N. a Bobadilla, S. C. Hebert, D. R. Alessi, R. P. Lifton, and G. Gamba, "Angiotensin II signaling increases activity of the renal Na-Cl cotransporter through a WNK4-SPAK-dependent pathway.," *Proc. Natl. Acad. Sci. U. S. A.*, vol. 106, no. 11, pp. 4384–9, 2009.

[20] C. A. Cuevas, X.-T. Su, M.-X. Wang, A. S. Terker, D.-H. Lin, J. A. McCormick, C.-L. Yang, D. H. Ellison, and W.-H. Wang, "Potassium Sensing by Renal Distal Tubules Requires Kir4.1," *J. Am. Soc. Nephrol.*, vol. 28, no. 6, pp. 1814–1825, 2017.

[21] I. Rubera, J. Loffing, L. G. Palmer, G. Frindt, N. Fowler-jaeger, D. Sauter, T. Carroll, A. Mcmahon, E. Hummler, and B. C. Rossier, "Collecting duct–specific gene inactivation of αENaC in the mouse kidney does not impair sodium and potassium balance," *J. Clin. Invest.*, vol. 112, no. 4, 2003.

[22] B. Kaissling and W. Kriz, "Structural Analysis of the Rabbit Kidney.," *Physiol. Zool.*, vol. 53, no. 2, p. 240, Apr. 1980.

[23] P. Ford, V. Rivarola, O. Chara, M. Blot-Chabaud, F. Cluzeaud, N. Farman, M. Parisi, and C. Capurro, "Volume regulation in cortical collecting duct cells: role of AQP2.," *Biol. Cell*, vol. 97, no. 9, pp. 687–697, 2005.

[24] S. Sasaki, K. Fushimi, K. Ishibashi, and F. Marumo, "Water channels in the kidney collecting duct," *Kidney Int.*, vol. 48, no. 4, pp. 1082–1087, 1995.

[25] Q. Guo, Y. Wang, P. Tripathi, K. R. Manda, M. Mukherjee, M. Chaklader, P. F. Austin, K. Surendran, and F. Chen, "Adam10 Mediates the Choice between Principal Cells and Intercalated Cells in the Kidney.," *J. Am. Soc. Nephrol.*, pp. 1–11, 2014.

[26] A. Roy, M. M. Al-Bataineh, and N. M. Pastor-Soler, "Collecting duct intercalated cell function and regulation," *Clin. J. Am. Soc. Nephrol.*, vol. 10, no. 2, pp. 305–324, 2015.

[27] A. Staruschenko, "Regulation of transport in the connecting tubule and cortical collecting duct," pp. 1541–1584, 2013.

[28] S. Masilamani, G.-H. Kim, C. Mitchell, J. B. Wade, and M. A. Knepper, "Aldosterone-mediated regulation of ENaC α, β, and γ subunit proteins in rat kidney," *J. Clin.*

Invest., vol. 104, no. 7, pp. R19–R23, 1999.

[29] U. Hasler, D. Mordasini, M. Bens, M. Bianchi, F. Cluzeaud, M. Rousselot, A. Vandewalle, E. Féraille, and P.-Y. Martin, "Long Term Regulation of Aquaporin-2 Expression in Vasopressin-responsive Renal Collecting Duct Principal Cells," *J. Biol. Chem.* , vol. 277, no. 12, pp. 10379–10386, Mar. 2002.

[30] P. Flamenco, L. Galizia, V. Rivarola, J. Fernandez, P. Ford, and C. Capurro, "Role of AQP2 during apoptosis in cortical collecting duct cells.," *Biol. Cell*, vol. 101, no. 4, pp. 237–250, 2009.

[31] H. J. Jung, S.-Y. Kim, H.-J. Choi, E.-J. Park, J.-S. Lim, J. Frøkiaer, S. Nielsen, and T.-H. Kwon, "Tankyrase-mediated β-catenin activity regulates vasopressin-induced AQP2 expression in kidney collecting duct mpkCCDc14 cells," *Am. J. Physiol. - Ren. Physiol.*, vol. 308, pp. F473–F486, 2015.

[32] M. U. Cheema, D. L. Irsik, Y. Wang, W. Miller-Little, K. A. Hyndman, E. S. Marks, J. Frøkiær, E. I. Boesen, and R. Norregaard, "Estradiol regulates AQP2 expression in the collecting duct: a novel inhibitory role for estrogen receptor α," *Am. J. Physiol. - Ren. Physiol.*, vol. 309, no. 4, pp. F305–F317, 2015.

[33] S. W. Kim, V. Gresz, A. Rojek, W. Wang, a S. Verkman, J. Frøkiaer, and S. Nielsen, "Decreased expression of AQP2 and AQP4 water channels and Na,K-ATPase in kidney collecting duct in AQP3 null mice.," *Biol. Cell*, vol. 97, no. 10, pp. 765–78, 2005.

[34] M. a Knepper, J. B. Wade, J. Terris, C. a Ecelbarger, D. Marples, B. Mandon, C. L. Chou, B. K. Kishore, and S. Nielsen, "Renal aquaporins.," *Kidney Int.*, vol. 49, no. 6, pp. 1712–7, 1996.

[35] L. G. Palmer and O. S. Andersen, "The two-membrane model of epithelial transport: Koefoed-Johnsen and Ussing (1958).," *J. Gen. Physiol.*, vol. 132, no. 6, pp. 607–612, 2008.

[36] J. J. Grantham, M. B. Burg, and J. Orloff, "The nature of transtubular Na and K transport in isolated rabbit renal collecting tubules," *J. Clin. Invest.*, vol. 49, pp. 1815–1826, 1970.

[37] L. Palmer and G. Frindt, "Conductance and Gating of Epithelial Na Channels from Rat Cortical Collecting Tubule," *J. Gen. Physiol.*, vol. 92, no. July, pp. 121–138, 1988.

[38] A. Anantharam, Y. Tian, and L. G. Palmer, "Open probability of the epithelial sodium channel is regulated by intracellular sodium.," *J. Physiol.*, vol. 574, no. Pt 2, pp. 333–347, 2006.

[39] Z. Krozowski, J. A. MaGuire, A. N. Stein-Oakley, J. Dowling, R. E. Smith, and R. K. Andrews, "Immunohistochemical localization of the 11 beta-hydroxysteroid dehydrogenase type II enzyme in human kidney and placenta.," *J. Clin. Endocrinol. Metab.*, vol. 80, no. 7, pp. 2203–2209, 1995.

[40] G. Frindt, Z. Ergonul, and L. G. Palmer, "Surface expression of epithelial Na channel protein in rat

kidney.," *J. Gen. Physiol.*, vol. 131, no. 6, pp. 617–27, 2008.

[41] G. Frindt, S. Masilamani, M. A. Knepper, and L. G. Palmer, "Activation of epithelial Na channels during short-term Na deprivation.," *Am. J. Physiol. Renal Physiol.*, vol. 280, no. 1, pp. F112-8, 2001.

[42] O. Staub, I. Gautschi, T. Ishikawa, K. Breitschopf, A. Ciechanover, L. Schild, and D. Rotin, "Regulation of stability and function of the epithelial Na+ channel (ENaC) by ubiquitination," *EMBO J.*, vol. 16, no. 21, pp. 6325–6336, 1997.

[43] J. A. Schafer and S. L. Troutman, "cAMP mediates the increase in apical membrane Na+ conductance produced in rat CCD by vasopressin," *Am. J. Physiol. - Ren. Physiol.*, vol. 259, no. 5, p. F823 LP-F831, Nov. 1990.

[44] V. Bugaj, O. Pochynyuk, and J. D. Stockand, "Activation of the epithelial Na+ channel in the collecting duct by vasopressin contributes to water reabsorption," *AJP Ren. Physiol.*, vol. 297, no. 5, pp. F1411–F1418, 2009.

[45] R. A. Fenton, L. Brønd, S. Nielsen, and J. Praetorius, "Cellular and subcellular distribution of the type-2 vasopressin receptor in the kidney.," *Am. J. Physiol. Renal Physiol.*, vol. 293, no. 3, pp. F748–F760, 2007.

[46] J. A. Schafer, S. L. Troutman, and E. Schlatter, "Vasopressin and mineralocorticoid increase apical membrane driving force for K+ secretion in rat CCD," *Am. J. Physiol. - Ren. Physiol.*, vol. 258, no. 1, p. F199 LP-F210, Jan. 1990.

[47] S. C. Hebert, "An ATP-regulated, inwardly rectifying potassium channel from rat kidney (ROMK)," *Kidney Int.*, vol. 48, no. 4, pp. 1010–1016, Oct. 1995.

[48] W.-H. Wang and G. Giebisch, "Regulation of potassium (K) handling in the renal collecting duct," *Pflugers Arch.*, vol. 458, no. 1, pp. 157–168, 2009.

[49] G. Frindt and L. G. Palmer, "Effects of insulin on Na and K transporters in the rat CCD," *Am J Physiol Ren. Physiol*, vol. 302, no. 10, pp. F1227-33, 2012.

[50] P. R. Grimm and S. C. Sansom, "BK channels in the kidney," *Curr. Opin. Nephrol. Hypertens.*, vol. 16, no. 5, pp. 430–436, 2007.

[51] C. B. Woda, A. Bragin, T. R. Kleyman, and L. M. Satlin, "Flow-dependent K(+) secretion in the cortical collecting duct is mediated by a maxi-K channel," *Am. J. Physiol. Physiol.*, vol. 280, no. 5, pp. F786–F793, 2001.

[52] H. Liapis, M. Nag, and D. M. Kaji, "K-Cl cotransporter expression in the human kidney.," *Am. J. Physiol.*, vol. 275, no. 6 Pt 1, pp. C1432-7, 1998.

[53] C. S. Wingo, "Reversible chloride-dependent potassium flux across the rabbit cortical collecting tubule," *Am. J. Physiol. - Ren. Physiol.*, vol. 256, no. 4, p. F697 LP-F704, Apr. 1989.

[54] D. H. Ellison, H. Velazquez, and F. S. Wright, "Stimulation of distal potassium secretion by low lumen chloride in the presence of barium,"

Am. J. Physiol. - Ren. Physiol., vol. 248, no. 5, p. F638 LP-F649, May 1985.

[55] J. Amorim, M. Bailey, R. Musa-Aziz, G. Giebisch, and G. Malnic, "Role of luminal anion and pH in distal tubule potassium secretion.," *Am. J. Physiol. Renal Physiol.*, vol. 284, no. 2, pp. F381–F388, 2003.

[56] T. Y. Besschetnova, E. Kolpakova-hart, Y. Guan, J. Zhou, B. R. Olsen, and J. V Shah, "Identification of signaling pathways regulating primary cilium length and flow-mediated adaptation," *Curr.Biology*, vol. 20, no. 2, pp. 182–187, 2011.

[57] H. a Praetorius, "The primary cilium as sensor of fluid flow: new building blocks to the model. A review in the theme: cell signaling: proteins, pathways and mechanisms.," *Am. J. Physiol. Cell Physiol.*, vol. 308, no. 3, pp. C198-208, 2015.

[58] R. G. Bjaelde, S. S. Arnadottir, M. T. Overgaard, J. Leipziger, and H. A. Praetorius, "Renal epithelial cells can release ATP by vesicular fusion," *Front. Physiol.*, vol. 4 SEP, no. September, pp. 1–11, 2013.

[59] J. Kim, Y. H. Kim, J. H. Cha, C. C. Tisher, and K. M. Madsen, "Intercalated cell subtypes in connecting tubule and cortical collecting duct of rat and mouse.," *J. Am. Soc. Nephrol.*, vol. 10, no. 1, pp. 1–12, 1999.

[60] E. Almomani, S. Kaur, R. Alexander, and E. Cordat, "Intercalated Cells: More than pH Regulation," *Diseases*, vol. 2, no. 2, pp. 71–92, 2014.

[61] S. R. Blomqvist, H. Vidarsson, S. Fitzgerald, B. R. Johansson, A. Ollerstam, R. Brown, A. E. G. Persson, G. Bergström, and S. Enerbäck, "Distal renal tubular acidosis in mice that lack the forkhead transcription factor Foxi1," vol. 113, no. 11, 2004.

[62] P. Svenningsen, J. L. Burford, and J. Peti-Peterdi, "ATP releasing connexin 30 hemichannels mediate flow-induced calcium signaling in the collecting duct.," *Front. Physiol.*, vol. 4, no. October, p. 292, 2013.

[63] F. McCulloch, R. Chambrey, D. Eladari, and J. Peti-Peterdi, "Localization of connexin 30 in the luminal membrane of cells in the distal nephron.," *Am. J. Physiol. Renal Physiol.*, vol. 289, no. 6, pp. F1304–F1312, Dec. 2005.

[64] F. Leviel, C. A. Hübner, P. Houillier, L. Morla, S. El Moghrabi, G. Brideau, H. Hatim, M. D. Parker, I. Kurth, A. Kougioumtzes, A. Sinning, V. Pech, K. A. Riemondy, R. L. Miller, E. Hummler, G. E. Shull, P. S. Aronson, A. Doucet, S. M. Wall, R. Chambrey, and D. Eladari, "The Na + -dependent chloride-bicarbonate exchanger SLC4A8 mediates an electroneutral Na + reabsorption process in the renal cortical collecting ducts of mice," vol. 120, no. 5, pp. 1627–1635, 2010.

[65] J. Canonica, C. Sergi, M. Maillard, P. Klusonova, A. Odermatt, R. Koesters, D. Loffing-cueni, J. Loffing, B. Rossier, S. Frateschi, and E. Hummler, "Adult nephron-specific MR-deficient mice develop a severe renal PHA-1 phenotype," *Eur J*

Physiol, no. 468, pp. 895–908, 2016.

[66] J. A. Davies and M. G. Davey, "Collecting duct morphogenesis," *Pediatr. Nephrol.*, vol. 13, no. 6, pp. 535–541, 1999.

[67] L. Gewin, N. Bulus, G. Mernaugh, G. Moeckel, R. C. Harris, H. L. Moses, A. Pozzi, and R. Zent, "TGF-beta Receptor Deletion in the Renal Collecting System Exacerbates Fibrosis," *J. Am. Soc. Nephrol.*, vol. 21, no. 8, pp. 1334–1343, 2010.

[68] T. D. Piscione, T. Phan, and N. D. Rosenblum, "BMP7 controls collecting tubule cell proliferation and apoptosis via Smad1-dependent and -independent pathways.," *Am. J. Physiol. Renal Physiol.*, vol. 280, no. 1, pp. F19-33, 2001.

[69] K. Sainio, P. Suvanto, J. Davies, J. Wartiovaara, K. Wartiovaara, M. Saarma, U. Arumae, X. Meng, M. Lindahl, V. Pachnis, and H. Sariola, "Glial-cell-line-derived neurotrophic factor is required for bud initiation from ureteric epithelium.," *Development*, vol. 124, no. 20, pp. 4077–4087, 1997.

[70] O. F. P. Santos, E. J. G. Barros, X.-M. Yang, K. Matsumoto, T. Nakamura, M. Park, and S. K. Nigam, "Involvement of Hepatocyte Growth Factor in Kidney Development," *Developmental Biology*, vol. 163, no. 2. pp. 525–529, 1994.

[71] J. Aigner, S. Kloth, M. L. Jennings, and W. W. Minuth, "Transitional differentition patterns of principal and intercalated cells during renal collecting duct development," *Ep. Cell. Biol.*, no. 4, pp. 121–130, 1995.

[72] S. S. El-dahr, Y. Li, J. Liu, E. Gutierrez, K. S. Hering-smith, S. Signoretti, J. Pignon, S. Sinha, and Z. Saifudeen, "p63 + ureteric bud tip cells are progenitors of intercalated cells," vol. 2, no. 9, pp. 1–9, 2017.

[73] H. Jeong, U. S. Jeon, B. Koo, W. Kim, S. Im, J. Shin, Y. Cho, J. Kim, and Y. Kong, "Inactivation of Notch signaling in the renal collecting duct causes nephrogenic diabetes insipidus in mice," vol. 119, no. 11, 2009.

[74] Z. Xiao, L. Chen, Q. Zhou, and W. Zhang, "Dot1l de fi ciency leads to increased intercalated cells and upregulation of V-ATPase B1 in mice," *Exp. Cell Res.*, vol. 344, no. 2, pp. 167–175, 2016.

[75] Q. Al-Awqati, "Cell biology of the intercalated cell in the kidney," *FEBS Lett.*, vol. 587, no. 13, pp. 1911–1914, 2013.

[76] X. Gao, D. Eladari, F. Leviel, B. Y. Tew, C. Miro-Julia, F. H. Cheema, L. Miller, R. Nelson, T. G. Paunescu, M. McKee, D. Brown, and Q. Al-Awqati, "Deletion of hensin/DMBT1 blocks conversion of - to -intercalated cells and induces distal renal tubular acidosis," *Proc. Natl. Acad. Sci.*, vol. 107, no. 50, pp. 21872–21877, 2010.

[77] C. E. Myers, R. E. Bulger, C. C. Tisher, and B. F. Trump, "Human ultrastructure. IV. Collecting duct of healthy individuals.," *Lab. Invest.*, vol. 15, no. 12, p. 1921, 1966.

[78] G. Fejes-Tóth and A. Náray-Fejes-Tóth, "Differentiation of renal beta-

intercalated cells to alpha-intercalated and principal cells in culture.," *Proc. Natl. Acad. Sci. U. S. A.*, vol. 89, no. 12, pp. 5487–91, 1992.

[79] H. Wu, L. Chen, Q. Zhou, X. Zhang, S. Berger, J. Bi, D. E. Lewis, Y. Xia, and W. Zhang, "Aqp2-Expressing Cells Give Rise to Renal Intercalated Cells," *J. Am. Soc. Nephrol.*, vol. 24, no. 2, pp. 243–252, 2013.

[80] H.-P. Gaeggeler, E. Gonzalez-Rodriguez, N. F. Jaeger, D. Loffing-Cueni, R. Norregaard, J. Loffing, J.-D. Horisberger, and B. C. Rossier, "Mineralocorticoid versus glucocorticoid receptor occupancy mediating aldosterone-stimulated sodium transport in a novel renal cell line.," *J. Am. Soc. Nephrol.*, vol. 16, no. 4, pp. 878–891, Apr. 2005.

[81] M. K. Mansley, W. Neuhuber, C. Korbmacher, and M. Bertog, "Norepinephrine stimulates the epithelial Na^+ channel in cortical collecting duct cells via α_2-adrenoceptors," *Am. J. Physiol. - Ren. Physiol.*, vol. 308, no. 5, pp. F450–F458, 2015.

[82] W. B. Reeves and T. E. Andreoli, "Sodium chloride transport in the loop of Henle, distal convoluted tubule, and collecting duct," *Kidney Physiol. Pathophysiol.*, pp. 1333–1370, 2000.

[83] S. Boulkroun, D. Ruffieux-Daidié, J.-J. Vitagliano, O. Poirot, R.-P. Charles, D. Lagnaz, D. Firsov, S. Kellenberger, and O. Staub, "Vasopressin-inducible ubiquitin-specific protease 10 increases ENaC cell surface expression by deubiquitylating and stabilizing sorting nexin 3.," *Am. J. Physiol. Renal Physiol.*, vol. 295, no. 4, pp. F889-900, 2008.

[84] S. De Seigneux, V. Leroy, H. Ghzili, M. Rousselot, S. Nielsen, B. C. Rossier, P. Y. Martin, and E. Féraille, "NF-κB inhibits sodium transport via down-regulation of SGK1 in renal collecting duct principal cells," *J. Biol. Chem.*, vol. 283, no. 37, pp. 25671–25681, 2008.

[85] A. Mukherjee, Z. Wang, C. L. Kinlough, P. A. Poland, A. L. Marciszyn, N. Montalbetti, M. D. Carattino, M. B. Butterworth, T. R. Kleyman, and R. P. Hughey, "Specific Palmitoyltransferases Associate with and Activate the Epithelial Sodium Channel *," vol. 292, no. 10, pp. 4152–4163, 2017.

[86] H. Fodstad, E. Gonzalez-Rodriguez, S. Bron, H. Gaeggeler, B. Guisan, B. C. Rossier, and J.-D. Horisberger, "Effects of mineralocorticoid and K+ concentration on K+ secretion and ROMK channel expression in a mouse cortical collecting duct cell line.," *Am. J. Physiol. Renal Physiol.*, vol. 296, no. 5, pp. F966–F975, May 2009.

[87] Y. Li, H. Hu, J.-B. Tian, M. X. Zhu, and R. G. O'Neil, "Dynamic coupling between TRPV4 and Ca2+-activated SK1/3 and IK1 K+ channels plays a critical role in regulating the K+-secretory BK channel in kidney collecting duct cells," *Am. J. Physiol. - Ren. Physiol.*, vol. 312, no. 6, p. F1081 LP-F1089, Jun. 2017.

[88] Y. Li, H. Hu, M. B. Butterworth, J.

Bin Tian, M. X. Zhu, and R. G. O'Neil, "Expression of a diverse array of Ca2+-activated K+ channels (SK1/3, IK1, BK) that functionally couple to the mechanosensitive TRPV4 channel in the collecting duct system of kidney," *PLoS One*, vol. 11, no. 5, pp. 1–31, 2016.

[89] K. E. Britton, M. K. Nawaz, C. C. Nimmon, E. Mlodkowska, M. Carroll, T. Horne, and M. Granowska, "Total and Intrarenal Flow Distribution in Healthy Subjects: Technique, Acute Effects of Ibopamine and of Indoramin," *Nephron*, vol. 43, no. 4, pp. 265–273, 1986.

[90] N. Stathopoulos and J. Hellums, "Shear stress effects on human embryonic kidney cells in vitro.," *Biotechnol. Bioeng.*, vol. 27, pp. 1021–1026, 1985.

[91] W. Seiller and K. H. Gertz, "Single nephron filtration, luminal flow and tubular fluid reabsorption along the proximal convolution and the pars recta of the rat kidney as influenced by luminal pressure changes," *Pfl??gers Arch. Eur. J. Physiol.*, vol. 371, no. 3, pp. 235–243, 1977.

[92] D. W. Good, H. Velázquez, and F. S. Wright, "Luminal influences on potassium secretion: low sodium concentration.," *Am. J. Physiol.*, vol. 246, no. 5 Pt 2, pp. F609-19, 1984.

[93] P. D. Cabral, J. L. Garvin, J. W. Verlander, S. Hong, V. Pech, J. L. Bailey, D. Agazatian, W. Sharon, T. M. Coffman, T. Le, T. Inagami, F. M. Whitehill, I. David, D. B. Farley, Y. H. Kim, S. M. Wall, P. D. Cabral, and J. L. Garvin, "Luminal flow regulates NO and O 2 − along the nephron Luminal flow regulates NO and O ⧖ 2 along the nephron," no. February 2011, pp. 1047–1053, 2012.

[94] K.-J. Jang and K.-Y. Suh, "A multi-layer microfluidic device for efficient culture and analysis of renal tubular cells," *Lab Chip*, vol. 10, no. 1, pp. 36–42, 2010.

[95] R. Baudoin, L. Griscom, M. Monge, C. Legallais, and E. Leclerc, "Development of a renal microchip for in vitro distal tubule models," *Biotechnol. Prog.*, vol. 23, no. 5, pp. 1245–1253, 2007.

[96] W. Liu, S. Xu, C. Woda, P. Kim, S. Weinbaum, and L. M. Satlin, "Effect of flow and stretch on the [Ca Effect of flow and stretch on the [Ca 2ƨ] i response of principal and intercalated cells in cortical collecting duct," *Am J Physiol Ren. Physiol Am. J. Physiol. - Renal Physiol.*, vol. 285, pp. 998–1012, 2003.

[97] M. B. Hovater, D. Olteanu, E. L. Hanson, N. L. Cheng, B. Siroky, A. Fintha, P. Komlosi, W. Liu, L. M. Satlin, P. D. Bell, B. K. Yoder, and E. M. Schwiebert, "Loss of apical monocilia on collecting duct principal cells impairs ATP secretion across the apical cell surface and ATP-dependent and flow-induced calcium signals," *Purinergic Signal.*, vol. 4, no. 2, pp. 155–170, 2008.

[98] K. Babinger and R. Witzgall, "Primary cilia and polycystic kidney disease," no. 1, pp. 8–13, 2010.

[99] R. Rohatgi and D. Flores, "Intra-

tubular hydrodynamic forces influence tubulo-interstitial fibrosis in the kidney," *Curr Opin Nephrol Hypertens*, vol. 4, no. 1, pp. 78–90, 2010.

[100] L. G. Palmer and G. Frindt, "Gating of the Na Channels in the rat cortical collecting tubule: Effect of Voltage and Membrane strech," *Am. J. Physiol.*, vol. 271, no. 5 Pt 2, pp. F1086–F1092, 1996.

[101] H. a Drummond, M. J. Welsh, and F. M. Abboud, "ENaC subunits are molecular components of the arterial baroreceptor complex.," *Ann. N. Y. Acad. Sci.*, vol. 940, pp. 42–7, 2001.

[102] M. Fronius and W. G. Clauss, "Mechano-sensitivity of ENaC: May the (shear) force be with you," *Pflugers Arch. Eur. J. Physiol.*, vol. 455, no. 5, pp. 775–785, 2008.

[103] F. T. Bosman and I. Stamenkovic, "Functional structure and composition of the extracellular matrix," *J. Pathol.*, vol. 200, no. 4, pp. 423–428, 2003.

[104] F. Genovese, A. a Manresa, D. J. Leeming, M. A. Karsdal, and P. Boor, "The extracellular matrix in the kidney: a source of novel non-invasive biomarkers of kidney fibrosis?," *Fibrogenesis Tissue Repair*, vol. 7, no. 1, p. 4, 2014.

[105] A. J. Engler, S. Sen, H. L. Sweeney, and D. E. Discher, "Matrix Elasticity Directs Stem Cell Lineage Specification," *Cell*, vol. 126, no. 4, pp. 677–689, 2006.

[106] J. L. Leight, M. A. Wozniak, S. Chen, M. L. Lynch, and C. S. Chen, "Matrix rigidity regulates a switch between TGF- 1-induced apoptosis and epithelial-mesenchymal transition," *Mol. Biol. Cell*, vol. 23, no. 5, pp. 781–791, 2012.

[107] R. G. Wells, "Tissue mechanics and fibrosis," *Biochim. Biophys. Acta - Mol. Basis Dis.*, vol. 1832, no. 7, pp. 884–890, 2013.

[108] T. M. DesRochers, L. Suter, A. Roth, and D. L. Kaplan, "Bioengineered 3D Human Kidney Tissue, a Platform for the Determination of Nephrotoxicity," *PLoS One*, vol. 8, no. 3, 2013.

[109] F. Pampaloni, E. G. Reynaud, and E. H. K. Stelzer, "The third dimension bridges the gap between cell culture and live tissue.," *Nat. Rev. Mol. Cell Biol.*, vol. 8, no. 10, pp. 839–845, 2007.

[110] S. V Murphy and A. Atala, "3D bioprinting of tissues and organs," *Nat. Biotechnol.*, vol. 32, p. 773, Aug. 2014.

[111] N. S. Bhise, J. Ribas, V. Manoharan, Y. S. Zhang, A. Polini, S. Massa, M. R. Dokmeci, and A. Khademhosseini, "Organ-on-a-chip platforms for studying drug delivery systems," *J. Control. Release*, vol. 190, pp. 82–93, 2014.

[112] I. T. Ozbolat and Y. Yu, "Bioprinting Toward Organ Fabrication: Challenges and Future Trends," *IEEE Trans. Biomed. Eng.*, vol. 60, no. 3, pp. 691–699, 2013.

[113] E. D. Miller, K. Li, T. Kanade, L. E. Weiss, L. M. Walker, and P. G. Campbell, "Spatially directed guidance of stem cell population migration by immobilized patterns of growth

factors," *Biomaterials*, vol. 32, no. 11, pp. 2775–2785, Apr. 2011.

[114] N. L'Heureux, S. Pâquet, R. Labbé, L. Germain, and F. A. Auger, "A completely biological tissue-engineered human blood vessel.," *FASEB J.*, vol. 12, no. 1, pp. 47–56, 1998.

[115] S. Einav, D. Gerber, P. D. Bryson, E. H. Sklan, M. Elazar, S. J. Maerkl, J. S. Glenn, and S. R. Quake, "Discovery of a hepatitis C target and its pharmacological inhibitors by microfluidic affinity analysis.," *Nat. Biotechnol.*, vol. 26, no. 9, pp. 1019–1027, Sep. 2008.

[116] R. Chang, K. Emami, H. Wu, and W. Sun, "Biofabrication of a three-dimensional liver micro-organ as an *in vitro* drug metabolism model," *Biofabrication*, vol. 2, no. 4, p. 045004, 2010.

[117] X. Zhang, B. Xu, D. S. Puperi, Y. Wu, J. L. West, and K. J. Grande-Allen, *Application of hydrogels in heart valve tissue engineering.*, vol. 25, no. 1–2. 2015.

[118] H. Lipson and M. Kurman, *Fabricated: The new world of 3D printing.* John Wiley & Sons, 2013.

[119] B. Mueller, "Additive manufacturing technologies–Rapid prototyping to direct digital manufacturing," *Assem. Autom.*, vol. 32, no. 2, 2012.

[120] P. F. Jacobs, *Rapid prototyping & manufacturing: fundamentals of stereolithography.* Society of Manufacturing Engineers, 1992.

[121] C. Sun, N. Fang, D. M. Wu, and X. Zhang, "Projection micro-stereolithography using digital micro-mirror dynamic mask," *Sensors Actuators A Phys.*, vol. 121, no. 1, pp. 113–120, 2005.

[122] K. L. K., "Kidney transplant outcomes: Does position on the match-run matter?," *Am. J. Transplant.*, vol. 18, no. 6, p. 1576, Mar. 2018.

[123] S. Said and G. T. Hernandez, "The link between chronic kidney disease and cardiovascular disease," *J. Nephropathol.*, vol. 3, no. 3, p. 99, 2014.

[124] X.-M. Meng, D. J. Nikolic-Paterson, and H. Y. Lan, "Inflammatory processes in renal fibrosis," *Nat. Rev. Nephrol.*, vol. 10, no. 9, pp. 493–503, 2014.

[125] G. J. Becker and T. D. Hewitson, "Animal models of chronic kidney disease: Useful but not perfect," *Nephrol. Dial. Transplant.*, vol. 28, no. 10, pp. 2432–2438, 2013.

[126] W. S. Redfern, "Inclusion of Safety Pharmacology Endpoints in Repeat-Dose Toxicity Studies," in *Principles of Safety Pharmacology*, M. K. Pugsley and M. J. Curtis, Eds. Berlin, Heidelberg: Springer Berlin Heidelberg, 2015, pp. 353–381.

[127] M. Bens, V. Vallet, F. Cluzeaud, L. Pascual-Letallec, A. Kahn, M. E. Rafestin-Oblin, B. C. Rossier, and A. Vandewalle, "Corticosteroid-dependent sodium transport in a novel immortalized mouse collecting duct principal cell line.," *J. Am. Soc. Nephrol.*, vol. 10, no. 5, pp. 923–34, 1999.

[128] B. Subramanian, D. Rudym, C. Cannizzaro, R. Perrone, J. Zhou, and D. L. Kaplan, "Tissue-Engineered Three-Dimensional *In Vitro* Models for Normal and Diseased Kidney," *Tissue Eng. Part A*, vol. 16, no. 9, pp. 2821–2831, 2010.

[129] S. N. Bhatia and D. E. Ingber, "Microfluidic organs-on-chips," *Nat. Biotechnol.*, vol. 32, no. 8, pp. 760–772, 2014.

[130] A. Tourovskaia, M. Fauver, G. Kramer, S. Simonson, and T. Neumann, "Tissue-engineered microenvironment systems for modeling human vasculature," *Exp. Biol. Med.*, vol. 239, no. 9, pp. 1264–1271, Sep. 2014.

[131] E. J. Weber, A. Chapron, B. D. Chapron, J. L. Voellinger, K. A. Lidberg, C. K. Yeung, Z. Wang, Y. Yamaura, D. W. Hailey, T. Neumann, D. D. Shen, K. E. Thummel, K. A. Muczynski, J. Himmelfarb, and E. J. Kelly, "Development of a microphysiological model of human kidney proximal tubule function," *Kidney Int.*, vol. 90, no. 3, pp. 627–637, 2016.

[132] K. A. Homan, D. B. Kolesky, M. A. Skylar-Scott, J. Herrmann, H. Obuobi, A. Moisan, and J. A. Lewis, "Bioprinting of 3D Convoluted Renal Proximal Tubules on Perfusable Chips," *Sci Rep*, vol. 6, p. 34845, 2016.

[133] D. B. Kolesky, K. A. Homan, M. A. Skylar-Scott, and J. A. Lewis, "Three-dimensional bioprinting of thick vascularized tissues," *Proc. Natl. Acad. Sci.*, vol. 113, no. 12, pp. 3179–3184, 2016.

[134] L. E. Bertassoni, M. Cecconi, V. Manoharan, M. Nikkhah, J. Hjortnaes, A. L. Cristino, G. Barabaschi, D. Demarchi, M. R. Dokmeci, Y. Yang, and A. Khademhosseini, "Hydrogel bioprinted microchannel networks for vascularization of tissue engineering constructs," *Lab Chip*, vol. 14, no. 13, pp. 2202–2211, 2014.

[135] W. Jia, P. S. Gungor-Ozkerim, Y. S. Zhang, K. Yue, K. Zhu, W. Liu, Q. Pi, B. Byambaa, M. R. Dokmeci, S. R. Shin, and A. Khademhosseini, "Direct 3D bioprinting of perfusable vascular constructs using a blend bioink," *Biomaterials*, vol. 106, no. 106, pp. 58–68, Nov. 2016.

[136] Y. He, F. Yang, H. Zhao, Q. Gao, B. Xia, and J. Fu, "Research on the printability of hydrogels in 3D bioprinting.," *Sci. Rep.*, vol. 6, p. 29977, 2016.

[137] J. Li, M. Chen, X. Fan, and H. Zhou, "Recent advances in bioprinting techniques: approaches, applications and future prospects," *J. Transl. Med.*, vol. 14, no. 1, p. 271, 2016.

[138] C. P. Ng, Y. Zhuang, A. W. H. Lin, and J. C. M. Teo, "A Fibrin-Based Tissue-Engineered Renal Proximal Tubule for Bioartificial Kidney Devices: Development, Characterization and In Vitro Transport Study," *Int. J. Tissue Eng.*, vol. 2013, pp. 1–10, 2013.

[139] H. D. Humes, D. a Buffington, S. M. MacKay, a J. Funke, and W. F. Weitzel, "Replacement of renal function in uremic animals with a

tissue-engineered kidney.," *Nat. Biotechnol.*, vol. 17, no. 5, pp. 451–455, 1999.

[140] D. W. Johnson, C. Sherborne, M. P. Didsbury, C. Pateman, N. R. Cameron, and F. Claeyssens, "Macrostructuring of emulsion-templated porous polymers by 3D laser patterning," *Adv. Mater.*, vol. 25, no. 23, pp. 3178–3181, 2013.

[141] M.-T. Grosse, M. Lamotte, M. Birot, and H. Deleuze, "Preparation of microcellular polysiloxane monoliths," *J. Polym. Sci. Part A Polym. Chem.*, vol. 46, no. 1, pp. 21–32, 2008.

[142] C. Youssef, R. Backov, M. Treguer, M. Birot, and H. Deleuze, "Preparation of Amazingly Hard polyHIPE material from a Direct Emulsion," *MRS Proc.*, vol. 1269, pp. 1269–FF03-07, 2010.

[143] S. Kovačič, K. Jeřábek, P. Krajnc, and C. Slugovc, "Ring opening metathesispolymerisation of emulsion templated dicyclopentadiene giving open porous materials with excellent mechanical properties," *Polym. Chem.*, vol. 3, no. 2, pp. 325–328, 2012.

[144] S. Caldwell, D. W. Johnson, M. P. Didsbury, B. A. Murray, J. J. Wu, S. A. Przyborski, and N. R. Cameron, "Degradable emulsion-templated scaffolds for tissue engineering from thiol-ene photopolymerisation," *Soft Matter*, vol. 8, no. 40, pp. 10344–10351, 2012.

[145] S. D. Kimmins, P. Wyman, and N. R. Cameron, "Photopolymerised methacrylate-based emulsion-templated porous polymers," *React. Funct. Polym.*, vol. 72, no. 12, pp. 947–954, 2012.

[146] R. Owen, C. Sherborne, T. Paterson, N. H. Green, G. C. Reilly, and F. Claeyssens, "Emulsion templated scaffolds with tunable mechanical properties for bone tissue engineering," *J. Mech. Behav. Biomed. Mater.*, vol. 54, pp. 159–172, 2016.

[147] T. P. Burton and A. Callanan, "A Non-woven Path: Electrospun Poly(lactic acid) Scaffolds for Kidney Tissue Engineering," *Tissue Eng. Regen. Med.*, 2018.

[148] E. Rosines, K. Johkura, X. Zhang, H. J. Schmidt, M. Decambre, K. T. Bush, and S. K. Nigam, "Constructing kidney-like tissues from cells based on programs for organ development: toward a method of in vitro tissue engineering of the kidney.," *Tissue Eng. Part A*, vol. 16, no. 8, pp. 2441–55, 2010.

[149] T. M. DesRochers, E. Palma, and D. L. Kaplan, "Tissue-engineered kidney disease models," *Adv. Drug Deliv. Rev.*, vol. 69–70, pp. 67–80, 2014.

[150] I. Maschmeyer, A. K. Lorenz, K. Schimek, T. Hasenberg, A. P. Ramme, J. Hubner, M. Lindner, C. Drewell, S. Bauer, A. Thomas, N. S. Sambo, F. Sonntag, R. Lauster, and U. Marx, "A four-organ-chip for interconnected long-term co-culture of human intestine, liver, skin and kidney equivalents," *Lab Chip*, vol. 15, no. 12, pp. 2688–2699, 2015.

[151] J. A. Ryan, "Cell Cloning by Serial Dilution in 96 Well Plates Protocol," *Life Sci.*, no. 4485, pp. 10–12, 2008.

[152] S. Andrews, "FastQC A Quality Control tool for High Throughput Sequence Data," *http://www.bioinformatics.babraham.ac.uk/projects/fastqc/*. .

[153] A. M. Bolger, M. Lohse, and B. Usadel, "Trimmomatic: a flexible trimmer for Illumina sequence data," *Bioinformatics*, vol. 30, no. 15, pp. 2114–2120, 2014.

[154] D. Kim, B. Langmead, and S. L. Salzberg, "HISAT: A fast spliced aligner with low memory requirements," *Nat. Methods*, vol. 12, no. 4, pp. 357–360, 2015.

[155] L. Wang, S. Wang, and W. Li, "RSeQC: quality control of RNA-seq experiments," *Bioinformatics*, vol. 28, no. 16, pp. 2184–2185, 2012.

[156] R. Patro, G. Duggal, and C. Kingsford, "Salmon: Accurate, Versatile and Ultrafast Quantification from RNA-seq Data using Lightweight-Alignment," *bioRxiv*, Jan. 2015.

[157] C. Soneson, M. I. Love, and M. D. Robinson, "Differential analyses for RNA-seq: transcript-level estimates improve gene-level inferences [version 1; referees: 2 approved]," *F1000Research*, vol. 4, no. 1521, 2015.

[158] M. D. Robinson and A. Oshlack, "A scaling normalization method for differential expression analysis of RNA-seq data," *Genome Biol.*, vol. 11, no. 3, p. R25, 2010.

[159] M. D. Robinson, D. J. McCarthy, and G. K. Smyth, "edgeR: a Bioconductor package for differential expression analysis of digital gene expression data.," *Bioinformatics*, vol. 26, no. 1, pp. 139–140, Jan. 2010.

[160] E. L. Boulpaep and J. F. Seely, "Electrophysiology of proximal and distal tubules in the autoperfused dog kidney," *Am. J. Physiol. Content*, vol. 221, no. 4, pp. 1084–1096, 1971.

[161] M. Scanziani and M. Häusser, "Electrophysiology in the age of light," *Nature*, vol. 461, no. 7266, pp. 930–939, 2009.

[162] E. L. Boulpaep, "Electrophysiology of the kidney," *Transp. Across Biol. Membr. G. Giebisch, DC Tosteson, HH Ussing, Ed. Springer-Verlag, Berlin, Ger.*, pp. 97–144, 1979.

[163] M. D. Breyer and Y. Ando, "Hormonal signaling and regulation of salt and water transport in the collecting duct," *Annu Rev Physiol*, vol. 56, pp. 711–739, 1994.

[164] K. Tomita, J. J. Pisano, and M. A. Knepper, "Control of sodium and potassium transport in the cortical collecting duct of the rat. Effects of bradykinin, vasopressin, and deoxycorticosterone.," *J. Clin. Invest.*, vol. 76, no. 1, pp. 132–136, 1985.

[165] R. E. Steele, J. S. Handler, A. Preston, and J. P. Johnson, "A device for sterile measurement of transepithelial electrical parameters of cultured cells," *J. tissue Cult. methods*, vol. 14, no. 4, pp. 259–263, 1992.

[166] H. Li, D. N. Sheppard, and M. J. Hug, "Transepithelial electrical measurements with the Ussing chamber," *J. Cyst. Fibros.*, vol. 3, pp.

123–126, 2004.

[167] L. Chen, J. W. Lee, C.-L. Chou, A. V. Nair, M. A. Battistone, T. G. Păunescu, M. Merkulova, S. Breton, J. W. Verlander, S. M. Wall, D. Brown, M. B. Burg, and M. A. Knepper, "Transcriptomes of major renal collecting duct cell types in mouse identified by single-cell RNA-seq," *Proc. Natl. Acad. Sci.*, p. 201710964, 2017.

[168] M. Langworthy, B. Zhou, M. de Caestecker, G. Moeckel, and H. S. Baldwin, "NFATc1 identifies a population of proximal tubule cell progenitors.," *J. Am. Soc. Nephrol.*, vol. 20, no. 2, pp. 311–321, 2009.

[169] Y. Kotelevtsev, J. R. Seckl, and J. J. Mullins, "11β-Hydroxysteroid dehydrogenases: key modulators of glucocorticoid action in vivo," *Curr. Opin. Endocrinol. Diabetes Obes.*, vol. 6, no. 3, 1999.

[170] J. M. Apostolakos and L. C. Caines, "Apparent Mineralocorticoid Excess Syndrome: A Case of Resistant Hypertension From Licorice Tea Consumption," *J. Clin. Hypertens.*, vol. 18, no. 10, pp. 991–993, 2016.

[171] M. A. Bailey, J. M. Paterson, P. W. F. Hadoke, N. Wrobel, C. O. C. Bellamy, D. G. Brownstein, J. R. Seckl, and J. J. Mullins, "A switch in the mechanism of hypertension in the syndrome of apparent mineralocorticoid excess.," *J. Am. Soc. Nephrol.*, vol. 19, no. 1, pp. 47–58, 2008.

[172] P. C. White, "11β-Hydroxysteroid Dehydrogenase and Its Role in the Syndrome of Apparent Mineralocorticoid Excess," *Am. J. Med. Sci.*, vol. 322, no. 6, pp. 308–315, 2001.

[173] D. Brown, T. G. Paunescu, S. Breton, and V. Marshansky, "Regulation of the V-ATPase in kidney epithelial cells: dual role in acid{\textendash}base homeostasis and vesicle trafficking," *J. Exp. Biol.*, vol. 212, no. 11, pp. 1762–1772, 2009.

[174] C. Norotte, F. S. Marga, L. E. Niklason, and G. Forgacs, "Scaffold-free vascular tissue engineering using bioprinting," *Biomaterials*, vol. 30, no. 30, pp. 5910–5917, 2009.

[175] X. Cui and T. Boland, "Human microvasculature fabrication using thermal inkjet printing technology," *Biomaterials*, vol. 30, no. 31, pp. 6221–6227, 2009.

[176] Q. Gao, Y. He, J. Fu, A. Liu, and L. Ma, "Coaxial nozzle-assisted 3D bioprinting with built-in microchannels for nutrients delivery," *Biomaterials*, vol. 61, pp. 203–215, 2015.

[177] D. F. Williams, "On the mechanisms of biocompatibility," *Biomaterials*, vol. 29, no. 20, pp. 2941–2953, 2008.

[178] T. Fujii, "PDMS-based microfluidic devices for biomedical applications," *Microelectron. Eng.*, vol. 61–62, pp. 907–914, 2002.

[179] A. Siddique, T. Meckel, R. W. Stark, and S. Narayan, "Improved cell adhesion under shear stress in PDMS microfluidic devices," *Colloids Surfaces B Biointerfaces*, vol. 150, pp. 456–464, 2017.

[180] S. Halldorsson, E. Lucumi, R. Gómez-Sjöberg, and R. M. T. Fleming, "Advantages and challenges of microfluidic cell culture in polydimethylsiloxane devices," *Biosens. Bioelectron.*, vol. 63, pp. 218–231, 2015.

[181] B. J. van Meer, H. de Vries, K. S. A. Firth, J. van Weerd, L. G. J. Tertoolen, H. B. J. Karperien, P. Jonkheijm, C. Denning, A. P. IJzerman, and C. L. Mummery, "Small molecule absorption by PDMS in the context of drug response bioassays," *Biochem. Biophys. Res. Commun.*, vol. 482, no. 2, pp. 323–328, 2017.

[182] R. N. Khuri, M. Wiederholt, N. Strieder, and G. Giebisch, "Effects of flow rate and potassium intake on distal tubular potassium transfer," *Am. J. Physiol.*, vol. 228, no. 4, pp. 1249–1261, 1975.

[183] M. A. Cortney, W. Nagel, and K. Thurau, "A micropuncture study of the relationship between flow-rate through the loop of Henle and sodium concentration in the early distal tubule," *Pfl??gers Arch. f??r die Gesamte Physiol. des Menschen und der Tiere*, vol. 287, no. 3, pp. 286–295, 1966.

[184] M. Ravi, V. Paramesh, S. R. Kaviya, E. Anuradha, and F. D. Paul Solomon, "3D cell culture systems: Advantages and applications," *J. Cell. Physiol.*, vol. 230, no. 1, pp. 16–26, 2015.

[185] M. Vinci, S. Gowan, F. Boxall, L. Patterson, M. Zimmermann, W. Court, C. Lomas, M. Mendiola, D. Hardisson, and S. A. Eccles, "Advances in establishment and analysis of three-dimensional tumor spheroid-based functional assays for target validation and drug evaluation," *BMC Biol.*, vol. 10, no. 1, p. 29, Mar. 2012.

[186] G. Efstratiadis, M. Divani, E. Katsioulis, and G. Vergoulas, "Renal fibrosis," *Hippokratia*, vol. 13, no. 4, pp. 224–229, 2009.

[187] D. Harjanto and M. H. Zaman, "Matrix mechanics and receptor-ligand interactions in cell adhesion.," *Org. Biomol. Chem.*, vol. 8, no. 2, pp. 299–304, 2010.

[188] D. Antoni, H. Burckel, E. Josset, and G. Noel, "Three-Dimensional Cell Culture: A Breakthrough in Vivo," *Int. J. Mol. Sci.*, vol. 16, no. 3, pp. 5517–5527, Mar. 2015.

[189] K. Shin, V. C. Fogg, and B. Margolis, "Tight Junctions and Cell Polarity," *Annu. Rev. Cell Dev. Biol.*, vol. 22, no. 1, pp. 207–235, Oct. 2006.

[190] C. Zihni, C. Mills, K. Matter, and M. S. Balda, "Tight junctions: from simple barriers to multifunctional molecular gates," *Nat. Rev. Mol. Cell Biol.*, vol. 17, p. 564, Jun. 2016.

[191] B. N. G. Giepmans and S. C. D. van IJzendoorn, "Epithelial cell–cell junctions and plasma membrane domains," *Biochim. Biophys. Acta - Biomembr.*, vol. 1788, no. 4, pp. 820–831, 2009.

[192] F. Hanner, C. M. Sorensen, N.-H. Holstein-Rathlou, and J. Peti-Peterdi, "Connexins and the kidney," *Am. J. Physiol. - Regul. Integr. Comp.*

Physiol., vol. 298, no. 5, pp. R1143–R1155, May 2010.

[193] R. Parent, M. J. Marion, L. Furio, C. Trépo, and M. A. Petit, "Origin and Characterization of a Human Bipotent Liver Progenitor Cell Line," *Gastroenterology*, vol. 126, no. 4, pp. 1147–1156, 2004.

[194] F. Trepiccione, G. Capasso, S. Nielsen, and B. M. Christensen, "Evaluation of cellular plasticity in the collecting duct during recovery from lithium-induced nephrogenic diabetes insipidus.," *Am. J. Physiol. Renal Physiol.*, vol. 305, no. 6, pp. F919-29, 2013.

[195] M. J. Briske-Anderson, J. W. Finley, and S. M. Newman, "The Influence of Culture Time and Passage Number on the Morphological and Physiological Development of Caco-2 Cells," *Proc. Soc. Exp. Biol. Med.*, vol. 214, no. 3, pp. 248–257, Mar. 1997.

[196] S. L. Wenger, J. R. Senft, L. M. Sargent, R. Bamezai, N. Bairwa, and S. G. Grant, "Comparison of Established Cell Lines at Different Passages by Karyotype and Comparative Genomic Hybridization," *Biosci. Rep.*, vol. 24, no. 6, p. 631 LP-639, Dec. 2004.

[197] W. H. Dantzler, "Regulation of renal proximal and distal tubule transport: sodium, chloride and organic anions," *Comp. Biochem. Physiol. Part A Mol. Integr. Physiol.*, vol. 136, no. 3, pp. 453–478, 2003.

[198] S. F. Ibrahim and G. van den Engh, "Flow Cytometry and Cell Sorting BT - Cell Separation: Fundamentals, Analytical and Preparative Methods," A. Kumar, I. Y. Galaev, and B. Mattiasson, Eds. Berlin, Heidelberg: Springer Berlin Heidelberg, 2007, pp. 19–39.

[199] J. Erenpreisa and M. S. Cragg, "Three steps to the immortality of cancer cells: senescence, polyploidy and self-renewal," *Cancer Cell Int.*, vol. 13, p. 92, Sep. 2013.

[200] K. P. Schoenfelder and D. T. Fox, "The expanding implications of polyploidy," *J. Cell Biol.*, vol. 209, no. 4, p. 485 LP-491, May 2015.

[201] D. Kim, B. Alptekin, and H. Budak, "CRISPR/Cas9 genome editing in wheat," *Funct. Integr. Genomics*, vol. 18, no. 1, pp. 31–41, 2018.

[202] V. Stovicek, I. Borodina, and J. Forster, "CRISPR–Cas system enables fast and simple genome editing of industrial Saccharomyces cerevisiae strains," *Metab. Eng. Commun.*, vol. 2, pp. 13–22, 2015.

[203] P.-Y. Tung, J. D. Blischak, C. J. Hsiao, D. A. Knowles, J. E. Burnett, J. K. Pritchard, and Y. Gilad, "Batch effects and the effective design of single-cell gene expression studies," *Sci. Rep.*, vol. 7, p. 39921, Jan. 2017.

[204] L. Chen, J. W. Lee, C.-L. Chou, A. V. Nair, M. A. Battistone, T. G. Păunescu, M. Merkulova, S. Breton, J. W. Verlander, S. M. Wall, D. Brown, M. B. Burg, and M. A. Knepper, "Transcriptomes of major renal collecting duct cell types in mouse identified by single-cell RNA-seq," *Proc. Natl. Acad. Sci.*, p. 201710964, 2017.

[205] H. Vidarsson, R. Westergren, M. Heglind, S. R. Blomqvist, S. Breton, and S. Enerbäck, "The Forkhead Transcription Factor Foxi1 Is a Master Regulator of Vacuolar H+-ATPase Proton Pump Subunits in the Inner Ear, Kidney and Epididymis," *PLoS One*, vol. 4, no. 2, p. e4471, Feb. 2009.

[206] I. Kurth, M. Hentschke, S. Hentschke, U. Borgmeyer, A. Gal, and C. A. Hübner, "The forkhead transcription factor Foxi1 directly activates the AE4 promoter," *Biochem. J.*, vol. 393, no. 1, p. 277 LP-283, Jan. 2006.

[207] J. Grassmeyer, M. Mukherjee, J. deRiso, C. Hettinger, M. Bailey, S. Sinha, J. E. Visvader, H. Zhao, E. Fogarty, and K. Surendran, "Elf5 is a principal cell lineage specific transcription factor in the kidney that contributes to Aqp2 and Avpr2 gene expression," *Dev. Biol.*, vol. 424, no. 1, pp. 77–89, 2017.

[208] D. Suma, A. Acun, and P. Zorlutuna, "Interdependence theory of tissue failure : bulk and boundary effects Subject Category : Subject Areas :," 2018.

[209] Y. Li, T. D. Majarian, A. W. Naik, G. R. Johnson, and R. F. Murphy, "Point process models for localization and interdependence of punctate cellular structures," *Cytom. Part A*, vol. 89, no. 7, pp. 633–643, 2016.

[210] E. A. Waddell, "Laser Ablation as a Fabrication Technique for Microfluidic Devices BT - Microfluidic Techniques: Reviews and Protocols," S. D. Minteer, Ed. Totowa, NJ: Humana Press, 2006, pp. 27–38.

[211] D. Huh, G. A. Hamilton, and D. E. Ingber, "From 3D cell culture to organs-on-chips," *Trends Cell Biol.*, vol. 21, no. 12, pp. 745–754, Mar. 2018.

[212] X. (James) Li, A. V Valadez, P. Zuo, and Z. Nie, "Microfluidic 3D cell culture: potential application for tissue-based bioassays," *Bioanalysis*, vol. 4, no. 12, pp. 1509–1525, Jun. 2012.

[213] S. M. Mantila Roosa, J. M. Kemppainen, E. N. Moffitt, P. H. Krebsbach, and S. J. Hollister, "The pore size of polycaprolactone scaffolds has limited influence on bone regeneration in an in vivo model," *J. Biomed. Mater. Res. - Part A*, vol. 92, no. 1, pp. 359–368, 2010.

[214] Y. Cao, G. Mitchell, A. Messina, L. Price, E. Thompson, A. Penington, W. Morrison, A. O'Connor, G. Stevens, and J. Cooper-White, "The influence of architecture on degradation and tissue ingrowth into three-dimensional poly(lactic-co-glycolic acid) scaffolds in vitro and in vivo," *Biomaterials*, vol. 27, no. 14, pp. 2854–2864, 2006.

[215] G. Akay, M. A. Birch, and M. A. Bokhari, "Microcellular polyHIPE polymer supports osteoblast growth and bone formation in vitro," *Biomaterials*, vol. 25, no. 18, pp. 3991–4000, 2004.

[216] D. R. Miller, J. W. Jarrett, A. M. Hassan, and A. K. Dunn, "Deep tissue imaging with multiphoton fluorescence microscopy," *Curr. Opin. Biomed. Eng.*, vol. 4, pp. 32–39, 2017.

[217] P. Theer, M. T. Hasan, and W. Denk, "Two-photon imaging to a depth of 1000 µm in living brains by use of a Ti:Al2O3 regenerative amplifier," *Opt. Lett.*, vol. 28, no. 12, pp. 1022–1024, 2003.

[218] K. Wang, W. Sun, C. T. Richie, B. K. Harvey, E. Betzig, and N. Ji, "Direct wavefront sensing for high-resolution in vivo imaging in scattering tissue," *Nat. Commun.*, vol. 6, pp. 1–6, 2015.

[219] N. G. Horton, K. Wang, D. Kobat, C. G. Clark, F. W. Wise, C. B. Schaffer, and C. Xu, "In vivo three-photon microscopy of subcortical structures within an intact mouse brain," *Nat. Photonics*, vol. 7, no. 3, pp. 205–209, 2013.

[220] D. Kobat, N. G. Horton, and C. Xu, "*In vivo* two-photon microscopy to 1.6-mm depth in mouse cortex," vol. 16, no., pp. 106014–106015, 2011.

[221] A. Petrosyan, I. Zanusso, M. Lavarreda-Pearce, S. Leslie, S. Sedrakyan, R. E. De Filippo, G. Orlando, S. Da Sacco, and L. Perin, "Decellularized Renal Matrix and Regenerative Medicine of the Kidney: A Different Point of View," *Tissue Eng. Part B Rev.*, vol. 22, no. 3, pp. 183–192, Dec. 2015.

[222] B. Bonandrini, M. Figliuzzi, E. Papadimou, M. Morigi, N. Perico, F. Casiraghi, C. Dipl, F. Sangalli, S. Conti, A. Benigni, A. Remuzzi, and G. Remuzzi, "Recellularization of Well-Preserved Acellular Kidney Scaffold Using Embryonic Stem Cells," *Tissue Eng. Part A*, vol. 20, no. 9–10, pp. 1486–1498, Dec. 2013.

[223] I. F. and M. W. and B. R. and N. B. and K. H. and I. U. and P. R. and A. K. and H. Stachelscheid, "Comparative characterization of decellularized renal scaffolds for tissue engineering," *Biomed. Mater.*, vol. 12, no. 4, p. 45005, 2017.

[224] D. E. Discher, P. Janmey, and Y. Wang, "Tissue Cells Feel and Respond to the Stiffness of Their Substrate," *Science (80-.).*, vol. 310, no. 5751, p. 1139 LP-1143, Nov. 2005.

[225] A. Asti and L. Gioglio, "Natural and synthetic biodegradable polymers: Different scaffolds for cell expansion and tissue formation," *Int. J. Artif. Organs*, vol. 37, no. 3, pp. 187–205, 2014.

[226] S. H. Kim, J. Turnbull, and S. Guimond, "Extracellular matrix and cell signalling: The dynamic cooperation of integrin, proteoglycan and growth factor receptor," *J. Endocrinol.*, vol. 209, no. 2, pp. 139–151, 2011.

[227] S. J. Yarwood and J. R. Woodgett, "Extracellular matrix composition determines the transcriptional response to epidermal growth factor receptor activation," *Proc. Natl. Acad. Sci.*, vol. 98, no. 8, p. 4472 LP-4477, Apr. 2001.

[228] G. Gamba, W. Wang, and L. Schild, *Sodium Chloride Transport in the Loop of Henle, Distal Convoluted Tubule, and Collecting Duct*, Fifth Edit., vol. 1. Elsevier Inc., 2013.

9 Appendix

- **Appendix 1:** Butterworth, Michael B. "The Tale of Two (Distal Nephron) Cell Types." *American Journal of Physiology-Renal Physiology*, vol. 314, 2018.

- **Appendix 2:** A. M. Assmus, M. K. Mansley, L. J. Mullins, A. Peter, and J. J. Mullins, "mCCDcl1 cells show Plasticity Consistent with the Ability to Transition between Principal and Intercalated Cells", *American Journal of Physiology-Renal Physiology, vol.* 314, nb 5, pp. 820-831, 2018.

9.1 Appendix 1: Am. J. Physiol. Editorial, *"The Tale of Two (Distal Nephron) Cell Types"* (in press), by Michael B. Butterworth (University of Pittsburgh School of Medecine, Pittsburgh, PA)

The kidney nephron represents an exquisite example of epithelial cell differentiation and specialization in one small tubule (6). Plasma filtrate passing down the length of a few millimetres will encounter at least 6 cell types, each highly specialized in form and function. The lineage of the cells lining the nephron are from 2 embryonic sources. The ureteric bud emerges from the mesonephric (Wolffian) duct and interacts with metanephric mesenchymal cells to form a cap mesenchyme. The renal vesicle formed from this interaction will ultimately develop into the more proximal structures (glomerulus and most of the mature nephron) with the ureteric bud forming the collecting duct (2). The distal convoluted tubule and collecting duct of the mature mammalian nephron are composed of principal and intercalated (alpha and beta) cells, and the developmental factors that determine terminal cell differentiation are still being investigated (7). These cell types are distinguished by their unique functional roles of, predominantly, ion and water transport for principal cells and acid and base secretions for intercalated cells. To study the function and mechanisms of regulation in these specialized epithelial cell types, researchers have long been interested in developing robust cell culture models that closely approximate the characteristics of these epithelial cells. Using the knowledge gained from in vivo and ex vivo investigations in renal tissue taken from a range of animal models, specific characteristics were sought in a principal cell model line. A robust cell line would polarize into epithelial monolayers when cultured on filter supports. The cells would have the ability to transport ions, predominantly sodium via endogenous epithelial sodium channels (ENaC) down an electrogenic gradient established by the Na^+-K^+-ATPase. Model cells would be capable of potassium transport through apical and basal potassium channels (most notably the apically located renal outer medullary potassium channel, ROMK). The cells would be sensitive to changes in osmotic gradients and be capable of water transport through aquaporins (Aqp2). And more importantly for functional studies, the cells should be sensitive to several hormonal inputs at physiological concentrations, most relevant for this renal nephron segment, this would include insulin, vasopressin and a true mineralocorticoid receptor response to aldosterone signalling. Many cell lines developed over the years exhibited some or several of these characteristics, but none had all of the desired traits (5). It was only when a spontaneously

transformed cell line was derived from a single clone obtained from micro-dissected mouse cortical collecting duct that a novel cell model, named $mCCD_{cl1}$, was developed that appeared to exhibit all these characteristics (4). This $mCCD_{cl1}$ line therefore stood-out for researchers in the field. The cells possessed 11-β-hydroxysteroid dehydrogenase type 2 (HSD11b2) and both mineralocorticoid and glucocorticoid receptors (MR and GR), ensuring a true mineralocorticoid response to physiological concentrations of aldosterone could be achieved (it was the best of times). The cell line is now routinely used in dozens of labs as a model murine principal cell line. However, in the paper by Assmus and colleagues (1), the authors probed deeper into the characteristics of this cell line. By deriving several sub-lines from the parental cells after serial dilution to single cells, they report that not only were some of the desired characteristics of principal cell-specific ion transport diminished or lost, markers to the other distal nephron-resident intercalated cells emerged. They demonstrate cells with intercalated cell-specific markers, in some cases markers for both principal and intercalated cells were observed in the same cells (it was the worst of times). What this study indicated is that characteristics of both principal and intercalated cells were transmitted from a single cell progenitor (via the single cell clonal lines) suggesting that the $mCCD_{cl1}$ cell line is plastic and may have the ability to derive both cell types. This finding adds a very important, novel and underappreciated trait to this cell line. Firstly, is requires labs using this line to carefully evaluate the phenotype of the cells they use, and to be aware that phenotypic regulation measured using one approach (for example electrophysiological methods) may only represent a sub-section of the cells present in culture, and to report their findings in light of this new information. However, it offers a unique opportunity to investigate in more depth the conditions that may give rise to particular cell lineages in the collecting duct. The developmental cues that facilitate terminal differentiation, and the ability of the distal nephron to plastically alter cell populations is an active area of research (3). These cells may represent a novel tool to investigate ideas of renal cell plasticity, progenitor and stem cell regeneration and cellular conversion. The tale of two cell types could therefore be addressed using a single cell model, potentially making this cell line even more valuable to renal researchers (perhaps it is the best of times again).

REFERENCES

1. **Assmus AM, Mansley MK, Mullins LJ, Peter A, Mullins JJ.** mCCDcl1 cells show Plasticity Consistent with the Ability to Transition between Principal and Intercalated Cells. *Am J Physiol – Renal.* (In Press) 2018.
2. **Costantini F.** Genetic controls and cellular behaviors in branching morphogenesis of the renal collecting system. *Wiley Interdiscip Rev Dev Biol* 1: 693-713, 2012.
3. **El-Dahr SS, Li Y, Liu J, Gutierrez E, Hering-Smith KS, Signoretti S, Pignon JC, Sinha S, and Saifudeen Z.** p63+ ureteric bud tip cells are

progenitors of intercalated cells. *JCI Insight* 2, 2017.

4. **Gaeggeler HP, Gonzalez-Rodriguez E, Jaeger NF, Loffing-Cueni D, Norregaard R, Loffing J, Horisberger JD, and Rossier BC.** Mineralocorticoid versus glucocorticoid receptor occupancy mediating aldosterone-stimulated sodium transport in a novel renal cell line. *J Am Soc Nephrol* 16: 878-891, 2005.
5. **Grenier FC.** Characteristics of renal collecting tubule cells in primary culture. *Miner Electrolyte Metab* 12: 58-63, 1986.
6. **Jacobson HR.** Functional segmentation of the mammalian nephron. *Am J Physiol* 241: F203-218, 1981.
7. **Roy A, Al-bataineh MM, and Pastor-Soler NM.** Collecting duct intercalated cell function and regulation. *Clin J Am Soc Nephrol* 10: 305-324, 2015

9.2 Appendix 2: Publication, Am J Physiol – Renal., 2018

$mCCD_{cl1}$ cells show Plasticity Consistent with the Ability to Transition between Principal and Intercalated Cells

A.M. Assmus, M.K. Mansley, L.J. Mullins, A. Peter, J.J. Mullins

University of Edinburgh/BHF Centre for Cardiovascular Science, The University of Edinburgh, Edinburgh, UK EH16 4TJ

Running title:

Plasticity of $mCCD_{cl1}$ cells